Search for R-parity violating supersymmetry in multilepton final states using the ATLAS detector

Matthew Henry Klein

Submitted in partial fulfillment of the
requirements for the degree of
Doctor of Philosophy
in the Graduate School of Arts and Sciences

COLUMBIA UNIVERSITY
2017

ABSTRACT

Search for R-parity violating supersymmetry in multilepton final states using the ATLAS detector

Matthew Henry Klein

This thesis presents a search for R-parity violating supersymmetry at $\sqrt{s} = 13\,\text{TeV}$, using approximately 13.3 $\text{fb}^{-1}$of data collected by ATLAS in 2015 and the first half of 2016. Events are required to contain at least four leptons (electrons or muons only) that are not the product of a Z boson decay, and this requirement results in a low Standard Model background and a high sensitivity to various physics models beyond the Standard Model. No significant deviations from the Standard Model are observed in data, and results are used to set upper limits on the event yields from processes beyond the Standard Model. In a simplified model of chargino production with indirect R-parity violating decays, limits are extended by approximately 400 GeV relative to the Run 1 search, excluding chargino masses below 1.1 TeV.

Contents

List of Figures

List of Tables

Chapter 1

Introduction

The LHC (Large Hadron Collider), designed to collide protons at a center-of-mass energy of 14 TeV, is the most energetic particle collider ever built [1].

Before the LHC began operation, two of the most popular theories for yet-to-be-discovered physics were the Higgs boson, the last piece of the Standard Model, and supersymmetry (SUSY), perhaps the most popular theory beyond the Standard Model. While the Higgs boson discovery was announced in 2012 jointly by the ATLAS and CMS collaborations [2], SUSY has continued to evade discovery.

Broadly speaking, there are two limiting factors in discovering new physics: cross-section and energy. First, making a discovery requires a minimum amount of data. Most obviously, if a process has a low cross-section, enough data must be collected so that these processes would be expected to occur. Further, Standard Model (SM) processes sometimes mimic what would be expected for new physics. To enable a discovery, enough of these new physics processes must occur to statistically separate a signal from the SM background. Therefore, the solution to cross-section limited theories is to collect more data.

Second, the new physics must be kinematically accessible. If a theory predicts particles with masses too high to actually be created in a collider, there is no hope of discovering them. In order to solve such a problem, the collision energy must be increased.

For the most popular SUSY models, the limiting factor has tended to be mass, and SUSY particles may be massive enough that they would have avoided detection in Run 1. For example, many models predict that gluinos would not be significantly higher than the TeV scale, and since such strong interactions would be expected to have high cross-sections, these models would have only remained undetected in Run 1 if their masses were too high to be created. As a result (and certainly not absolutely), increases in collision energy are associated with significant increases in SUSY phase space available for discovery, while increases in the total data collected tend to be associated with more modest improvements.

The LHC increased the collision energy from 8 TeV to 13 TeV in 2015, and this was the largest planned energy increase. A lack of a discovery in Run 2, while not fatal to SUSY in general, means that SUSY will probably not be discovered by the LHC. This thesis documents a search for a family of SUSY models that are particularly sensitive to collision energy, consisting of events with at least four light leptons not consistent with Z decays. While the amount of data considered in this search is still significantly smaller than the full Run 1 dataset and the expected final Run 2 dataset, it is enough to exclude most of the available phase space for our benchmark model. Since this is the last large energy increase, the sensitivity of the LHC to these models will only undergo modest improvements over the remaining LHC lifetime, and the phase space that will ever be available to the LHC for this model is excluded.

The theoretical motivation for SUSY and the particular models considered in this search are discussed in section 2. Also discussed in the section is the modeling of SM background processes and the SUSY signal processes.

Section 3 discusses the nature of the LHC and the ATLAS detector, focusing on the elements of the ATLAS detector that are relevant for this physics search. Also described is the simulation of the ATLAS detector and the interaction of particles with each of the detector subsystems.

Section 4 outlines the reconstruction process that is applied to data and simulation, building objects that represent physics objects from detector energy deposits.

This process is applied to both ATLAS data and physics simulation.

Section 5 discusses the actual physics search, including the search optimization, SM background estimation, systematics, and validation of the search methods in data. The section relies on data for the background estimation and the validation subsections, but the subset of the data that would include the SUSY events themselves are only discussed in the next section.

Section 6 gives the results for the search, including both the SUSY interpretation of the results and a detailed look at the observed signal region events. Lastly, the outlook of SUSY in general is discussed in Section 7.

Chapter 2

Theoretical Foundation

2.1 Standard Model

The Standard Model is a complete, self-consistent model of particle physics. Starting from a set of fields defining the quarks and leptons, a set of local symmetries, the Higgs sector, and a set of constants, it predicts the behavior of all the particle interactions that can occur at the LHC.

By assumption, the Standard Model is based on a $SU(3) \times SU(2) \times U(1)$ underlying local symmetry [3, 4], which itself results in the gauge bosons that exist in the theory. The representation of each of the generations of quark and lepton fields in each symmetry group is given, such that the phenomenology of the theory agrees with experiment. Further, the number of generations is taken to be three, though this assumption is not strictly necessary, and the Standard Model could be extended in a somewhat simple manner to contain a fourth generation at a high enough mass to have avoided experimental detection thus far [5]. Next, the spin zero (spin zero is required to retain Poincaré invariance) Higgs field, with a nonzero vacuum expectation value, is postulated by the theory and is responsible for providing masses to the W and Z bosons and potentially the quarks and fermions [6].

Lastly, the nineteen free parameters of the Standard Model are fixed at the values that result in agreement between theory and experimental results. These parameters can be taken to correspond to the gauge couplings of the symmetries (three), the masses of the fundamental massive fermions (nine), the independent parameters in the

CKM matrix (four), discussed below, and the free parameters in the Higgs potential (three) [7]. Thus, while the Standard Model is largely empirical by design in terms of the fields and gauge symmetries, it forms a self-consistent model of the set of the experimental results observed in particle physics experiments.

The $SU(3)$ symmetry is unbroken, with eight massless gauge bosons (gluons) corresponding to the adjoint representation of $SU(3)$ and for which the relevant charge is commonly referred to as color. Among the fundamental Standard Model fermions, only the quarks interact through the strong force and are in the fundamental representation of $SU(3)$. All other fundamental particles lie in the singlet representation and do not interact directly through the strong force. The strong force is also self-interacting and includes interactions summarized in Fig. 2.1.

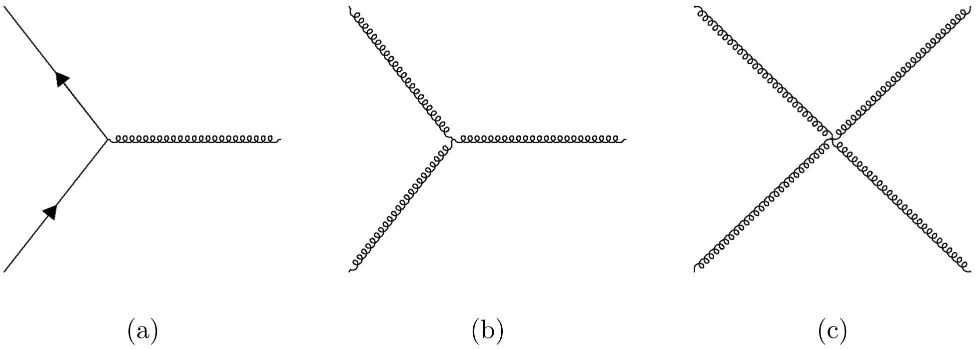

Figure 2.1: Feynman diagrams corresponding to the strong interaction

Among the fundamental forces, the strong force is potentially the strongest, with a coupling constant greater than one. However, bare quarks are not directly observed in particle colliders, and all particles comprised of quarks (hadrons) are always $SU(3)$ singlet states, composed of either three quarks (baryon), a quark and antiquark (meson), or potentially more exotic combinations of more than three quarks (e.g. pentaquarks, first observed by LHC-B in 2015 [8]). Only higher order strong interactions can occur between hadrons, which are largely responsible for holding protons and neutrons together in atomic nuclei.

That the coupling constant of the strong interaction is greater than one significantly complicates calculations involving the strong interaction. In fact, the expansion of the amplitude of a particular process into an infinite sum (the basis for Feynman diagrams) is no longer mathmatically justified, so that perturbation theory (and the concept of a Feynman diagram) would not apply to calculations involving the strong interaction [9].

However, due to the gluon-gluon interactions and the interference of different diagrams, the strong force decreases in strength at high energy and small distances, in a process known as asymptotic freedom [10, 11]. Perturbative calculations can thus be performed for the high energy interactions that are generally of the most interest in particle collider experiments.

As an extra complication, after quarks or gluons form in a high energy particle interaction, they undergo the process of hadronization, in which color singlet states (hadrons), photons, and other particles are formed. This process involves lower energy particles, for which the strong force is non-perturbative, so other techniques are reqired for calculating these processes. For example, the string model [12], treats the strong force between two particles as a string that increases in tension as the particles are separated, such that, when enough tension is built, the string breaks and spawns two new particles and new strings connecting them to the original particles (very simplified description). This method, used by the PYTHIA generator for example, is justified, since it produces results that agree with data, as opposed to the use of a direct bottom up calculation.

The relevant gauge bosons for the $SU(2)$ symmetry are the three W^i bosons, corresponding to the adjoint representation of $SU(2)$. The charges for $SU(2)$ and $U(1)$ are commonly referred to as weak isospin and hypercharge, respectively. The $SU(2)$ interacts with the left-handed components of the fields of the fundamental fermions (i.e. the left-handed fermions are in the **2** representation of $SU(2)$, while the right handed fermions are in **1**), but all fundamental fermions have a nonzero (and rational) hypercharge. Thus, unlike the strong interaction, all particles interact through the electroweak interaction to some degree. This statement is a bit of a tautology, as particles must interact through at least one of the forces to be discovered in the first place, and a particle that did not interact through any of the fundamental forces would not be discovered.

A summary of the Standard Model fermions is given in the table below, along with their corresponding representations in each of the symmetry groups [12]. The columns labeled L_x correspond to the lepton numbers for each lepton flavor, a conserved quantity in all known processes in the Standard Model. The columns labeled C, S, B, and T are the quark flavor numbers, conserved in all processes except weak interactions.

Through the introduction of the scalar Higgs field and the Higgs mechanism [13], in **1** in $SU(3)$, **2** in $SU(2)$, and a $U(1)$ charge of 1, the $SU(2) \times U(1)$ symmetry is spontaneously broken. The result is the $U(1)_{em}$ symmetry with the massless photon as the mediator gauge boson, and the weak nuclear force, with the massive Z and $W^{\pm}$ as the mediators. The photon, Z, and W can be represented as linear combinations of the W^i and B^0 bosons, according to

$$A_\mu = \sin(\theta_W) \times W^3_\mu + \cos(\theta_W) \times W^3_\mu \tag{2.1}$$

$$Z_\mu = -\cos(\theta_W) \times W^3_\mu + \sin(\theta_W) \times W^3_\mu \tag{2.2}$$

$$W^{\pm}_\mu = \frac{1}{\sqrt{2}}(W^1_\mu \mp iW^2_\mu) \tag{2.3}$$

The angle θ_W, a constant in the theory determined from experiment, is the weak mixing angle. It can be expressed as a function of the coupling constants of the $SU(2)$ and $U(1)$ ($\alpha_{SU(2)}$ and $\alpha_{SU(1)}$) symmetries as [14]

$$\sin(\theta_W) = \frac{\alpha_{SU(1)}}{\sqrt{\alpha^2_{SU(2)} + \alpha^2_{U(1)}}} \tag{2.4}$$

Field	mass (MeV)	$SU(3)$	$SU(2)$	$U(1)$	$U(1)_{em}$	L_e	L_μ	L_τ	C	S	B	T
$\begin{pmatrix} e_L \\ \nu_{e,L} \end{pmatrix}$	0.5110 (appr.) –	**1**	**2**	-1	-1	1	0	0	0	0	0	0
$\begin{pmatrix} \mu_L \\ \nu_{\mu,L} \end{pmatrix}$	105.7 (appr.) –	**1**	**2**	-1	-1	0	1	0	0	0	0	0
$\begin{pmatrix} \tau_L \\ \nu_{\tau,L} \end{pmatrix}$	1777 (appr.) –	**1**	**2**	-1	-1	0	0	1	0	0	0	0
e_R	0.5110 (appr.)	**1**	**1**	-2	-1	1	0	0	0	0	0	0
μ_R	105.7 (appr.)	**1**	**1**	-2	-1	0	1	0	0	0	0	0
τ_R	1777 (appr.)	**1**	**1**	-2	-1	0	0	1	0	0	0	0
$\begin{pmatrix} u_L \\ d_L \end{pmatrix}$	$2.3 + 0.7 - 0.5$ $4.8 + 0.5 - 0.3$	**3**	**2**	$\frac{1}{3}$	$\frac{2}{3}$ $\frac{-1}{3}$	0	0	0	0	0	0	0
$\begin{pmatrix} c_L \\ s_L \end{pmatrix}$	$1290 + 50 - 110$ $95 + 5 - 5$	**3**	**2**	$\frac{1}{3}$	$\frac{2}{3}$ $\frac{-1}{3}$	0	0	0	1 0	0 1	0	0
$\begin{pmatrix} t_L \\ b_L \end{pmatrix}$	$172440 \pm 130 \pm 470$ $4180(\bar{M}S) \pm 30$	**3**	**2**	$\frac{1}{3}$	$\frac{2}{3}$ $\frac{-1}{3}$	0	0	0	0	0	1 0	0 1
u_R	$2.3 + 0.7 - 0.5$	**3**	**1**	$\frac{4}{3}$	$\frac{2}{3}$	0	0	0	0	0	0	0
d_R	$4.8 + 0.5 - 0.3$	**3**	**1**	$\frac{-2}{3}$	$\frac{-1}{3}$	0	0	0	0	0	0	0
c_R	$1290 + 50 - 110$	**3**	**1**	$\frac{4}{3}$	$\frac{2}{3}$	0	0	0	1	0	0	0
s_R	$95 + 5 - 5$	**3**	**1**	$\frac{-2}{3}$	$\frac{-1}{3}$	0	0	0	0	1	0	0
t_R	$172440 \pm 130 \pm 470$	**3**	**1**	$\frac{4}{3}$	$\frac{2}{3}$	0	0	0	0	0	1	0
b_R	$4180(\bar{M}S) \pm 30$	**3**	**1**	$\frac{-2}{3}$	$\frac{-1}{3}$	0	0	0	0	0	0	1

Table 2.1: Summary of Standard Model fermions. All have a spin of $\frac{1}{2}$ and have a corresponding antiparticle with opposite quantum numbers and conjugate representations. The $U(1)_{em}$ charge, given for convenience, is redundant with repect to the $U(1)$ charge and $SU(2)$ representation.

$$\cos(\theta_W) = \frac{\alpha_{U(1)}}{\sqrt{\alpha_{SU(2)}^2 + \alpha_{U(1)}^2}} \tag{2.5}$$

Due to the high masses of the Z and W (approximately 91.2 GeV and 80.4 GeV, respectively), the weak nuclear force has a short range and is only relevant over short distances or in high energy interactions. The weak interactions are particularly important in particle physics, since interactions involving the W are the only flavor changing processes in the Standard Model. The electroweak flavor conserving interactions are summarized by the Feynman vertices in Fig. 2.2. The electroweak flavor changing interactions are summarized by the Feynman vertices in Fig. 2.3. To avoid redundancy, the diagrams corresponding to flipping the arrow directions and W charge are not shown. In all of these diagrams, electric charge is conserved at the vertices, reflecting the conservation of electric charge in the Standard Model.

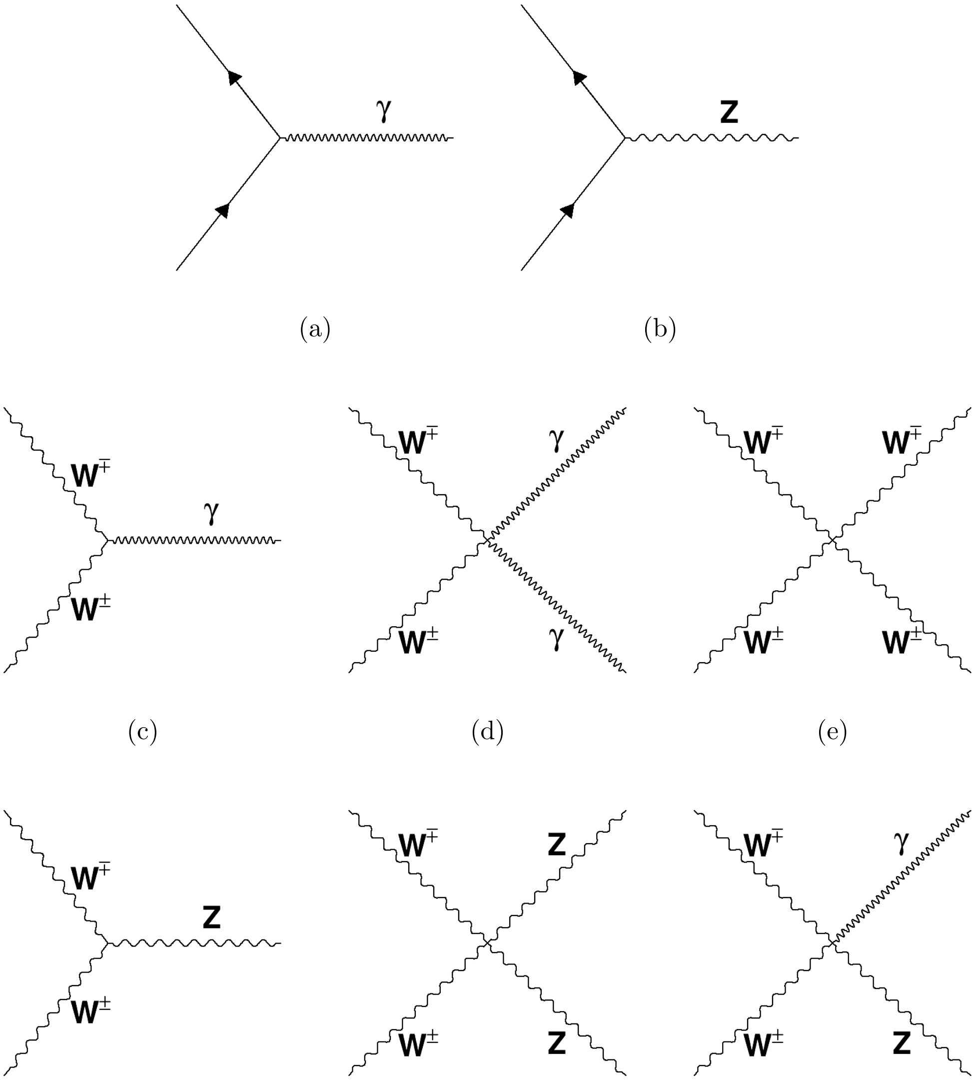

(a) (b)

(c) (d) (e)

(f) (g) (h)

Figure 2.2: Feynman diagrams corresponding to the flavor conserving electroweak interactions

Leptons and quarks differ in the manner in which such flavor changing processes occur. While a charged lepton may convert only to the neutrino of the same generation when emitting a W, a quark can convert to a quark from any of the three generations, with different probability. As a result, the lepton flavor quantum numbers are absolutely conserved in the Standard Model through all the fundumental interactions, while the quark flavor quantum numbers are not. The degree to which quarks of different generations mix is given by the CKM matrix [15, 16]. From an experimental point of view, of particular importance is the manner in which b-quarks mix with the other quark flavors, since, in collider experiments, b-quarks have a distinctive experimental signature that must be taken into account.

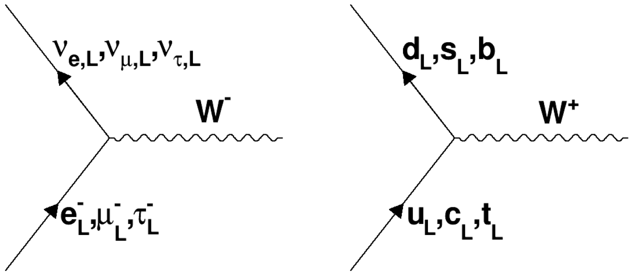

(a) (b)

Figure 2.3: Feynman diagrams corresponding to the flavor conserving electroweak interactions

2.2 Beyond the Standard Model

The Standard Model is a full, self-consistent model, in that it does not explicitly have missing pieces. However, it does not represent a complete picture of the universe, as it does not explain numerous experimental observations. Most experimentally obvious, gravity is not explained by the model, the existence of which appears to be beyond dispute (e.g. the discovery of gravity waves [17]). Due to the weakness of gravity at the energy scales relevant to particle colliders, there is no experimental evidence of quantum gravity, limiting the theoretical progress that can be made in incorporating gravity into the theory. However, there are theoretical models of quantum gravity, generally involving a theoretical massless spin two graviton, and the potential connection between supersymmetry and gravity is discussed in the next section.

Next, neutrino oscillation, first observed in solar neutrinos [18], requires neutrinos to have a mass splitting to account for this oscillation [19]. By design, the Standard Model only includes massless neutrinos, and any explanation of neutrino masses is beyond the Standard Model, requiring the introduction of massless neutrinos requires the addition of ν_R fields. Though, unlike the theoretical graviton, neutrinos can be directly observed, the difficulty in actually detecting them complicates efforts to determine neutrino properties with high precision.

From experimental evidence [20], dark matter is composed of massive particles, also unexplained by the Standard Model. Beyond the potential mass range and the requirement that such particles have a $U(1)_{em}$ charge of zero and lie in the $\mathbf{1}$ representation of $SU(3)$ (i.e. they do not interact electromagnetically or strongly, but do interact gravitationally and weakly), little is known about the nature of these theoretical particles. As such, any theory that predicts a massive enough stable, neutral, and non-strongly interacting particle could be a candidate for dark matter (or, potentially, any set of theories, if dark matter is not composed of a single type of particle). As will be discussed in the next section, in some of its forms, supersymmetry is one of these candidate theories.

While not, strictly speaking, an unexplained experimental result, the Standard Model is also theoretically troubling due to its high degree of fine-tuning. The model is comprised of a number of constants which take seemingly arbitrary values, and in order to justify such apparent arbitrariness, it is theoretically desireable that the particular values of these parameters be the results of some underlying unknown phenomena. Of particular importance are quantities that seem to take values orders of magnitude smaller than what would be expected based on naturalness arguments (roughly speaking, the idea that the free dimensionless constants in a theory should be of the same order, unless there is a good reason why they should not be). One example is the strong CP problem - the strong force does not violate CP-invariance, for no apparent reason [21]. More strikingly, the cosmological constant is much smaller than would be expected by naturalness arguments, by 120 orders of magnitude [22]. Unless there exists an underlying reason that enforces this behavior, it seems entirely arbitrary (and, apparently quite lucky) that it takes such a small value, and, while arguments have been made to explain this behavior (e.g. relating to multiverse theories or the anthropic principle), resolving this particular problem is beyond the scope of collider physics.

From the point of view of this physics search, the most important fine-tuning problem is the Hierarchy problem, relating to the observed mass of the Higgs boson. In general, the observed mass of a particle can be seen as the sum of its bare mass and the loop corrections to the propagator, but this method is complicated by the fact that loop diagrams generally diverge. This divergence can generally be resolved by introducing an ultraviolet cutoff (only integrating the possible phase space of the virtual particles internal to the relevant Feynman diagrams up to some large, fixed value) and renormalizing [23]. However, in the absence of other effects, terms linear or higher in order with respect to this ultraviolet cutoff can appear in the calculation of the propagator.

In reality, there are underlying reasons that eliminate this effect. For fermions, the mass term only involves the coupling of left-handed and right-handed fields, while the kinetic term and the interaction terms only involve the coupling of left-handed with left-handed fields or right-handed with right-handed fields. As such, loop diagrams give no extra correction to the terms coupling the mass term, and the fermion mass does not acquire a high order correction [7].

For gauge bosons, the corrections to the mass are more subtle. Performing a calculation of the loop corrections to the propagator in the manner previously described does give terms divergent with respect to the ultraviolet cutoff. However, such terms would inherently break gauge invariance (the breaking of gauge invariance by the introduction of mass terms for gauge fields was the reason for introducing the Higgs field in the first place). Since the method of applying the ultraviolet cutoff was a bit arbitrary to start with, in the context of gauge fields it is instead concluded that the exact method of using a constant ultraviolet cutoff does not make physical sense for gauge fields. If, instead, a gauge-invariant method is used, the observable mass can be taken to be unaffected by the loop diagrams [7].

For the Higgs boson (and potentially any scalar fundamental particle), there is not an apparent reason why such loop diagrams would not contribute high order corrections to the observed mass. Specifically, one loop diagrams would be expected to contribute terms quadratic in the ultraviolet cutoff. The observed Higgs mass is however not large - it is measured to be approximately 125 GeV [2]. In the absence of other effects, this would then mean that the sum of higher order terms in the observed Higgs mass would have to almost entirely cancel out. Since this sum depends on a number of seemingly arbitrary and independent Standard Model constants, shifting any of these constants by a slight value would result in the Higgs mass growing dramatically. Either the Standard Model constants are fine-tuned in an exact way to give a small Higgs mass, or there is some underlying phenomena that resolves this fine-tuning problem.

One last troubling aspect of the Standard Model is the lack of gauge coupling unification. The nature of the fundamental interactions in the Standard Model appears arbitrary. In particular, it is unclear why there is an $SU(3)$ symmetry and separate, unrelated $SU(2)$ and $U(1)$ symmetries. From a theoretical point of view, it is desirable that this seemingly arbitrary behavior be a manifestation of some underlying theory. The values of the coupling constants for the strong, weak, and electromagnetic forces all depend on the energy scale and distance scale of an interaction, and theories involving the unification of these interactions (and in a much harder problem, gravity as well), generally require that, at some high enough energy scale, the separateness of the different forces disappears [24].

However, if the forms of the coupling constant functions are extrapolated far beyond the energy scales probed by particle colliders, the three constants almost meet at a particular value, on the order of 10^{15} GeV [25]. This almost-intersecting appears too close to be coincidental, but the lack of them actually meeting points to some other unknown theory that might account for this effect.

2.3 Supersymmetry

Supersymmetry (SUSY) is an extension to the Standard Model that resolves many of the previously discussed problems. In its simplest form, the theory introduces a new global symmetry with respect to which the equations of motion are invariant. In order to define this symmetry, a new set of so-called superfields are introduced, generally expressed in terms of Standard Model particle and Supersymmetric particle fields. These superfields are in the same representations in each of the $SU(3)$ and

$SU(2)$ symmetry groups as the corresponding original SM fields, except that also they can undergo a supersymmetric transformation, effectively rotating the particle and superparticle fields into each other, a transformation that leaves the equations of motion unchanged.

Supersymmetry itself can be arbitrarily complicated, but this search and its theoretical interpretation uses minimal supersymmetric Standard Model (MSSM), corresponding to supersymmetry in its simplest form. A single supersymmetric counterpart to every Standard Model field, differing in spin by $\frac{1}{2}$, is introduced, and the MSSM Lagrangian is expressed in terms of the superfields. Further, the MSSM requires an extension to the Higgs sector, adding a second Higgs doublet in order to explain the masses of the quarks and fermions in the theory [26].

The MSSM may explain dark matter by virtue of introducing a new set of particles, including one that could have properties consistent with indirect dark matter evidence. If the least massive SUSY particle (LSP) is stable, it would be required to be only weakly and gravitationally interacting, to have avoided astronomical observation thus far. The LSP is not be required to be massive enough to be consistent with astronomical evidence, but a large portion of the SUSY phase space, particularly after removing the region excluded by previous experiment, involves a high mass stable LSP.

While each field has a corresponding supersymmetric counterpart, the relations between SM particles and their superpartners is a little more complicated for gauge bosons. The B^0 and W^i fields each have supersymmetric counterparts, but these superfields and the Higgs fields mix in a different way than do the SM gauge bosons. As a result, the photon and $W^{\pm}$ bosons do not each individually have a counterpart, but instead there are predicted to be four neutral $\tilde{\chi}_i^0$ and two charged $\tilde{\chi}_i^{\pm}$.

Supersymmetry may also resolve the Hierarchy problem. In theory, each loop diagram correction to the Higgs mass would have a corresponding diagram involving the supersymmetric counterpart of the particle involved in the loop. And, the correction from each diagram would have the same magnitude but opposite sign. Thus, by introducing SUSY, the mass divergence disappears for all orders with respect to the ultraviolet cutoff. This behavior is not perfect with massive superparticles, and if such particles have high mass, then fine-tuning again becomes a problem. For this reason, the masses of SUSY particles are constrained if the Hierarchy problem is to be resolved, though the exact nature of these constraints depends on the particular version of the MSSM, or SUSY in general, that is considered [27].

Supersymmetry allows for gauge coupling unification, though, in this case, the exact reason is a bit less intuitive and is not a simple manner of different terms directly cancelling each other. To start with, the coupling constants in the Standard Model can be calculated as a function of the coupling constant at some measureable energy scale, the number of fermion generations, the number of scalars, and the representation of each field in each symmetry (and the charge for the $U(1)$ symmetry). If the dependence is instead calculated for the MSSM, extra terms are added to the equation for the supersymmetric fields and the extra scalars. As it happens, in the MSSM the three gauge couplings end up intersecting at an energy scale of approximately 2×10^{16} GeV. This behavior seems too suspicious to be coincidental and is one of the primary motivators for SUSY. This behavior is not a property of SUSY in general, since the addition of new fields (including the addition of more scalar fields, as happens in certain generalizations of SUSY) generally removes this high energy convergence. The MSSM gains further credibility in this regard relative to other SUSY models. However, as with the Hierarchy problem, gauge unification only occurs if the SUSY particles are not too massive. In particular, particles cannot be significantly beyond the TeV scale for unification to occur [7].

Further, if it is generalized slightly, SUSY results in the necessary existence of gravity. Enforcing local invariance (previously only global invariance was required) of the equations of motion with respect to the SUSY transformations requires the addition of a spin-2 particle (and corresponding supersymmetric spin-$\frac{3}{2}$ particle), in a manner analogous to the other symmetries. And, a massless spin-2 particle would have the properties required of and in fact be indistinguishable from the graviton. The SUSY transformation then seems like a likely candidate for the symmetry corresponding to gravity [28]. Unlike the previously mentioned motivators of SUSY, this particular property does not require that SUSY particles have low mass. If SUSY is not discovered in particle colliders, it will likely remain a popular theory at higher energy scales at least, largely due to its potential connection with gravity.

The MSSM contains many free parameters (at least 120, though the exact number depends on which constants are excluded), and the exact phenomenology depends on the particular MSSM model. This full range in parameter space can be drastically decreased when theoretical and experimental constraints are applied. First, it is required that SUSY resolves at least some of the theoretical problems it is intended to resolve. In particular, SUSY is required to solve the Hierarchy problem, though a subset of models that also explain dark matter may be considered. Second, SUSY must be in agreement with experimental results. For example, regions in phase space where CP-violating terms would allow for an observable effect on Standard Model behavior are excluded. Also, certain terms can potentially allow for proton instability, which would be an observable effect [29].

Due to this large number of free parameters, particularly to the SUSY symmetry breaking that must occur for SUSY to have evaded observation thus far, it is experimentally unfeasible to consider the full available phase space. It is theoretically desirable that the MSSM constants take specific values due to some underlying effects, similar to the case of the SM. So, for example, a much smaller set of underlying constants may result in all the SUSY breaking parameters. In this case, the actual properties of SUSY are not known, and the determination of underlying models that result in observable effects allows for testing specific models instead of the MSSM as a whole. In particular, there are a few models predicting the manner in which SUSY particles acquire mass. These theories generally assume there is a so-called hidden sector at high energy, where SUSY is broken. While the nature of the particles and particle interactions in this sector are not directly observable, they can have effects on lower energy sectors (the observable sector) through loop diagrams, for example. One example of the methods of SUSY breaking are mSUGRA (minimal SUperGRAvity), where five free parameters result in the much larger set of MSSM breaking parameters [30]. However, this particular search is less focused on the exact nature of the symmetry breaking.

2.3.1 R-parity

The general MSSM Lagrangian includes terms corresponding to interactions that make the LSP unstable. Many SUSY models set such terms to zero, as otherwise there would be no dark matter candidate. Specifically, the MSSM contains terms involving the decay of the SUSY lepton counterparts (sleptons), which in turn allows for $\tilde{\chi}_1^0$ decay, as shown in Fig. 2.4.

Effectively, the stability of the LSP can be enforced through the introduction of a new symmetry, R-parity, defined as

$$R = (-1)^{3(B-L)+2s} \tag{2.6}$$

In this case, B is the baryon number, L is the lepton number, and s is the spin of a field. The R-parity is calculated for each field, and the R-parity of a system is the product of the individual values. Each SM particle has an R-parity of $+1$, and each superparticle has an R-parity of -1 [31], so the conservation of this quantity in the Standard Model is trivially true, as it will be $+1$ in any system. However, once supersymmetry is introduced, unless the R-parity violating Lagrangian terms are set to zero, R-parity is not necessarily conserved.

A potentially stronger motivator for R-parity is that R-parity violating terms allow for proton decay. For example, the terms allow for two quarks in a proton to join to form an object which then can decay semileptonically. Such processes would result in proton instability, which is not consistent with present experimental limits. However, in order for protons to be stable with a long enough lifetime to be consistent with the observed lower bounds on the proton lifetime, it is sufficient for at most one of the R-parity violating terms to be nonzero [32]. For example, in the above example, this would mean only one of the two involved vertices is allowed, so that the full decay could not occur.

The aim of this search is to target such R-parity violating (RPV) decays. Most SUSY searches performed by ATLAS have high $E_{\mathrm{T}}^{\mathrm{miss}}$-dependent event signatures, by virtue of having high mass (and as a result, generally high momentum) effectively invisible particles. General ATLAS SUSY searches miss these RPV SUSY models, due to their different topology. Further, by assumption exactly one of the RPV terms is non-zero, meaning that only one of the RPV coupling searches (only fully

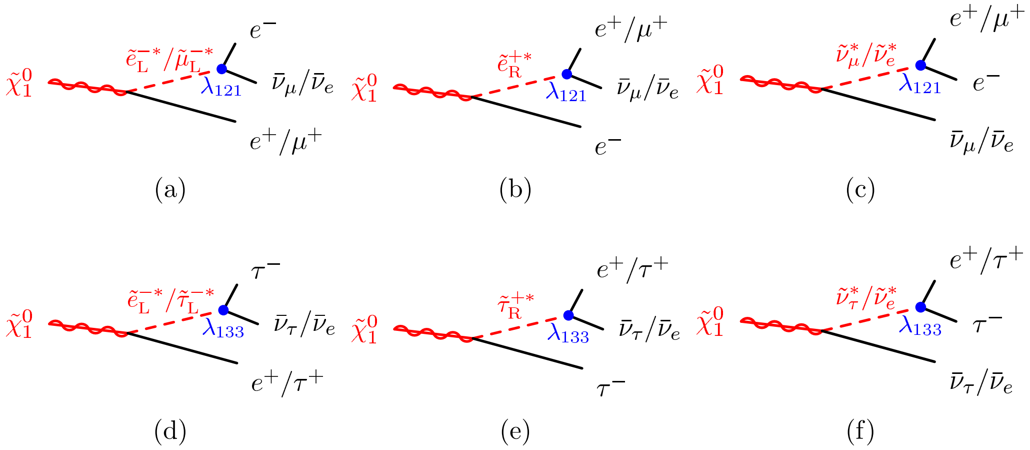

Figure 2.4: Feynman diagrams corresponding to the $\tilde{\chi}_1^0$ decay. Not shown are diagrams with e and μ flipped.

hadronically decaying LSP, only leptonically decaying LSP, or mixed decays) would be expected to detect RPV models.

This search is focused on the detection of general SUSY models where the fully leptonic RPV term in the MSSM is nonzero, a family of models to which this search is uniquely sensitive. These models generally result in event signatures with at least four high momentum leptons (two from each of two LSPs). Such decays tend to have low cross-sections relative to strong interactions, but the dramatic nature of the signature allows for relatively easy identification of these processes. A few examples of processes resulting in at least four leptons is given in Fig. 2.5.

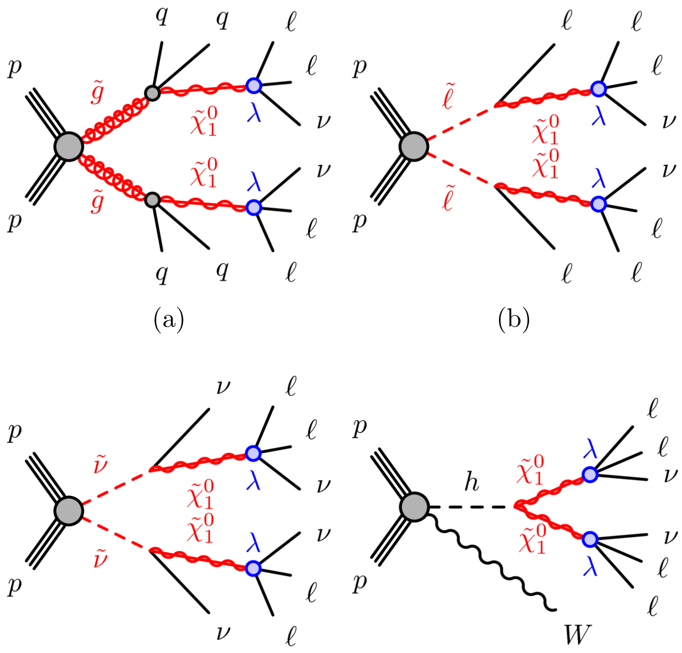

(a) (b)

(c) (d)

Figure 2.5: Example Feynman diagrams of processes for which this search is sensitive. Examples include gluino pair production (a), slepton pair production (b), sneutrino pair production (c), and associated higgsino-W production (d). In cases where a $\tilde{\chi}_1^0$ decays to three objects, it is assumed to occur through one of the diagrams in Fig. 2.4

2.3.2 Benchmark Model

For the purpose of actually designing a physics search, it is convenient to have a benchmark model with which to optimize the methods used. In this case, the benchmark model corresponds to the particular set of processes shown in Fig. 2.6.

In the model, wino-like $\tilde{\chi}_1^{\pm}$ are pair-produced, and the lightest SUSY particle (LSP) is a bino-like $\tilde{\chi}_1^0$. The $\tilde{\chi}_1^{\pm}$ decays to the LSP while emitting a W boson, and the $\tilde{\chi}_1^0$ subsequently decays via an RPV interaction. The decay is mediated by the following lepton-number-violating superpotential term:

$$W_{LL\bar{E}} = \frac{1}{2}\lambda_{ijk}L_iL_j\bar{E}_k. \tag{2.7}$$

Here, the left-handed $\mathrm{SU(2)_L}$ doublet superfields are given by $L_{i/j}$, while $\bar{E}_k$ are the right-handed $\mathrm{SU(2)_L}$ singlet superfields. The indices i, j and k are generation indices, while λ_{ijk} is a collection of 9 new Yukawa couplings satisfying $\lambda_{jik} = -\lambda_{ijk}$. This RPV interaction allows the following decay of the $\tilde{\chi}_1^0$ LSP:

$$\tilde{\chi}_1^0 \to \ell_k^{\pm}\ell_{i/j}^{\mp}\nu_{j/i}, \tag{2.8}$$

with the allowed lepton flavours depending on the indices of the associated λ_{ijk} couplings. Thus, every signal event contains a minimum of four charged leptons, and potentially up to six if the W bosons both decay leptonically.

Sample	$\tilde{\chi}_1^0$ branching ratios		
$LL\bar{E}12k$	$e^+e^-\nu$ (1/3)	$e^{\pm}\mu^{\mp}\nu$ (1/3)	$\mu^+\mu^-\nu$ (1/3)

Table 2.2: Decay modes and branching ratios for the $\tilde{\chi}_1^0$ LSP in the RPV wino model.

The nine λ_{ijk} RPV couplings allow the $\tilde{\chi}_1^0$ to decay to every possible combination of charged lepton pairs in principle. The $LL\bar{E}12k$ ($k \in 1, 2$) scenarios include only decays to electrons and muons, as indicated in Table 2.2. The naming is inspired by the couplings that can produce the associated decays: λ_{121} and λ_{122} for $LL\bar{E}12k$.

These decay patterns cannot be produced by a single non-zero $LL\bar{E}$ coupling, but interpretations of “pure” coupling scenarios could be obtained by appropriate reweighting of the simulated events, analogous to the procedures used in Ref. [33].

Events are considered with $\tilde{\chi}_1^{\pm}$ masses between 500 GeV and 1200 GeV and $\tilde{\chi}_1^0$ masses between 10 GeV and $m_{\tilde{\chi}_1^{\pm}} - 10\,\mathrm{GeV}$. In theory, electrons, muons, and tau leptons can all be produced in these processes. However, because of the much lower purity of tau reconstruction and the extra analysis complications, this search focuses purely on decays into electrons and muons. If these decays produce tau leptons more frequently than the light leptons (electrons and muons), then this search is less sensitive to these models.

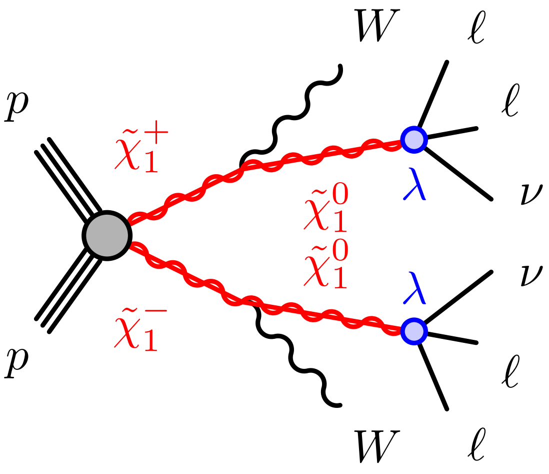

Figure 2.6: Diagram of the benchmark SUSY model of $\tilde{\chi}_1^{\pm}$ production with indirect RPV decays considered in this analysis.

2.4 Modeling of Physics Processes

The physics processes used in the search, both background and signal samples, are simulated using a Monte Carlo (MC) method. There are multiple stages to the generation of the simulated samples, described below.

2.4.1 Parton Distribution Function

The parton distribution function (PDF) of a hadron refers to the probability of finding a particular parton (quark or antiquark of a certain flavor or a gluon) with a particular momentum fraction of the hadron. In the context of pp collisions in the LHC, the proton PDF is an crucial element in modeling physics processes. The PDF depends on the energy scale of an interaction. In particular, for low energy proton interactions, the vast majority of the momentum in each proton is expected to be carried by the up-quarks and down-quark, but at higher energy, antiquarks and quarks of other flavors are also energetic and copiously produced.

Calculating the proton PDF is complicated by its somewhat non-perturbative nature and in practice relies on data. The first PDF used in this search is NNPDF2.3, which relies on data from a number of different experiments, including LHC data from 2010. A large number (>3000) of data points are computed by looking at Z and W production and jet production in different experiments. Then, a fit is performed to data to produce the PDF [34]. Similar methods are used for the other PDFs used for the physics process modeling, CTEQ6L1 [35] and CT10 [36].

2.4.2 Physics Process Generation

In general, energetic processes, particularly high energy pp interactions, can be calculated using perturbative techniques, with various corrections to account for the parts that are not truly perturbative [12]. Hadronization and the underlying event, however, are lower energy processes and require non-perturbative methods.

Different generators have different methods of combining the perturbative hard processes with the methods used for soft processes. To start with, each method calculates processes either at leading-order (LO), next-to-leading-order (NLO), or next-to-next-to-leading-order (NNLO). Generally, performing a calculation at higher order allows for a more precise calculation but introduces more complications that must be taken into account.

For all generators except SHERPA, the PYTHIA 8 or PYTHIA 6 generator is used to calculate the hadronization process [12], while SHERPA uses its own hadronization implementation. PYTHIA 8 is further used to generate the extra low-energy parton scattering processes (pile-up) that occur in each bunch crossing.

The generators used for each process considered in this search are given below, as well as the order used in the cross-section calculation. Where relevant, the PYTHIA underlying event (UE) tune is given, where the A2 tune is used for pile-up processes.

In cases where multiple entries are listed for a particular process, the first listed entry is used as the default, and the other entries are used in validating the default samples and in the calculation of systematics. As a general rule, SHERPA samples are given lower priority in cases where another sample is available, in particular POWHEG for diboson samples andMADGRAPH for $t\bar{t}Z$. MADGRAPH 5_aMC@NLO is used for the Z and W processes due to its better ability than POWHEG to model events containing a large number of extra partons, events that are particularly important as a background in this search.

The SUSY samples are calculated at leading order, as the exact modeling of the signal is less important, and the large number of different models requires computational speed.

Process	Generator(s)	Full/fast sim	Cross-section calculation	UE tune	PDF set
$t\bar{t}Z$, $t\bar{t}W$, $t\bar{t}WW$	MadGraph 5_aMC@NLO + Pythia 8	Fullsim	NLO	A14	NNPDF23LO
$t\bar{t}Z$ (S)	Sherpa	AF-II	NLO	Default	CT10
tWZ	aMC@NLO + Pythia 8	Fullsim	NLO	A14	NNPDF23LO
ZZ, WZ, $W\ W$	Powheg + Pythia 8	Fullsim	NLO	AZNLO	CTEQ6L1
ZZ (S)	Sherpa	AF-II	NLO	Default	CT10
$t\bar{t}$	Powheg + Pythia 6	Fullsim	NNLO+NNLL	Perugia2012	
Z+jets , W+jets	MadGraph 5_aMC@NLO + Pythia 8	Fullsim	NNLO	A14	NNPDF23LO
Higgs (ggH, WH, ZH, VBF H)	Powheg + Pythia 8	Fullsim	NNLO+NNLL	Perugia2012	CT10
($t\bar{t}H$)	aMC@NLO + Pythia 8	Fullsim	NLO	UE EE5	CTEQ6L1 (CT10ME)
VVV (WWZ, WZZ, ZZZ, WWW)	Sherpa	Fullsim	NLO	Default	CT10
$tt\bar{t}$, $t\bar{t}t\bar{t}$	MadGraph 5_aMC@NLO + Pythia 8	Fullsim	NLO	A14	NNPDF23LO
$b\bar{b}$, $c\bar{c}$	Pythia 8	Fullsim	NLO	A14	NNPDF23LO
SUSY signal	MadGraph 5 + Pythia 8	AF-II	LO	A14	NNPDF23LO

Table 2.3: Summary of the simulated SM background samples used in this analysis. Samples marked with an “(S)” are used for a cross-check of yields and systematic studies.

Chapter 3

The LHC and ATLAS

3.1 Large Hadron Collider

The LHC (Large Hadron Collider), designed to collide protons at a center-of-mass energy of 14 TeV, at an instantaneous luminosity of 10^{34} $\mathrm{cm}^{-2}s^{-1}$, or 10 $\mathrm{nb}^{-1}s^{-1}$, and with a 25 ns spacing between proton bunches, is the most energetic particle collider ever built [1].

The protons themselves originate from Linac2 and then pass through a series of synchrotrons: the Proton Synchrotron Booster (PSB), Proton Synchrotron (PS), and Super Proton Synchrotron (SPS). In each stage, proton energy increases, such that protons have a design energy of 450 GeV when they enter the LHC itself.

Protons can then be accelerated to the design energy of 7 TeV in the LHC, a 26.7 km ring, originally constructed for LEP (Large Electron-Positron Collider [37]), where a magnetic field keeps protons circulating at constant momentum. There are two proton beams traveling in opposite directions in the storage ring, so the in order to keep each beam at constant momentum, the beams are in separate vacuum chambers with separate magnetic fields. The ring is designed with specific interaction points, where the beams can potentially meet and cause *pp* collisions. Four points are used by the large physics experiments, ATLAS, CMS, LHC-B, and ALICE, shown in Fig. 3.1. ATLAS [38] and CMS [39] are the two large general purpose detectors. The other two are more specialized. ALICE [40] is designed for heavy ion collisions and LHC-B [41] designed for b-physics. Three smaller, specialized experiments share the caverns of the large experiments. TOTEM [42] measures the total pp cross-section, elastic scattering and diffraction, and shares its location with CMS. LHCf [43] measures neutral particles in the very forward region, used to calibrate models used in the study of Extremely High-Energy Cosmic-Rays. LHCf shares its site with ATLAS at ±140 m from the interaction point. MoEDAL [44], sharing its site with LHC-B, is designed to detect different types of highly ionizing exotic particles, particularly magnetic monopoles.

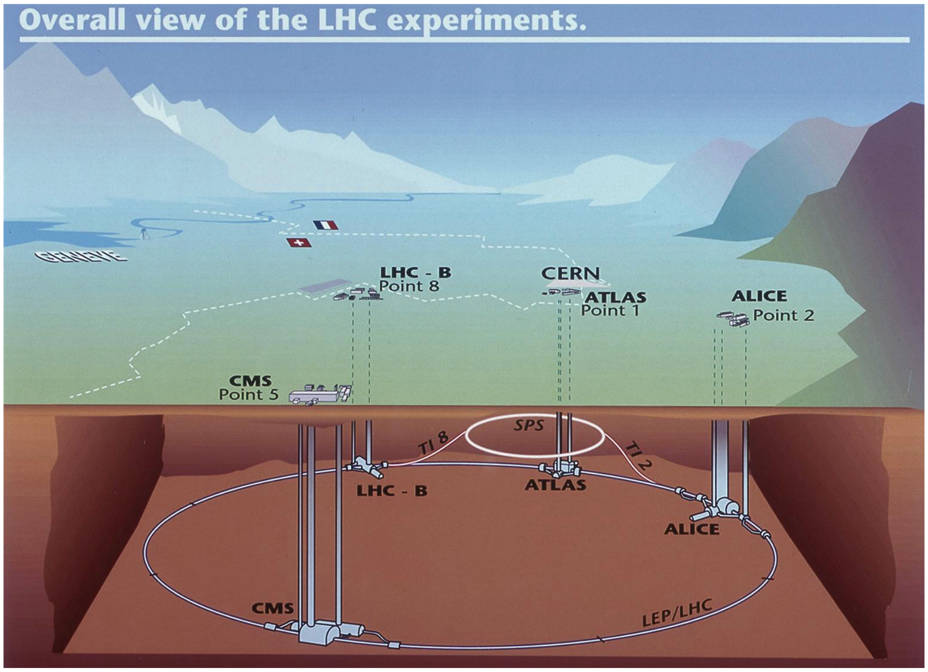

Figure 3.1: Diagrams of the LHC [45].

Following technical difficulty [46], the LHC began Run 1 in 2010 at significantly below the design specifications, at a center-of-mass energy of 7 TeV and with a 50 ns bunch spacing. The energy was increased to 8 TeV at the end of 2011, and it operated at 8 TeV until the end of Run 1 in early 2013. In total, an integrated luminosity of 47 ± 1.6 pb^{-1} was delivered in 2010, and 5.5 ± 0.10 fb^{-1} was delivered in 2011, both at 7 TeV [47]. Most of the data from Run 1 was delivered at 8 TeV in 2012, at 22.7 ± 0.43 fb^{-1} [48]. A diagram of the integrated luminosity as a function of time is shown in Fig. 3.2. The diagram also shows the data actually recorded by ATLAS, as well as the data that is usable by analyses (5.2).

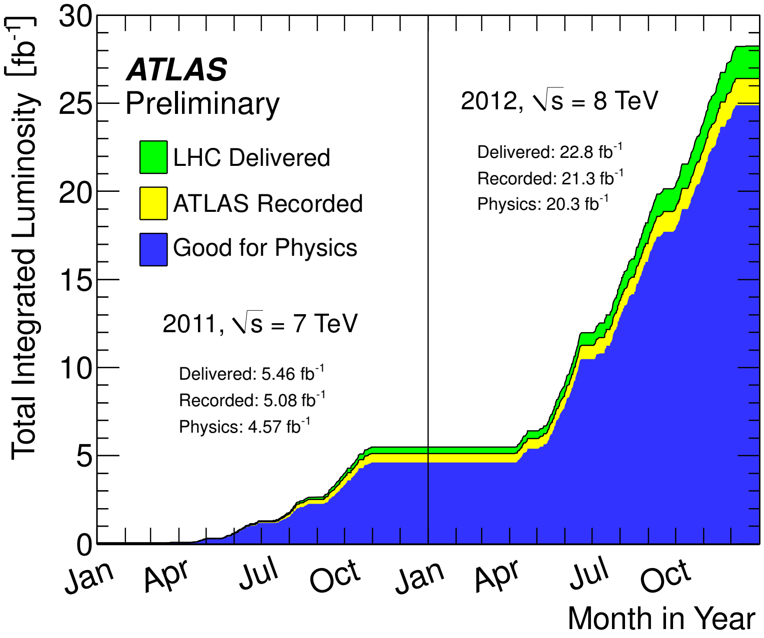

Figure 3.2: Integrated luminosity as a function of time [49].

The LHC shut down from the end of Run 1 to the beginning of Run 2 in mid-2015. During Run 2, the LHC operates at a center-of-mass energy of 13 TeV, and for most of the run, and for all the data included in this search, the bunch spacing is 25 ns. The data in this search corresponds to 13.3 fb^{-1}collected by ATLAS between 2015 and mid-2016, shown in Fig. 3.3a.

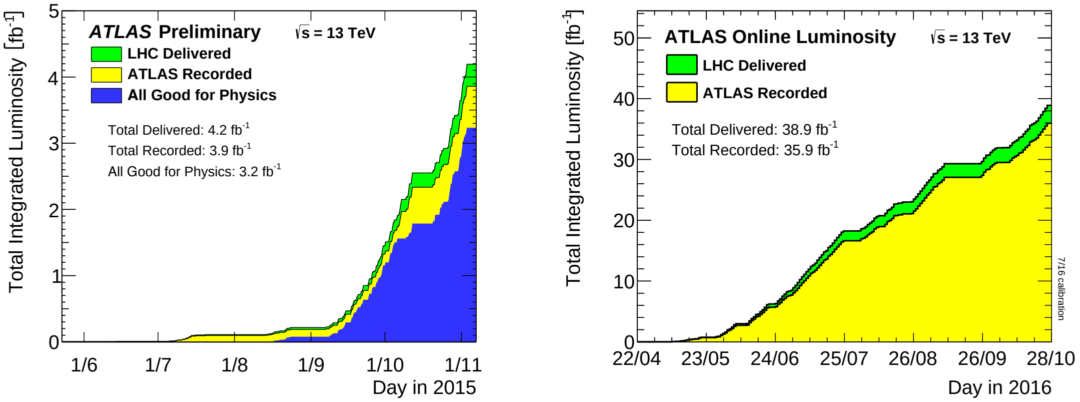

(a) 2015

(b) 2016

Figure 3.3: Integrated luminosity as a function of time in 2015 [50] and 2016 [51]. This search includes the full 25 ns 2015 dataset and the 2016 dataset up to July 10.

3.2 ATLAS

From the point of view of physics studies, the ATLAS detector has three primary systems, each targeting a different (but not exclusive) set of particles, with an extra detector system that measures luminosity. The focus of this section is the granularity and range covered by each detector system, as these properties drive the strategies used in this physics search. This section is derived almost entirely from material from the ATLAS technical paper [38], except for the specific sections for which other citations are given. A diagram of the ATLAS detector is shown in Fig. 3.4.

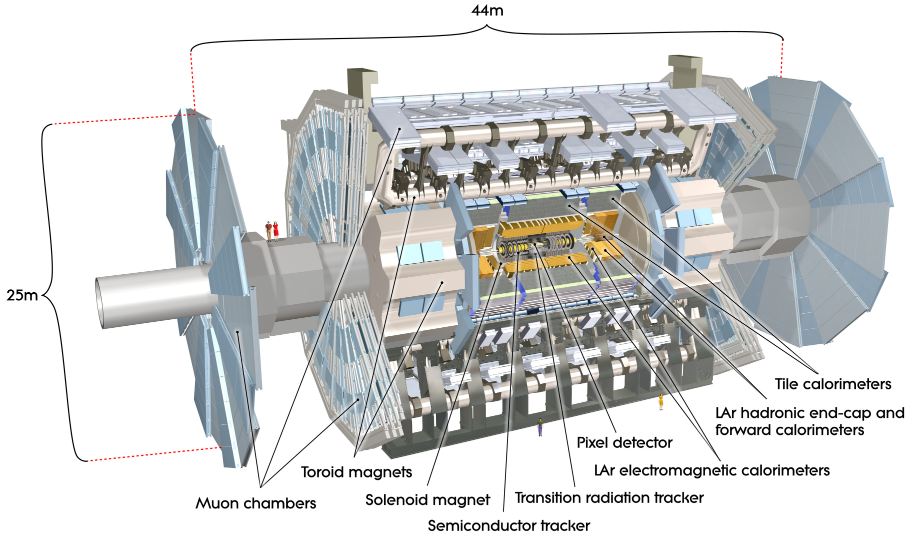

Figure 3.4: Full diagram of ATLAS

Detector ranges are given in terms of the azimuthal angle ϕ, extending from 0 to 2π, and the pseudorapidity η. η can be expressed in terms of the polar angle θ, assuming the latter takes a value of 0 at the positive z axis, as

$$\eta = -\ln(\tan(\frac{\theta}{2})) \tag{3.1}$$

η then takes a value of $+\infty$ at $\theta = 0$ and $-\infty$ at $\theta = \pi$. The pseudorapidity can be seen as the relativistic limit of the rapidity, expressed as

$$y = \frac{1}{2}\ln(\frac{E + p_z}{E - p_z}) \tag{3.2}$$

since, in the relativistic limit,

$$y = \frac{1}{2}\ln(\frac{E + p_z}{E - p_z}) \approx \frac{1}{2}\ln(\frac{|\vec{p}| + p_z}{|\vec{p}| - p_z}) = \frac{1}{2}\ln(\frac{1 + \cos(\theta)}{1 - \cos(\theta)}) = -\ln(\frac{\sin(\theta/2)}{\cos(\theta/2)}) = \eta \tag{3.3}$$

The rapidity, y, is a convenient measure in particle physics, since it is invariant with respect to boosts. If two objects are separated by Δy in one reference frame, they will have the same separation in any inertial reference frame, boosted in the z direction. As such, the size of an object, when expressed in terms of Δy, is invariant with respect to a boost in the z direction. Further, the derivative of η with respect to θ at $\theta = 0$ is 1, so that, if a massless object has some shape in terms of θ and ϕ in its rest frame (in the z direction), it will have that same shape when expressed in terms of η and ϕ, and due to the boost invariance of η, it will have the same shape in a frame boosted in the z direction. Particles produced in pp collisions tend to be highly relativistic, so that η is a good approximation for y. While y is used in practice in the physics search when calculating angular separations between objects, η is useful in terms of detector design, due to the direct correspondence between η, z, and radius for particles originating from $z = 0$.

An overview is given of each of the primary detector systems, including a summary of the physical structure of each detector and a basic description of how the measurements from each detector element are turned into phyical quantities representing particles. A description of how these quantities are then used to build the objects and quantities relevant for physics studies are given in section 4.

3.2.1 Inner Detector

The inner detector, a diagram of which is shown in Fig. 3.5 allows for precise measurements of charged particles only. A charged particle passing through the detector leaves a series of energy deposits in different detector elements, and these hits are combined to reconstruct the particle's original path. Due to the solenoid 2T magnetic field in the inner detector, the curvature of the track (in the x-y plane) gives a measurement of the momentum of the particle (or, momentum multiplied by charge), perpendicular to the direction of the beampipe (p_{T}). Further, the track includes impact parameter information, so that charged particles' origins can be precisely determined.

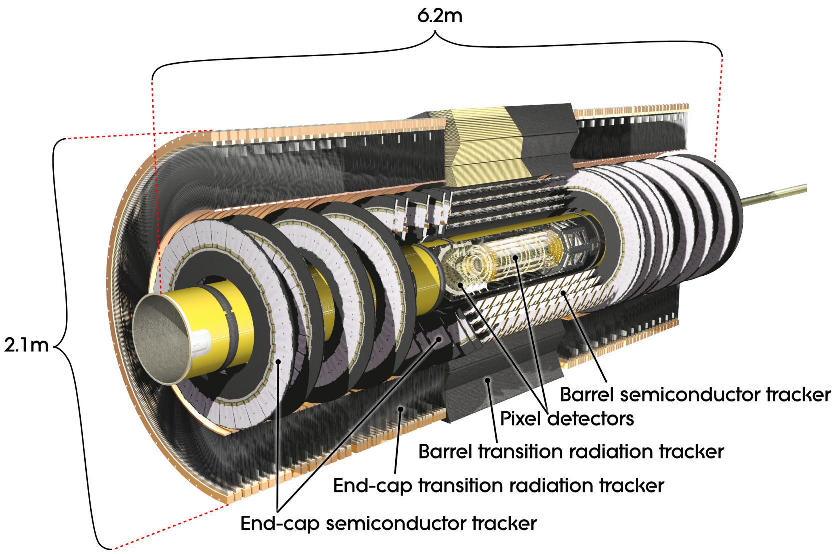

Figure 3.5: Diagram of the ATLAS inner detector

The inner detector is further divided into thee subsystems: the pixel detector, the silicon microstrip tracker (SCT), and the TRT (Transition Radiation Tracker), shown in Fig. 3.6. The SCT and pixel detectors have coverage up to $|\eta| = 2.5$, while the TRT only extends to $|\eta| = 2$. The innermost pixel layer, the IBL (Insertable B-Layer [52]), is not shown in these diagrams, as it was not a part of the original ATLAS design.

The pixel detector consists of four layers of silicon detectors, where the innermost layer, the IBL was inserted between Run 1 and Run 2. With the exception of the IBL, each layer has a separate barrel region, parallel to the beampipe and divided into staves, where each stave has $1 \times N$ modules in length × width, and endcap region, perpendicular to the beampipe and divided into sectors. The barrel has twenty-two, thirty-eight, and fifty-two staves for the first, second, and third layers, respectively, with thirteen modules per stave. In the endcap region, all layers have eight sectors of forty-eight modules each.

The pixel detector is composed of (mostly) 50×400 μm^2 pixels, for a total of 80.4×10^6 pixels, where each pixel hit includes the $\eta \times \phi$ corredinates where a particle crossed that layer of the detector. The IBL includes an extra 6.02×10^6 pixels, divided into 14 staves with pixels of somewhat different design than for the other pixel layers, at 50×250 μm^2 [52]. In the outermost region of the IBL, a different module and pixel design is used, but these modules lie outside the region in which tracking actually takes place ($|\eta| > 2.5$). By design, within the target η range, particles will traverse three layers of the pixel detector, as well as the IBL.

The SCT, also consisting of silicon detectors, is composed of strip detectors instead of individual pixels. Each strip measures 80×126000 μm^2, so that a measurement is only performed in one direction. However, each layer of the detector includes a double layer of strips oriented so that the two together provide the hit coordinates in both directions. There are four layers in the barrel and nine in the endcap (on each side), arranged so that each particle is expected to pass through four layers (or, eights strips).

The TRT is composed of 4 mm diameter straw tubes, providing hit information only in the ϕ direction. In the barrel, the straw tubes are 144 cm long and are arranged parallel to the beam axis. In the endcaps, they are arranged radially. While the TRT provides less coverage in η and provides no direct η information, particles traversing the TRT potentially interact with far more detector elements (typically 36 [38]), and combining the TRT with the silicon detectors improves the momentum measurement by improving the measurement of the track curvature.

A charged particle passing through the inner detector activates a number of detector elements along its path. In the pixel detector and SCT, a particle will generally activate multiple nearby pixels or strips in each layer, and in order to actually reconstruct an individual hit, nearby pixels or strips in each layer are combined into hits. For example, for the pixel detector, the actual position where a particle crossed a particular detector element is accurately determined using a NN (neural network) technique, which relies on detailed information about the pixel cluster shape [53].

Tracks are reconstructed objects representing individual charged particles, reconstructed using the ATLAS tracking algorithm [54]. The baseline tracking algorithm follows an inside-out approach, in which three-point seeds are found between the pixel detector and SCT, and then a combinatorial Kalman filter is used to add hits to the track seed, moving outward. Alternatively, back-tracking starts with TRT segments and adds other hits in an inward direction. Back-tracking is useful for tracks originating from secondary interactions, such as tracks from the delayed decay of a b-hadron. Lastly, tracks may be reconstructed purely from TRT hits, referred to as TRT-only tracks [54].

Track selection is based on a set of selection parameters that balance track reconstruction efficiency and fake track rate [55]. The path of a particle has seven unknown parameters - three representing the initial position of the particle, two representing the angle the particle travels from its origin, and one corresponding to the momentum. Under perfect conditions, tracks must have at least six hits to resolve all the unknown parameters, but due to detector-level and pile-up effects more stringent requirements are applied to tracks. The set of quantities that are used to select tracks is outlined below.

- Due to the 2T magnetic field, the significant curvature of tracks with $p_{\mathrm{T}} <$ 400 MeV means they do not reach the end of the inner detector and cannot be reconstructed. Tracks are required to have $p_{\mathrm{T}} > 400$ MeV.

- The tracker extends to $|\eta| = 2.5$, and tracks are required to satisfy $|\eta| < 2.5$.
- Tracks are required to have a minimum number of hits in the IBL, B-layer, pixel detector, SCT, pixel detector plus the SCT, and TRT, $N^{\mathrm{hits}}_{\mathrm{IBL}}$, $N^{\mathrm{hits}}_{\mathrm{B-layer}}$, $N^{\mathrm{hits}}_{\mathrm{Pixel}}$, $N^{\mathrm{hits}}_{\mathrm{SCT}}$, $N^{\mathrm{hits}}_{\mathrm{Si}}$, $N^{\mathrm{hits}}_{\mathrm{TRT}}$, respectively.
- In order to remove fake or poorly measured tracks, requirements are placed on the use of individual hits in multiple tracks. Defining a shared hit as a hit used by at least two tracks, tracks are required to contain at most $N^{\mathrm{shared}}_{\mathrm{module}}$ shared pixel or SCT modules, where a shared pixel (SCT) module contains at least one (two) shared hits.
- Holes occur if a track intersects an active detector element but does not result in a hit, and tracks are required to contain at most $N^{\mathrm{hole}}_{\mathrm{Pixel}}$ and $N^{\mathrm{hole}}_{\mathrm{Si}}$ in the pixel detector and the pixel detector plus the SCT, respectively.
- In certain circumstances, it is useful to consider TRT hits, $N^{\mathrm{Outliers}}_{\mathrm{TRT}}$, that are near a track but not used in the track fit as if they belong to the track.

These quantities are then used to actually select tracks. A different set of criteria is placed on the tracks when trying to reconstruct each type of physics object, summarized below.

- Electrons:
  - $N^{\mathrm{hits}}_{\mathrm{Si}} \geq 7$
  - $N^{\mathrm{hits}}_{\mathrm{Pixel}} \geq 1$
- Muons:
  - $N^{\mathrm{hits}}_{\mathrm{SCT}} \geq 5$
  - $N^{\mathrm{hits}}_{\mathrm{Pixel}} \geq 1$

  - $N_{\mathrm{Si}}^{hole} \leq 2$
  - if $0.1 \leq |\eta| \leq 1.9$, then $N_{\mathrm{TRT}}^{\mathrm{hits}} + N_{\mathrm{TRT}}^{\mathrm{Outliers}} \geq 6$ and $N_{\mathrm{TRT}}^{\mathrm{Outliers}} < 9 \times N_{\mathrm{TRT}}^{\mathrm{hits}}$

- Hadrons in jets:
  - $N_{\mathrm{Si}}^{\mathrm{hits}} \geq 7$
  - $N_{\mathrm{module}}^{\mathrm{shared}} \leq 1$
  - $N_{\mathrm{Si}}^{hole} \leq 2$
  - $N_{\mathrm{Pixel}}^{hole} \leq 1$

- Hadrons not in jets:
  - if $|\eta| \leq 1.65$, then $N_{\mathrm{Si}}^{\mathrm{hits}} \geq 9$
  - if $|\eta| \leq 1.65$, then $N_{\mathrm{Si}}^{\mathrm{hits}} \geq 11$
  - $N_{\mathrm{module}}^{\mathrm{shared}} \leq 1$
  - $N_{\mathrm{Si}}^{\mathrm{hole}} \leq 2$
  - $N_{\mathrm{Pixel}}^{\mathrm{hole}} = 0$
  - $N_{\mathrm{IBL}}^{\mathrm{hits}} + N_{\mathrm{B-layer}}^{\mathrm{hits}} \geq 1$

These criteria will be used in the next section. For charged hadrons in jets, at low η, the efficiency peaks at a 91% efficiency but decreases to an efficiency of 73% at $\eta = 2.5$, as tracks at higher η must pass through more material. For charged hadrons not in jets, at low η, the efficiency peaks at a 86% efficiency but decreases to an efficiency of 63% at $\eta = 2.5$. The efficiency for charged hadrons at $p_{\mathrm{T}} = 500$ MeV is approximately 85% (78%) and increases with p_{T} until it plateaus at a 90% (85%) efficiency a $p_{\mathrm{T}} = 5\,\mathrm{GeV}$. Charged particles lose energy at material surfaces, and the amount of energy lost depends on the particle type, which affects the particle's path. In general, all tracks are assumed to be charged pions, and the energy loss of pions is taken into account in the tracking procedure. Most importantly, electrons may lose a very different amount of energy than hadrons, in which case the hadronic assumption may result in the track failing the track reconstruction procedure. As such, track reconstruction may be run separately for different particle hypotheses, and when relevant, are referred to as electron hypothesis tracks or pion hypothesis tracks [56].

The event hard-scatter primary vertex is defined as the reconstructed vertex with the largest $\sum p_T^2$ of constituent tracks. Tracks are required to have $p_{\mathrm{T}} > 0.5\,\mathrm{GeV}$ and to satisfy quality criteria designed to reject poorly measured and fake tracks. Tracks are assigned to vertices based on the track-to-vertex association resulting from the vertex reconstruction [54].

3.2.2 Calorimeter

The calorimeter, a diagram of which is shown in Fig. 3.7, measures the energy of entering particles. Unlike the inner detector, which does not significantly alter the energy of particles that pass through it, the calorimeter absorbes particles completely, so that few particles (aside from muons) pass all the way through the calorimeter.

The calorimeter is broadly divided into four subsystems: the electromagnetic (EM) calorimeter, the tile calorimeter, the hadronic end-cap, and the forward calorimeter. They are sampling calorimeters, in which different materials are used as the absorber and the active material. With the exception of the forward calorimeter, the calorimeters are designed to have constant granularity with respect to $\Delta\eta \times \Delta\phi$.

The EM calorimeter, intended to detect electromagnetically interacting particles (charged particles or photons), covers $|\eta| < 3.2$ and has lead absorbers and LAr (Liquid Argon) as the active material. The exact structure is somewhat complicated, with different structures in different detector layers and different η regions. Broadly speaking, it has a high granularity region, $|\eta| < 2.5$, with granularity down to $\Delta\eta \times \Delta\phi = 0.025 \times 0.025$ for certain elements, and a lower granularity region, $2.5 <$

$|\eta| < 3.2$, with a granularity of $\Delta\eta \times \Delta\phi = 0.1 \times 0.1$. The high granularity region coincides with the range of the inner dectector, such that precise electron and photon measurements can be made within that region. Outside that region, no attempt is made to reconstruct electrons or photons, and the calorimeter is only used for jets (to be described later), for which precise measurements are less important for this search.

The tile calorimeter detects particles interacting through the strong force. Since electromagneticly interacting particles are expected to be absorbed in the EM calorimeter, the tile calorimeter generally will absorb neutral hadrons. The system covers $|\eta| < 1.7$ and has steel absorbers and scintillating tiles as the active material. As with the EM calorimeters, the layers do not all have the same granularity, but across the full η region the highest granularity layers have $\Delta\eta \times \Delta\phi = 0.1 \times 0.1$.

The hadronic end-cap covers $1.5 < |\eta| < 3.2$, and extends the functionality of the tile calorimeter to $|\eta| = 3.2$, with copper as the absorber and LAr as the active material. It has a granularity of $\Delta\eta \times \Delta\phi = 0.1 \times 0.1$ for $1.5 < |\eta| < 2.5$ and $\Delta\eta \times \Delta\phi = 0.2 \times 0.2$ for $2.5 < |\eta| < 3.2$.

The forward calorimeter is the only system covering $3.2 < |\eta| < 4.9$. It is segmented in $\Delta x \times \Delta y$ instead of $\Delta\eta \times \Delta\phi$, with granularity generally on the order of centimeters in each direction. The innermost layer, composed of copper, serves as the electromagnetic part, and the other two layers, composed of tungsten, serve as the hadronic part, with LAr as the active material in all three layers. In general, the forward calorimeter has significantly worse performance than the inner regions, and it is only used in a limited sense in this search.

The ATLAS calorimeters record the energy deposited in each cell in each event. Individual cell energy depositions are affected by electronic and pile-up noise, and instead of using cells directly in reconstructing more complex objects, we combine cell readings into clusters of cells and use clusters in further reconstruction steps.

This process has the added benefit of improving the agreement between data and simulation, as clusters are less sensitive to shower shape modeling.

The first clustering algorithm, topological clustering (topoclustering) [57], groups nearby cells into dynamically sized clusters, allowing for reconstructing particles with a wide range of shower shaps, while attempting to determine whether each cell's energy deposition results from the hard-scatter interaction or noise. The specific low-level details of topological clustering balance the improved noise suppression and degraded energy resolution of using tighter versus looser cell energy thresholds. First, cells with high significance (defined here as deposited energy divided by noise, $S > 4$) are automatically characterized as hard-scatter. Cells with energy depositions resulting purely from noise are distributed independently of the hard-scatter interaction, on average, while cells originating from actual particle energy depositions tend to be grouped together around locations where a hard-scatter particle interacted with the detector. As such, low and intermediate significance cells ($S > 2$ and $S > 0$, respectively) likely result from noise if they are isolated from any high significance cells, while low significance cells neighboring high significance cells likely do not result from noise. The topoclustering algorithm is defined below.

- Cluster Building
    - Identify cells with high significance ($S > 4$) and identify such cells as protoclusters.
    - Iteratively associate $S > 2$ cells to neighboring protocluster (seed + associated cells).
    - Associate $S > 0$ cells to neighboring protocluster (not iteratively, one layer).
- Cluster Splitting

- Local maxima in each cluster, require each maxima have energy greater than 500 MeV and at least four neighbors, all of which have a smaller signal.
- Identify each maximum as a separate cluster.
- If a cell borders multiple maxima, it is shared between the two highest energy clusters, with the fraction of the cell associated to each cluster is a function of the cluster energies and distances from the cell.

High momentum electrons and photons have generally similar shower shapes, and in order to reconstruct a particular type of particle, the allowance for arbitrary shower shape is no longer necessary. Egamma clusters are fixed size objects used in reconstructing electrons and photons, where the exact cluster dimensions balance noise suppression and energy resolution. In particular, egamma clusters have $\Delta\eta \times \Delta\phi = 0.025 \times 0.025$, corresponding to an $N_\eta \times N_\phi = 200 \times 256$ cluster grid for $|\eta| < 2.5$ [57]. No attempt is made to reconstruct egamma clusters outside this η range, as the lack of tracking information outside this range would significantly degrade the performance of electron reconstruction techniques, which is central to this study. Egamma clusters are seeded by sliding a window of size $\Delta\eta \times \Delta\phi = 3 \times 5$ across η and ϕ and selecting clusters with $E_\mathrm{T} > 2.5\,\mathrm{GeV}$ [56]. If two clusters are too close together (i.e. have $\Delta\phi < 0.3$), the clusters are taken to be duplicates, and the lower energy cluster of the pair is rejected.

3.2.3 Muon Spectrometer

The muon spectrometer (MS), shown in Fig. 3.8, allows for the reconstruction of tracks belonging to charged particles that pass through the calorimeters. In practice such particles are generally muons, but it is possible for very high momentum particles in jets to pass through the calorimeter and be detected by the muon spectrometer.

The MS covers $|\eta| < 2.7$, so that muons can be reconstructed up to higher η than electrons. It has three layers, and, like the inner detector, there are separate cylindrical detectors in the barrel region and end-caps in the forward region. For the most part, the MS is composed of MDT's (Monitored Drift Tubes), though the innermost layer for $2.0 < |\eta| < 2.7$ is composed of CSC's (Cathode Strip Chambers). The MDT's do not provide information corresponding to the ϕ direction but allow for precise p_{T} measurement. The CSC's however, do allow for measurement in both directions.

RPC's (Resistive Plate Chambers) cover $|\eta| < 1.05$ and allow for measurement in both directions in all three layers. TGC's (Thin Gap Chambers) cover $1.05 < |\eta| < 2.7$ and also allow for measurement in both direction in all three layers. RPC's and TGC's are used to trigger events in $|\eta| < 2.4$.

The magnetic field in the MS is toroidal in shape and is variable in strength but is generally between 1 T and 8 T. Due to the higher magnetic field present in the MS than the ID, as well as the larger geometric shape of the detector, reconstruction in the MS allows for a 10% uncertainty for $p_{\mathrm{T}} = 1\,\mathrm{TeV}$ tracks. Unlike in the inner detector, the magnetic field affecting the MS is toroidal, bending tracks in the η direction and not the ϕ direction.

In order to actually reconstruct MS tracks, the first step is to build muon segments in each of the MS subsystems. MDT segments are built by performing a straight-line fit to the hits in each layer, where RPC or TGC hits complement this information by providing the orthogonal coordinate. In the CSC's, a combinatorial search is performed in the η and ϕ planes. Next, middle layer segments are used as the seeds for track building, in an attempt to combine seeds in different layers to form full MS tracks, using segment quality and compatibility to combine different segments. Then, a similar method is performed, but using outer or inner layer segments as seeds for the track building. Track candidates are required to contain at least two segments, or potentially just one high-quality segment in the barrel-endcap transition region. Lastly, a full track fit is performed, using the hits in each segment, and a MS track is accepted if the fit has high enough quality [58].

3.2.4 Forward Detectors

A set of forward detectors are used to measure the instantaneous luminosity, necessary for correctly deriving and applying process cross-sections. Before Run 2, the forward detector systems were, in order of increasing distance from the interaction point, LUCID (LUminosity measurement using Cherenkov Integrating Detector, at $\pm 17m$), ZDC (Zero-Degree Calorimeter, at $\pm 140m$), and ALFA (Absolute Luminosity For ATLAS, at $\pm 240m$). In general, the systems measure forward inelastic pp scattering, which is turned into a luminosity measurement. Between Run 1 and Run 2, a new system was added, the DBM (Diamond Beam Monitor, at $\eta = \pm 3.2$), which further measures luminosity [59].

3.2.5 Trigger System

The vast majority of bunch crossings are not of interest from the point of view of physics searches, and it is computationally unfeasible to record all of them. The trigger system serves to first identify interactions that might be of interest to physics analyses during operation, using the L1 (Level-1, ”online”) trigger, and then to use a software-based trigger, the HLT (High-Level Trigger) to further filter the accepted events based on more stringent requirements. The L1 trigger is designed to accept 100 kHz, and at 40 MHz, corresponding to an acceptance of 0.25%, and the HLT further filters events to 1 kHz [60].

Due to the speed at which decisions must occur, only limited detector information is available to the L1 trigger. In particular, inner detector information is not available, and decisions are based on calorimeter and muon information only. Triggering can occur due to a number of different event properties, but due to the nature of this search, only lepton-based triggers are considered. The specific details of the trigger usage are discussed in a later section, but each of the relevant L1 and HLT triggers requires that events contain either one, two, or three light leptons.

3.3 Simulation and Digitization

A detailed simulation of the ATLAS detector is used to process the detector signals produced by generated MC events. Two versions of the simulation process exist, designated FullSim (Full Simulation) and FastSim (Fast Simulation, or AF-II for the specific version). In FullSim, GEANT4 is used to propagate every particle through the full ATLAS detector, including time-dependent alignment and distortion effects [61]. Alternatively, in AF-II, a number of much faster methods are used to simulate different parts of the detector. In particular, interactions of particles with the calorimeter systems can be replaced with presimulated showers stored in memory. While not used for background samples in this search (except one sample used for systematic studies), AF-II is particularly useful for signal samples, due to the large number of samples produced and the computational cost of GEANT4. The output of the simulation step is a set of hits in each of the detector elements, which contain energy, spacial coordinates, and time. The next step is digitization, which turns the hits into actual output readings. The specific details of simulation and digitization are complicated and vary across different detector elements, but a detailed example is given for the pixel detector.

In the digitization of the pixel detector, the input to digitization is a list of locations where a particle entered and exited each detector element, as well as the deposited energy (E) and the time the interaction occured. Then, each particle path is broken down into a fixed number (N) of equally spaced energy deposits ($\frac{E}{N}$) along the path. Next, each energy deposit ($\frac{E}{N}$) is broken down into a fixed number of charged bunches, and each bunch is propagated to the surface of the detector element, taking into account electric and magnetic fields, the interaction of neighboring cells, thermal noise, other sources of noise, individual cell properties from a database, and timing effects. The total potential difference resulting from all the charges at the surface is then calculated for each cell, which is translated into a time-above-threshold (if any) for each individual cell, the input to reconstruction.

In general, beyond the hard-scatter interaction, it is necessary to also include pile-up interactions. Simulation (GEANT4) can be run separately for each interaction in an event, but digitization processes all the interactions together, since the output of digitization is not a simple addition of the individual signals that would have been produced by each interaction separately. As a result, generally pile-up interactions are superimposed on the hard-scatter interaction during the digitization process. To use the same example as before, in the pixel digitization, the propagation of charges to detector surfaces happens separately for each interaction, but then a few of the pixel-level effects, as well as the determination of the time-over-threshold for each pixel, are processed for all interactions together.

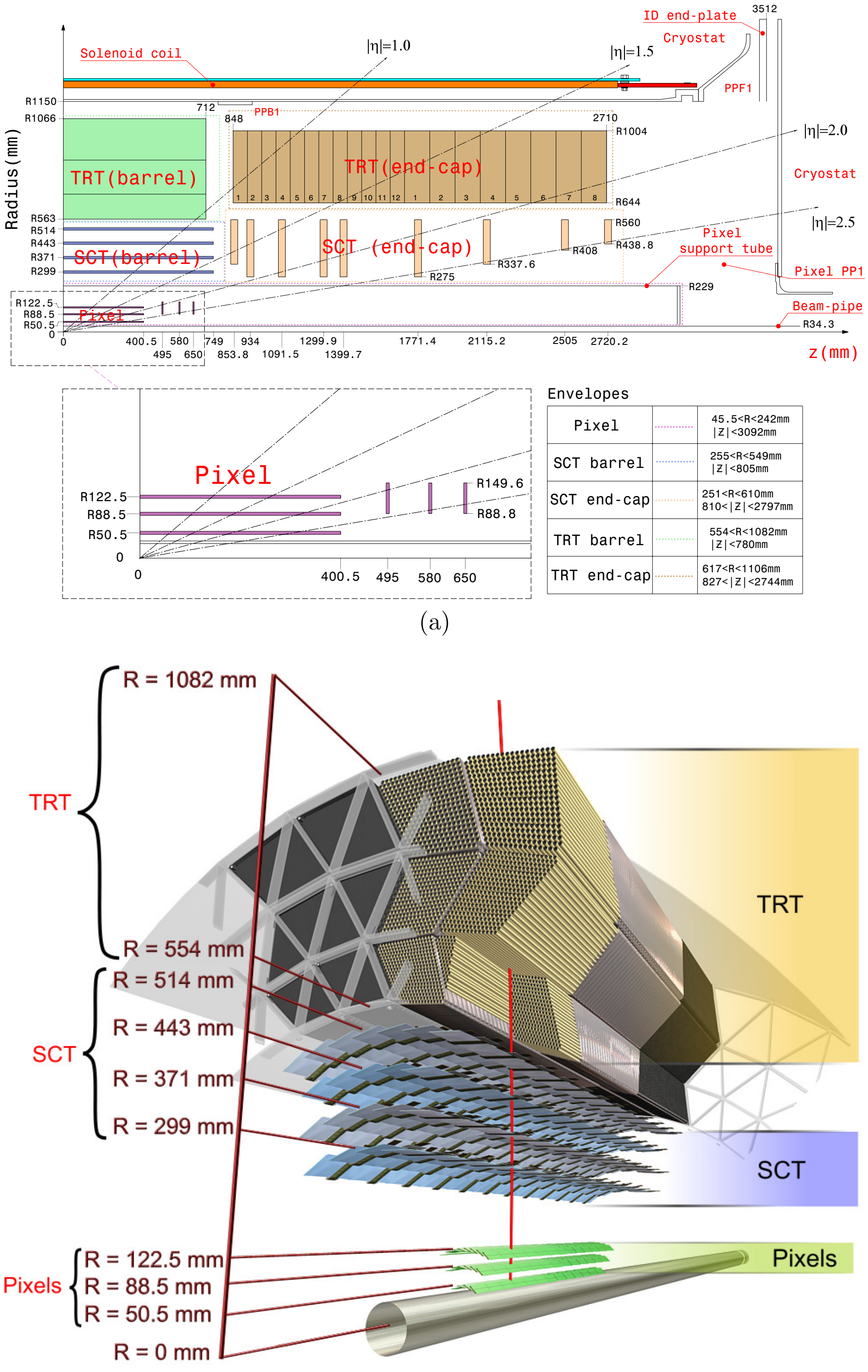

(a)

(b)

Figure 3.6: Diagrams of the inner detector systems.

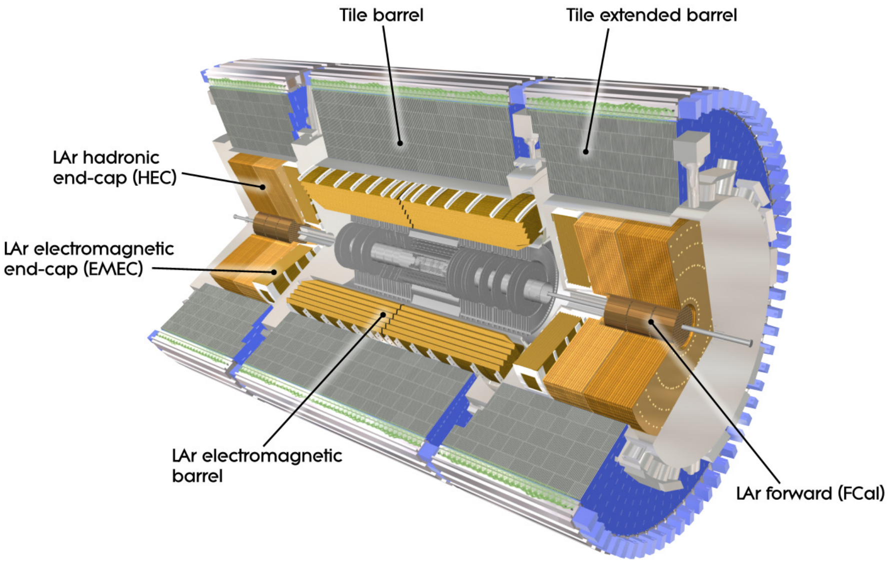

Figure 3.7: Diagram of the ATLAS calorimeter

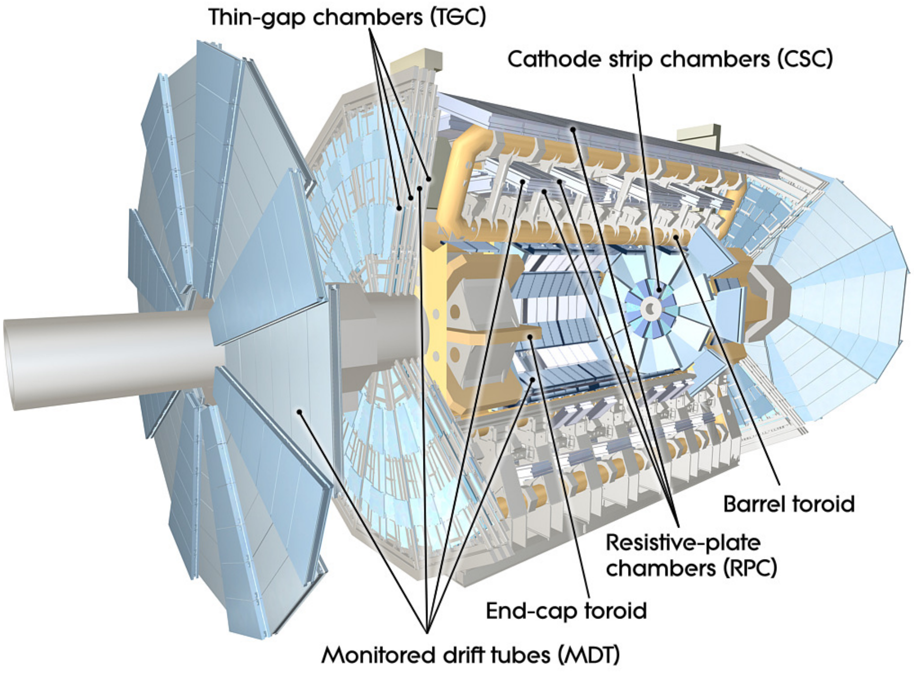

Figure 3.8: Diagram of the ATLAS muon spectrometer

Chapter 4

Object Reconstruction

4.1 Reconstructing Physics Objects

Clusters and tracks are intended to represent individual electrons, muons, photons, or hadrons. However, the particles of interest to physics analyses are those produced by the hard scatter interaction, as opposed to particles from the parton shower or FSR (Final State Radiation). For the purposes of this physics search, the particles that must be reconstructed are electrons, muons, and jets, where jets represent hadrons originating from individual quarks or gluons. Noninteracting particles (e.g. neutrinos), are partially reconstructed using a more complicated process of missing transverse momentum ($E_{\mathrm{T}}^{\mathrm{miss}}$).

4.1.1 Reconstructing Electrons

Electrons are detected by both the inner detector and the electromagnetic calorimeter, matching an ID track to an egamma cluster. First, to be considered, egamma clusters must have a well-defined core, requiring that the ratio of the energy in $\Delta\eta \times \Delta\phi = 3 \times 7$ cells centered at the egamma coordinates is greater than 0.65 of the energy $\Delta\eta \times \Delta\phi = 7 \times 7$. Second, egamma clusters must not have significant interaction with the hadronic calorimeters, requiring that the transverse energy in the hadronic calorimeter is less than 10% of the transverse energy in the EM cluster (for $|\eta| < 0.8$, only the first layer of the hadronic calorimeter is considered, as pile-up is higher in the more central region, and hadronic deposits may result from pile-up). Third, either an electron or pion hypothesis track is required to lie within $\Delta R < 0.3$ with respect to the egamma cluster. In practice, electron hypothesis track reconstruction is not run on all track seeds, but if a track seed has $\Delta R < 0.3$, and if a pion hypothesis track cannot be built satisfying the tracking requirements, then electron hypothesis track reconstruction is run on the seed. Fourth, the track is extrapolated to the middle layer of the EM calorimeter, and it is required that the track be close to the cluster. For this extrapolation procedure, the matching is attempted using both the measured track momentum and the cluster momentum, and the matching is successful if either attempt is successful. In the track momentum attempt, the track is required to have $\Delta\phi < 0.2(0.05)$ with respect to the EM cluster, if the track is curving toward (away) from the cluster, and for non-TRT-only tracks, it is required that $\Delta\eta < 0.05$. In the cluster momentum attempt, the track is required to have $\Delta\phi < 0.1(0.05)$ with respect to the EM cluster, if the track is curving toward (away) from the cluster, and for non-TRT-only tracks, it is required that $\Delta\eta < 0.05$. Fifth, non-TRT-only tracks are rereconstructed using a tracking algorithm optimized for electron reconstruction (Gaussian Sum Filter) [62] and are required to have $\Delta\phi < 0.1$ with respect to the EM cluster. In the TRT-only case, the track is required to have $\Delta\phi < 0.03(0.02)$ with respect to the EM cluster, if the track is curving toward (away) from the cluster, and $\Delta\eta < 0.35(0.2)$ in the TRT barrel (endcap). Sixth, the cluster is rebuilt using a process optimized for electron position and energy resolution [56].

At this point, a multivariate technique (LH [56]) is used, taking into account a set of cluster and track based variables. For the purposes of this study, two different working points are used, referred to hereafter as VeryLoose and Medium, where VeryLoose electrons are a subset of Medium electrons.

Separate isolation variables are calculated using calorimeter and tracking information. The calorimeter isolation is calculated by taking ΣE_{T} of all topoclusters with $\Delta R < 0.2$ with respect to the electron, subtracting the 5×7 cell grid centered at the electron, with extra corrections to account for leakage outside the window and for pile-up. The track isolation is calculated by taking Σp_{T} of all tracks with $\Delta R < min(0.2, 10\,\mathrm{GeV}/E_{\mathrm{T}})$ with respect to the electron track, applying the track quality and impact parameter requirements and not including the electron track itself. For the actual electron isolation requirements, p_{T} dependent isolation requirements are used [63], where the actual working point used in this search is named GradientLoose. Particularly for processes involving decays of low mass particles ($\leq 50\,\mathrm{GeV}$), leptons frequently are close together in ΔR in the final state, and it is necessary to remove the contribution of nearby leptons from each other's isolation. This subtraction is imperfect, since it relies on assumptions about energy deposited by the two different particles and results in correlations in the isolation of the two particles.

Lastly, electrons are required to be associated to the primary vertex by requiring $|z_0 sin(\theta)| < 0.5$ mm and $d_0/\sigma(d_0) < 5$.

For simplicity, the terminology for electron classification is summarized below, where in all cases electrons are required to also satisfy $p_{\mathrm{T}} > 7\,\mathrm{GeV}$ and $|\eta| < 2.47$.

- Baseline electrons: satisfy VeryLoose identification criteria
- Signal electrons: satisfy Medium identification, isolation, and vertex association criteria
- Loose electrons: satisfy baseline electron criteria but not signal criteria (fails isolation or Medium criteria)

4.1.2 Reconstructing Muons

Muons potentially interact with all three primary detector systems. Three different muon reconstruction methods are considered, described in order of decreasing priority. First, combined muons are the purist muon type, built by matching an inner detector track and a muon spectrometer track. Then, a global refit is performed to optimize the muon measurement, using both outside-in (extrapolate inward from MS) and inside-out (extrapolate outward from inner detector) techniques. Segment-tagged muons are built from an inner detector track and at least one muon spectrometer segment, useful for low momentum muons (significantly curved by the stronger MS magnetic field) or muons in certain detector regions. Lastly, standalone muons have a muon spectrometer track but no inner detector track. Such muons allow for muon acceptance outside the inner detector range, from $2.5 < |\eta| < 2.7$. In cases where a track is assigned to both a segment-tagged and a combined muon, the segment tagged muon is rejected.

As with electrons, an isolation selection may be applied for muons, using the same working point (GradientLoose) [58]. Muons are classified as loose or signal muons, with baseline muons containing the two categories. However, loose and signal muons only differ in the isolation and vertex association requirements applied to signal muons but not loose baseline muons. Signal muons are required to be associated to the primary vertex by requiring $|z_0 sin(\theta)| < 0.5$ mm and $d_0/\sigma(d_0) < 3$, corresponding to a tighter $d_0/\sigma(d_0)$ requirement for muons than electrons.

4.1.3 Reconstructing Jets

Quarks or gluons produced in the hard-scatter interaction hadronize to form jets of lower energy particles, mostly hadrons and photons. The jet reconstruction process combines nearby calorimeter energy deposits to reconstruct single physics objects representing these hadronized quarks or gluons. FASTJET 2.4.3 is used to reconstruct anti-k_t [64] jets from topo-clusters with a distance parameter $R = 0.4$. Tracks are assigned to jets using a technique known as ghost association [65]. Effectively, tracks are included in the clustering procedure, assigning them infinitesimal momentum so that they do not interfere with the clustering but are included in the final clustered jets. These tracks are used in overlap removal, jet vertex association, and the missing transverse momentum calculation, all of which are described later.

Calorimeter jets are calibrated using pile-up subtraction followed by a jet-energy-scale (JES) response correction, as described in detail in Refs. [66, 67]. Jets are required to have $p_{\mathrm{T}} > 20\,\mathrm{GeV}$, and no quality criteria are applied, aside from the event cleaning criteria (next section).

Assigning jets to vertices is more ambiguous than for leptons, since, while tracks (with their corresponding origin information) may be associated to jets, an individual jet may contain tracks from multiple vertices. Further, pile-up jets (jets not originating from the primary vertex) themselves come in two basic types with somewhat different properties. A QCD pile-up jet is an actual jet originating from a single pile-up vertex. A stochastic pile-up jet originates from a combination from energy depositions from multiple different vertices and potentially detector-level effects - effectively, a fake jet. Jets are assigned to the primary vertex using the jet vertex tagger (JVT), optimized to reject both QCD and stochastic pile-up jets. The JVT discriminant is built out of the combination of two jet variables, corrJVF and R_{pT}, that provide information to separate hard-scatter from pile-up jets. The quantity corrJVF is defined as

$$\mathrm{corrJVF} = \frac{\sum_k p_{\mathrm{T}}^{trk_k}(PV_0)}{\sum_l p_{\mathrm{T}}^{trk_l}(PV_0) + \frac{p_{\mathrm{T}}^{\mathrm{PU}}}{(k\cdot n_{\mathrm{trk}}^{\mathrm{PU}})}}. \tag{4.1}$$

where PV_i denotes the reconstructed event vertices (PV_0 is by convention the hard-scatter vertex), and $\sum_k p_{\mathrm{T}}^{trk_k}(PV_0)$ is the scalar p_{T} sum of the tracks that are associated with the jet and originate from the hard-scatter vertex. The term $p_{\mathrm{T}}^{\mathrm{PU}} = \sum_{i\geq 1}\sum_l p_{\mathrm{T}}^{trk_l}(PV_i)$ denotes the scalar p_{T} sum of the tracks associated with the jet and originating from pile-up vertices. To correct for the linear increase of $\langle p_{\mathrm{T}}^{\mathrm{PU}}\rangle$ with the total number of pile-up tracks per event ($n_{\mathrm{trk}}^{\mathrm{PU}}$), we divide $p_{\mathrm{T}}^{\mathrm{PU}}$ in the corrJVF definition by $(k \cdot n_{\mathrm{trk}}^{\mathrm{PU}})$ with $k = 0.01$ [68]. corrJVF represents the relative fraction of tracks associated to the jet that originate from the primary vertex as opposed to the hard-scatter vertex. The variable R_{pT} is defined as the scalar p_{T} sum of the tracks that are associated with the jet and originate from the hard-scatter vertex divided by the fully calibrated jet p_{T}^{jet}, which includes pile-up subtraction:

$$R_{\mathrm{pT}} = \frac{\sum_k p_{\mathrm{T}}^{trk_k}(PV_0)}{p_{\mathrm{T}}^{jet}}. \tag{4.2}$$

R_{pT} represents the consistency of the calorimeter and inner detector jet measurements. Both R_{pT} and corrJVF are large for hard-scatter jets and small for pile-up jets. The JVT discriminant is built by defining a 2-dimensional likelihood based on a k-nearest neighbor (kNN) algorithm [69]. Jets are defined as pile-up and rejected if they satisfy $p_{\mathrm{T}} < 60\,\mathrm{GeV}$ (pile-up jets tend to be soft), $|\eta| < 2.4$ (no vertex association can be performed outside the inner detector range), and $JVT < 0.59$, corresponding to a hard-scatter efficiency of approximately 92% in the range of validity. The efficiency and fake rate of JVT are shown in Fig. 4.1, demonstrating the independence of the hard-scatter efficiency and pile-up jet efficiency as a function of the average number of interactions per bunch crossing, μ. The effectiveness of JVT decreases with increasing jet p_{T}, both due to the improved relative momentum resolution at higher p_{T} and the increased amount of available tracking information on average for higher p_{T} jets. JVT allows for a rejection of $> 98\%$ of pile-up jets at a hard-scatter jet efficiency of 92%.

Jets are classified as signal and baseline, purely based on their kinematic variables. Baseline jets satisfy $p_{\mathrm{T}} > 20\,\mathrm{GeV}$ and $|\eta| < 4.9$, while signal jets satisfy $p_{\mathrm{T}} > 40\,\mathrm{GeV}$ and $|\eta| < 2.8$.

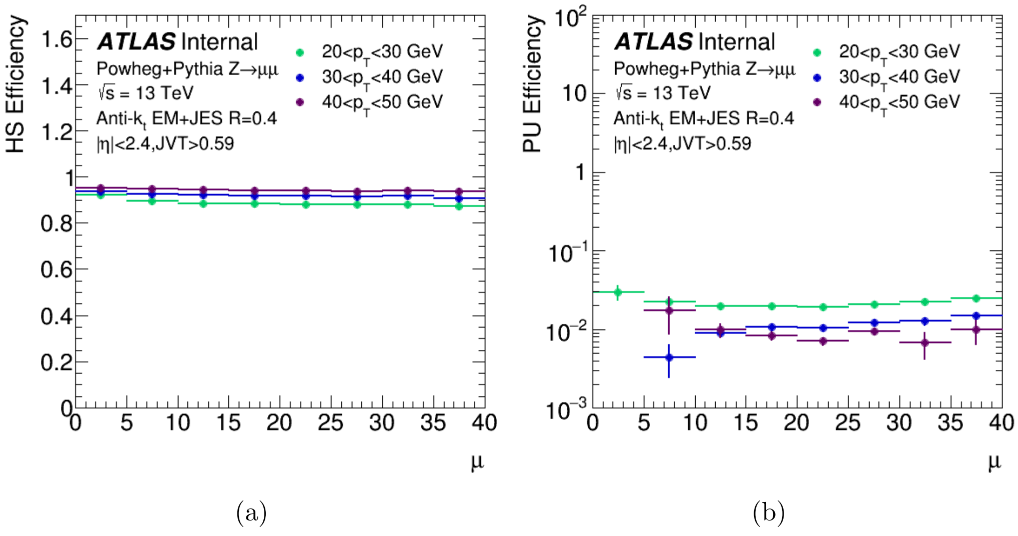

Figure 4.1: JVT efficiency for hard-scatter and pile-up jets in the central region

4.2 Reconstruction Ambiguity

Each physics object reconstruction algorithm is run independently. As such, a group of constituents may be reconstructed as multiple different physics objects of different types. For example, electrons are almost always also reconstructed as jets, as each object type relies on a large energy deposit in the calorimeter. In order to turn a set of reconstructed objects into a final set of physics objects, this ambiguity needs to be resolved.

4.2.1 Overlap Removal

If two objects overlap at all, at least one of the objects is discarded. This approach is perhaps more conservative than necessary, as it is possible for two objects to be close together and partially overlapping. However, since the Standard Model background lepton multiplicity is a sharply falling distribution, any sort of double counting could dramatically increase the Standard Model background. On the other hand, the slightly lower signal efficiency that would result from dropping nearby objects that are actually distinct objects is more tolerable from an analysis point of view. As a result, this simple method is used instead of trying to reconstruct nearby objects.

The decision of which to discard is based on the priority of each object type and the nature of the overlap of the two objects. First, if an electron and a muon share a track, the electron is rejected. This is because, while an inner detector track and potentially a calorimeter deposition can be ambiguous between and electron and muon, a muon spectrometer track will not result from an electron. Second, if an electron and a jet have $\Delta R < 0.2$, the jet is removed. Electrons always have calorimeter depositions that may be reconstructed as jets, and jet reconstruction makes no effort to confirm that a calorimeter deposition is hadronic in nature. Third, if an electron and a jet have $0.2 < \Delta R < 0.4$, the electron is removed. If an electron is near the outside of a jet, the electron likely results from the decay of some particle in the jet, as opposed to being the source of the jet (i.e. the electron is not prompt). Fourth, if a muon and jet satisfy $\Delta R < 0.2$ or the muon is ghost-associated to the jet, and if the jet has fewer than two associated primary vertex tracks or the jet and muon satisfy $p_T^{muon}/p_T^{jet} > 0.5$ and $p_T^{muon}/\Sigma p_T^{jettracks} > 0.7$, then the jet is removed. In these cases, the jet is taken to be the result of muon energy loss in the calorimeter and is rejected. Sixth, if the above criteria are not satisfied and if $\Delta R < 0.4$ the muon is removed. As in the case of electrons, in such cases the muon is taken to result from an interaction within the jet.

4.2.2 Low Mass Resonances

Lastly, a cut is placed on the invariant mass of pairs of leptons in order to remove leptons originating from hadron decays and the Drell-Yan background. These processes can potentially be a significant background to the relevant SUSY processes, but the real danger is that these processes are not well modeled in MC. Since the size of these backgrounds is then potentially unknown, it is desirable to eliminate them. The dilepton spectrum is shown in Fig. 5.41, applying the same event selection described in section 5, except requiring exactly two leptons instead of four. Particularly for the dimuon distribution, peaks are clearly visible for a number of the low-mass resonances. For technical reasons, the size of each peak does not necessarily correspond to the cross-section for the corresponding resonance, as the event selection efficiency decreases as the invariant mass decreases. For the dielectron distribution, the very low mass resonances are harder to detect, both due to a very low selection efficiency and due to the difficulty of reconstructing close-by calorimeter signals. The dimuon and electron-muon cases are comparitively easy to reconstruct, as the tracks of the two leptons can be reconstructed to very low separation, and in the electron-muon case, the calorimeter signal is expected to originate almost completely from the electron. Based on the invariant mass distribution, leptons are rejected if they have invariant mass with respect to any opposite sign lepton (baseline, passing ambiguity resolution) less than $4\,\mathrm{GeV}$, in order to reject low mass resonances. These lepton pairs are not required to have the same flavor, as electron-muon decays often occur from heavy flavor hadrons. The Υ resonance can also form a significant background, and same-flavor opposite-sign lepton pairs are rejected if their mass is in the range $8.4 < m < 10.4\,\mathrm{GeV}$.

From the point of view of this physics search, the exact size and location of this window determines the sensitivity to the benchmark signal grid points with a $\tilde{\chi}_1^0$ mass of $10\,\mathrm{GeV}$ (shown in Fig. 4.3). The dilepton mass is always less than $10\,\mathrm{GeV}$, as the neutrino from the decay is not included. In each of these distributions, the plotted value is the lowest reconstructed dilepton mass pair of each type in each event. The integral of each distribution in each figure may be less than one if there are no lepton pairs satisfying the particular criteria for that figure or if the value for a particular event is out-of-range. In essence, the integral of each distribution is the fraction of reconstructed events that would be rejected by a particular low invariant mass veto

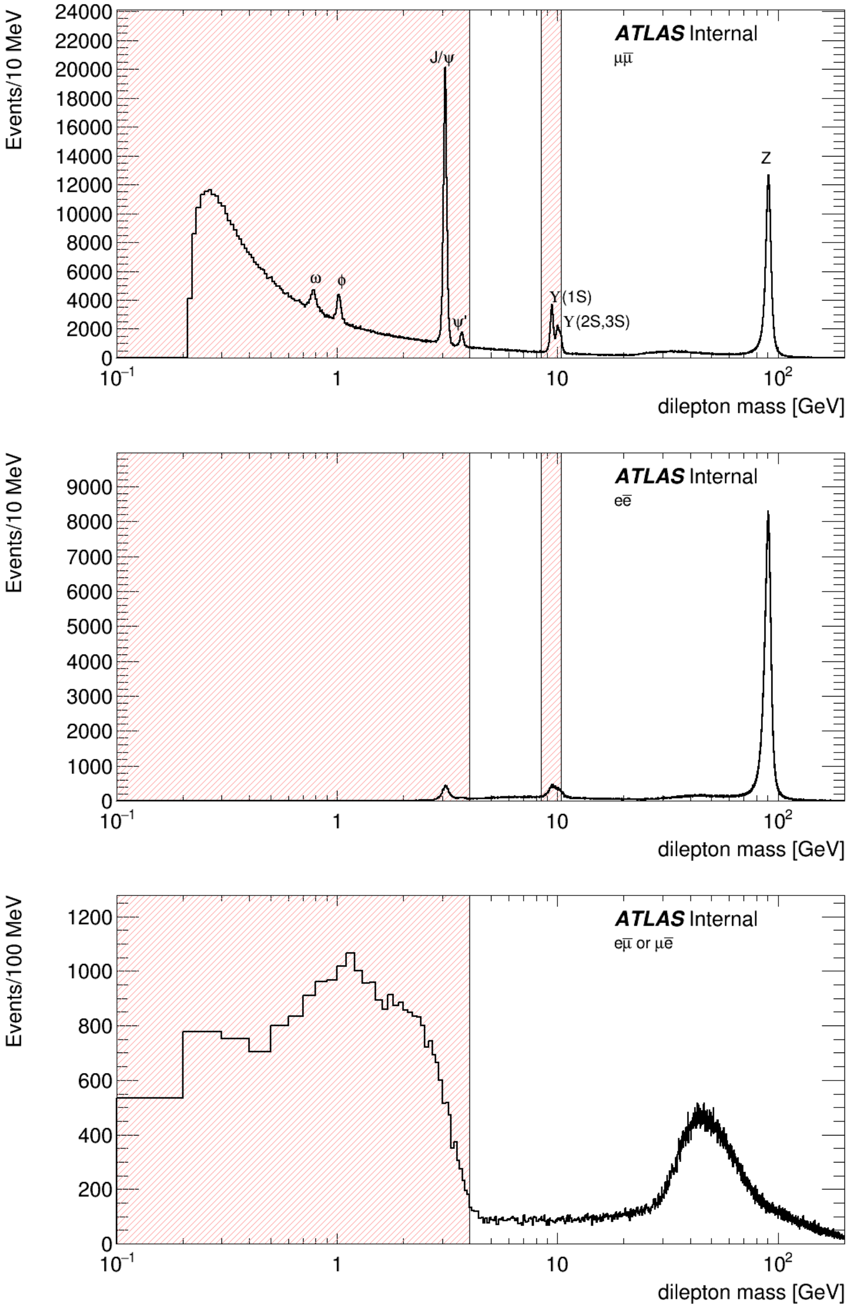

Figure 4.2: Dilepton resonances, showing shaded regions that are excluded.

on lepton pairs.

The samples shown in these figures include an equal number of simulated events in the dielectron, dimuon, and electron-muon subfigures, and the relatively small number of events in the dielectron subfigure is due to the lower close-by electron reconstruction efficiency described above. On the other hand, the electron-muon and dimuon yields are approximately the same. Also of note is that the distribution is largely unchanged for the different chargino mass points, and the problem of remaining sensitive to low $\tilde{\chi}_1^0$ mass points is not avoided by only considering high chargino mass. From these plots, any low mass rejection will significantly reduce signal sensitivity. The more complicated method of vetoing low mass resonances as opposed to the simplified method (used by most electroweak searches) of vetoing all lepton pairs with an invariant mass below some higher threshold (e.g. 12 GeV) is used with the low $\tilde{\chi}_1^0$ mass points in mind.

This low invariant mass veto is taken to be the last step in the overlap removal process. It is a lepton-specific and not event-wide removal, as events are kept if there is a low mass resonance, except that the leptons in the low mass resonance are removed.

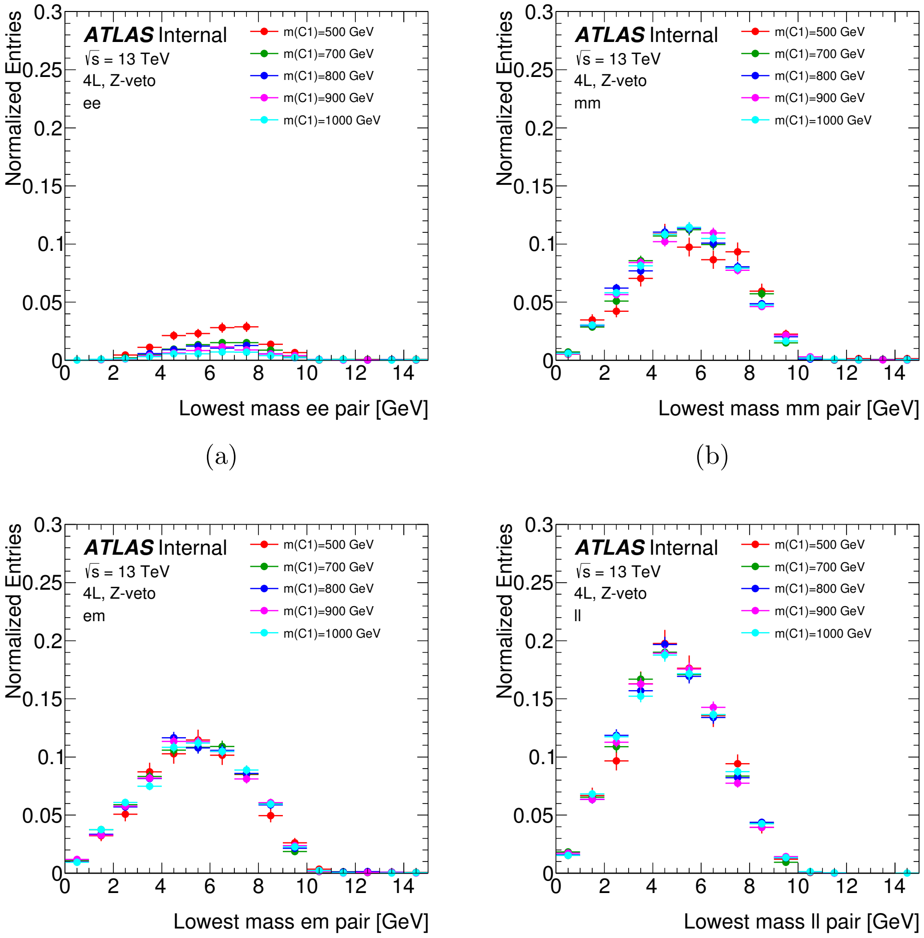

(a) (b)

(c) (d)

Figure 4.3: Fraction of signal events with low mass lepton pairs in each of the signal grid points with a low mass $\tilde{\chi}_1^0$.

4.3 Neutrinos

Stable particles that do not interact through the electromagnetic force (seen by the inner detector and electromagnetic calorimeter, and possibly the muon spectrometer) or the strong force (seen by the hadronic calormeter) are invisible to the ATLAS detector. In the Standard Model and in some considered supersymmetry models, the only particles satisfying these criteria are neutrinos. In any collision, the sum of the momenta of all final state particles must be zero, in the direction transverse to the beampipe. If the momenta of all the visible final state particles in an event are vectorially added to get a result other than zero, it is an indication of some noninteracting particle(s) in the event [70].

$E_{\mathrm{T}}^{\mathrm{miss}}$ can be calculated as

$$E_{x(y)}^{\mathrm{miss}} = -\sum_{i\in\{\mathrm{electrons}\}} p_{x(y),i}^{\mathrm{ele}} - \sum_{i\in\{\mathrm{muons}\}} p_{x(y),i}^{\mathrm{muon}} - \sum_{i\in\{\mathrm{jets}\}} p_{x(y),i}^{\mathrm{jet}} - \sum_{i\in\{\mathrm{soft\ signals}\}} p_{x(y),i}^{\mathrm{soft}} \tag{4.3}$$

where the last term represents a sum over everything else in the event, aside from objects included in the other terms. Calculating the last two terms introduces extra complications. For the jet sum, the conventional overlap removal described previously is too restrictive. For example, if a lepton radiates a collinear photon, the photon would ordinarily be removed, but not including the photon could then give a sizeable apparent $E_{\mathrm{T}}^{\mathrm{miss}}$. Second, while $E_{\mathrm{T}}^{\mathrm{miss}}$ could be calculated purely from hard objects (electrons, muons, and jets), soft jets (those with $p_{\mathrm{T}} < 20\,\mathrm{GeV}$) and contributions from the underlying event can have sizeable momentum, and not including such contributions could also give a sizeable apparent $E_{\mathrm{T}}^{\mathrm{miss}}$. However, the question of what to actually include in the soft term is somewhat complicated.

4.3.1 Ambiguity Resolution

Conventional overlap removal is no longer sufficienct when reconstructing $E_{\mathrm{T}}^{\mathrm{miss}}$. For the purpose of $E_{\mathrm{T}}^{\mathrm{miss}}$, double counting an object with a particular momentum vector is just as harmful as leaving out an object of the same momentum vector from the calculation. Thus, the conservative approach used in overlap removal is no longer sufficient. Ambiguity resolution attempts to resolve ambiguity between every object in an event, both physics objects and unclassified constituent objects.

From the point of view of this search, there is no ambiguity between electrons and muons. In essence, electrons are primarily calorimeter objects, while muons are primarily inner detector and MS (3.2.3) objects. However, the overlap with jets needs to be taken into account. If an electron overlaps a jet, the topoclusters associated to the electron are removed from the jet p_{T}. If over half of the jet p_{T} remains, the calibrated jet p_{T} is included in the $E_{\mathrm{T}}^{\mathrm{miss}}$ calculation, corrected for the topoclusters associated to the electron. This method then allows recovery of, for example, jets resulting from FSR, or electrons resulting from heavy flavor decay.

In the case of muons, muons deposit a small amount of energy in the calorimeter, so if a muon overlaps a jet, the expected muon energy loss is removed from the jet. Further, a somewhat complicated set of selection criteria are used to further classify the overlapping jet. If the jet appears to be pile-up (in which case the JVT requirement described previously would be affected by the presence of the muon and would no longer be reliable), it is removed from consideration. If the jet appears to be FSR, it is included in the calculation, but no jet calibration is used. Otherwise, the jet is included in the calculation as a normal, calibrated jet.

4.3.2 Unassociated Constituents

In order to take into account soft jets and the underlying event, a number of strategies are possible. In particular, unassociated topoclusters could be used, or tracks could be used. Using only clusters is potentially problematic, since many of these clusters would result from pile-up interactions or noise, and clusters may have significant uncertainty in their p_{T}. Using only tracks removes these complications, but then neutral objects and objects with $|\eta| > 2.5$ are not included in the calculation. A comparison is shown in simulated Z+jets , W+jets, and $t\bar{t}$ events in Fig. 4.4. In each plot, $E_{\mathrm{T}}^{\mathrm{miss}}$ indicates the use of tracks in the soft term, and $E_{\mathrm{T}}^{\mathrm{miss,calo}}$ used clusters in the soft term. $p_{\mathrm{T}}^{\mathrm{miss}}$ is shown for reference and includes tracks in the soft term and also tracks instead of jets in the jet term. Using tracks in place of clusters gives a better resolution in all the shown samples and also has less pile-up dependence. As a result, the $E_{\mathrm{T}}^{\mathrm{miss}}$ calculation that is actually used includes only tracks in the soft term.

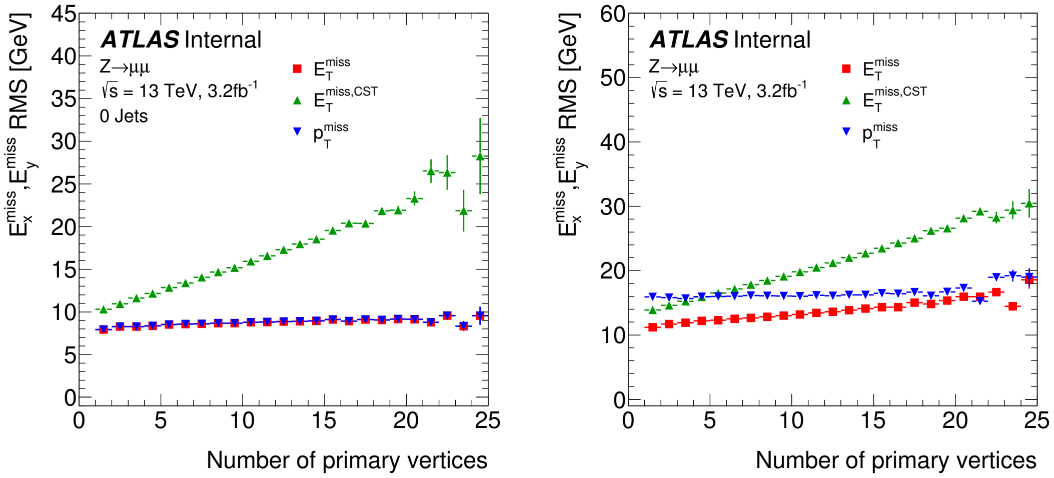

(a) Data Z, $N_{jet} = 0$

(b) Data Z, inclusive

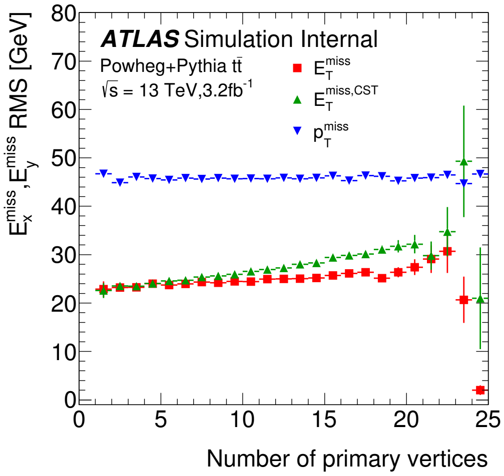

(c) MC simulations, $t\bar{t}$

Figure 4.4: Comparison of the reference E_T^{miss} resolution with the resolutions of the track-only based variant p_T^{miss}, and the reconstruction variant $E_T^{\text{miss,calo}}$ employing a calorimeter-based soft term. The resolutions are shown as function of the pile-up activity measured in terms of the number of reconstructed vertices N_{PV} for (a) an exclusive Z sample without jets with $p_T > 20\,\text{GeV}$ and (b) an inclusive Z sample, both collected from data. In (c), the resolution of the E_T^{miss} reconstruction variants in a final state with significant jet activity and $p_T^{\nu} > 0$ is compared using MC simulations of $t\bar{t}$ production.

4.3.3 Data/MC Agreement

E_T^{miss} potentially suffers from significant mismodeling in simulation, and the scale of the disagreement is strongly dependent on the generator. Examples are shown in Fig.

4.5, showing the overall $E_{\mathrm{T}}^{\mathrm{miss}}$ distribution, the distributions of $E_{x(y)}^{\mathrm{miss}}$, and the ΣE_{T} distribution (the scalar sum of p_{T} for all included objects in the $E_{\mathrm{T}}^{\mathrm{miss}}$ calculation). The overall distribution gives agreement when the systematic uncertainties are taken into account, but the ΣE_{T} distributions differ significantly when comparing data and MC. This disagreement may have multiple sources, ranging from underlying event modeling, hard-scatter process modeling, and uncertainties in the detector simulation (GEANT4). Because of this disagreement, physics searches generally should not be directly dependent on ΣE_{T}.

The distributions of the individual $E_{\mathrm{T}}^{\mathrm{miss}}$ terms are shown in Fig. 4.6. Individual terms potentially disagree between data and MC, and it is therefore desirable that physics searches do not rely directly on individual $E_{\mathrm{T}}^{\mathrm{miss}}$ terms. As a result, for the purpose of search optimization, shown in the next section 5, the only vectorial quantity that is considered is the full $E_{\mathrm{T}}^{\mathrm{miss}}$ value.

As a final check, the $E_{\mathrm{T}}^{\mathrm{miss}}$ resolution is shown again in 4.7, comparing data and MC. Agreement is observed between data and MC. $E_{\mathrm{T}}^{\mathrm{miss}}$ is taken to be a well-behaved variable to be used in physics searches (including this one).

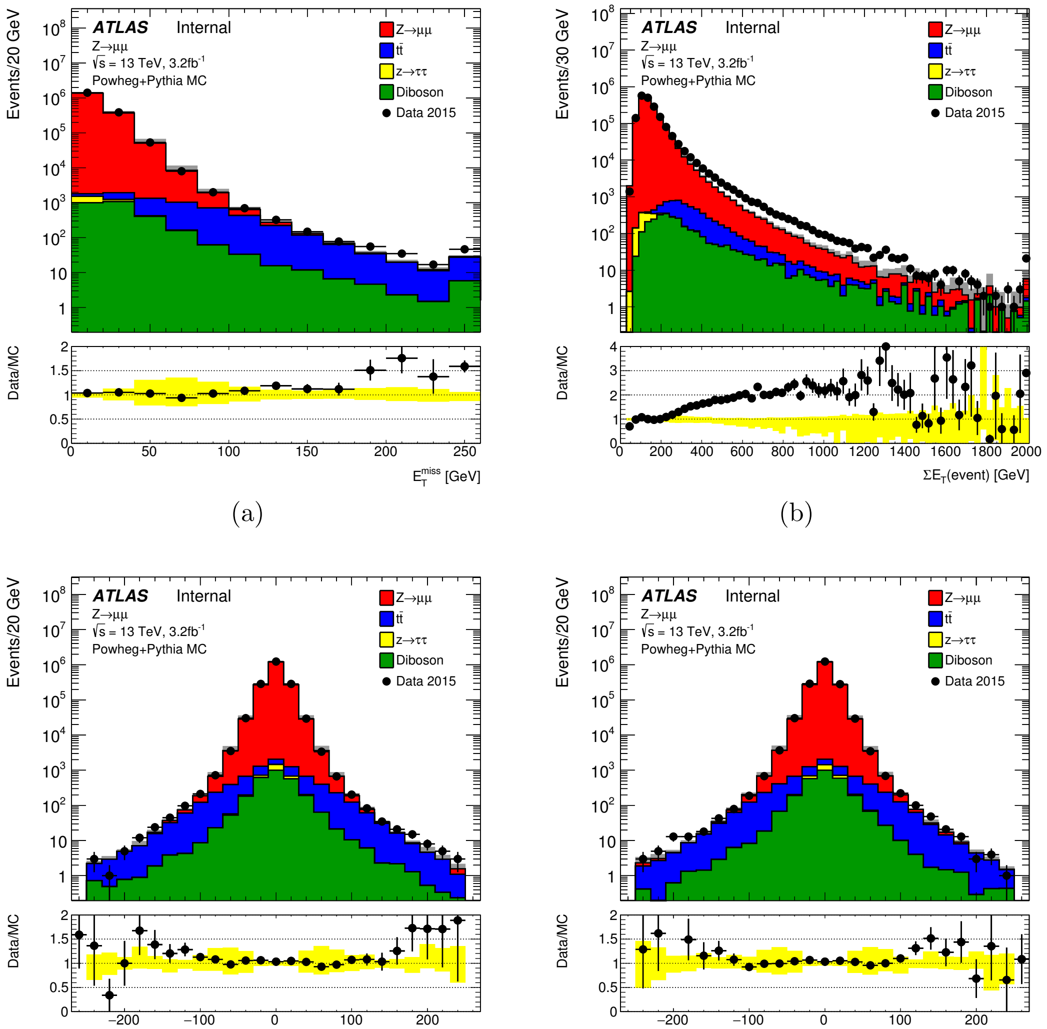

(a) (b) (c) (d)

Figure 4.5: Distributions of (a) $E_{\mathrm{T}}^{\mathrm{miss}}$, (b) ΣE_{T}, (c) E_x^{miss} and (d) E_y^{miss} for an inclusive sample of Z events extracted from data and compared to MC simulations including all relevant backgrounds.

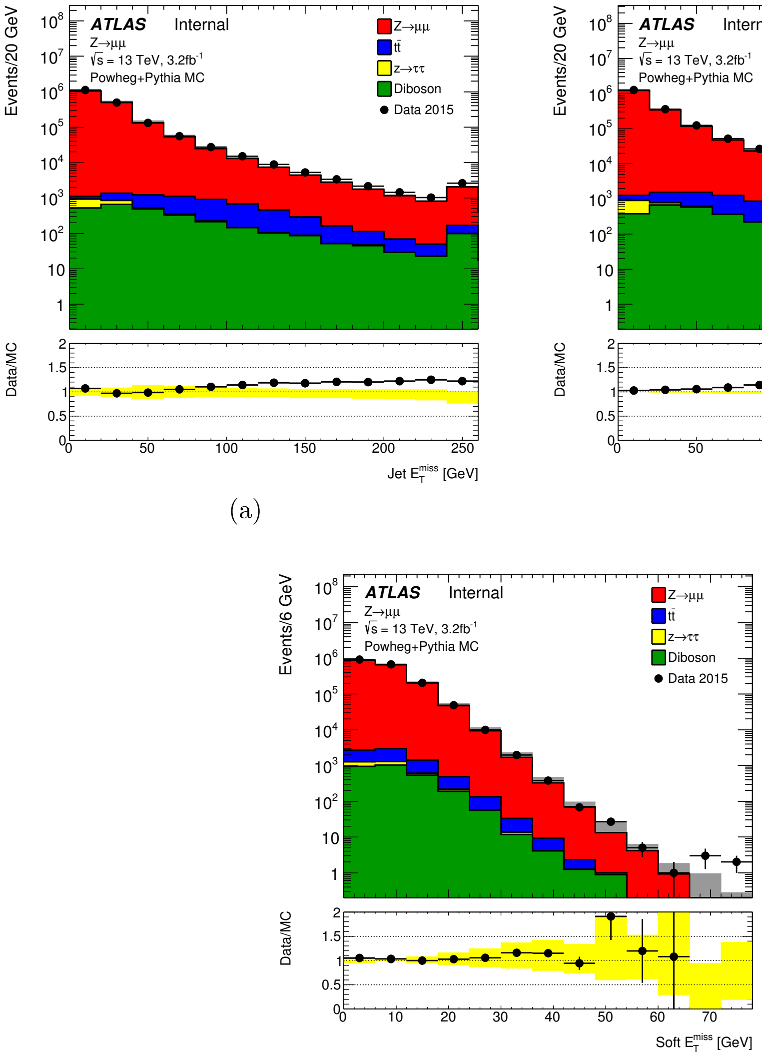

(a)

(b)

(c)

Figure 4.6: Distributions of (a) the jet term $E_{\mathrm{T}}^{\mathrm{miss,jet}}$, (b) the muon term $E_{\mathrm{T}}^{\mathrm{miss},\mu}$, and (c) the soft term $E_{\mathrm{T}}^{\mathrm{miss,soft}}$ for the inclusive samples of Z events in data, compared to MC simulations including all relevant backgrounds.

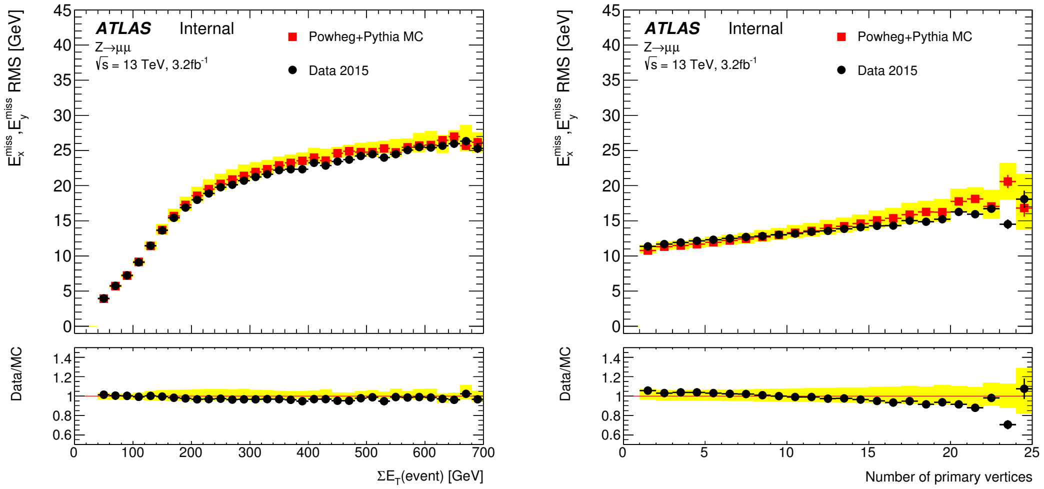

(a) (b)

Figure 4.7: The width of the $E_{x(y)}^{\text{miss}}$ distributions (a) in bins of ΣE_{T} and (b) in bins of the number of primary vertices in an inclusive sample of Z events. MC simulations are overlaid to data, and the ratios are shown below the respective plot.

Chapter 5

Search Methods

This section outlines the entire RPV 4L SUSY search. First, the trigger selection is discussed, which is the only part of the event selection that is performed partially during data-taking ("online") (5.1). Then, the preselection criteria are outlined, which selects events based on minimal selection criteria and event quality (5.2). Next, the weighting scheme (5.3) is described, in which MC samples are weighted to give the same distributions as data. The optimization of the search and the motivation for the final selection criteria are then outlined (5.4). The irreducible background estimation is then discussed, focusing on the estimation of the uncertainty on the irreducible background and on the validation of the estimate for dedicated validation regions (5.5). The reducible background estimation is discussed next, relying on data-driven techniques (5.6). Lastly, the final validation regions are analyzed, where these regions differ from the signal regions only by kinematic cuts (5.7).

The signal regions, control regions, and validation regions are all summarized in Table 5.1, where each region will be used in at least one of the following sections. The definition of m_{eff} is discussed in section 5.4, and N_{signal} and N_{loose} are the number of signal and loose leptons, respectively, where loose and signal lepton definitions are mutually exclusive (4.1.1).

Other selection criteria are used for specific purposes on MC samples only, but in all cases the selection criteria are described in the text. In particular, regions referred to as xLyl contain *exactly* x signal leptons and at least y loose leptons if $y > 0$, or *at least* x signal leptons and at least y loose leptons if $y = 0$. The reason for this

Name	Region Type	N_{signal}	N_{loose}	m_{eff}	Mass selection	section
SRA	Signal	≥ 4	≥ 0	≥ 600 GeV	Z-veto	6
SRB	Signal	≥ 4	≥ 0	≥ 900 GeV	Z-veto	6
VR	Validation	≥ 4	≥ 0	< 600 GeV	Z-veto	5.7.1
CR1-SRA	Control	$= 3$	≥ 1	≥ 600 GeV	Z-veto	5.6.7
CR2-SRA	Control	$= 2$	≥ 2	≥ 600 GeV	Z-veto	5.6.7
CR1-SRB	Control	$= 3$	≥ 1	≥ 900 GeV	Z-veto	5.6.7
CR2-SRB	Control	$= 2$	≥ 2	≥ 900 GeV	Z-veto	5.6.7
CR1-VR	Control	$= 3$	≥ 1	< 600 GeV	Z-veto	5.6.7
CR2-VR	Control	$= 2$	≥ 2	< 600 GeV	Z-veto	5.6.7
4L	Validation	≥ 4	≥ 0	< 600 GeV	-	5.3,5.7.2
2L2l	Validation	$= 2$	≥ 2	-	-	5.3,5.7.2
VR-ZZ	Validation	$= 4$	$= 0$	-	$= 2Z$	5.5.1
VR-$t\bar{t}Z$	Validation	$= 4$	$= 0$	> 600 GeV	$= 1Z, = 1e\mu$	5.5.2
VR-CO2L	Validation	$= 2$	$= 1$	-	2L1l in Z window	5.6.5
VR-CO3L	Validation	$= 3$	$= 0$	-	3L in Z-window	5.6.5
VR-HF1L	Validation	$= 1$	$= 1$	-	in text	5.6.4
VR-HF2L	Validation	$= 2$	$= 0$	-	in text	5.6.4

Table 5.1: Summary of all considered regions involving data-MC comparison. The first set of regions includes the signal regions and the control regions used in performing data-driven background estimations. The second set includes validation regions used to validate specific quantities or methods used in the analysis. Regions labeled "Signal" are the regions which would contain SUSY signal events and are used to set limits. Regions labeled "Control" are used to calculate specific quantities used in further calculations. Regions labeled "Validation" are used to check specific quantities or assumptions used in the search, where the results of the comparisons are not directly used elsewhere. The "section" column gives the sections containing data/MC comparisons of each region. The regions may be used for MC-only purposes outside of the listed sections.

definition is so that, if $x + y = 4$ (i.e. there are at least four leptons), no events will appear in more than one region xLyl.

5.1 Trigger Selection

Due to the high lepton multiplicity, triggering is highly efficient. The strategy is to allow for a large set of single, double, and triple lepton triggers, and events are accepted if they satisfy any of them, giving an efficiency greater than 98% for events that would otherwise satisfy the offline selection criteria of having four signal leptons. In general, triggers may be prescaled, in which case only some fraction (e.g. every tenth event) of events passing the trigger are actually saved. However, in this analysis, only unprescaled triggers are used, and in all cases, only the lowest unprescaled triggers are considered (i.e. triggers are not included if they are strictly a subset of another unprescaled trigger) [60].

In each case, there is a trigger matching requirement, meaning that the objects that actually activated the trigger online are required to be classified as signal objects offline. So, for example, if an event contained a loose lepton that activated a trigger and a signal lepton that did not, the event would not pass the trigger matching requirement, even though it passed the trigger requirement. To perform this matching, signal leptons are required to be within $\Delta R < 0.15$ from the relevant trigger object. In general, triggers do not behave as step functions at the trigger p_T threshold, and the exact trigger efficiency near the p_T threshold may be poorly modeled in simulation. As a result, the triggering leptons are required to pass offline p_T thresholds that ensure the lepton is sufficiently far away from the turn-on of the trigger efficiency. Using this strategy, the efficiency from each trigger can be taken to be $\sim 100\%$; otherwise, trigger modeling would be an issue. In every case, the offline p_T threshold is taken to be 1 GeV higher than the HLT (3.2.5) p_T requirement, to account for p_T differences that can arise from the offline lepton p_T calibration.

This p_T threshold is generally higher than the minimum p_T at which electrons and muons can be reconstructed (5 GeV for muons and 7 GeV for electrons), but the trilepton triggers potentially allow for acceptance of events composed only of low p_T leptons. In general, it is also important to ensure that the offline lepton identification and isolation criteria are at least as tight as the criteria used in each trigger, and this is accomplished by only including signal leptons (i.e. not baseline leptons) in the trigger matching requirement.

The full list of triggers in 2015 and 2016 data are found in Table 5.2 and Table 5.3, where the offline threshold column lists the minimum p_{T} threshold applied to leptons used in the trigger matching. In multilepton triggers, a list of p_{T} thresholds is given, each threshold corresponding to one of the required leptons. For example, for the HLT_2e12_lhloose_mu10 trigger, each of the electrons is required to have $p_{\mathrm{T}} > 13\,\mathrm{GeV}$, and the muon is required to have $p_{\mathrm{T}} > 11\,\mathrm{GeV}$, as indicated by the 13,13,11 entry in the table. In general, 2016 triggers may be tighter than the 2015 triggers, as the higher instantaneous luminosity in 2016 necessitates tighter triggers to keep the same acceptance rate. In most cases, the name of each trigger can be broken down into the L1 trigger and the HLT, where by definition the HLT is always tighter than the L1 trigger.

Trigger	Detail	offline threshold [GeV]
Single e	HLT_e24_lhmedium_L1EM20VH HLT_e60_lhmedium	25 61
Single μ	HLT_mu20_iloose_L1MU15 HLT_mu40	21 41
Double e	HLT_2e12_lhloose_L12EM10VH	13,13
Double μ	HLT_2mu10 HLT_mu18_mu8noL1	11,11 19,9
Triple e	HLT_e17_lhloose_2e9_lhloose	18,10,10
Triple μ	HLT_mu18_2mu4noL1 HLT_3mu6	19,5,5 7,7,7
Combined $e\mu$	HLT_e17_lhloose_mu14 HLT_e24_lhmedium_L1EM20VHI_mu8noL1 HLT_e7_lhmedium_mu24 HLT_2e12_lhloose_mu10 HLT_e12_lhloose_2mu10	18,15 25,9 8,25 13,13,11 13,11,11

Table 5.2: The 2015 triggers used and the offline threshold used ensuring that the lepton(s) triggering the event are in the plateau region of the trigger efficiency.

This same set of triggers is used in all the considered control regions, validation regions, and signal regions, with the sole exception of the heavy flavor validation region, VR-HF (5.6.4).

Trigger	Detail	offline threshold [GeV]
Single e	HLT_e24_lhmedium_nod0_ivarloose	25
	or HLT_e24_lhtight_nod0_ivarloose	25
	HLT_e60_lhmedium_nod0	61
Single μ	HLT_mu24_ivarloose	25
	or HLT_mu24_ivarmedium	25
	HLT_mu40	41
	or HLT_mu50	51
Double e	HLT_2e15_lhvloose_nod0_L12EM13VH	16,16
Double μ	HLT_2mu10[_nomucomb]	11,11
	or HLT_2mu14[_nomucomb]	15,15
	HLT_mu20_mu8noL1	21,9
Triple e	HLT_e17_lhloose_nod0_2e9_lhloose_nod0	18,10,10
Triple μ	HLT_mu20_2mu4noL1	21,5,5
	HLT_3mu4	5,5,5
	or HLT_3mu6	7,7,7
Combined $e\mu$	HLT_e7_lhmedium_mu24	8,25
	HLT_e17_lhloose_nod0_mu14	18,15
	HLT_e24_lhmedium_L1EM20VHI_mu8noL1	25,9
	HLT_e12_lhloose_nod0_2mu10	13,11,11
	HLT_2e12_lhloose_nod0_mu10	13,13,11

Table 5.3: The 2016 triggers used and the offline threshold used ensuring that the lepton(s) triggering the event are in the plateau region of the trigger efficiency.

5.2 Preselection

Prior to analysis-specific selection criteria, a set of preselection requirements are applied in order to reject events with detector problems or problems with reconstruction (i.e. online or offline problems). These criteria, standardized across physics analyses, serve to reduce background in the search and to reject events that would not be correctly modeled in simulation.

First, a GRL (Good Runs List) requirement is applied. Both the detector and collected data are monitored during data-taking and offline, and the GRL is a centrally provided list of runs and lumiblocks during which the detector is functioning adequately for the data to be usable, where lumiblocks each correspond to a particular time period. There are potentially different GRL versions for any given dataset corresponding to looser or tighter criteria. For example, the 2015 GRL has different versions corresponding to inclusion or rejection of a block of data in which the IBL was off, which is not included in this search. For MC, this selection is irrelevant and not applied.

Events are further removed if an error of some form is registered in one of the detector subsystems, in particular the LAr calorimeter. As opposed to the GRL stage, at this stage events are removed on an event-by-event basis as opposed to lumiblock-by-lumiblock basis. These criteria are also entirely standardized across physics analyses. Since this selection is based entirely on online information, it is not modeled or included as an effect in the simulation [71].

Events are required to have a primary vertex. If no vertex of high enough quality can be found by track reconstruction, no reliable lepton impact parameter selection can be applied, and these events are removed. Generally, this includes the requirement that there be at least two tracks associated to the vertex, though, due to the requirement that there be at least four associated leptons to the vertex, the two track requirement is somewhat redundant for this analysis. When selecting a primary vertex, physics analyses are entirely standardized, though it is possible for some studies not to apply this requirement. This selection applies to both data and simulation [54].

In some cases, an ambiguous jet can be observed, resulting from detector issues or beam backgrounds. A set of jet cleaning criteria are applied to remove such events, due to the ambiguity in classifying such events and the lack of modeling these events in the simulation. These criteria are not completely standardized, though there is a set of centrally provided recommended working points. The working point used in this search is called `LooseBad`, and this requirement is applied to both data and MC [71].

Muon reconstruction allows for a precise measurement of the impact parameters for each muon. Events are vetoed if they contain a muon with $z_0 > 1mm$ or $d_0 > 0.2mm$ in order to reject events with muons not actually originating from LHC pp collisions, particularly from cosmic sources. These cuts are not strictly looser than the impact parameter cuts applied to signal muons, and the cosmic veto will sometimes reject events with muons resuling from heavy flavor decays or secondary vertices from other sources. In particular, muons originating from b quark decays in $t\bar{t}$ are somewhat suppressed. However, the muons originating from the considered SUSY models do not display this behavior and are not suppressed by the cosmic veto. In effect, the cosmic veto behaves as a slight tightening of the impact parameter requirements and is applied to both signal and loose muons. It is particularly important that these criteria are applied to both data and MC.

Muon momentum is determined almost entirely from tracking information, and the resolution degrades at higher p_{T}. It is possible for a high p_{T} muon in particular to have a dramatically mismeasured momentum, and since this search relies on high momentum leptons, the ambiguity of including or not including muons in such cases necessitates vetoing such events. Events are vetoed if the relative track momentum error, determined during the tracking process, is lager than 0.2, and this requirement is applied to both data and MC.

The final preselection is trigger matching, requiring offline signal leptons to match trigger leptons, as described previously.

Table 5.4 gives a summary of the fraction of events in data remaining after each cleaning cut is applied successively. For technical reasons, events are required to have at least two leptons and to pass at least one trigger in a looser trigger selection than that used in the search before being included in this table.

Of particular note is the large number of events rejected by the cosmic veto, indicating that it is rejecting more than just events with actual cosmic muons. The

Cleaning Requirement	Efficiency
GRL Requirement	0.938
LAr Error Rejection	0.937
Trigger Requirement	0.834
Primary Vertex	0.834
Bad Jet Cleaning	0.831
Cosmic Muon Rejection	0.753
Bad Muon Rejection	0.753
Trigger Matching	0.260

Table 5.4: The selection efficiency of cleaning requirements, where the total sample constitutes the number of data events with at least two leptons with $p_{\mathrm{T}} > 9\,\mathrm{GeV}$ and passing trigger requirements.

large drop in efficiency after the trigger matching is a little misleading, since only signal leptons are used in trigger matching. The trigger matching then implicitly requires events to have at least one high p_{T} signal lepton or multiple lower p_{T} signal leptons, causing the drop in efficiency. None of the other preselection criteria have an impact on event selection efficiency that is larger than expected or problematic.

Table 5.5 gives a summary of the fraction of events in an example signal grid point, with $m_{\tilde{\chi}_1^\pm} = 900\,\mathrm{GeV}$ and $m_{\tilde{\chi}_1^0} = 50\,\mathrm{GeV}$ 2.3.2. This time, an extra row is added, which includes the selection efficiency of the two lepton and the loose trigger requirements. Some of these requirements are not applicable to MC, particularly the GRL and the LAr error requirement, but they are included for consistency with the previous table.

The preselection has approximately a 97% efficiency, with the largest drop occurring for the cosmic veto. However, the drop still only accounts for 1.8% of events, and the preselection appears to have a tolerable effect on signal efficiency.

Cleaning Requirement	Efficiency
Two Leptons and Loose Trigger	0.999
GRL Requirement	0.999
LAr Error Rejection	0.999
Trigger Requirement	0.997
Primary Vertex	0.997
Bad Jet Cleaning	0.990
Cosmic Muon Rejection	0.972
Bad Muon Rejection	0.971
Trigger Matching	0.968

Table 5.5: The selection efficiency of cleaning requirements, where the total sample constitutes the number of events for this particular grid point (5000).

5.3 Reweighting Events

In general, a number of weights have to be applied to MC sample events to produce final distributions that agree with data. To start with, MC events are normalized to the integrated luminosity measured in data, multiplied by the cross-section (including higher order effects and generator filter efficiency) for the relevant process, as well as any event-specific generator weights that were calculated in the production of a sample. As an example of the use of event weights, the distribution of p_{T}^{Z} in Z+jets events is sharply falling, but since the events with higher p_{T}^{Z} tend to be more interesting to physics studies, and since producing samples with enough events to contain a large enough number of high p_{T}^{Z} events is a computational burden, samples are often produced with a larger fraction of high p_{T}^{Z} events than data. In such a case, the event weight restores the same p_{T}^{Z} in MC and data. The process cross-sections and uncertainties are discussed further in section 5.5.4.

Object weights are also applied in general, accounting for reconstruction differences between data and MC. For example, electrons may be reconstructed more frequently in MC than data, in which case a scale factor would be applied to MC to reproduce the same number of events as data. The process object weights and uncertainties are discussed further in section 5.5.3.

Lastly, the data conditions assumed when producing the simulated samples do not necessarily correspond to the conditions of the data actually collected. In particular, MC samples are produced assuming a predefined pile-up profile, giving the expected number of pile-up events that would occur on top of any process of interest. To account for this effect, MC samples are all reweighted according to their pile-up profiles relative to the measured pile-up profile in data. For example, the distributions of data and MC in VR and CR2 (defined in Table 5.1) are shown in Fig 5.1, demonstrating the distribution of the number of the number of vertices in each event before and after pile-up reweighting. This reweighting tends to decrease the effective statistics for any MC sample. In a few cases, it is useful to remove the pile-up reweighting requirement. In all cases, it is stated whenever the requirement it removed.

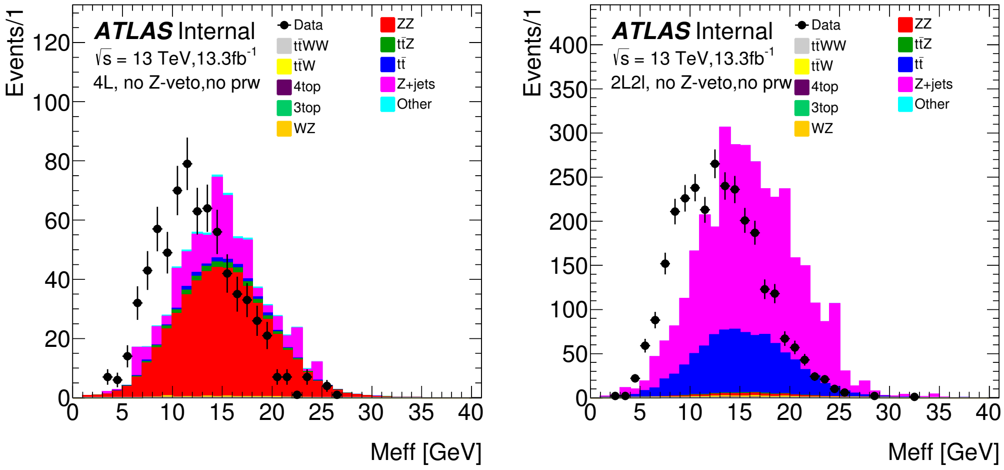

(a) 4L before reweighting (b) 2L2l before reweighting

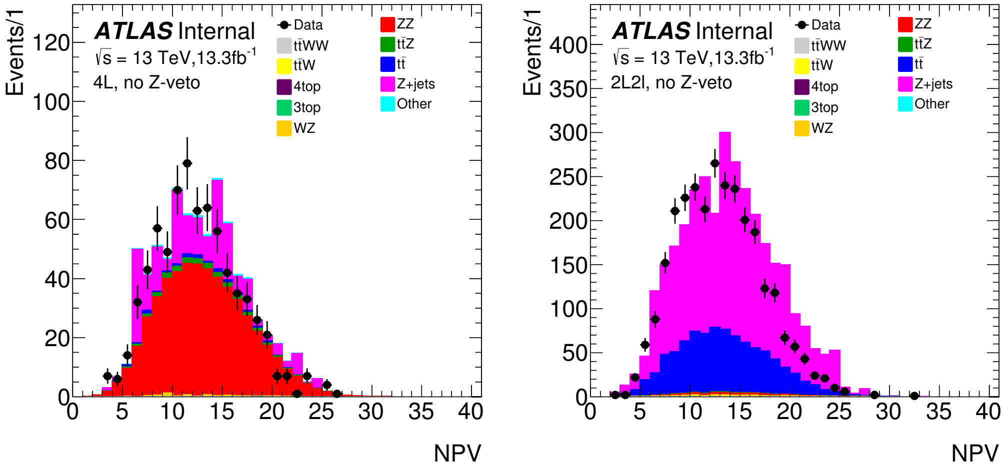

(c) 4L after reweighting (d) 2L2l after reweighting

Figure 5.1: N_{vertex} distribution for 4L events before and after pile-up reweighting (data vs mc), and CR2 events after pile-up reweighting.

5.4 Optimization

This section describes the optimization of the event selection criteria used in the search. So as not to inadvertently bias the search, data is not included at this stage, and the search optimization is based purely on simulation. All optimization studies are performed assuming an integrated luminosity of $10\,\mathrm{fb}^{-1}$, the projected total integrated luminosity used for this search. The discovery significance is computed using the `RooStats::BinomialExpZ` function [72–74], assuming a flat 50% systematic uncertainty on the SM background estimation. As will be shown in section 5.5.4 when discussing the actual background estimation, an uncertainty of 50% is larger than the final uncertainty, but it is sufficient for the purpose of optimizing the signal regions. In the tightest considered signal regions, the uncertainty becomes dominated by statistical effects, and it matters less what systematic uncertainties are assumed.

Before applying any further selection criteria, requiring four leptons already results in a small Standard Model background. The background is dominated by two processes - ZZ and Z+jets , with smaller contributions from $t\bar{t}Z$, $t\bar{t}$, Higgs processes, and other interactions of lesser importance. The $t\bar{t}$ and Z+jets backgrounds are composed of events that have fake leptons, the estimation of which is determined from data using a method described in the next section.

Further optimization is necessary due to the low cross-section in the signal models, but the signal region decisions, and in particular the choice of variables used in the optimization, are designed to be as general as possible.

5.4.1 Optimization of Z-veto

Most SM backgrounds with four leptons are composed of events with at least one on-shell Z. Since the considered signal samples do not have a Z, the Standard Model background can be largely eliminated by first applying a Z-veto . A leptonically decaying Z most commonly decays into a same-flavor opposite-sign (SFOS) pair, and a sizeable reduction in the number of background events can be accomplished simply by rejecting events that contain a same flavor, opposite sign (SFOS) lepton pair within a fixed window of the Z mass. However, four lepton decays ($Z \rightarrow 4\ell$) occur less frequently, with a branching fraction of $3.20 \pm 0.25\ (stat) \pm 0.13\ (syst) \times 10^{-6}$ [75]. Further, while direct three lepton decays cannot occur (e.g. because of electric charge conservation), decays of the form $Z \rightarrow \ell^+\ell^-\gamma$ do occur, where the photon is emitted as FSR (Final State Radiation). In such cases, the photon may convert to an electron through interaction with the detector, resulting in three lepton final states. Photon conversions occur frequently. For example, for high momentum, photons are observed to be converted approximately 50% of the time [76]. However, the rate at which such converted photons are reconstructed as electrons depends on the ability to identify the source of electron tracks. In particular, converted photon tracks tend not to include a hit in the innermost layer of the pixel detector. This reconstruction efficiency is less well-defined and harder to predict, and measurement of this efficiency relies on comparisons between data and simulation. As a result, three lepton decays have a less well-defined branching fraction, since they depend on the nature of reconstruction and the modeling of the detector.

The distribution of the invariant masses calculated from two, three, and four lepton combinations in Standard Model backgrounds all contain peaks around the Z mass, as shown in Fig. 5.2. In each case, the plotted value for each event is the lepton combination with a mass closest to the Z. For example, in the two lepton plot, there are up to four combinations of two (SFOS) leptons, and whichever combination is closest to the Z mass is the plotted value. In reality, this plotted quantity is the value of interest. If events are vetoed when they contain a lepton combination near the Z mass, only the combination closest to the Z mass actually matters. The two lepton case is by far the most sharply peaked, indicating a comparatively small number of

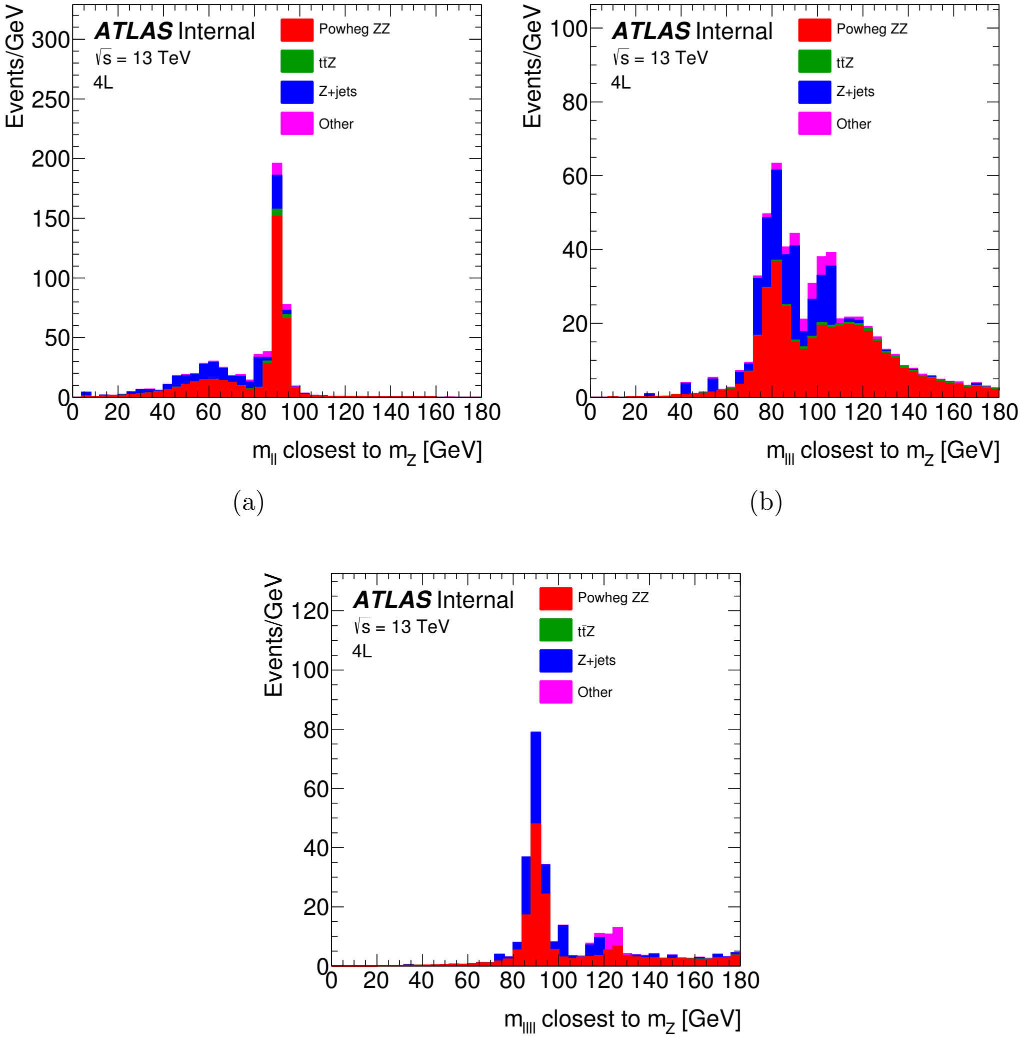

(a)

(b)

(c)

Figure 5.2: Background distributions of the invariant mass of SFOS(a), SFOS+l(b), and SFOS+SFOS(c) combinations.

events with a three or four lepton decay. In the three lepton case, there are potentially four different ways to choose the three leptons (depending on the lepton charges and flavors) from which to calculate the mass, and since the combination closest to the Z mass is plotted, the wide secondary peak to the right of the Z peak is a result of random matching between leptons from different sources. In the four lepton case, there is only one way of selecting the four leptons, and most events have a four lepton mass higher than the range on the x-axis.

Vetoing events in the peak regions significantly reduces the SM background, as shown in Fig. 5.3. In each case, events are required to contain at least four signal leptons, and events are rejected if some combination of leptons has mass within some threshold (given by the x-axis) of the Z mass. The second plot includes an extra kinematic cut, similar to what is used in the final event selection. The plots differ because the m_{eff} (5.4.2) cut largely eliminates the Z+jets background, and at high m_{eff} (generally corresponding to leptons having higher p_{T}), it is less likely for a four lepton combination to give a mass within the Z window. The distributions are cumulative, and the y-axis gives the fraction of remaining events if a veto is applied. Since the two lepton decays are by far the most frequent, each curve includes the two lepton veto and then applies multilepton decays on top of it. In each case, the fraction of events rejected does not necessarily reflect the sum of the number of events in each peak individually, as it is possible for an event to contain, for example, both a two lepton mass and a three lepton mass close to the Z mass. In particular, due to the low lepton masses included in this search, a pair of leptons may be close to the Z mass and still be close to the Z mass when an extra low p_{T} lepton is included in the calculation.

The reduction in the signal yield depends on the signal point in question, as some of the points are more likely to produce combinations of leptons that happen to lie near the Z mass, particularly from the $\tilde{\chi}_1^0$ decays 2.3.2, as shown in Fig. 5.4. The

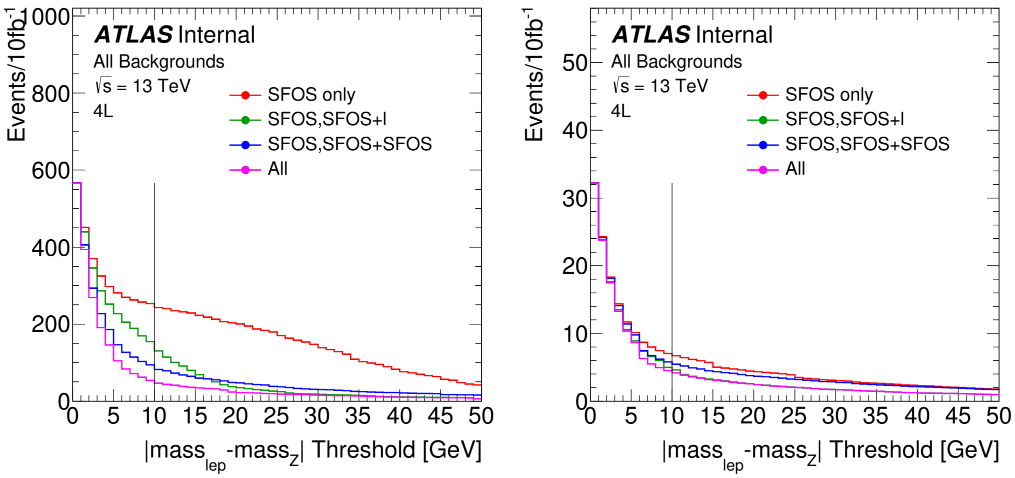

(a) $m_{\text{eff}} > 0$

(b) $m_{\text{eff}} > 500\,\text{GeV}$

Figure 5.3: Fraction of background remaining after rejecting events in a window around the Z mass, considering only dilepton and multilepton decays. (a) and (b) are the same, except that (b) contains an extra kinematic requirement (m_{eff}, described in the next section), which allows for a more realistic evaluation of the impact of the Z-veto.

mass distributions are largely insensitive to the $\tilde{\chi}_1^{\pm}$ masses, and the included plots show four different $\tilde{\chi}_1^0$ mass points at constant $\tilde{\chi}_1^{\pm}$ mass. For high $\tilde{\chi}_1^0$ masses, the Z veto has a relatively small effect, as it is unlikely in such cases to have a lepton combination near the Z mass in such cases. In the low $\tilde{\chi}_1^0$ mass region, the two lepton veto begins to reject a large fraction of events, as it is possible for the combination of the two charged leptons from the $\tilde{\chi}_1^0$ decay to have a mass in the window. However, the two lepton mass from the $\tilde{\chi}_1^0$ decays is a widely peaked distribution due to the extra neutrino from the decay, and a narrow Z-veto will not reject an unacceptable fraction of events. On the other hand, the three and four lepton decays do not appear to reject a large portion of the signal events and have a much smaller effect on the signal events than background events, relative to the number of events rejected by the two lepton veto. Even though the these three and four lepton decays form a relatively small portion of the background, then, the removal of these events improves the sensitivity to signal events.

The projected significance produced from rejecting events containing a lepton combination with an invariant mass within some window of the Z mass can be seen in Fig. 5.5. Precise optimization is complicated by low statistics in the simulated Z+jets and $t\bar{t}$ samples, which is the cause of the apparent steps in the figure. In practice, almost all the grid points appear to benefit from widening the Z veto window (except the 200 GeV $\tilde{\chi}_1^0$ mass points). However, in the interest of generalizing the search as far as possible and not overdoing the optimization for the particular benchmark SUSY models, the Z veto window is taken to be as small as possible, where the window width is at the approximate location where the the first derivative of the significance with respect to the window width is equal to one. The window width is taken as 10 GeV, and it is found that rejecting events with any of the three considered Z decays within 10 GeV of the Z mass effectively removes the SM background without degrading performance significantly in any of the considered signal grid points. Beyond this point, every plot assumes a Z-veto in the event preselection.

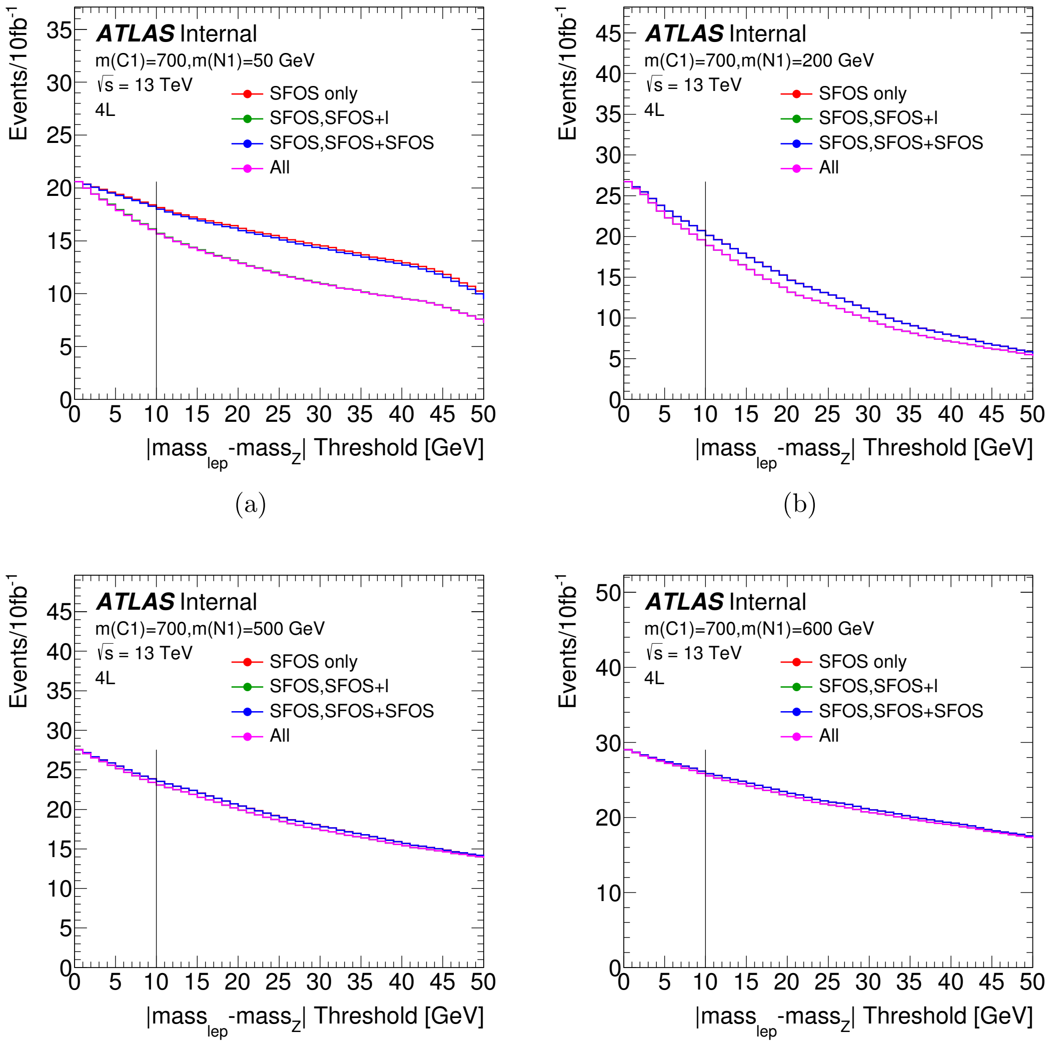

(a) (b)

(c) (d)

Figure 5.4: Signal grid distributions of the invariant mass for four signal grid points. All distributions show the same $\tilde{\chi}_1^{\pm}$ mass but different $\tilde{\chi}_1^0$ mass.

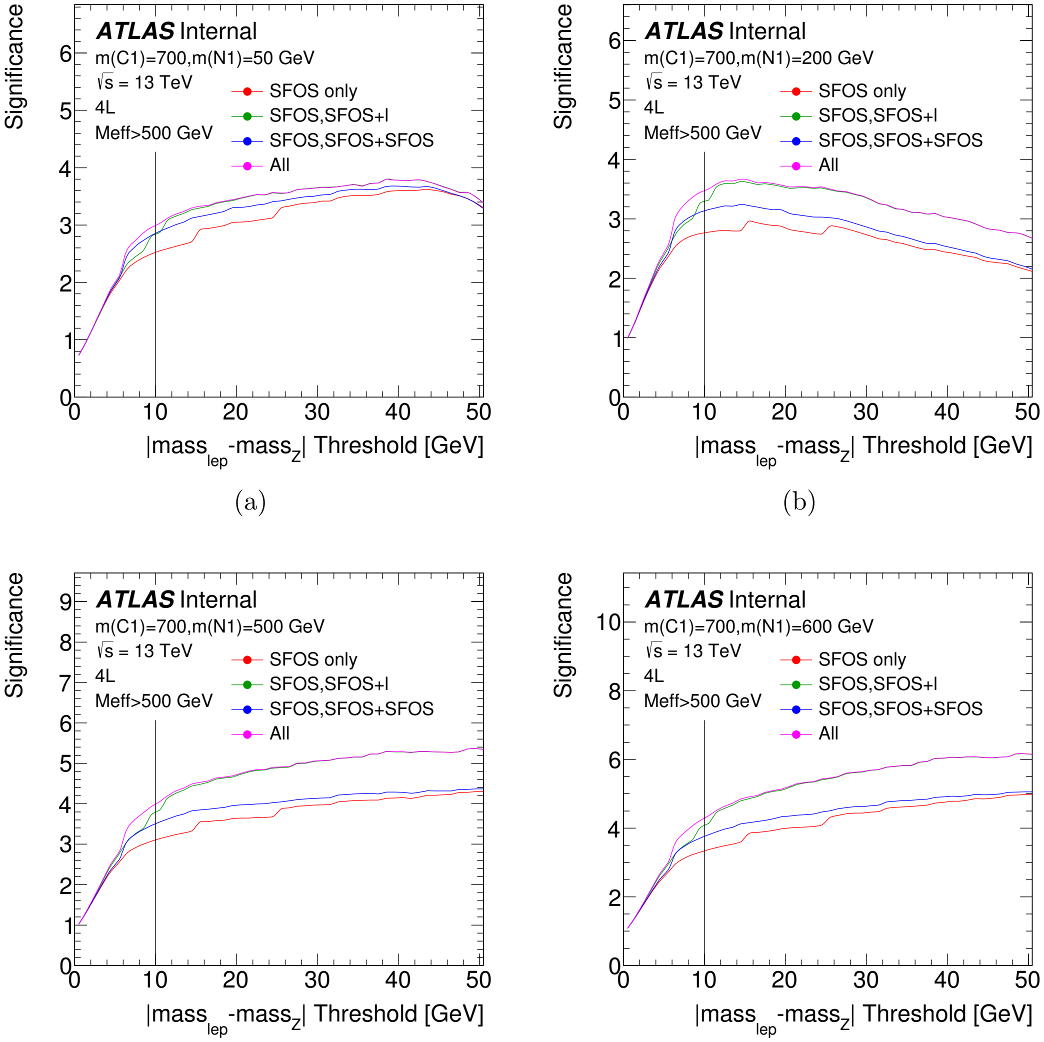

(a)

(b)

(c)

(d)

Figure 5.5: Significance as a function of Z-window size for four example signal grid points.

5.4.2 Energy Scale

Beyond the explicit assumption that events contain at least four leptons, none of which come from a Z, little is known a priori about the events for which we are searching. One assumption that is made, however, is that all the signals take place at a high energy scale. In particular, any processes at a low energy scale to which we would be senstive have already been excluded in earlier searches, and the goal of this search is to extend SUSY signal sensitivity beyond earlier limits. The chosen variable that gives an estimate of an event's energy scale is denoted the effective mass, m_{eff}, though, at this point, m_{eff} has not yet been quantitatively defined. The goal in the following discussion is to find a sensical and calculable formula for defining m_{eff}.

The energy scale of an event can be defined as the invariant mass of the system consisting of all the final state particles in the event. In essence, this value can be taken to represent the mass of a hypothetical particle that decayed through some decay chain into all the final state particles. If a hypothetical particle P decays into some arbitrary number of observable final state objects with momenta p_i (indexed by i), the mass of P can be calculated from p_i, according to

$$M^2 = (\sum_i E_i)^2 - (\sum_i p_{x,i})^2 - (\sum_i p_{y,i})^2 - (\sum_i p_{z,i})^2 \tag{5.1}$$

Since the mass M is a Lorentz scalar, we can evaluate the equation in the frame in which $\sum_i p_{z,i}$ is zero. Since the individual transverse momentum of each inital parton is approximately zero, $\sum_i p_{x,i}$ and $\sum_i p_{y,i}$ will be zero (4.3), as long as all final state particles are included in the calculation. In the relativistic limit, E_i is very nearly $|\vec{p}_i|$. This leaves us with

$$M^2 = (\sum_i |\vec{p}_i|)^2 \tag{5.2}$$

Finally, we find that

$$M = \sum_i |\vec{p}_i| = \sum_i \frac{p_T}{|\mathtt{sin}(\theta)|} \tag{5.3}$$

where θ corresponds to the angle in the reference frame that is boosted with respect to the detector, which will generally be different from the ATLAS frame. This equation is not useful in reality, as we know neither the initial longitudinal momentum of the system nor how much longitudinal momentum may have been lost in the direction of the beampipe in the final state. Given that $|\mathtt{sin}(\theta)| \leq 1$, at the very least we have

$$M = \sum_i \frac{p_T}{|\mathtt{sin}(\theta)|} \geq \sum_i p_T \equiv m_{\text{eff}} \tag{5.4}$$

Thus, the mass of the original particle is greater than or equal to m_{eff}.

In general, M does not correspond to a mass resonance. However, in the case where at least two particles with masses M_i are produced in some interaction, M is the invariant mass of the system, and we have

$$M > \sum_i M_i \tag{5.5}$$

by conservation of energy and momentum.

It is not guaranteed that m_{eff} will be large if M is large, but it is guaranteed that M is large if the measured m_{eff} is large. A very small portion of SM events have a large M value, and the number of SM events with a large m_{eff} is strictly smaller (barring systematic effects). On the other hand, for signal samples, $\sum_i M_i$ is always large by design, and for the benchmark signal grid specifically, it is always at least 1 TeV (two $\tilde{\chi}_1^{\pm}$ with masses of 500 GeV each). M is then always larger than 1 TeV, so that, for the signal samples, large m_{eff} values are always kinematically allowed. In practice, m_{eff} does tend to be large if M is large, and as will be shown, m_{eff} is a powerful variable in separating signal from background.

In summary, the p_{T} sum of objects in an event is an effective measure of the energy scale at which an event takes place. In order to actually calculate m_{eff}, we need to choose which objects in an event should actually be included in the calculation. In principle, we could consider every reconstructed object, including, for example, low energy tracks. However, including lower momentum objects increases the sensitivity of the variable to pile-up, the underlying event, and mismeasured objects. By extension, it increases the observed differences between data and MC, as described in section 4. Another complication is that events may contain neutrinos (or hypothetical weakly interacting stable particles), for which nothing beyond $E_{\mathrm{T}}^{\mathrm{miss}}$, the total transverse momentum of all invisible objects, is known. $E_{\mathrm{T}}^{\mathrm{miss}}$ tends to be large on average if an event contains multiple invisible objects, so that $E_{\mathrm{T}}^{\mathrm{miss}}$ is useful to include directly in the m_{eff} definition. The following definition is used, including only signal objects in the m_{eff} definition:

$$m_{\mathrm{eff}} = \sum_i p_{T,i}^{\text{signal electron}} + \sum_i p_{T,i}^{\text{signal muon}} + \sum_i p_{T,i}^{\text{signal jet}} + E_{\mathrm{T}}^{\mathrm{miss}} \tag{5.6}$$

The agreement of m_{eff} between data and MC in the primary irreducible background is discussed in section 5.5. Any m_{eff} disagreement in the reducible backgrounds is irrelevant, as the reducible background yields are calculated from data (5.6). In all regions xLyl with $y > 0$, the m_{eff} definition is modified to include loose leptons as well. This loosening is important in order to produce consistent m_{eff} distributions between the control regions, signal regions, and validation regions. In these regions, m_{eff} is instead defined by:

$$m_{\mathrm{eff}} = \sum_i p_{T,i}^{\text{baseline electron}} + \sum_i p_{T,i}^{\text{baseline muon}} + \sum_i p_{T,i}^{\text{signal jet}} + E_{\mathrm{T}}^{\mathrm{miss}} \tag{5.7}$$

where baseline and signal objects are defined in section 4.

Alternatively, more restricted definitions can be considered, for example including only the lepton momentum sum, given the high lepton multiplicity in all the considered final states. All of the considered variables tend to have steeply falling distributions for the SM backgrounds (Fig. 5.6), and a high enough threshold on any of the variables could potentially remove the SM backgrounds. Since the lepton p_{T} sum may be large in all signal samples, while the jet sum may be large in a significant portion of the SM background events (in particular $t\bar{t}Z$, with generally two b-jets), including only lepton p_{T} is conceptually the most reasonable alternate method.

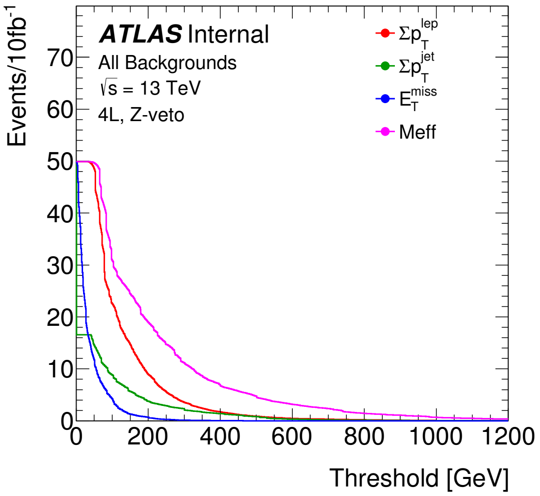

Figure 5.6: Cumulative scale variable distribution in SM backgrounds

In the benchmark signal grid, m_{eff} increases for higher $\tilde{\chi}_1^{\pm}$ masses, and the relative importance of the jet part of m_{eff} relative to the lepton part increases with the mass splitting between the $\tilde{\chi}_1^{\pm}$ and the $\tilde{\chi}_1^0$, corresponding to a higher mass W being produced in the decay. m_{eff} is not the optimal variable in every signal point, as in cases where the SUSY signal is not expected to produce high momentum jets. Including jets in the calculation allows for a higher background yield relative to signal. However, of the different scale variables considered in the cumulative distributions in Fig. 5.7, m_{eff} is the most stable across the entire signal grid, and it is the scale variable choosen in the signal region definitions. Unlike most SUSY searches, specifically searches for SUSY with R-parity, compressed regions are not a problem in this search, as a small mass splitting between the $\tilde{\chi}_1^{\pm}$ and $\tilde{\chi}_1^0$ will result in a final state with high lepton momenta and high $E_{\mathrm{T}}^{\mathrm{miss}}$. In this sense, there is no case where m_{eff} is no longer effective, and the only region of the grid in which the search is less sensitive is the very low mass $\tilde{\chi}_1^0$ case, where it may be difficult to reconstruct all four leptons, and where the low mass veto rejects a large fraction of events.

The shapes of these distributions are also interesting due to their potential ability to distinguish signal models. If a signal were to be discovered, the shape of the m_{eff} distribution could give some insight into the masses of the observed $\tilde{\chi}_1^\pm$. In particular, across the signal grid points, the $\tilde{\chi}_1^\pm$ mass corresponds to the location where the m_{eff} distribution begins to fall. This is less of a clear interpretation for the other considered variables when taken separately, and this is another motivation for only considering m_{eff}.

The significance distributions are shown in Fig. 5.8, and behavior is observed as is expected from the distributions. The significance peak shifts to the right for higher $\tilde{\chi}_1^\pm$ mass, but it is desirable to have simple signal regions defined by a fixed m_{eff} threshold. A relatively low threshold is chosen (relative to the considered $\tilde{\chi}_1^\pm$ masses) for the optimized signal region, $m_{\text{eff}} > 900\,\text{GeV}$. This threshold is to the left of the peaks in the significance distributions for all grid points with $\tilde{\chi}_1^\pm$ mass greater than 500 GeV, based purely on the outlined optimization procedure. This is especially true, since the 500 GeV points are already excluded from earlier searches. It therefore seems to make sense to use a higher m_{eff} threshold.

In reality, at this point further optimization degrades performance for statistical reasons (described in more detail in Appendix B). Since the number of data events in control regions are used to calculate the number of reducible background events in the signal region (Section 5.6), the statistical uncertainty of the data yield in the control region translates into an uncertainty on the signal regions' reducible background. If the selection criteria are too tight, the number of expected data events in the control region becomes small, and then this increase in the uncertainty of the reducible background in the signal region degrades the sensitivity of the search.

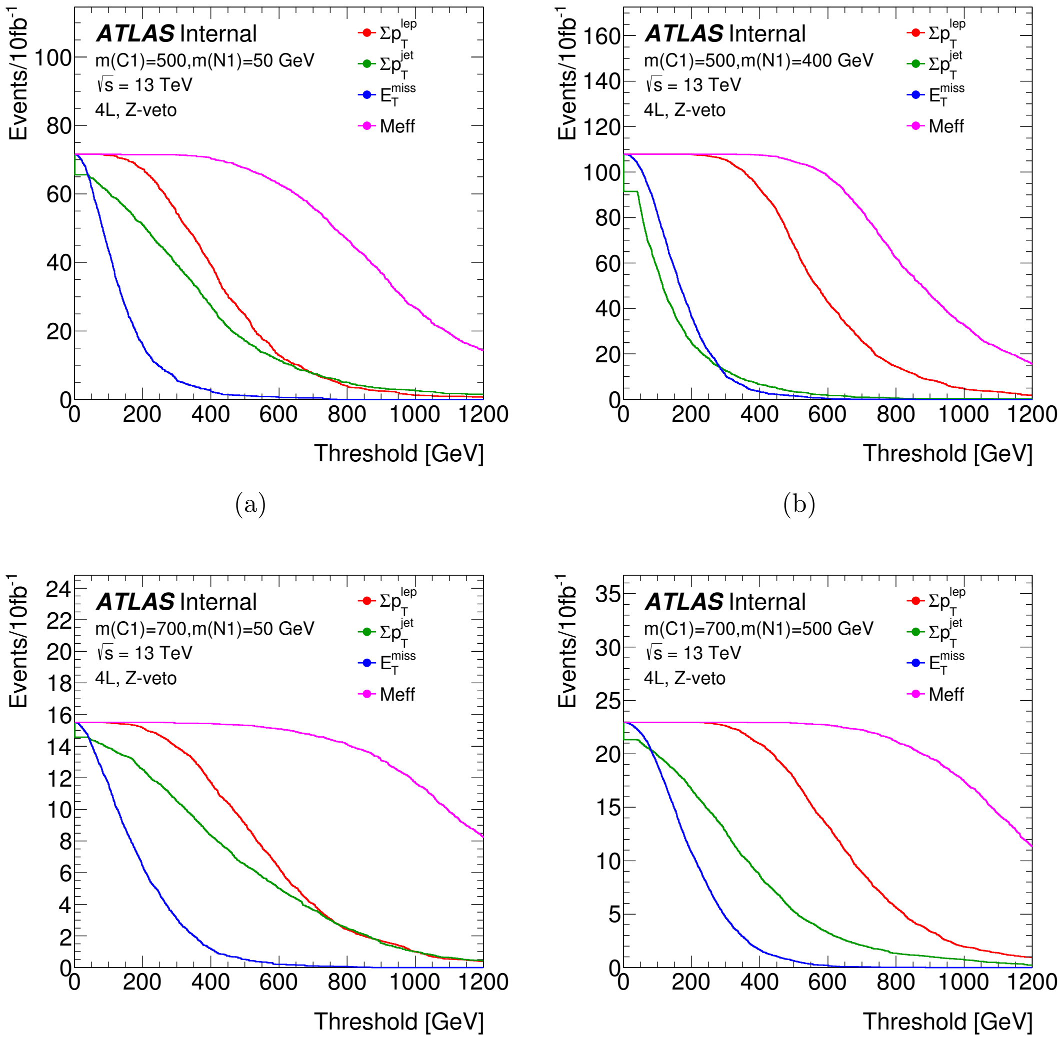

(a) (b)

(c) (d)

Figure 5.7: Cumulative distributions of m_{eff} and its constituents are shown in four example signal grid points.

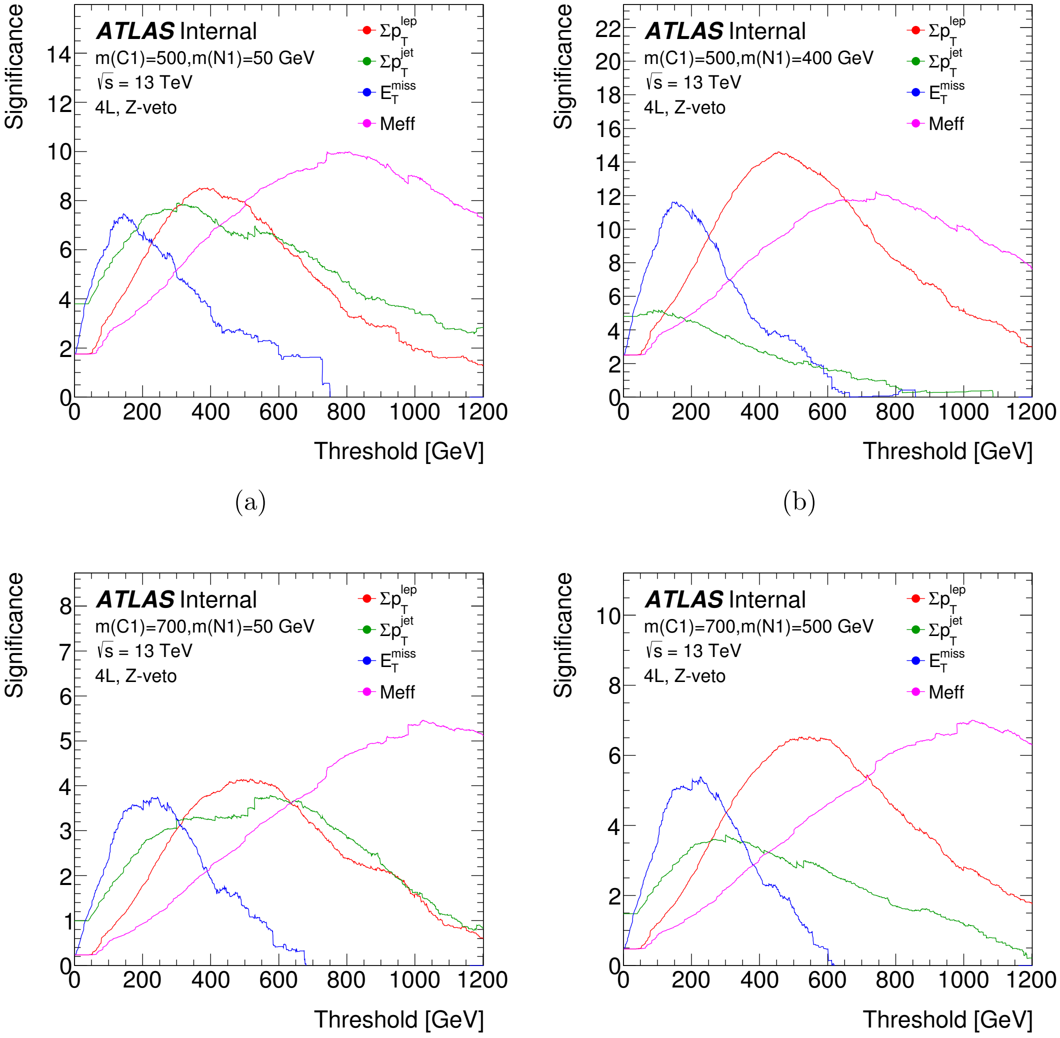

(a) (b)

(c) (d)

Figure 5.8: Projected significance as a function of threshold of m_{eff} and its constituents are shown in four example signal grid points.

The expected number of events in the primary control region is shown in Fig. 5.9. Taking into account the requirement that the control region contains at least ten events, 900 GeV is the largest possible threshold. In fact, this requirement was the primary motivator for many of the selection criteria described in Section 4, since the looseness of the baseline lepton requirements, in terms of lepton identification, lepton p_{T} threshold, and overlap removal decisions, was chosen to ensure that enough events populated the control regions. In these plots, the red distribution (`Default selection`) corresponds to the lepton selection criteria used in this search, and the other curves correspond to the tightening of at least one of the following criteria:

- `no NearLepCorr.`: Lepton isolation is not corrected for nearby leptons
- p_{T}^{lep}: Muons and electrons are required to have $p_{\mathrm{T}} > 10\,\mathrm{GeV}$
- `LooseEl`: Baseline electrons are required to pass the LooseLH identification (this search uses VeryLooseLH)
- `bjet OR`: In the overlap removal, b-tagged jets are given priority over leptons

The orange curve ($p_{\mathrm{T}}^{lep} > 10\,\mathrm{GeV}$,`b-jet OR`, `LooseEl`) corresponds to the standard lepton selection used in SUSY searches, which results in an unacceptable number of events for the purposes of this search.

A second signal region is also defined, using the strictly looser requirement $m_{\mathrm{eff}} > 600\,\mathrm{GeV}$, and a validation region is defined to have $m_{\mathrm{eff}} < 600\,\mathrm{GeV}$. The looser signal region serves to potentially identify SUSY signals with different properties than the benchmark model. If a signal were actually seen in SRB, it might be the case that $600 < m_{\mathrm{eff}} < 900\,\mathrm{GeV}$ would be contaminated by signal events, and for this reason it is desirable that the cutoff between the validation region and optimized signal region not occur at the same m_{eff} threshold. In a sense, the region included in SRA but not SRB acts as a buffer between the validation region and optimized signal region, SRB. To summarize, the tight signal region (SRB) is optimized for the benchmark

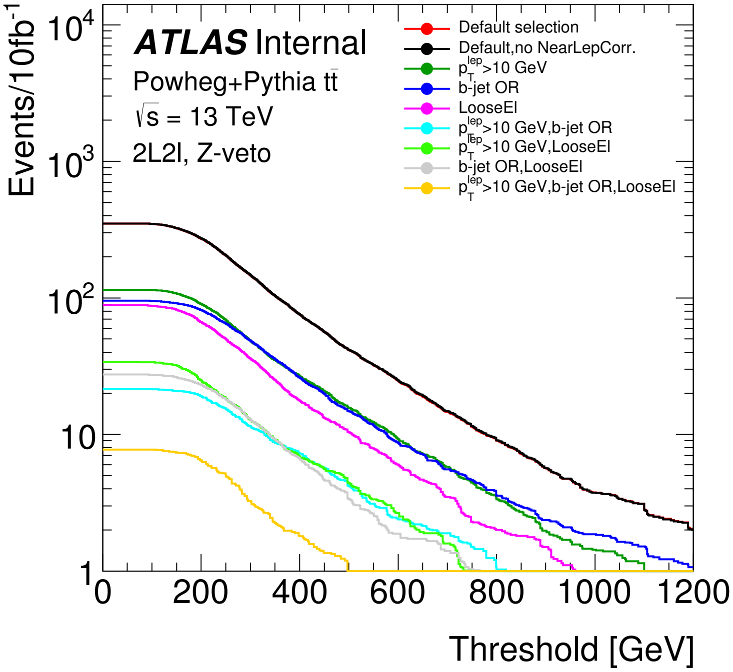

(a)

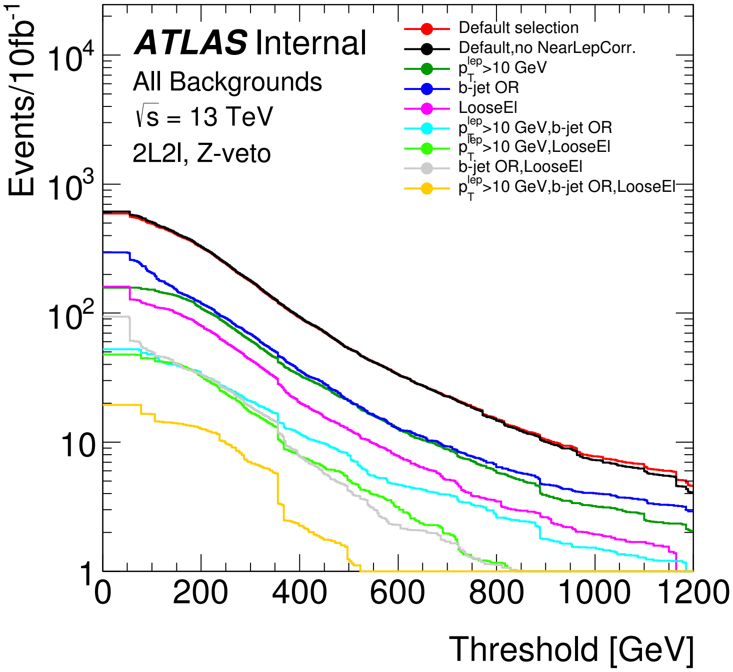

(b)

Figure 5.9: Number of events in CR2 from $t\bar{t}$ and inclusive backgrounds using more conventional overlap removal and lepton selection criteria.

supersymmetry model used in this analysis, and the loose signal region (SRA) serves as a catch-all for other types of supersymmetry models.

5.5 Irreducible Backgrounds

The irreducible background in the signal regions is dominated by $t\bar{t}Z$ and ZZ. Section 5.7 is dedicated to the MC modeling in the primary validation region, but the general agreement between data and MC and between the different generators for each MC sample is presented in this section. Of particular importance is the comparison of the m_{eff} distributions between data and MC for each of the primary irreducible backgrounds, as it is necessary to show that m_{eff} is well behaved (compared to the misbehaving ΣE_{T}, for example, as shown in Section 4).

5.5.1 ZZ Validation with ZZ Selection

In order to validate the use of a simulation-only estimate of the ZZ background in the signal regions, we first check the agreement between data and simulation in a dedicated validation region, corresponding to events with two on-shell Z bosons, each decaying leptonically. The results of this comparison are not directly used in the background estimate in the signal regions, and the agreement in this validation region does not imply that there is necessarily agreement in the signal regions. However, if there were disagreement in this validation region, we would then expect disagreement between data and simulation in the signal regions, and this comparison serves as a baseline check of the agreement between data and simulation.

POWHEG [77] MC and data are compared by requiring a ZZ event selection:

- Events contain exactly four signal leptons and no extra baseline leptons
- Events contain two SFOS (Same-Flavor, Opposite-Sign)) pairs, each of which has a mass between 66 GeV and 116 GeV

Beyond these requirements, the same preselection criteria are applied as are given in section 5.2. The kinematic distributions are shown for MC and data in Fig. 5.10.

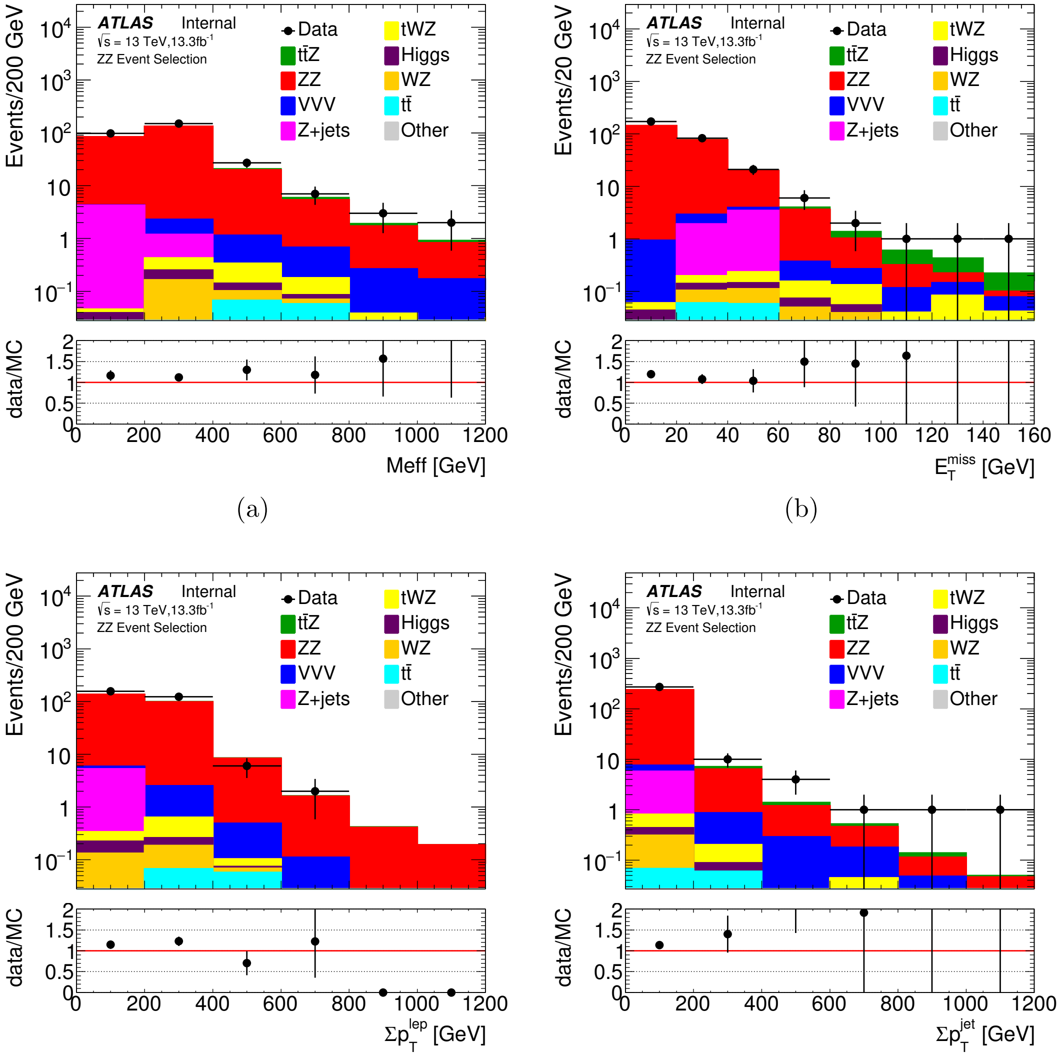

(a) (b)

(c) (d)

Figure 5.10: Distribution of m_{eff} and its constituents in MC and data in the ZZ validation regions. Displayed uncertainties are statistical only.

For the m_{eff} distribution, agreement is observed in all the bins, taking into account only the statistical uncertainty. Overall, the MC underestimates the data, with 252 ± 4 events in MC and 288 ± 17 events in data. However, detector and theoretical uncertainties are not applied, and an overall normalization difference is not problematic in this case. As will be shown in secion 5.5.4, this difference of normalization is in fact smaller than the applied theoretical uncertainty. More important would be if the disagreement between data and MC increased with m_{eff}, since the theoretical uncertainties in particular are applied to the overall normalization and would not be expected to account for a m_{eff} dependent disagreement. A m_{eff} dependent disagreement is not observed (within the statistical uncertainty), so a m_{eff} dependent disagreement is not an issue, within the statistical uncertainty. Larger disagreement is observed for the individual terms, though this behavior is itself not problematic. For example, the jet p_{T} sum appears to be underestimated in MC, consistent with POWHEG's general underestimation of jet multiplicity. $E_{\text{T}}^{\text{miss}}$ appears to be well-modeled and does not show more significant disagreement than does m_{eff}, and $E_{\text{T}}^{\text{miss}}$ itself still appears to be a well behaved variable in this context. Of course, the process in question does not contain true $E_{\text{T}}^{\text{miss}}$ (i.e. high p_{T} neutrinos are not produced), so the agreement between the $E_{\text{T}}^{\text{miss}}$ distributions reflects the agreement in the scale of the mismeasurement of $E_{\text{T}}^{\text{miss}}$, and not a difference in the neutrino modeling of the process. In a sense, the agreement of the $E_{\text{T}}^{\text{miss}}$ distributions validates the modeling of the hadronic activity in the event (i.e. the component of the event that is generally mismeasured and difficult to quantify) and detector-specific properties, as opposed to a validation of the neutrino production spectrum.

As a cross-check, the observed yield can be compared to the observed ZZ yield in data in the 2015 ZZ cross-section measurement [78]. The observed yield in the paper is 63 events for 3.2fb^{-1}, corresponding to approximately 262 events in 13.3fb^{-1}. This is not a completely consistent comparison, as the lepton selection criteria are different between the two measurements (and neither selection is strictly tighter than the other), but at the very least the results seen in the measurement in this search and the measurement in the 2015 paper do not yield dramatically different or contradictory results.

5.5.2 $t\bar{t}Z$ Validation with $t\bar{t}Z$ Selection

In order to validate the use of an simulation only estimate of the $t\bar{t}Z$ background in the signal regions, we first check the agreement between data and simulation in a dedicated validation region, corresponding to events with one on-shell Z, decaying leptonically, and two other leptons with different charge and different flavor. As in the ZZ validation, the results of this comparison are not directly used in the background estimate in the signal regions, and the agreement in this validation region does not imply that there is necessarily agreement in the signal regions. However, if there were disagreement in this validation region, we would then expect disagreement between data and simulation in the signal regions, and this comparison serves as a baseline check of the agreement between data and simulation.

MadGraph [79] MC and data are compared by requiring a $t\bar{t}Z$ event selection:

- Events contain exactly four signal leptons and no extra baseline leptons
- Events contain an SFOS pair with a mass between 81 GeV and 101 GeV
- Beyond the lepton pair corresponding to the Z, events contain exactly one electron and one muon
- $m_{\text{eff}} > 600\,\text{GeV}$

The first requirement serves to remove triboson backgrounds and potentially other rare processes resulting in more than four leptons. The second requirement removes rare processes, such as $t\bar{t}VV$ and events with fake leptons. The third requirement is the most important, since it rejects the dominant ZZ background. These criteria alone do not result in high $t\bar{t}Z$ purity for low m_{eff}, due to large contributions from Z+jets in particular. It is possible to achieve a much higher $t\bar{t}Z$ purity, particularly for low m_{eff}, by requiring a b-tagged jet. However, doing so complicates the comparison by introducing a dependence on flavor tagging modeling. Instead, only the high m_{eff} regime is considered, as $t\bar{t}Z$ only becomes a dominant background for high m_{eff}

anyway (i.e. $t\bar{t}Z$ is important in SRA and SRB but not VR). For high m_{eff}, the distributions comparing data and MC are shown in Fig. 5.11.

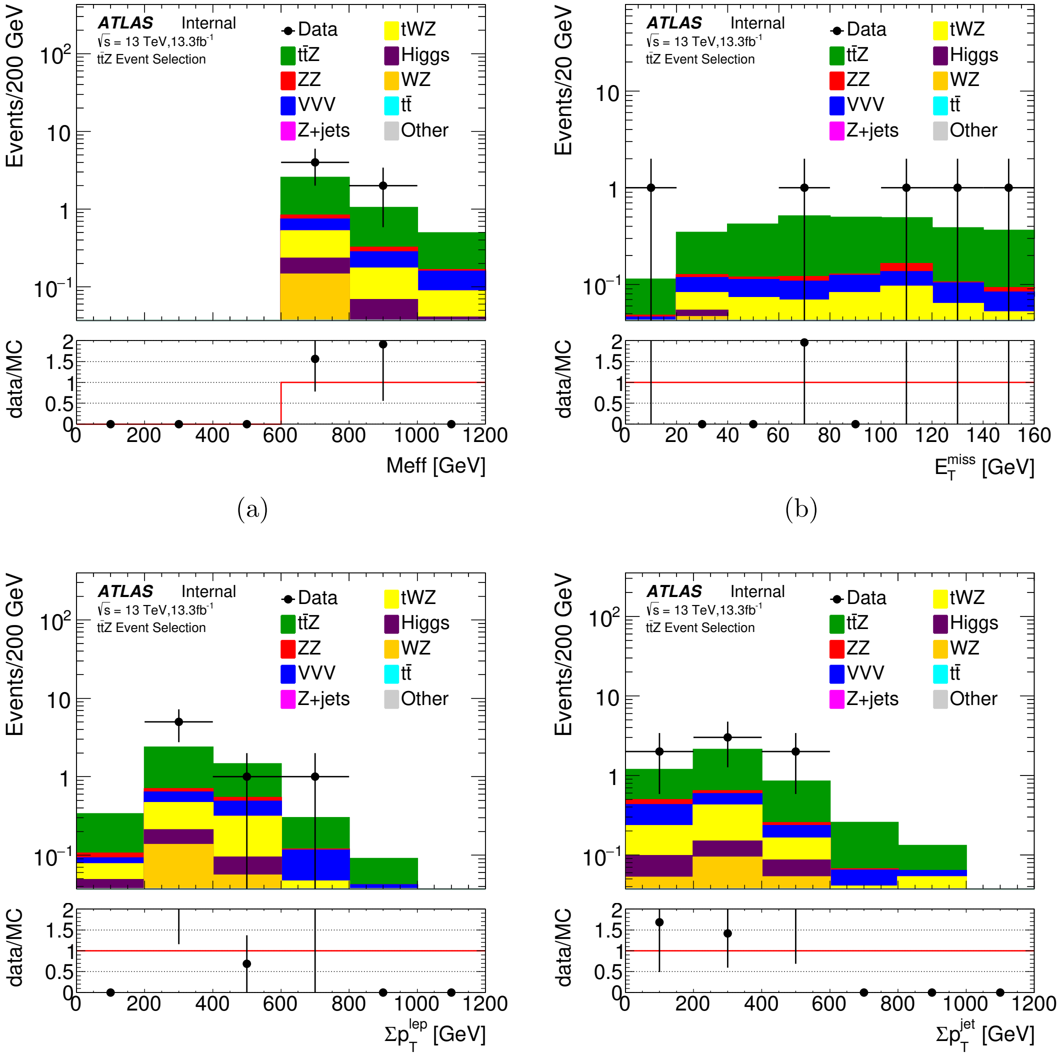

(a) (b)

(c) (d)

Figure 5.11: Distribution of m_{eff} and its constituents in MC and data in the $t\bar{t}Z$ validation regions.

The issue of low statistics complicates the effort to compare data and MC yields. Statistical agreement is observed between data and MC in the m_{eff} distributions. The m_{eff} region where this comparison is performed is consistent with the loose signal region, SRA. Not enough statistics are available for any comparison in SRB, and the theoretical and detector uncertainties are taken to be valid in the high m_{eff} region. The comparison of the distributions does not raise any figurative red flags.

5.5.3 Detector Uncertainties

Experimental uncertainties, most importantly uncertainties on the lepton efficiency scale factors, are estimated using the prescriptions supplied by the relevant combined performance groups. In general, each source of uncertainty is derived by finding an event selection that allows for a direct comparison of data and MC in a situation that is strongly dependent on the modeling of a very specific parameter.

A summary of the total experimental uncertainty on $t\bar{t}Z$ and ZZ is shown in Figure 5.12, where the total effect is on the order of 5%. In cases where it applies, there is both a scale-up and a scale-down variety of each systematic variation, corresponding to scaling the relevant quantity by $\pm 1\sigma$. There is no down variation for resolution systematics (only applied to jets and $E_{\text{T}}^{\text{miss}}$), as the simulation can be broadened with gaussian smearing, while the reverse is difficult.

The uncertainty is dominated by the uncertainty on the electron efficiency scale factor. This dominance is to be expected, as each lepton in an event provides a source of uncertainty, and there are always at least four of them. The kinematic uncertainties (uncertainties on lepton or jet calibrated p_{T}) are less important, due to the nature of this search. The kinematic uncertainties only matter if an event is very near the edge of one of the regions, either by having m_{eff} near 600 GeV or 900 GeV or by containing a lepton close to the minimum lepton p_{T}. These are relatively rare occurrences. The kinematic uncertainties are more relevant in searches based on locating multiparticle resonances, in which case the uncertainties can widen peaks. At high m_{eff}, statistical effects result in a poorly behaved kinematic systematic distributions, since shifting individual events to the left or right of the m_{eff} threshold can cause large shifts in the distributions.

Details for the electron, muon, jet and $E_{\mathrm{T}}^{\mathrm{miss}}$ systematics can be seen in Figure 5.13 for $t\bar{t}Z$ and ZZ. Only the cumulative distributions are shown, and the particular values at 600 GeV and 900 GeV correspond each systematic uncertainty in SRA and SRB, respectively. The jet kinematic uncertainties can have a larger effect at high m_{eff}, because they are effectively double counted in the m_{eff} calculation. If a jet has high momentum and its momentum is systematically modified, the new p_{T} will be used in both $\sum_i p_{\mathrm{T}}^{\mathrm{jet}}$ as well as $E_{\mathrm{T}}^{\mathrm{miss}}$.

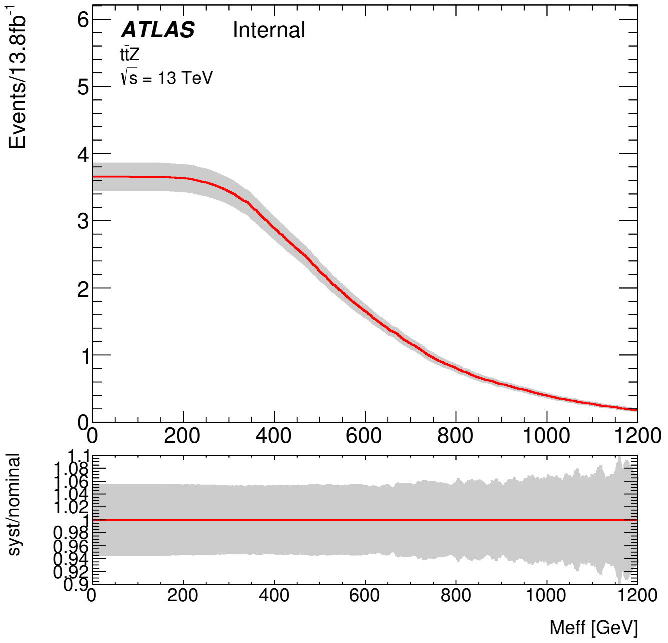

(a) $t\bar{t}Z$

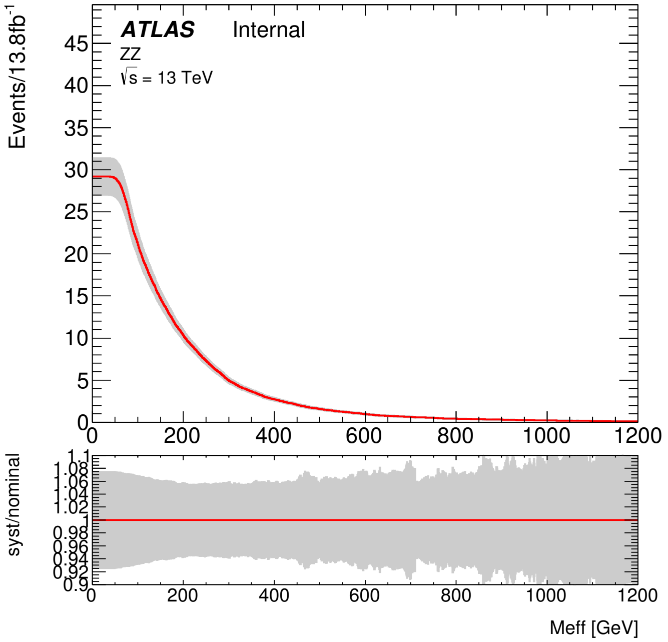

(b) ZZ

Figure 5.12: Summary of the systematic uncertainties from detector-level sources for $t\bar{t}Z$ (a) and ZZ (b). Yields are cumulative to show the effect of an m_{eff} requirement.

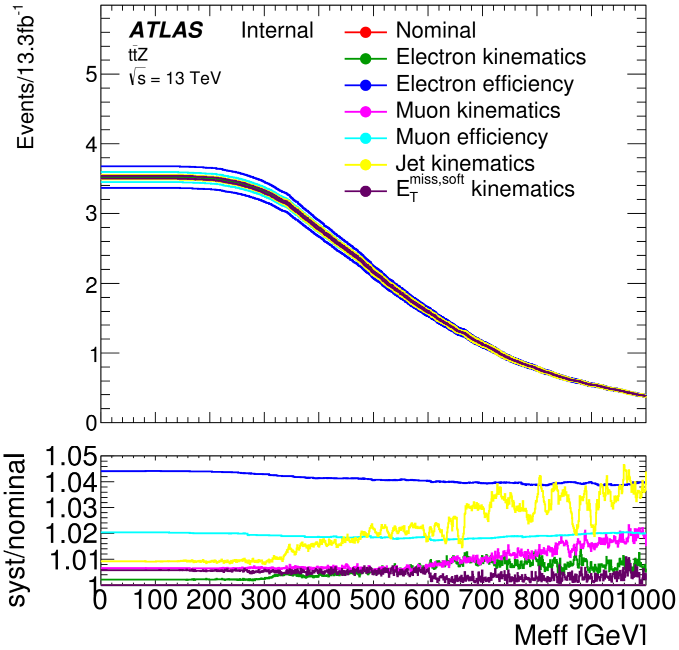

(a) $t\bar{t}Z$

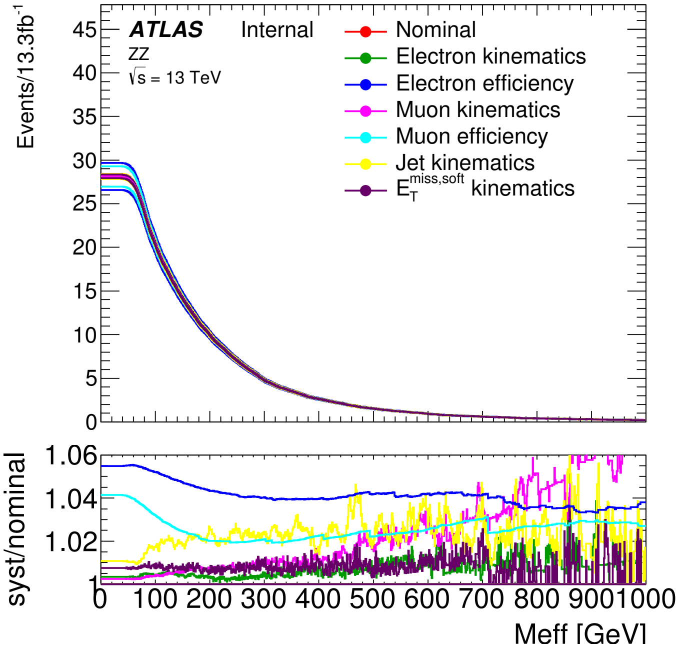

(b) ZZ

Figure 5.13: Breakdown of the systematic uncertainties from detector-level sources for $t\bar{t}Z$ (a) and ZZ (b). Yields are cumulative to show the effect of an m_{eff} requirement.

5.5.4 Theoretical Uncertainties

Theoretical uncertainties are uncertainties that do not depend on the ATLAS detector, and these uncertainties generally result from varying parameters in the sample generation. From a technical point of view, these uncertainties are generally divided into four different types.

The first type is the uncertainty on the cross-section for a particular process. These uncertainties are centrally provided by the Physics Modelling Group [80, 81] and originate from the uncertainty on the theoretical cross-section calculation. Technically, these uncertainties are applied as a constant variation for each sample and are given in Table 5.6 in the rows labeled σ. The rows labeled $A\epsilon$ show the combination of the other three types of systematics, in samples where all three are calculated. For samples with low importance and high cross-section uncertainty, a large, constant uncertainty is applied, and these uncertainties are designated by $\sigma A\epsilon$.

Experimental (% of total SM)		Theoretical (% of each process)	
e efficiency	3.9%	σ: $t\bar{t}Z$	12%
μ efficiency	1.9–2.8%	σ: $t\bar{t}W$	13%
Jet energy scale	3.0–3.4%	σ: ZZ,WZ	6%
Luminosity	2.9%	σ: VVV/tWZ	20%
MC statistics	2.7–2.5%	$A\epsilon$: ZZ	56–80%
CR statistics	4.5–6.4%	$A\epsilon$: $t\bar{t}Z$	9–12%
		$\sigma A\epsilon$: VH/VBF H	20%
		$\sigma A\epsilon$: ggF H/ $t\bar{t}H$	100%

Table 5.6: Summary of systematic uncertainties applied to irreducible backgrounds. For reference, both theoretical and experimental uncertainties are included [82].

The second type of uncertainty includes scale factor uncertainties, which are applied as an event weight in an event-by-event manner. These uncertainties result from uncertainties in the parton density function and from varying the factorization and renormalization scales.

The third type involves uncertainties in the parton showering (hadronization) and the underlying event. These uncertainties are not applied as event weights. Instead, an entirely separate set of samples is produced for each variation, and the distributions from the nominal sample and systematically varied samples are compared. For the purposes of this search, these systematic uncertainties are applied to $t\bar{t}Z$ but not ZZ, but since ZZ does not have a large hadronic component (e.g. $\sum_i p_{\mathrm{T}}^{\mathrm{jet}}$ tends to be small), these systematic uncertainties are less important for ZZ.

The fourth type of uncertainty comes from comparing different generators. For the primary irreducible backgrounds, $t\bar{t}Z$ and ZZ, the nominal sample distributions are compared to the distributions for the available alternate generator, and the difference between their cumulative distributions is applied as a systematic uncertainty. In practice, the second and third types of systematics tend to be much smaller than the fourth type, when the fourth type is calculated and used.

For ZZ, this uncertainty is applied by comparing the m_{eff} distribution of the nominal Powheg sample and a Sherpa sample, shown in Fig. 5.14. In these comparisons, the $gg \rightarrow ZZ$ samples are not included, as the $gg \rightarrow ZZ$ processes are modeled separately and only exist in the Sherpa generator. However, $gg \rightarrow ZZ$ accounts for at most 10% of the full ZZ yield, as shown in Fig. 5.18. For reference, the leading Feynman diagrams for ZZ are shown in Fig. 5.19 [83].

Due to limited ZZ statistics when using Sherpa, pile-up reweighting is not applied, as doing so tends to decrease the available statistics. For a direct simulation comparison, a lack of pile-up reweighting is not an issue, since both samples were produced with the same pile-up profile. As can be seen in Fig. 5.14, Sherpa generally predicts over 50% more events at high m_{eff} than does Powheg. The distributions of the components of m_{eff} are shown in Fig. 5.15, Fig. 5.16, and Fig. 5.17, where Sherpa is found to predict higher values for all variables. This behavior is not unexpected, as Sherpa (2.1) is known to overestimate the jet multiplicity and $E_{\mathrm{T}}^{\mathrm{miss}}$ values across most samples, relative to Powheg. Nevertheless, this difference is taken as a systematic uncertainty and in practice dominated the ZZ theoretical uncertainty.

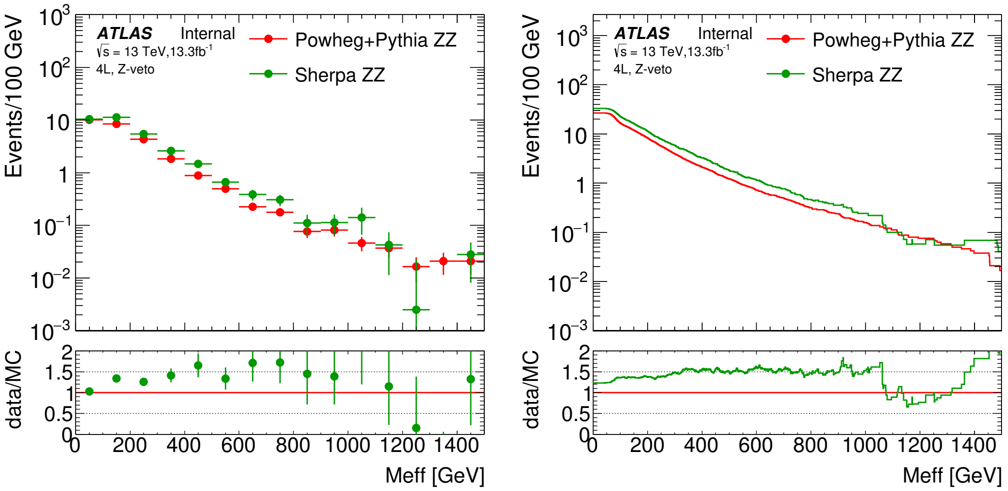

(a) (b)

Figure 5.14: Comparison of m_{eff} distribution (a) and cumulative m_{eff} distribution (b) in two ZZ generators

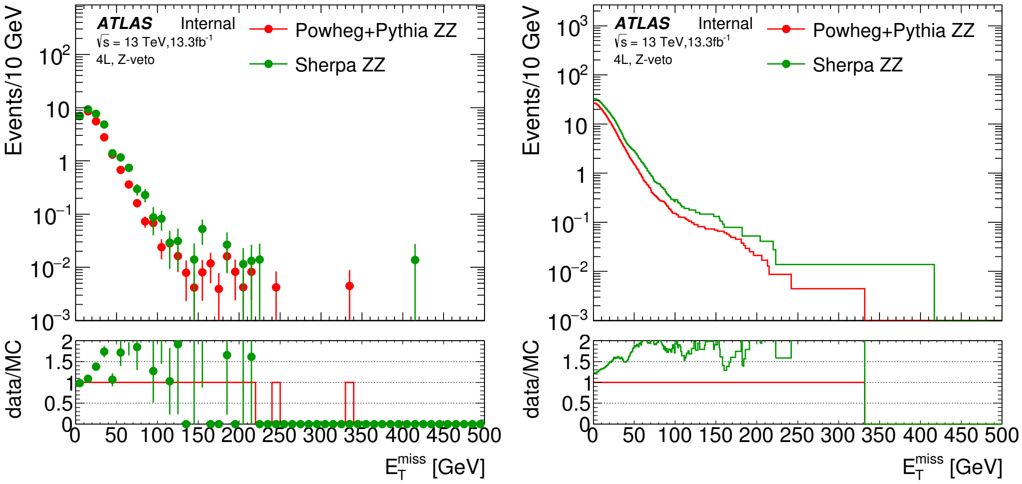

(a) (b)

Figure 5.15: Comparison of $E_{\text{T}}^{\text{miss}}$ distribution (a) and cumulative $E_{\text{T}}^{\text{miss}}$ distribution (b) in two ZZ generators

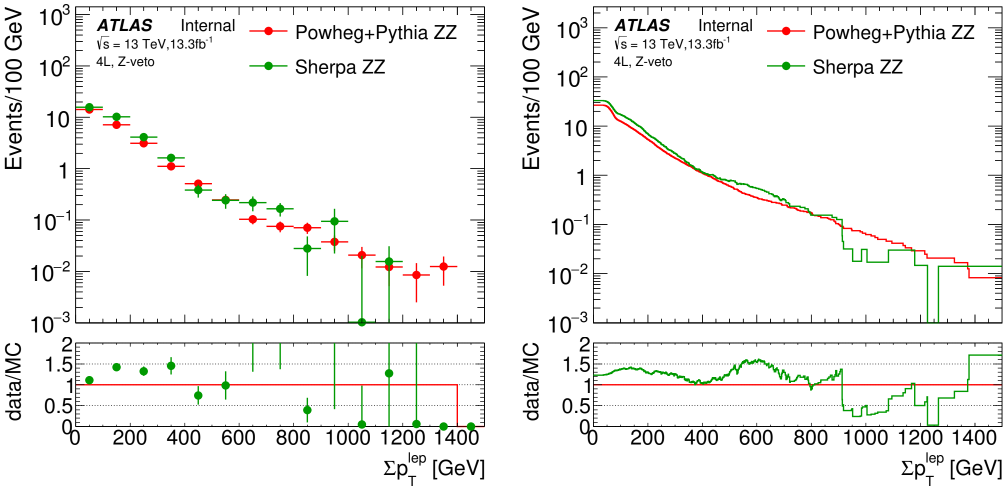

(a)

(b)

Figure 5.16: Comparison of $\sum_i p_{\mathrm{T}}^{\mathrm{lep}}$ distribution (a) and cumulative $\sum_i p_{\mathrm{T}}^{\mathrm{lep}}$ distribution (b) in two ZZ generators

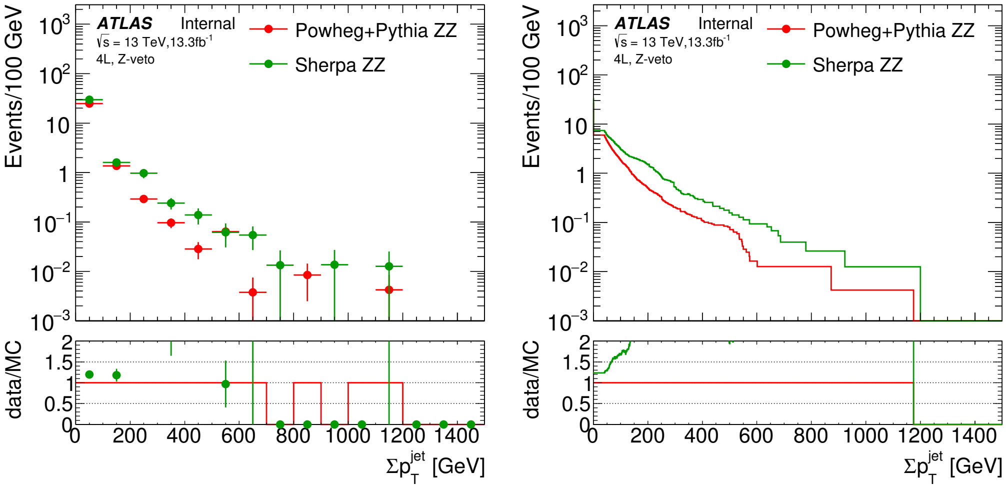

(a)

(b)

Figure 5.17: Comparison of $\sum_i p_{\mathrm{T}}^{\mathrm{jet}}$ distribution (a) and cumulative $\sum_i p_{\mathrm{T}}^{\mathrm{jet}}$ distribution (b) in two ZZ generators

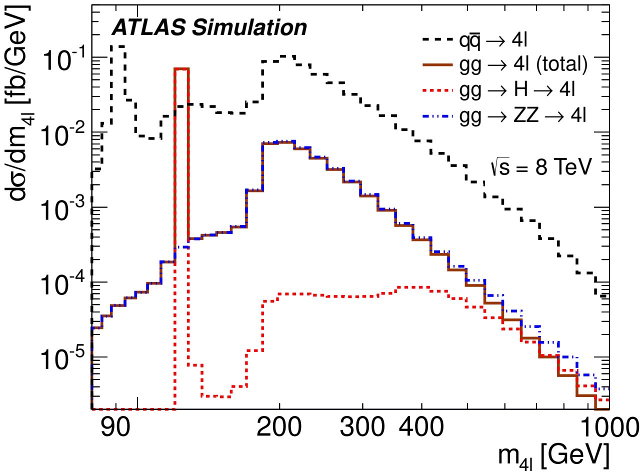

Figure 5.18: Breakdown of 4L events by source, as documented in the 8 TeV ATLAS paper [83]

Compared to ZZ, the generator comparison for $t\bar{t}Z$ produces more well-behaved results. As shown in Fig. 5.20, differences tend to be on the order of 10%, and this difference is taken as a systematic uncertainty. The component distributions are shown in Fig. 5.21, Fig. 5.22, and Fig. 5.23, demonstrating that the individual terms tend to agree well and with approximately the same level of agreement, up to the statistical uncertainty dominated tails.

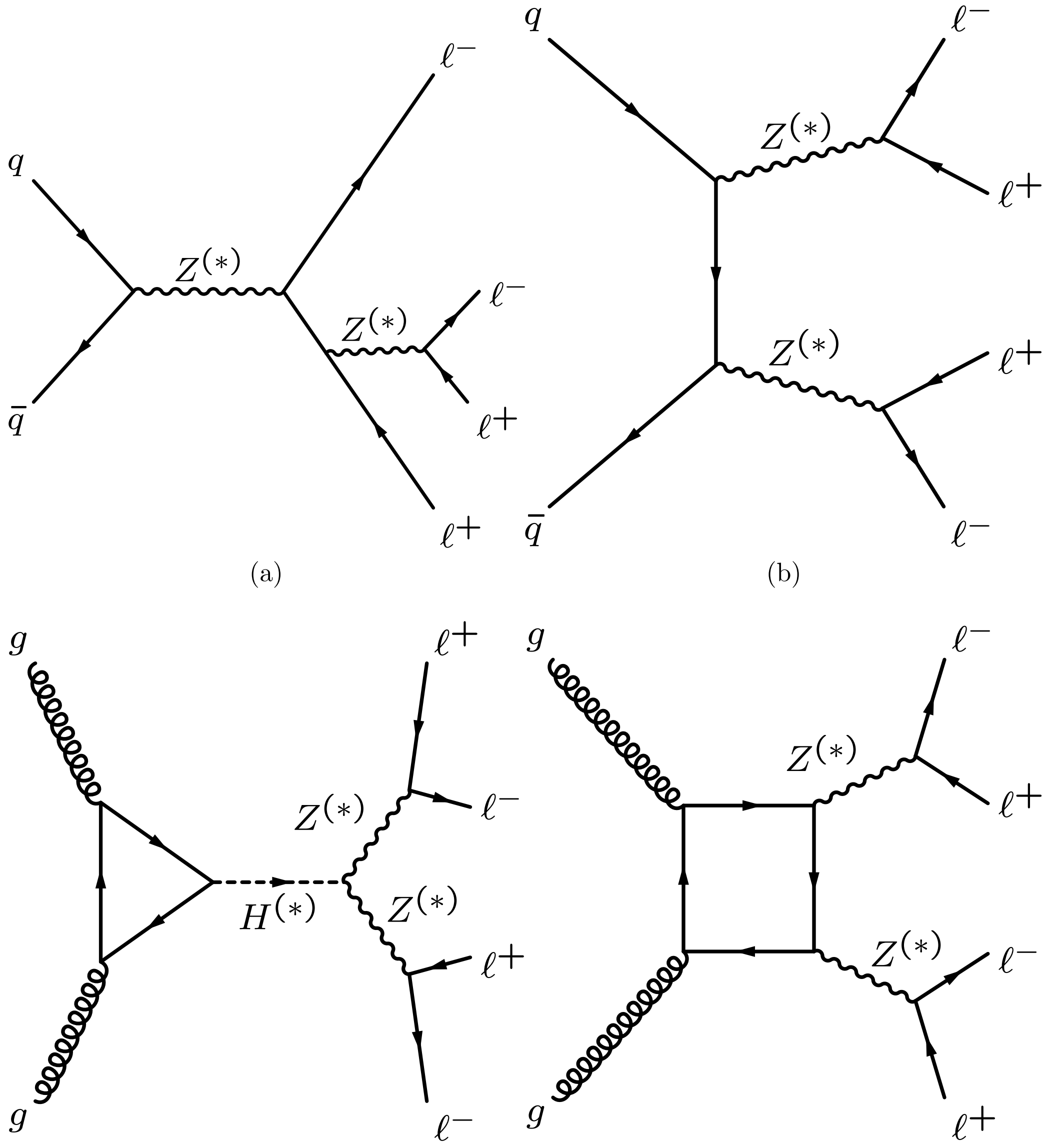

Figure 5.19: Leading Feynman diagrams resulting in 4L production, as documented in the 8 TeV ATLAS paper [83]

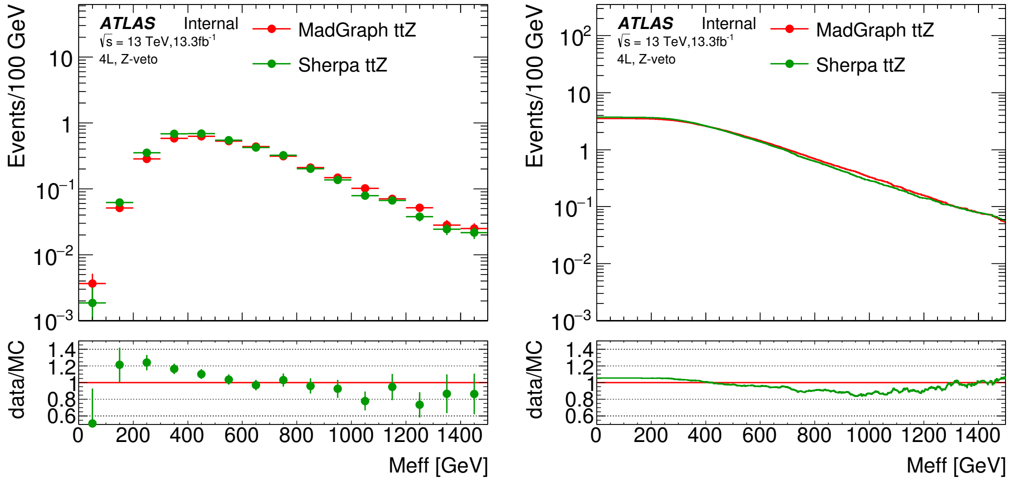

(a) (b)

Figure 5.20: Comparison of m_{eff} distribution (a) and cumulative m_{eff} distribution (b) in two $t\bar{t}Z$ generators

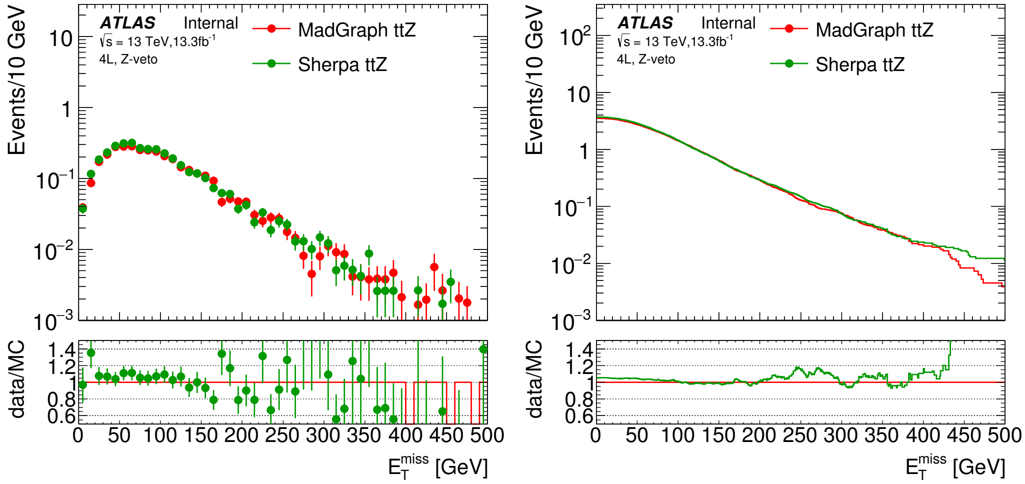

(a) (b)

Figure 5.21: Comparison of $E_{\mathrm{T}}^{\mathrm{miss}}$ distribution (a) and cumulative $E_{\mathrm{T}}^{\mathrm{miss}}$ distribution (b) in two $t\bar{t}Z$ generators

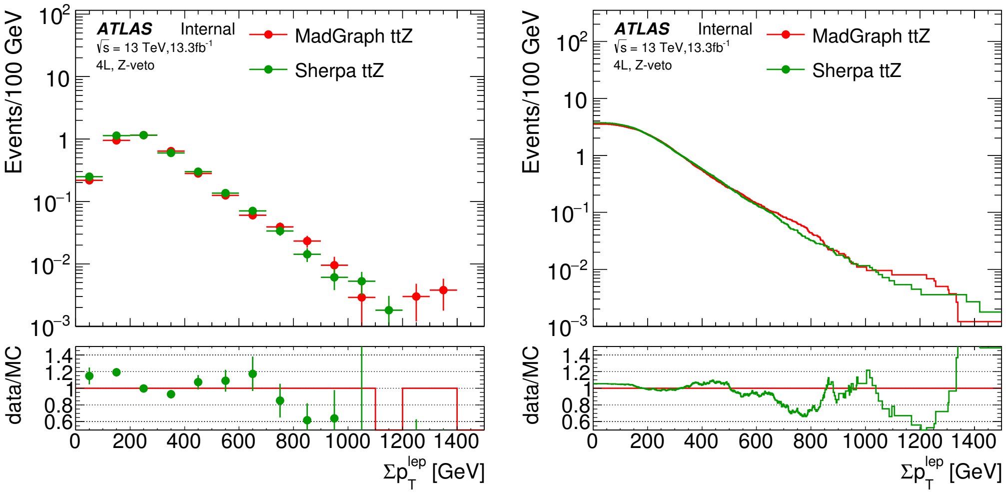

(a)

(b)

Figure 5.22: Comparison of $\sum_i p_{\mathrm{T}}^{\mathrm{lep}}$ distribution (a) and cumulative $\sum_i p_{\mathrm{T}}^{\mathrm{lep}}$ distribution (b) in two $t\bar{t}Z$ generators

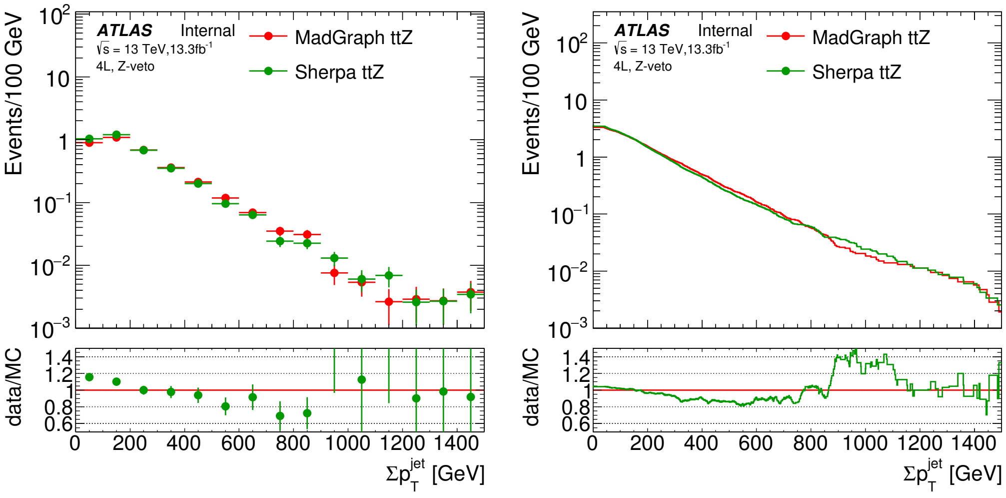

(a)

(b)

Figure 5.23: Comparison of $\sum_i p_{\mathrm{T}}^{\mathrm{jet}}$ distribution (a) and cumulative $\sum_i p_{\mathrm{T}}^{\mathrm{jet}}$ distribution (b) in two $t\bar{t}Z$ generators

5.6 Reducible Backgrounds

A data-driven method is used to quantify the reducible background in the signal and validation regions, based on the data yields in control regions. Section 5.6.1 discusses the sources and nature of ”fake” leptons. Section 5.6.2 derives the formula for calculating the reducible background. Section 5.6.3 compares the self-consistency of the method, in order to justify the approximations used in the method. The remaining sections (5.6.4,5.6.5,5.6.6,5.6.7) are devoted to validating the method in data.

5.6.1 Fake Factors in MC

Electrons are classified according to these definitions

- Prompt electrons: originate from prompt decay of W, Z, top quark, Higgs, or undiscovered SUSY particle
- Heavy flavor (HF) electrons: originate from decay of c or b hadrons
- Conversion (Conv, CO, or CONV) electrons: originate from the interactions of photons with the silicon detector
- Light flavor (LF) electrons: originate from misidentified light flavor jets

Heavy flavor electrons are real electrons, but they originate from sources that are not of interest. Since heavy flavor hadrons form as part of jets, heavy flavor leptons tend not to be isolated, and the isolation requirement largely eliminates electrons from these sources. Further, leptons originating from heavy flavor decays tend to have larger impact parameters, so the vertex association of signal electrons further reduces the number of heavy flavor electrons. Conversion electrons similarly are actual electrons, but since they form only through the interaction of a photon with the detector, they are not of interest from the point of view of a physics search. They can be largely removed through the impact parameter selection, since conversion electrons would be expected to have tracks originating from a detector element and not the primary vertex. Further, conversions can be suppressed through a requirement on the number of track hits. For example, if an electron originated from a conversion in the second layer of the pixel detector, there would not be a hit in the innermost layer. Light flavor electrons are not real electrons, and the electron identification criteria are designed to eliminate them. To simplify the notation, all leptons that are not prompt are referred to as fake leptons.

The effectiveness of the isolation and identification criteria in reducing the numbers of fake leptons from different sources is studied by comparing the numbers of loose and signal leptons. Particularly useful is the fake factor, defined as $F = L/l$, where $L(l)$ is the rate at which a lepton from some source and physics process (classified with truth information and not measureable in reality) and with a set of kinematic variables, will be reconstructed and classified as a signal (loose) lepton.

Fig. 5.24 shows the fake factor for the three sources of fake electrons, measured in $t\bar{t}$ simulation in events containing exactly two prompt signal leptons and at least one fake lepton, either signal or loose (i.e. from 3L and 2L1l). Due to the smaller number of conversion and light flavor electrons relative to heavy flavor electrons in $t\bar{t}$ events, the light flavor and conversion fake factors are parametrized using a much lower granularity than is the heavy flavor fake factor. For the most part, the isolation and more stringent identification requirements of signal versus loose electrons serve to eliminate the vast majority of light flavor and conversion electrons, while, for low momentum electrons at high $|\eta|$, a sizeable portion of baseline heavy flavor electrons satisfy signal electron criteria. Sizeable momentum and η dependence is observed for all fake electron sources, and for the purposes of the actual reducible background measurements, the fake factors are parametrized as a function of both electron p_{T} and η.

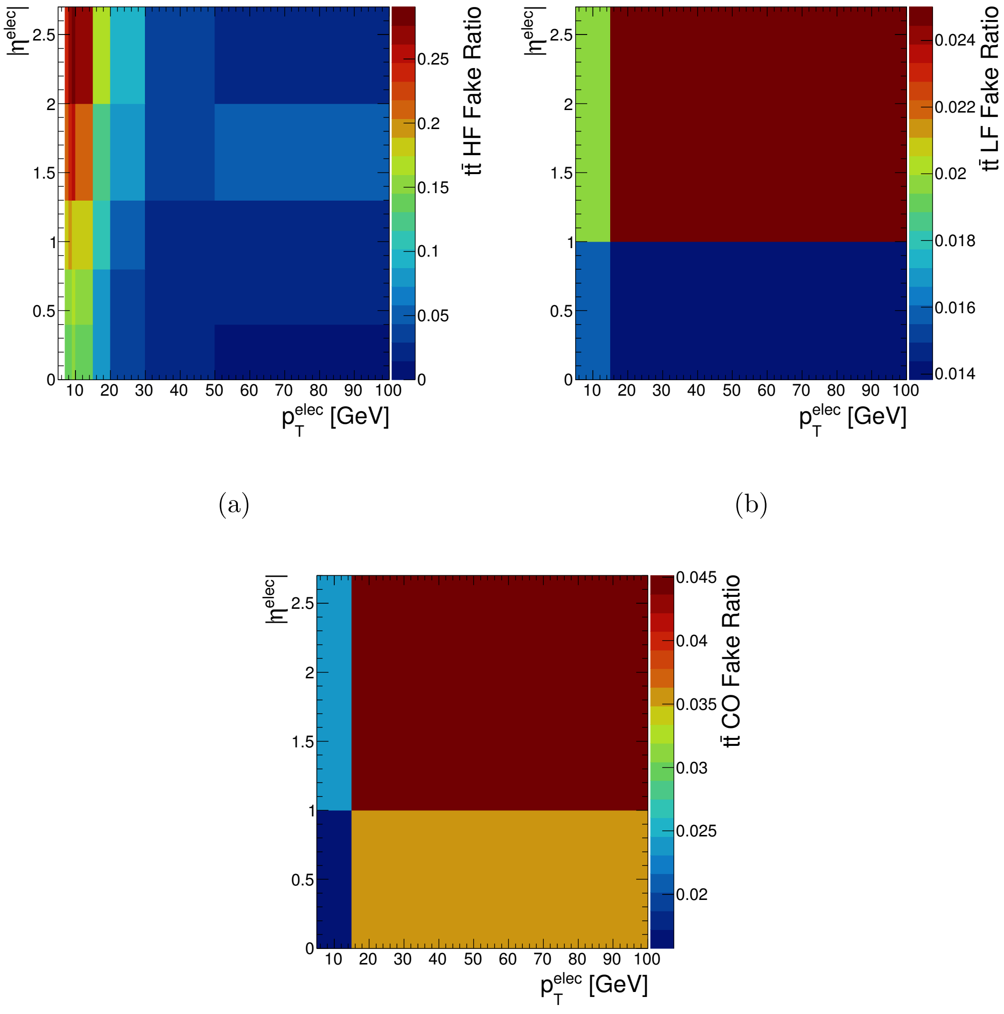

(a)

(b)

(c)

Figure 5.24: Fake ratio for HF, LF, and CO electrons in $t\bar{t}$ events.

Muons are classified according to these definitions

- Prompt muons: originate from prompt decay of W, Z, top quark, Higgs, or undiscovered SUSY particle
- Heavy flavor (HF) muons: originate from decay of c or b hadrons
- Light flavor (LF) muons: originate from anywhere else, generally from light flavor decays

Light flavor muons in reality refers to muons from multiple different sources (e.g. from $\pi^{\pm}$ decay), but distinguishing between muons from these different sources is generally not a difficulty, since they have a low rate of occurrence.

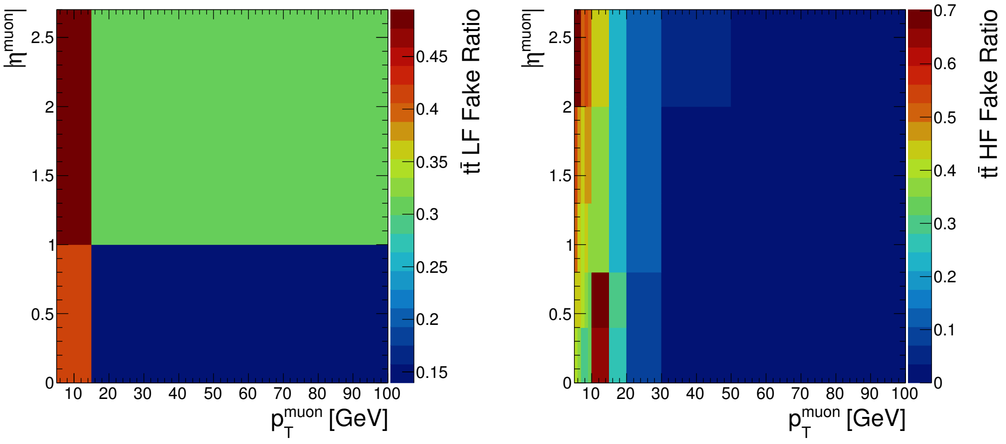

(a) (b)

Figure 5.25: Fake ratio for HF and LF muons in $t\bar{t}$ events.

Fig. 5.25 shows the fake factor for the two sources of fake muons, measured in $t\bar{t}$ simulation in events containing exactly two prompt signal leptons and at least one fake lepton, either signal or loose. The isolation requirements serve to decrease the number of heavy flavor and light flavor muons by a significant margin, and while a large fraction still remain, the small number of fake muons satisfying even the baseline requirements means that fake electrons are a much larger source of fake leptons than are fake muons. As with electrons, significant dependence is observed on both p_{T} and η, and the fake factors used in the reducible background measurement are parametrized as a function of p_{T} and η.

5.6.2 Applying the Fake Factors

A data-driven method is used to quantify the reducible background in the signal and validation regions, based on the data yields in control regions. A similar method is used as was performed for the Run 1 paper [84]. The actual formula used for calculating the reducible background is given at the end of the section, and most of the section is devoted to deriving this formula.

In theory, the reducible background can be expressed conceptually as

$$N_{SR} = \sum_{\vec{p},s_1,s_2,\vec{l_1},\vec{l_2}}^{2L} \left(R(\vec{p}, s_1, s_2, \vec{l_1}, \vec{l_2}) L(s_1, \vec{l_1}) L(s_2, \vec{l_2}) \right) + \sum_{\vec{p},s_1,\vec{l_1}}^{3L} \left(R(\vec{p}, s_1, \vec{l_1}) L(s_1, \vec{l_1}) \right) \tag{5.8}$$

The two sums correspond to processes with two prompt leptons and three prompt leptons, respectively. In general, there would also be two more terms corresponding to processes with one (e.g. W+jets) or zero (e.g. multijet) prompt leptons, but in practice these events are an insignificant portion of the 4L yield. These processes are not shown in figures due to limited statistics in simulation.

The independent parameters are defined as follows. The parameter $\vec{p}$ is a vector of all possible event properties (e.g. the process - $t\bar{t}$, the prompt lepton kinematics, jet kinematics, etc.), with the exception of the specific objects that fake prompt leptons (e.g. the fake lepton p_{T} is not included in $\vec{p}$). The parameters $\vec{l_1}$ and $\vec{l_2}$ are vectors of the measureable parameters specific to each object that can fake a prompt lepton. The parameters s are the true source of each object that can fake a lepton (e.g. if it is a heavy flavor jet or a light flavor jet). By definition, s is discrete, and its only possible values are HF, CO, or LF (5.6.1). To summarize, $\vec{p}$, $\vec{l_1}$, $\vec{l_2}$, s_1, and s_2 together form a complete picture of an event, where the $\vec{l}$ parameters are measureable, while the $\vec{p}$ parameters and s parameters are not, in general. The goal is then to determine the method for calculating the reducible background in a way that depends only on the $\vec{l}$ parameters.

Next, the dependent parameters are defined as follows. R is the rate at which events of each type occur, which in general will depend on all the event specific parameters. L is the rate at which objects of each particular type will be reconstructed as signal leptons and will in general only depend on the properties of the specific object in question (e.g. the probability that a converted photon will be reconstructed as an electron does not depend on the properties of some other jet somewhere else in the detector). Lastly, take l to be the rate at which objects of each particular type will be reconstructed as loose leptons. The measureable fake factors can be defined in terms of the functions L and l as $F(s_i, \vec{l_i}) = L(s_i, \vec{l_i})/l(s_i, \vec{l_i})$, as defined in the section 5.6.1. The reducible background can then be written as

$$N_{SR} = \sum_{\vec{p}, s_1, s_2, \vec{l_1}, \vec{l_2}}^{2L} \Big(R(\vec{p}, s_1, s_2, \vec{l_1}, \vec{l_2}) F(s_1, \vec{l_1}) l(s_1, \vec{l_1}) F(s_2, \vec{l_2}) l(s_2, \vec{l_2}) \Big) + \sum_{\vec{p}, s_1, \vec{l_1}}^{3L} \Big(R(\vec{p}, s_1, \vec{l_1}) F(s_1, \vec{l_1}) l(s_1, \vec{l_1}) \Big) \quad (5.9)$$

However, this formula can be simplified due to the nature of the reducible background processes. As shown in Fig. 5.26, three prompt lepton events ($t\bar{t}W$, WZ, and WWW) are insignificant compared to two prompt lepton events, particularly $t\bar{t}$ and Z+jets .

Due to the low importance of three prompt lepton sources, as well as the high statistical uncertainty that would accompany any data-driven method of measuring the three prompt lepton event yield in the signal region, the second sum is dropped from the reducible background estimate, and the three prompt lepton event yield in the signal regions is taken purely from simulation, with the appropriate systematic uncertainties. The reducible background can then be written as

$$N_{SR} = \sum_{\vec{p},s_1,s_2,\vec{l_1},\vec{l_2}}^{2L} \left(R(\vec{p}, s_1, s_2, \vec{l_1}, \vec{l_2}) F(s_1, \vec{l_1}) l(s_1, \vec{l_1}) F(s_2, \vec{l_2}) l(s_2, \vec{l_2}) \right) \tag{5.10}$$

In a similar manner, the number of reconstructed CR2 events can be written as a function of the event-specific parameters:

$$N_{CR2}(\vec{p}, s_1, s_2, \vec{l_1}, \vec{l_2}) = R(\vec{p}, s_1, s_2, \vec{l_1}, \vec{l_2}) l(s_1, \vec{l_1}) l(s_2, \vec{l_2}) \tag{5.11}$$

so that the yield in the signal region can be written

$$N_{SR} = \sum_{\vec{p},s_1,s_2,\vec{l_1},\vec{l_2}}^{2L} \left(F(s_1, \vec{l_1}) F(s_2, \vec{l_2}) N_{CR2}(\vec{p}, s_1, s_2, \vec{l_1}, \vec{l_2}) \right) \tag{5.12}$$

The $\vec{p}$ parameters only appear in N_{CR2}, the values of which are measured directly as the CR2 yield. The above equation can then be rewritten as a sum over individual CR2 events (indexed by i), as

$$N_{SR} = \sum_i \left(F(s_1^i, \vec{l_1}^i) F(s_2^i, \vec{l_2}^i) \right) \tag{5.13}$$

where effectively a multidimensional integral over the event parameters is converted to a one dimensional integral over event index. The independent variables can all be parametrized by the event index.

This equation cannot be solved exactly. The l parameters are measured on an event-by-event basis, since they correspond to the loose lepton kinematics, but the s parameters are unknown. Instead, the equation is approximated by calculating the F parameters by averaging over the values for each fake lepton source, weighting each by its frequency of occurrence from simulation (Fig. 5.27).

Using this method, the fake factor can be approximated as

$$F(s, \vec{l}) \approx \sum_j \left(s_j(\vec{l}) \cdot F(j, \vec{l}) \right) \tag{5.14}$$

where s_j represents the fraction of fake loose leptons in control region events that have truth source labeled j, which can in general depend on lepton kinematics. Since the $\vec{l}$ parameters are defined as the measureable parameters specific to a particular lepton, this formula can be evaluated. Conceptually, $\vec{l}$ includes every measureable property of a lepton, including lepton type (i.e. electron or muon), p_{T}, η, ϕ, shape variables, track quality, etc. In practice, however, aside from lepton type, the strongest and simplest dependence is on p_{T} and potentially on η. $s_j(\vec{l})$ is parametrized in terms of only lepton type and p_{T}, while $F(j, \vec{l})$ is parametrized in terms of lepton type, p_{T}, and η.

Specifically using this information, the fake factor can be written as

$$F(s, \vec{l}) \approx s_{\mathrm{HF}}(t, p_{\mathrm{T}}) \cdot F_{\mathrm{HF}}(t, p_{\mathrm{T}}, \eta) + s_{\mathrm{CO}}(t, p_{\mathrm{T}}) \cdot F_{\mathrm{CO}}(t, p_{\mathrm{T}}, \eta) + s_{\mathrm{LF}}(t, p_{\mathrm{T}}) \cdot F_{\mathrm{LF}}(t, p_{\mathrm{T}}, \eta) \tag{5.15}$$

However, there is one final complication in the method. The fake factors F are calculated in MC, but the modeling of the fake factors is not guaranteed to be correct in simulation. Ideally, the fake factors could be measured in data in a set of control regions. However, since the fake factors depend on both the process and the lepton kinematics, which will generally be different between the actual reducible background processes and the theoretical control region process, the fake factor cannot be measured and applied directly. Instead, the fake factors that are used are calculated from MC, and an overall scale factor is applied to the fake factors that accounts for the disagreement between data and MC in the signal region. The fake factor then becomes

$$\begin{aligned} F(s, \vec{l}) \approx\, & sf_{HF}(t) \cdot s_{\mathrm{HF}}(t, p_{\mathrm{T}}) \cdot F_{\mathrm{HF}}(t, p_{\mathrm{T}}, \eta) + sf_{CO}(t) \cdot s_{\mathrm{CO}}(t, p_{\mathrm{T}}) \cdot F_{\mathrm{CO}}(t, p_{\mathrm{T}}, \eta) \\ & + sf_{LF}(t) \cdot s_{\mathrm{LF}}(t, p_{\mathrm{T}}) \cdot F_{\mathrm{LF}}(t, p_{\mathrm{T}}, \eta) \end{aligned} \tag{5.16}$$

where sf is the scale factor comparing data and MC. At this point, the values of F and s that are used in the reducible background calculation have already been shown in Fig. 5.24, Fig. 5.25, and Fig. 5.27, but the scale factors, sf, have not yet been derived. In practice, a scale factor of 1 ± 0.25 is taken for all fake lepton sources, and the justification for this method is the focus of section 5.6.4, section 5.6.5, and section 5.6.6.

Finally, the reducible background is straightforward to calculate, as

$$N_{SR} = \sum_i \left(F(t_1^i, p_{T,1}^i, \eta_1^i) F(t_2^i, p_{T,2}^i, \eta_2^i) \right) \tag{5.17}$$

where the $F(t_1^i, p_{T,1}^i, \eta_1^i)$ and $F(t_2^i, p_{T,2}^i, \eta_2^i)$ parameters are calculated using equation 5.16.

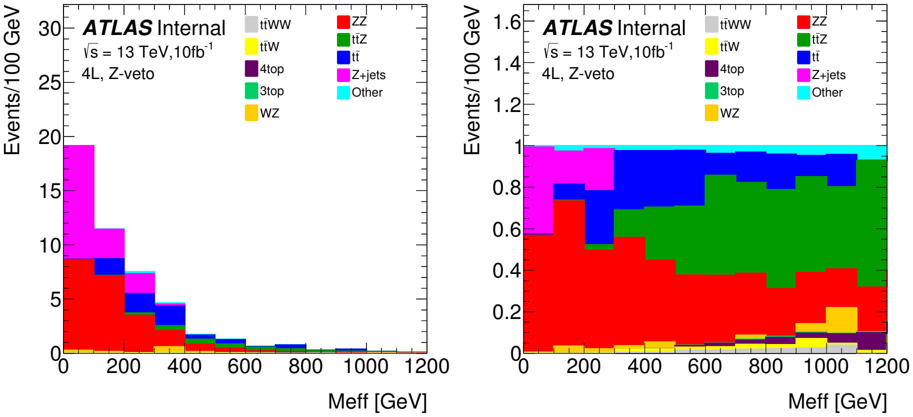

(a) 4ℓ yield (b) 4ℓ composition

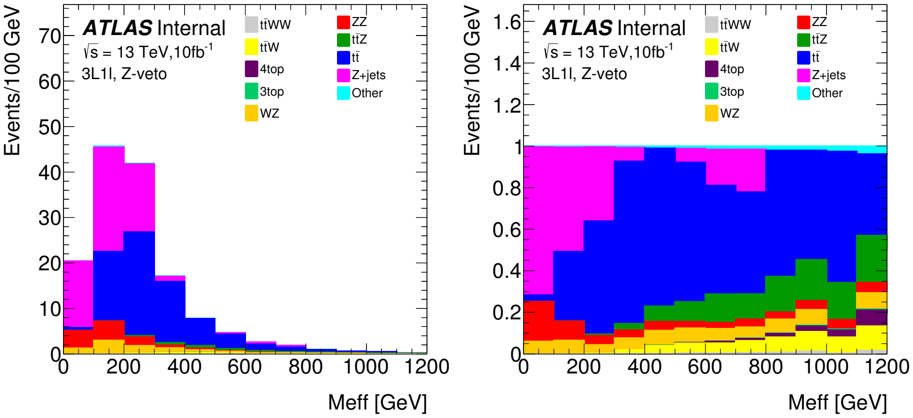

(c) CR1 yield (d) CR1 composition

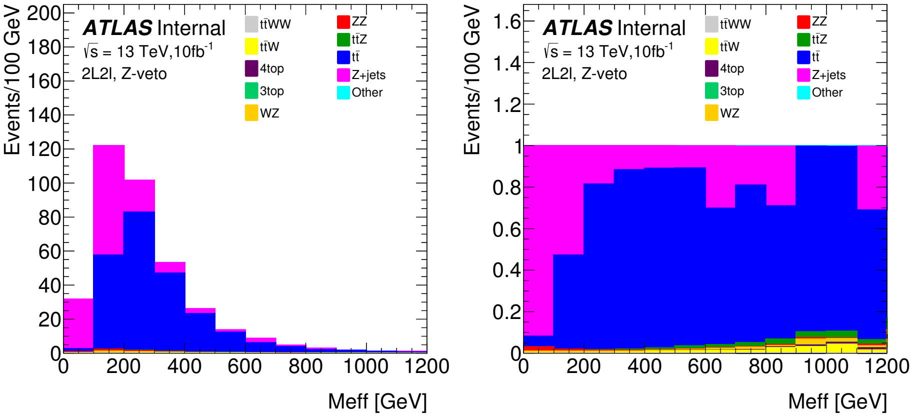

(e) CR2 yield (f) CR2 composition

Figure 5.26: The SR and CR yields and composition in MC events, normalized to $10\,\text{fb}^{-1}$ of data.

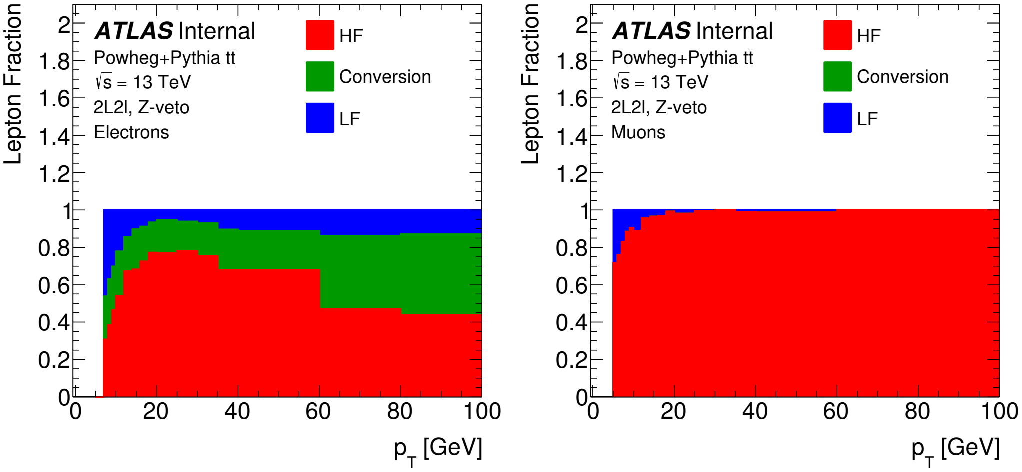

(a) Electrons (b) Muons

Figure 5.27: Composition of $t\bar{t}$ events in CR2.

5.6.3 MC Closure Test for Fake Factor Method

In order to confirm the self-consistency of the method, the fake factor and source fraction weighted yield in simulation is compared directly to the signal region yield in simulation for $t\bar{t}$ events. Given that the fake factors and source fractions are taken from $t\bar{t}$ simulation, the signal region yield and weighted control region yields are expected and found to be consistent (Fig. 5.28) within the statistical uncertainty. This uncertainty is large for the signal region yield due to the small number of simulated events in the signal region.

Direct comparison of the consistency of the full reducible background (i.e. not just $t\bar{t}$) in the signal and control regions in simulation is complicated due to limited Z+jets statistics in the signal region. Instead, a direct comparison is performed for 3L and 2L1l regions in simulated $t\bar{t}$ and Z+jets events, in order to demonstrate the self-consistency of the method for Z+jets and for the full reducible background (Fig. 5.29). In all of these comparisons, the fake fractions are taken from 2L1l and 3L events in $t\bar{t}$ simulation and applied as a function of lepton p_{T} and η. The source fractions are taken from 2L2l $t\bar{t}$ simulation, applied as a function of lepton p_{T} only, due to limited statistics.

In all cases, the method outlined is found to be self-consistent.

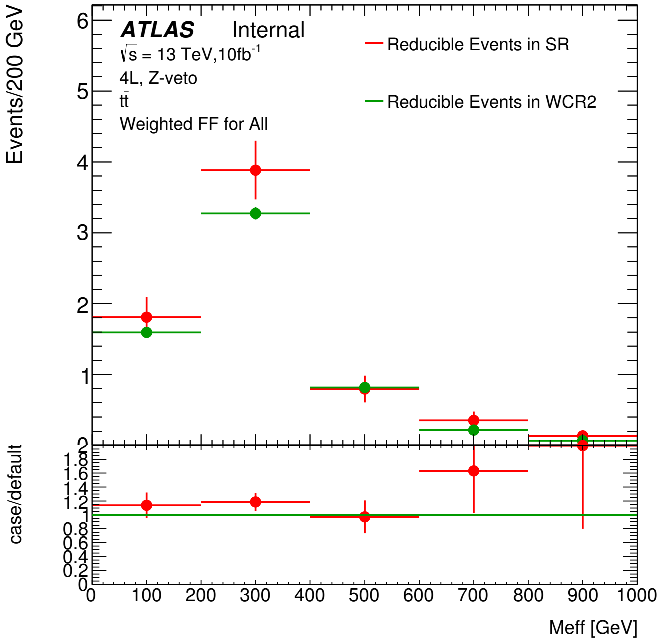

(a)

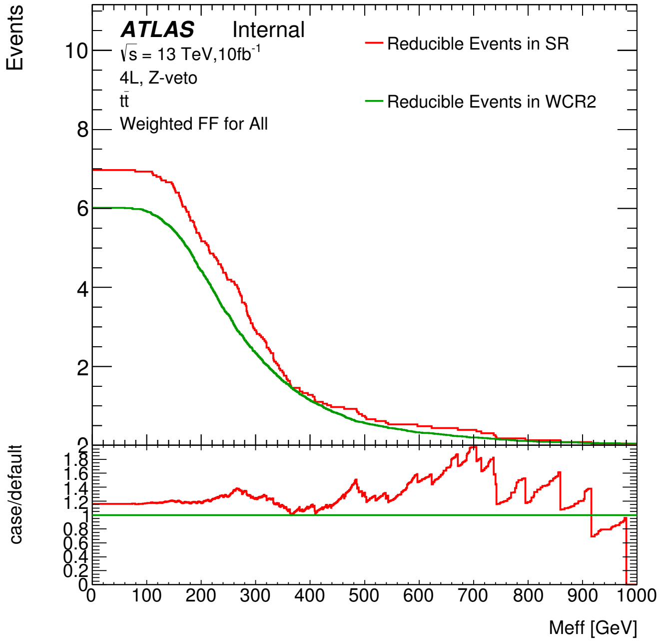

(b)

Figure 5.28: The results of the closure test of the fake factor method, using $t\bar{t}$ 2L2l events.

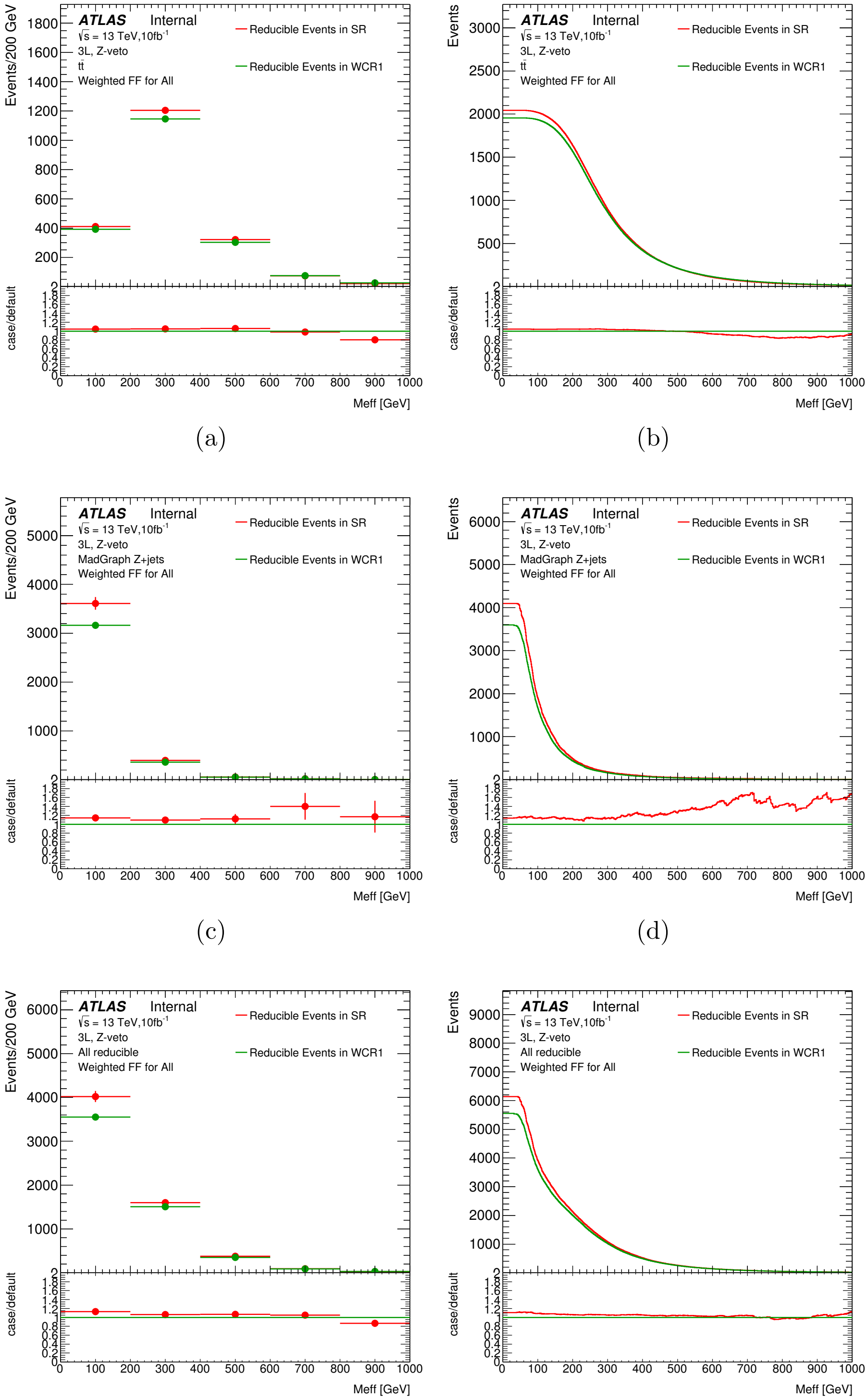

(a) (b)

(c) (d)

(e) (f)

Figure 5.29: The results of the closure test of the fake factor method, using (a)-(b) $t\bar{t}$ 2L1l events only, (c)-(d) Z+jets 2L1l events only, and (e)-(f) all reducible 2L1l events. (b), (d), and (f) show cumulative yields.

5.6.4 Heavy Flavor Fake Factor Validation

This section discusses the validation of the heavy flavor lepton modeling in data. The results are given at the end of the section [85].

A pure sample of heavy flavor leptons can be found in $b\bar{b}$ events, using a method similar to the Run 1 paper [84]. Events are required to have two muons, or an electron and a muon, where one signal muon, the tag muon, is required to fail the overlap removal due to overlap with a b-jet (see overlap removal criteria in section 4). The other lepton, the probe lepton, is required to pass the overlap removal. In this manner, the tag lepton is known (or, assumed) to come from a heavy flavor decay. If other potential sources of b-jets can be eliminated, in particular $t\bar{t}$ and W events, then $b\bar{b}$ becomes the dominant source of events with this topology. If there is only one observed b-jet in the event, specifically the one overlapping the tag muon, then it is most likely the case that the other b-jet is not observed because it is the source of the probe lepton. The probe lepton is then taken to be a heavy flavor lepton.

$E_{\mathrm{T}}^{\mathrm{miss}}$ and other kinematic variables upper bounds are placed on the system to suppress W background ($E_{\mathrm{T}}^{\mathrm{miss}} < 60\,\mathrm{GeV}$). To suppress $t\bar{t}$ background it is required that $N_{\mathrm{jets}} < 4$, and this selection yields a high $b\bar{b}$ purity. Then, the scale factors are calculated by comparing the number of events where the probe lepton is a signal lepton versus a loose lepton.

The scale factor is not seen to significantly depend on the lepton p_{T} or η, therefore flat scale factors are calculated as:

- $sf^{\mathrm{HF}}(e) = 1.04 \pm 0.10$ (Run1 0.69 ± 0.05)
- $sf^{\mathrm{HF}}(\mu) = 0.84 \pm 0.06$ (Run1 0.84 ± 0.11)

For simplicity, a constant scale factor of 1 ± 0.25 is applied when performing the actual reducible background calculation, as this window contains both the central values and statistical uncertainties on the individual electron and muon scale factors.

5.6.5 Conversion Fake Factor Validation

The conversion electron fake factors are validated in $Z \to \mu\mu\gamma$, where the γ is emitted as final state radiation. Selecting for events containing two muons and an electron, such that the invariant mass of the three lepton system is within a window of the Z mass, gives a sample pure in conversion electrons. In all cases, electrons are required to have a minimum separation in $\Delta R > 0.2$ with respect to either of the muons in the event, in order to avoid cases where a photon is emitted collinearly with a muon. The invarant mass distribution in simulation is shown in Fig. 5.30, giving the breakdown of the relevant physics processes. The entire considered Z mass window is found to be pure in Z+jets events relative to other sources, with no other SM source forming a significant background. In each plot, 3L indicates a three signal lepton requirement, and 2L1l indicates a two signal muon and loose electron requirement.

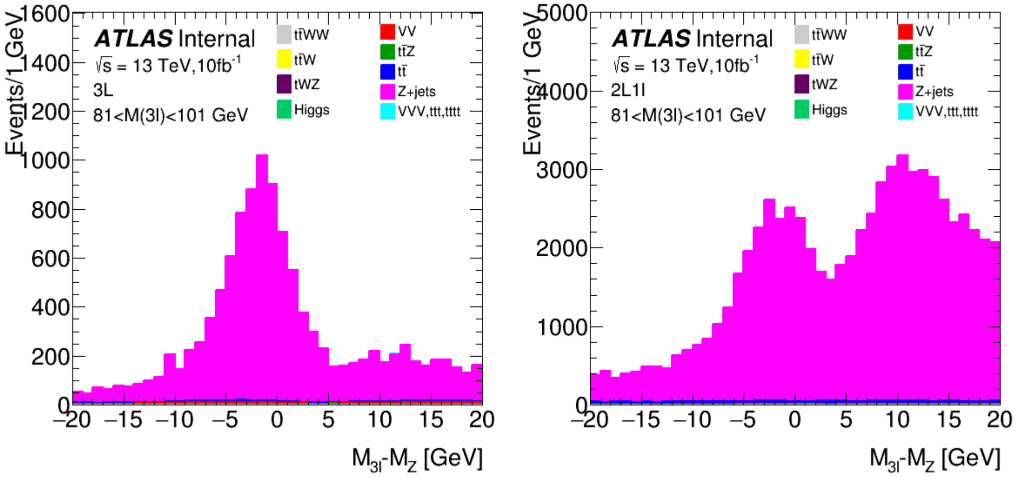

(a) (b)

Figure 5.30: Number of events with trilepton mass near the Z mass, broken down by process, for 3L(a) and 2L1l(b).

The same distribution is shown in Fig. 5.31, dividing the distribution by fake lepton type instead of process. A high degree of light flavor contamination is observed unless a tight window around the Z mass is used. More importantly, including masses above the Z mass results in a high contamination from LH electrons in the 2L1l region, and this behavior results from the topology of events containing LF or HF electrons versus conversion electrons. In particular, FSR events are expected to give a mass near the Z mass, while LF or HF electrons originate from jets. These jets most frequently recoil against the Z and give three object invariant masses greater than the Z mass.

The chosen window corresponds to $84 < M_Z < 91\,\text{GeV}$. Increasing the ceiling further increases the contamination from heavy flavor electrons in both the signal region and the control region, and, more importantly, it dramatically increases the contamination in the control region from light flavor electrons. Decreasing the floor of the window increases the light flavor contamination of the control region without significantly increasing the fraction of events that lie in the window.

Within this mass window, the fake electron source breakdown is included in Fig. 5.32. The control region conversion purity below 10 GeV is found to be approximately 70%, rising to over 90% at 15 GeV. In the signal region the purity is over 10% from 7 GeV.

Finally, the fake factors can be compared in data and simulation, shown in Fig. 5.33. Data and simulation are found to agree within the statistical uncertainty in all bins. A global scale factor of 1 ± 0.25 is used, covering the disagreement in the range $0 < p_{\mathrm{T}}^{ele} < 70\,\text{GeV}$, and for points above this range, the scale factor lies within the statistical uncertainty.

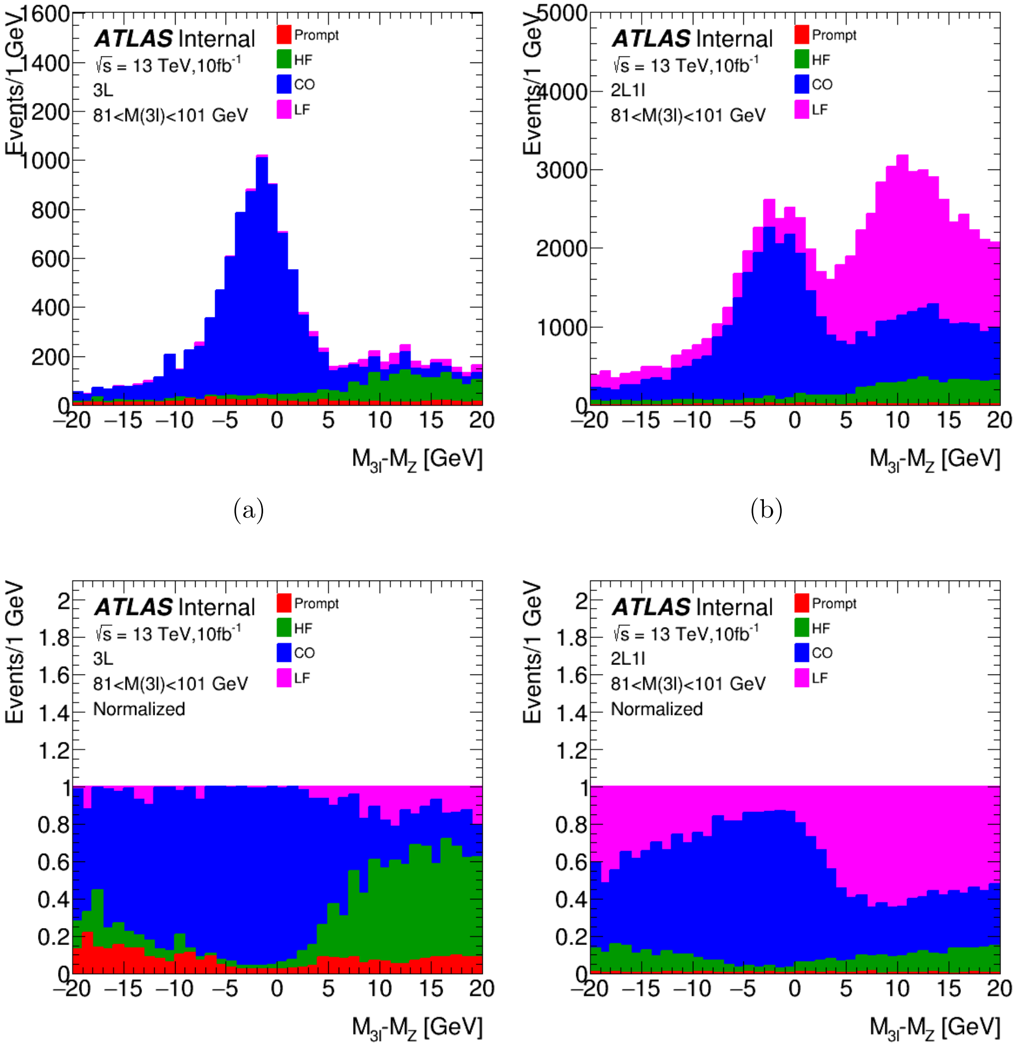

(a) (b)

(c) (d)

Figure 5.31: Trilepton mass distributions, broken down by electron source, for 3L(a) and 2L1l(b), as well as the normalized fraction of events for 3L(c) and 2L1l(d).

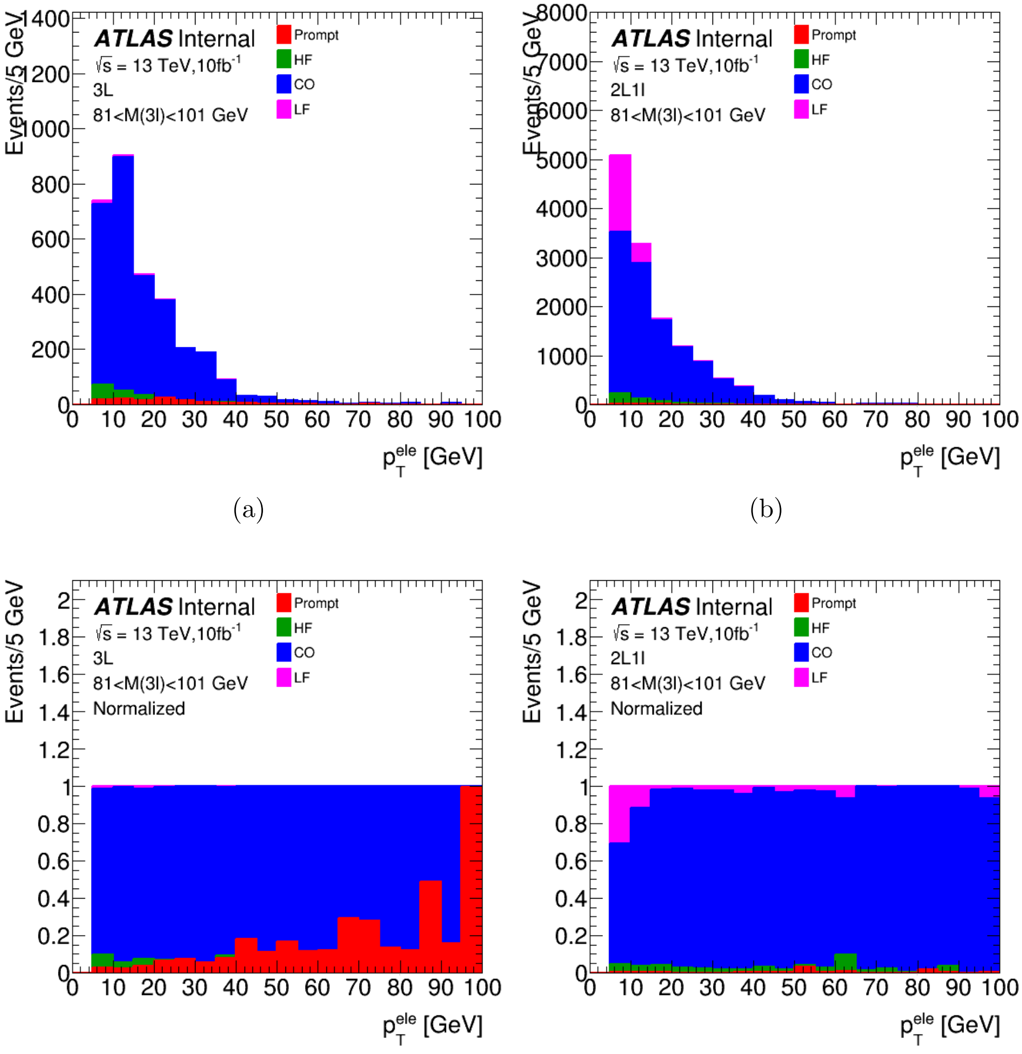

(a) (b)

(c) (d)

Figure 5.32: Number of events with trilepton mass near the Z mass, broken down by electron source, for 3L(a) and 2L1l(b), as well as the normalized fraction of events for 3L(c) and 2L1l(d).

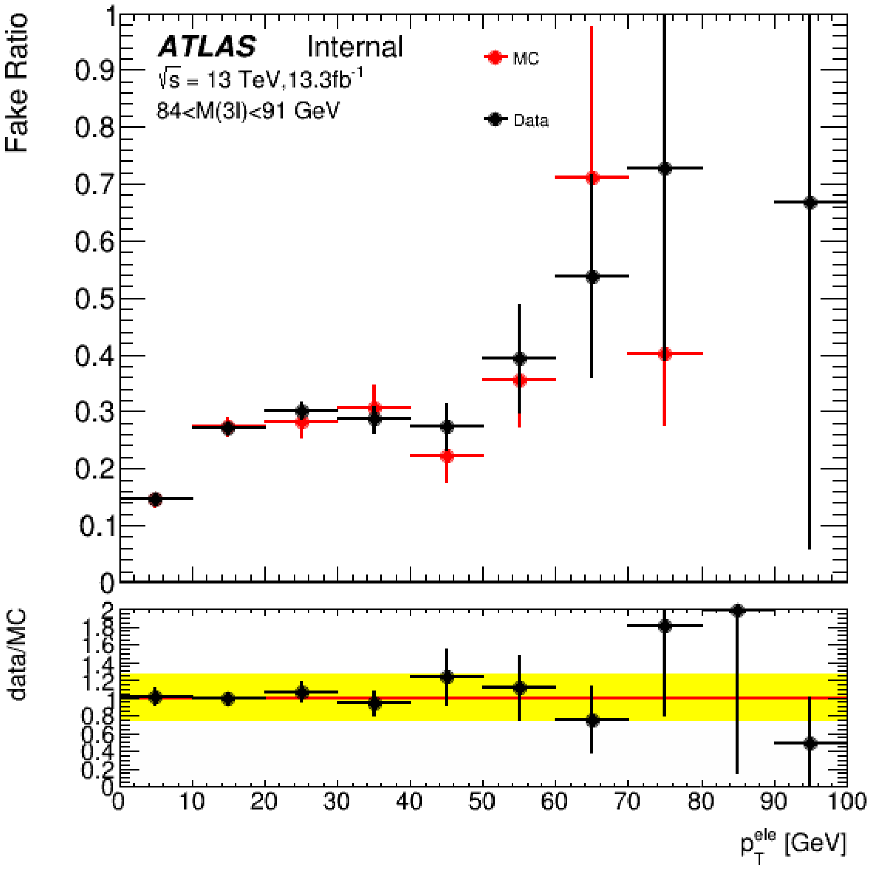

Figure 5.33: Fake ratio for data and MC, where the ratio plot gives the scale factor between them. The yellow band corresponds to the scale factor and corresponding uncertainty that is actually used.

5.6.6 Light Flavor Fake Factor Validation

A determination of the light flavor scale factors between data and MC is complicated by the low light flavor fake factor, since there are generally very few light flavor signal leptons. As a result, while it is easy to select for events with a loose light flavor lepton, it is difficult to select for events with a signal light flavor lepton, since the signal lepton will most often be heavy flavor in origin. However, the low fake factor (rate at which leptons are classified as signal versus loose leptons) means that the scale factor (modeling difference in simulation versus data) and uncertainty on the scale factor are both entirely insignificant in determining the final reducible background estimate.

As a simplified example, the inclusive fake factors and source fractions can be used, where the inclusive values are taken to be the integral over the fake factor and source fractions. The total fake factor is then

$$F_{\text{inclusive}} = F_{hf} \cdot s_{hf} \cdot sf_{hf} + F_{co} \cdot s_{co} \cdot sf_{co} + F_{lf} \cdot s_{lf} \cdot sf_{lf} \tag{5.18}$$

$$F_{\text{inclusive}} = 0.12 \cdot 0.54 \cdot (1 \pm 0.25) + 0.03 \cdot 0.23 \cdot (1 \pm 0.25) + 0.02 \cdot 0.23 \cdot (X) \tag{5.19}$$

$$F_{\text{inclusive}} = (0.065 \pm 0.016) + (0.007 \pm 0.002) + 0.005(X) \tag{5.20}$$

where X is an unknown light flavor scale factor.

In this case, the uncertainty in the heavy flavor scale factor would correspond to more than a 300% uncertainty on the light flavor scale factor, and the light flavor scale factor and its uncertainty are taken to be insignificant. For technical simplicity, a scale factor of 1 ± 0.25 is assumed, to be consisent with the scale factors for heavy flavor and light flavor leptons. This same line of reasoning implies that the conversion scale factors are also insignificant, but since the conversion lepton source fraction increases significantly at high lepton p_{T}, it is still possible that the conversion lepton scale factor would be relevant beyond this simplified model.

As a final comparison, the same calculation is performed for muons, giving

$$F_{\text{inclusive}} = 0.27 \cdot 0.90 \cdot (1 \pm 0.25) + 0.44 \cdot 0.10 \cdot X \tag{5.21}$$

and

$$F_{\text{inclusive}} = (0.24 \pm 0.06) + 0.04X \tag{5.22}$$

In this case, the uncertainty on the heavy flavor muon scale factor corresponds to a 150% uncertainty on the light flavor muon scale factor. The effect is larger than in the electron case, but light flavor muons are still insignificant, and a light flavor muon scale factor of 1 ± 0.25 is applied for technical simplicity.

5.6.7 Final Reducible Background Yield

The final control region yields is shown in Fig. 5.34. The yields in simulation are shown for reference and show good agreement with data, though this agreement is not necessary, as the search does not depend on the control region yield being well-modeled. The yield in 3L1l is also shown for reference, though this yield is not used in the calculation due to low statistics, as described in section 5.6. The control region statistics in CR2 do not end up being a limiting factor of the analysis, largely due to the greater than expected integrated luminosity. The CR2 is observed to contain 49 events above $M_{eff} > 600\,\mathrm{GeV}$ and 18 events above $M_{eff} > 900\,\mathrm{GeV}$. For reference, from simulation 44.6 events are expected above $M_{eff} > 600\,\mathrm{GeV}$ and 13.9 events are expected above $M_{eff} > 900\,\mathrm{GeV}$.

The final piece of the reducible background estimate is to remove double counting of backgrounds with more than two prompt leptons. As shown in Fig. 5.26, a small number of events with three or four prompt leptons end up in the control region, and since these backgrounds are already included in the background estimate using their signal region yields directly, double counting will result if the CR2 yields of these backgrounds are not subtracted off of the total CR2 yield. Since the CR2 yields of these backgrounds are not measureable separately from the inclusive CR2 yield, the CR2 yields are taken directly from simulation. The CR2 yield of three prompt and four prompt lepton backgrounds is then directly subtracted from the CR2 yield in data.

This method then gives the final reducible background yields

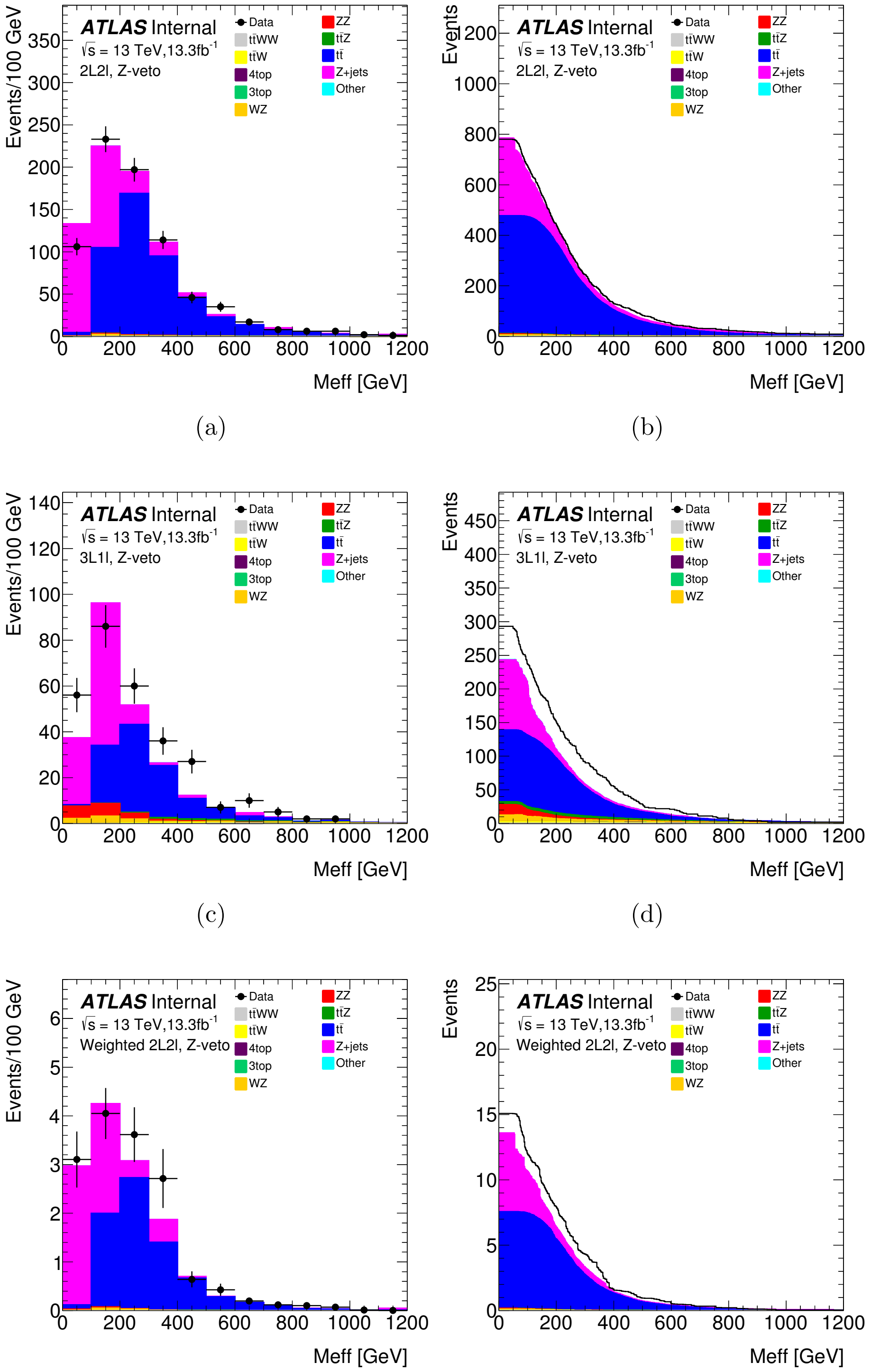

(a) (b)

(c) (d)

(e) (f)

Figure 5.34: (a) m_{eff} distribution and (b) cumulative distributions of m_{eff} in CR2. (c) m_{eff} distribution and (d) cumulative distributions of m_{eff} in CR1. (e) m_{eff} distribution and (f) cumulative distributions of m_{eff} in CR2 after weighting events by the light lepton fake factors derived from HF leptons in $t\bar{t}$.

SRA: 0.48 ± 0.24

SRB: 0.11 ± 0.05

VR: 16 ± 6

which are discussed in more detail in Section 5.7.

5.7 Validation Region

The general validation of the default background estimate is shown here. The irreducible background is estimated from MC while the reducible background is estimated from data using the weighting method. The m_{eff} selection used in the signal regions is reversed in these validation regions (e.g. $m_{\text{eff}} < 600\,\text{GeV}$ for 4L, See Table 5.1).

5.7.1 Comparison of Data with Simulation

The results for the 4L VR are given in Table 5.7, where good agreement is seen between the expectation and observed yields (especially given the limited statistics in the dataset used for the reducible background). Distributions of m_{eff} are shown in Fig. 5.35 for the reducible background taken either from MC, from MC with the fake factor method applied, or from data. Good agreement is seen across the m_{eff} distribution given the limited statistics. In all three cases, the data and irreducible background distributions are identical, and the only difference is the method used for calculating the reducible background. The agreement across the different methods of calculating the reducible background follows from the direct reducible background comparison shown in Fig. 5.34.

Fig. 5.36 shows the same comparison for $E_{\text{T}}^{\text{miss}}$. $E_{\text{T}}^{\text{miss}}$ is well-modeled in the core of the distribution, but disagreement begins to appear in the tail of the distribution.

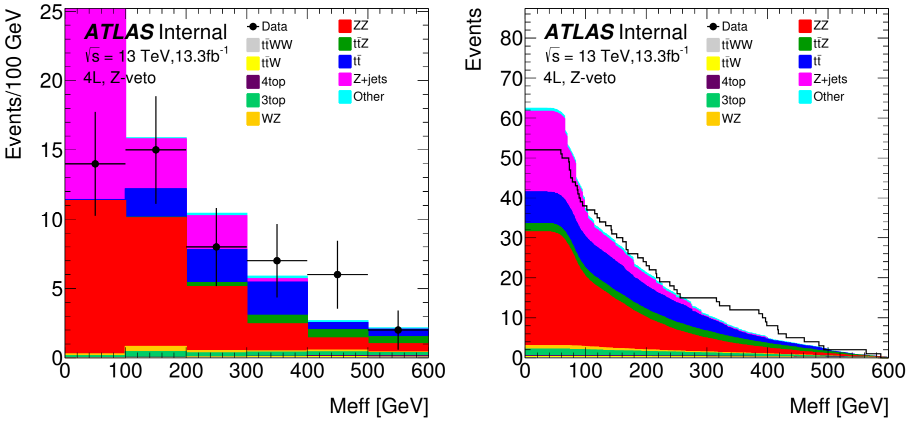

(a) Pure MC (b) Cumulative, pure MC

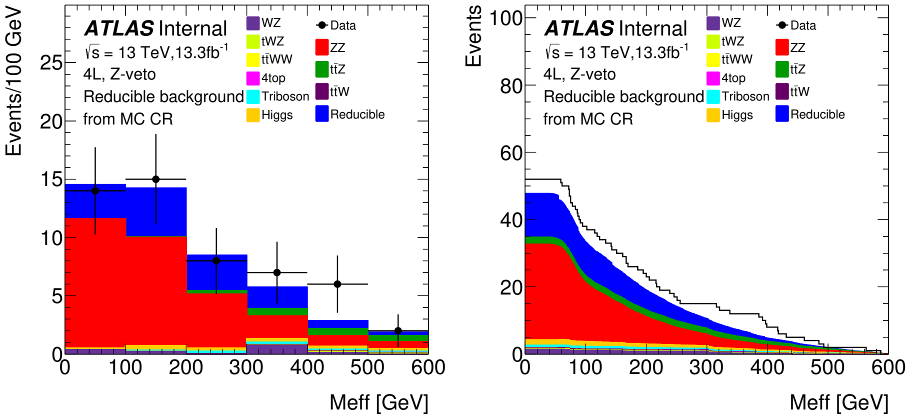

(c) Fake factors on MC (d) Cumulative, FF on MC

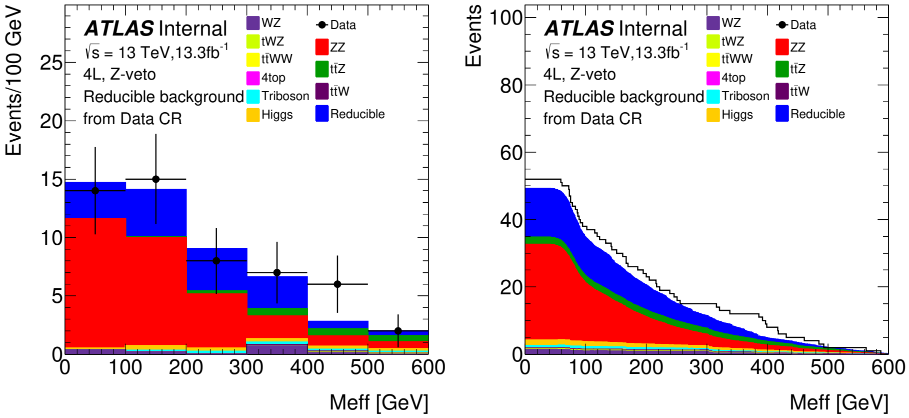

(e) Fake factors on data (f) Cumulative, FF on data

Figure 5.35: m_{eff} distribution(a)(c)(e) and cumulative m_{eff} distribution(b)(d)(f) in the 4L low m_{eff} VR0. The reducible background is taken directly from MC in (a)(b), from the weighted MC control region yield in (c)(d), and from the weighted data control region yield in (e)(f).

Sample	4L VR ($m_{\text{eff}} < 600\,\text{GeV}$)
Irreducible	
ZZ	29 ± 5
$t\bar{t}Z$	2.04 ± 0.23
Higgs	1.6 ± 1.4
VVZ	0.72 ± 0.14
tWZ	0.20 ± 0.07
$t\bar{t}WW$	0.045 ± 0.010
$t\bar{t}t\bar{t}/\ tt\bar{t}$	0.020 ± 0.002
1-fake ℓ reducible	
WZ	0.89 ± 0.08
$t\bar{t}W$	0.240 ± 0.020
WWW	0.012 ± 0.001
2-fake ℓ reducible (from data)	16 ± 6
ΣSM	50 ± 6
Data	53

Table 5.7: Expected and observed yields for $13.3\,\text{fb}^{-1}$ in the 4L low m_{eff} VR0. Uncertainties are statistical and systematic added in quadrature.

However, given the low statistics, both in data and simulation, the excess is not statistically significant. The distributions of the lepton p_{T} sum and the jet p_{T} sum are shown in Fig. 5.37 and Fig. 5.38, respectively. As in the case of m_{eff}, significant disagreement is not observed, but the statistics are limited.

Next, the lepton p_{T} and η distributions in the low m_{eff} VR are shown in Fig. 5.39 and Fig. 5.40. Since there are always at least four leptons in every event, each plot has the same overall normalization. In the p_{T} distributions, of particular note is the distribution of the fourth lepton, since that distribution directly demonstrates the effect of increasing the lepton p_{T} threshold. Most events are observed to have $p_{\text{T}}^{\text{lepton4}} < 10\,\text{GeV}$, so that most of the validation region events would be rejected if the lepton p_{T} threshold were to be increased. The η distributions show expected behavior and are peaked at low η and gradually decrease at higher η.

In order to validate the treatment of low mass lepton pairs, the invariant mass of OS and SFOS pairs in the VR are shown in Figure 5.41. Good agreement is seen

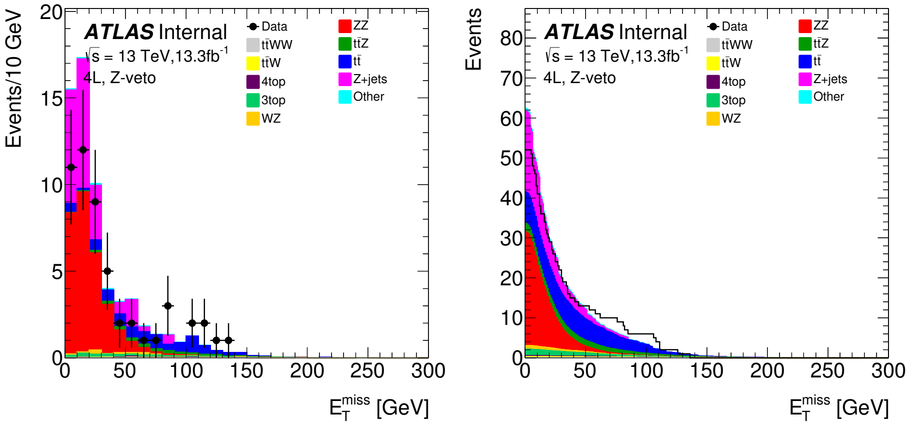

(a) Pure MC (b) Cumulative, pure MC

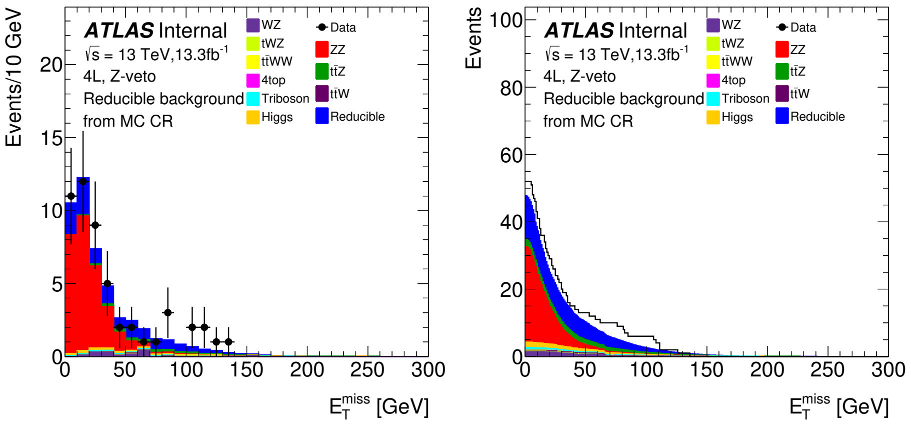

(c) Fake factors on MC (d) Cumulative, FF on MC

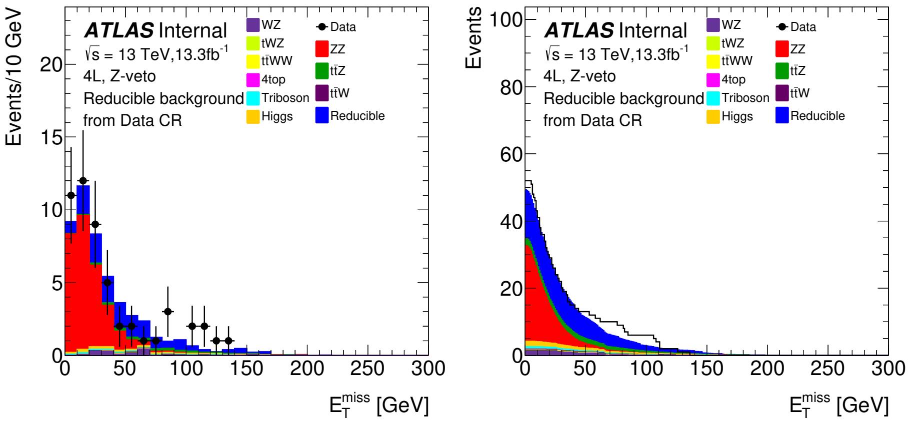

(e) Fake factors on data (f) Cumulative, FF on data

Figure 5.36: $E_{\mathrm{T}}^{\mathrm{miss}}$ distribution(a)(c)(e) and cumulative $E_{\mathrm{T}}^{\mathrm{miss}}$ distribution(b)(d)(f) in the 4L low $E_{\mathrm{T}}^{\mathrm{miss}}$ VR0. The reducible background is taken directly from MC in (a)(b), from the weighted MC control region yield in (c)(d), and from the weighted data control region yield in (e)(f).

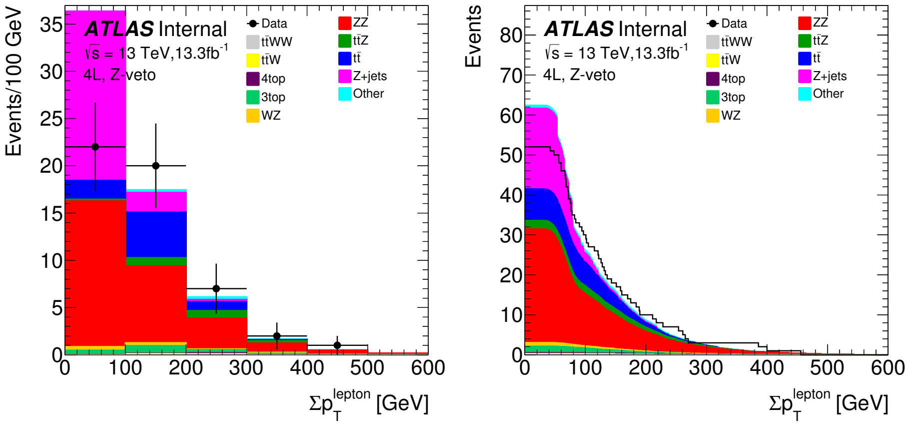

(a) Pure MC

(b) Cumulative, pure MC

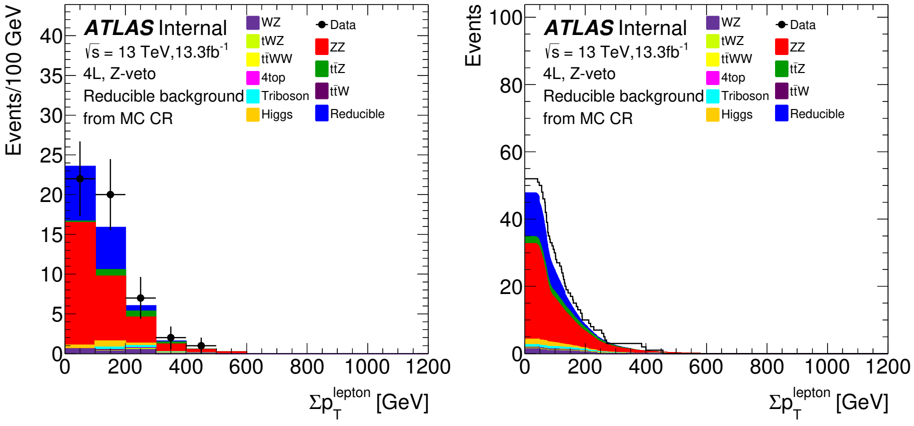

(c) Fake factors on MC

(d) Cumulative, FF on MC

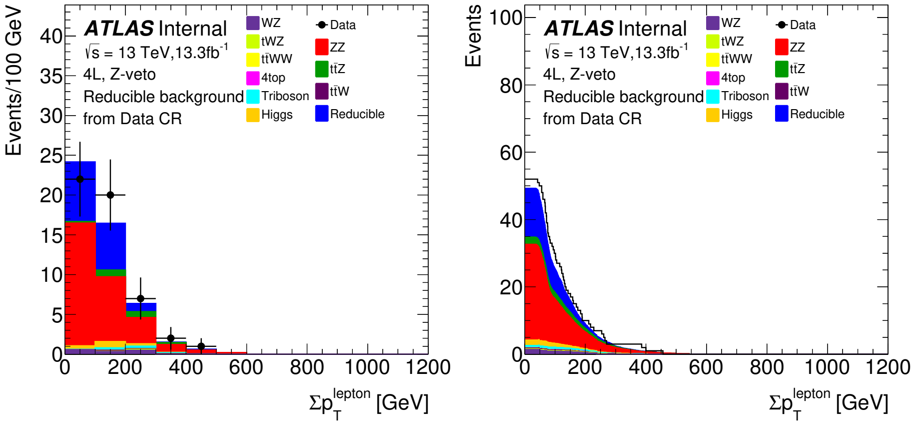

(e) Fake factors on data

(f) Cumulative, FF on data

Figure 5.37: $\sum_i p_{\mathrm{T}}^{\mathrm{lep}}$ distribution(a)(c)(e) and cumulative $\sum_i p_{\mathrm{T}}^{\mathrm{lep}}$ distribution(b)(d)(f) in the 4L low $\sum_i p_{\mathrm{T}}^{\mathrm{lep}}$ VR0. The reducible background is taken directly from MC in (a)(b), from the weighted MC control region yield in (c)(d), and from the weighted data control region yield in (e)(f).

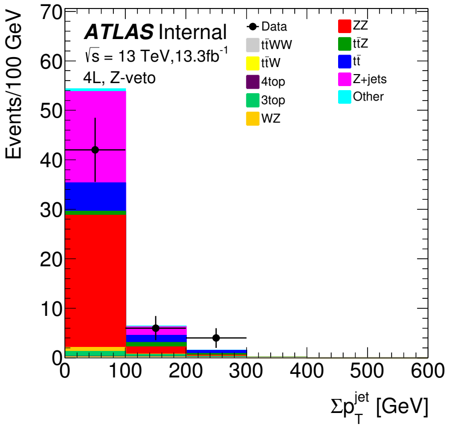

(a) Pure MC

(b) Cumulative, pure MC

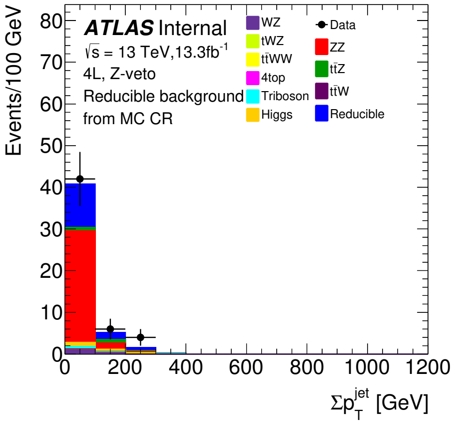

(c) Fake factors on MC

(d) Cumulative, FF on MC

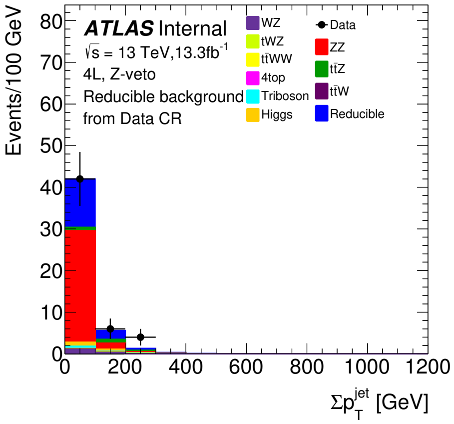

(e) Fake factors on data

(f) Cumulative, FF on data

Figure 5.38: $\sum_i p_{\mathrm{T}}^{\mathrm{jet}}$ distribution(a)(c)(e) and cumulative $\sum_i p_{\mathrm{T}}^{\mathrm{jet}}$ distribution(b)(d)(f) in the 4L low $\sum_i p_{\mathrm{T}}^{\mathrm{jet}}$ VR0. The reducible background is taken directly from MC in (a)(b), from the weighted MC control region yield in (c)(d), and from the weighted data control region yield in (e)(f).

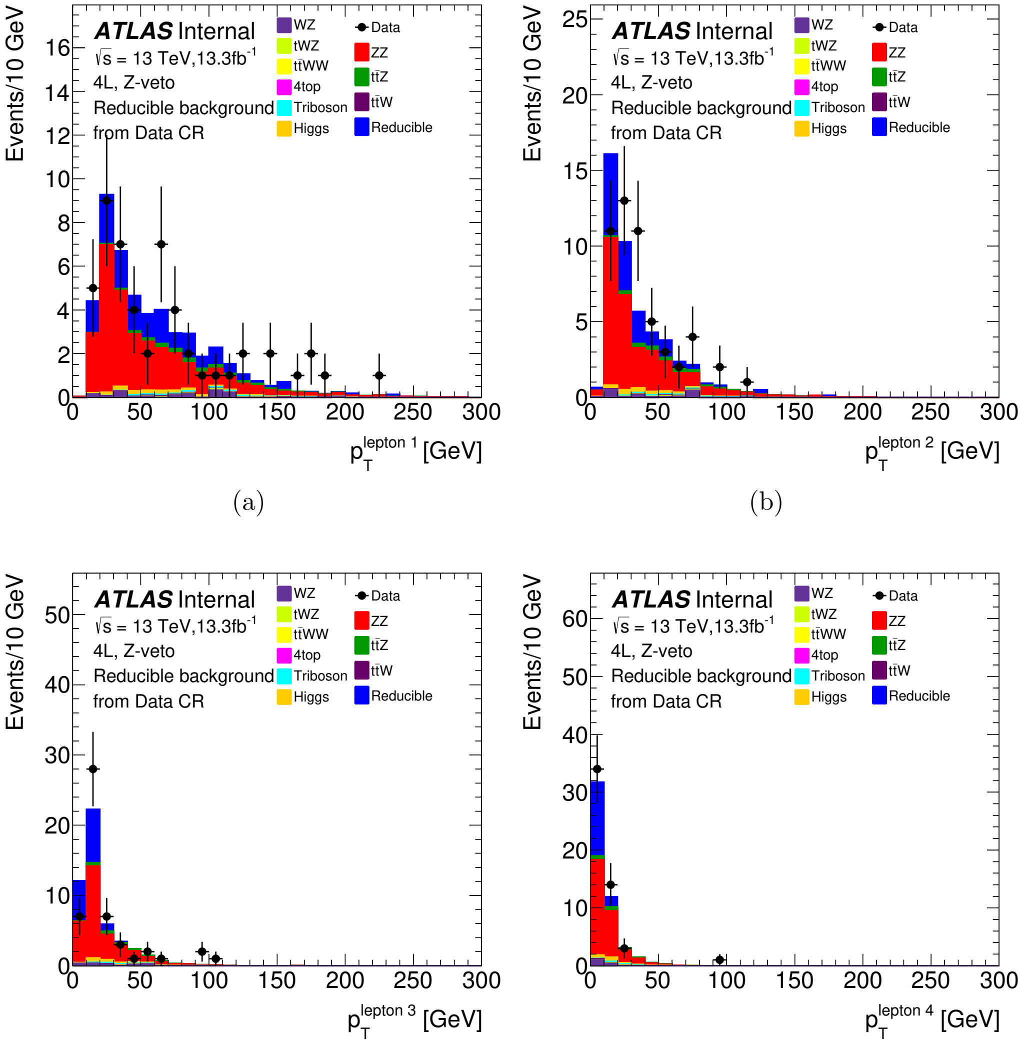

(a) (b)

(c) (d)

Figure 5.39: The p_{T} distributions of the four leptons in the low m_{eff} validation region, using the reducible background measured in data. The leptons are numbered in order of increasing p_{T}.

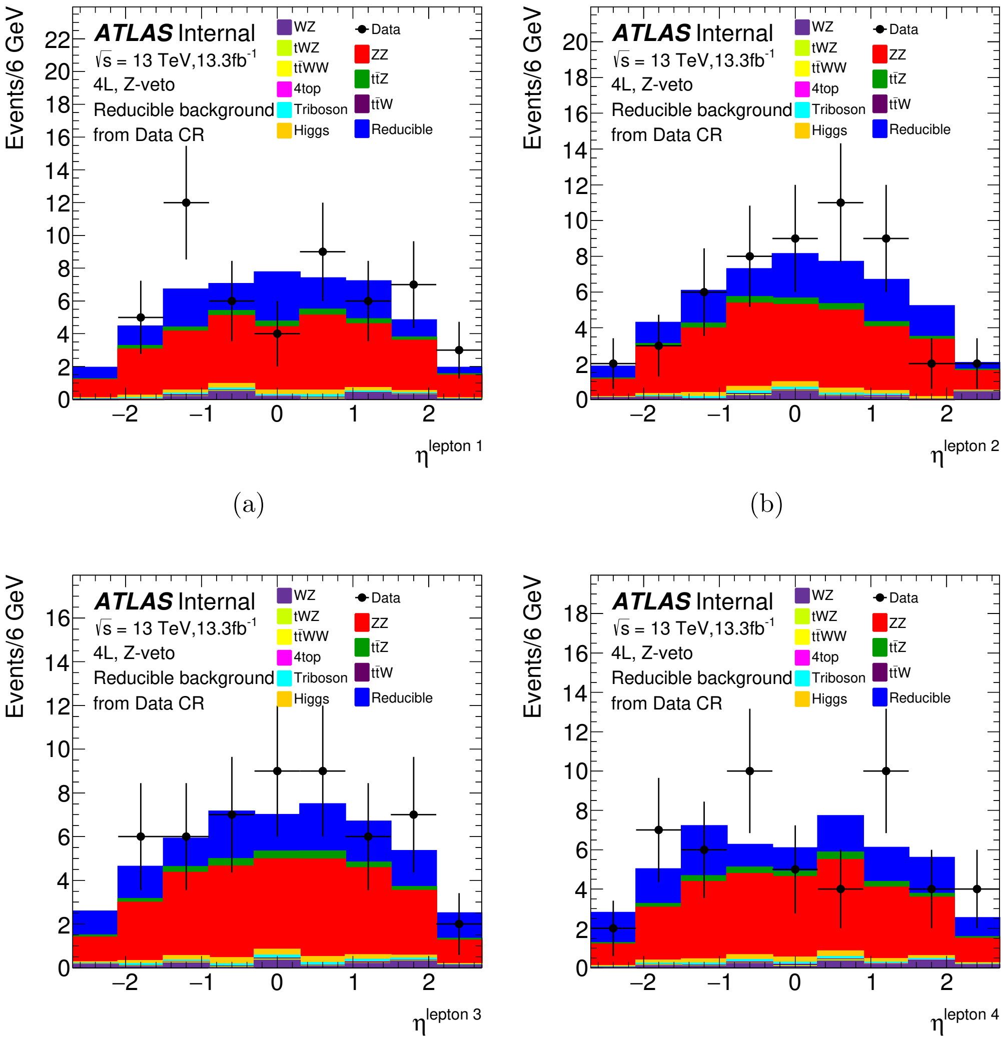

(a) (b)

(c) (d)

Figure 5.40: The η distributions of the four leptons in the low m_{eff} validation region, using the reducible background measured in data. The leptons are numbered in order of increasing p_{T}.

between the expected and observed data; however, for the very lowest mass lepton pairs, there is a slight underprediction. This underprediction at low mass is not expected to be an issue in the high-m_{eff} signal regions, where low mass decays are rare (see Figure 5.42). This is confirmed in Figure 5.42c and Figure 5.42d, where low mass decays in data are also seen to lie at small m_{eff}.

Lastly, in order to peform a comparison in the validation region with higher statistics, the individual electron and muon p_{T} are plotted together in one figure, instead of separating them out individually in Fig. 5.43. Due to the somewhat larger statistics ($> 2\times$), the distributions are not as dominated by statistical uncertainty, allowing for a more meaningful comparison of data and MC. The systematic uncertainties are also included in these plots, including all the detector and theory uncertainties described in section 5.6. Some disagreement is observed in some of the bins, but statistical uncertainties are still large. Further, precise lepton p_{T} modeling is not a requirement for the search, and lepton p_{T} mismodeling is one of the motivators for not performing event selection on $\sum_i p_{\mathrm{T}}^{\mathrm{lep}}$ directly.

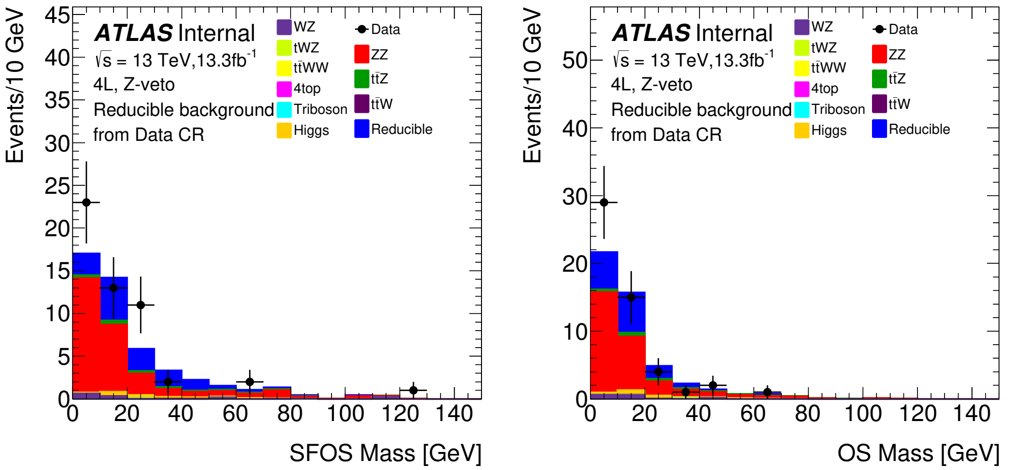

(a) m_{SFOS} in VR0

(b) m_{OS} in VR0

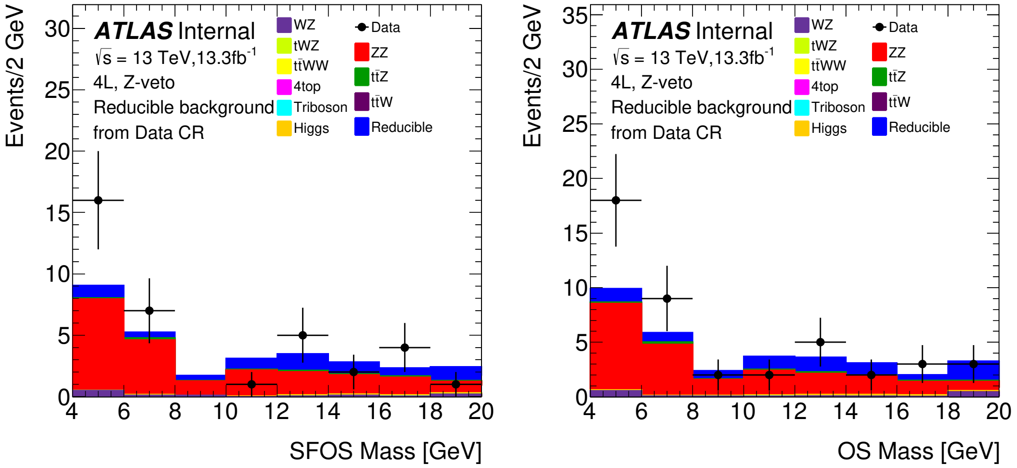

(c) m_{SFOS} in VR0 (zoom)

(d) m_{OS} in VR0 (zoom)

Figure 5.41: Dilepton mass distributions in the low m_{eff} validation region, using the reducible background measured in data. The very low mass region is zoomed in on in (c) and (d).

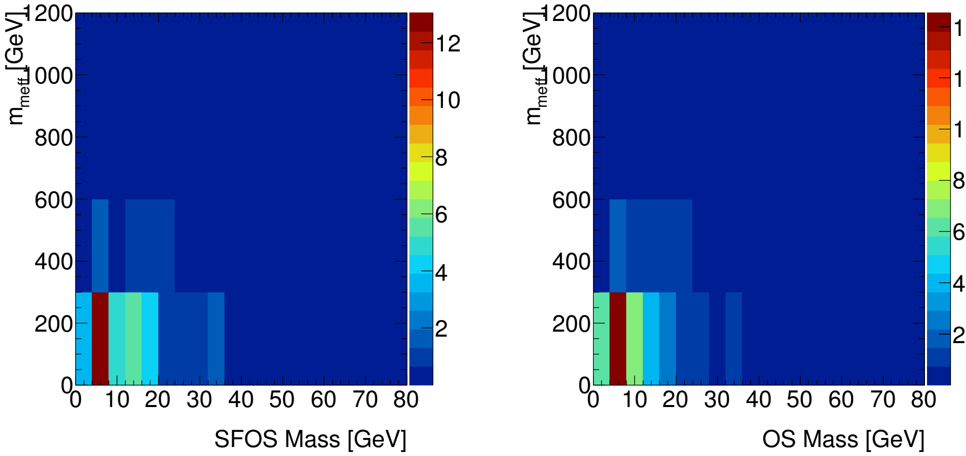

(a) m_{SFOS} vs m_{eff} in MC VR0 events (b) m_{OS} vs m_{eff} in MC VR0 events

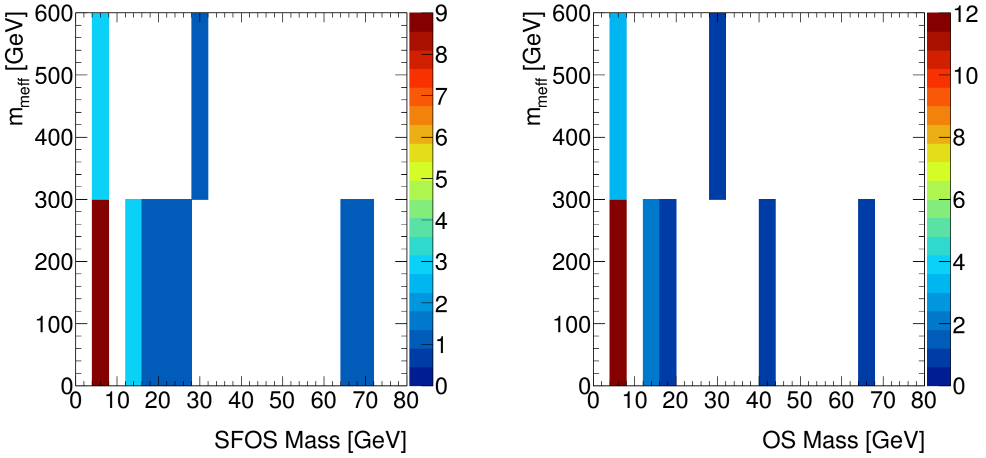

(c) m_{SFOS} vs m_{eff} in data VR0 events (d) m_{OS} vs m_{eff} in data VR0 events

Figure 5.42: Correlation between low invariant mass events and m_{eff} in data and MC.

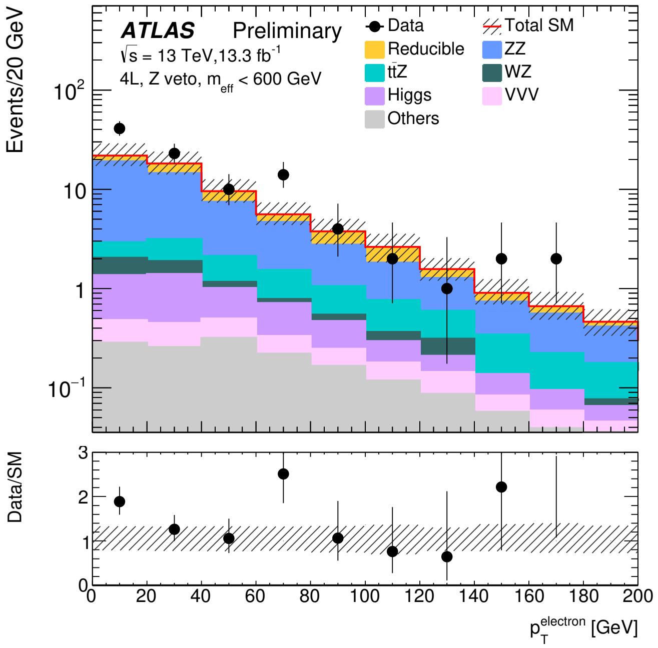

(a)

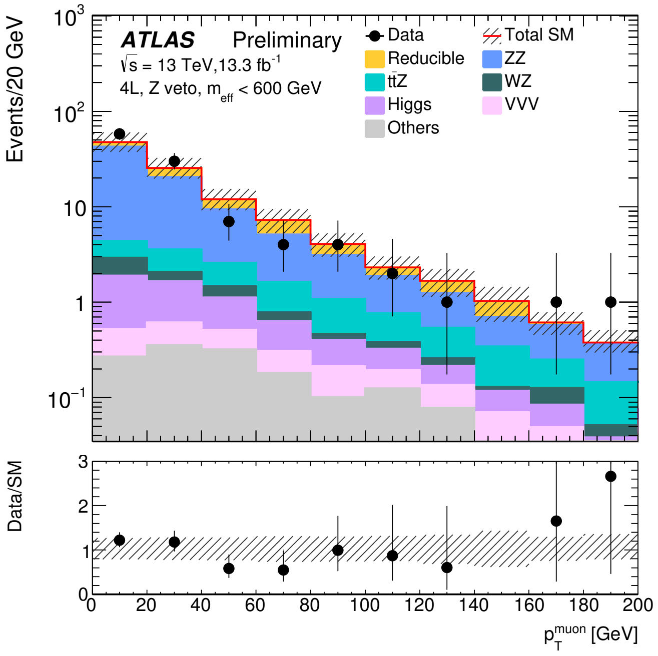

(b)

Figure 5.43: For VR events, (a) the electron p_{T} and (b) the muon p_{T} distributions for data and the estimated SM backgrounds. The irreducible and 1-fake lepton backgrounds are estimated from MC simulation while the 2-fake lepton background is estimated from data. "Others" is the sum of the tWZ, $t\bar{t}WW$, $t\bar{t}t\bar{t}$, $tt\bar{t}$, $t\bar{t}W$, and WWW backgrounds. Both the statistical and systematic uncertainties are included in the shaded band.

5.7.2 Self-consistency Study

Lastly, a final validation of data can be performed through studying its self-consistency. In order to have enough statistics for a meaningful comparison, the Z-veto is removed for these comparisons, and comparisons are shown for both 4L and 2L2l. While this event selection will give a different process composition compared to the normal event selection in the validation region, it is necessary in order to perform a comparison of this type, so that the comparisons are not dominated by statistical uncertainties. In figures where a selection efficiency (ϵ) is plotted, the denominator of the efficiency calculation is the number of events passing the preselection criteria as well as containing at least four baseline leptons. As a result, for example, $\epsilon_{4L} + \epsilon_{3L1l} + \epsilon_{2L2l} + \epsilon_{1L3l} + \epsilon_{4l} = 1$, though only the first and third terms in the sum are actually shown.

The dependence of the selection efficiency on pile-up is compared in Fig. 5.44. In each comparison, the red line corresponds to the average value across the full dataset. With the exception of the first two low-statistics bins, agreement is observed between the different bins, and significant pile-up dependence is not observed. Pile-up thus does not have a significant effect on the search, as the reconstruction of each object type successfully removes the effects of pile-up, for the most part. This is an important (and necessary) observation, since pile-up is not well-modeled. If, for example, the efficiency were observed to increase with pile-up, it would be difficult to argue that pile-up modeling effects were not an issue.

Lastly, the dependence of the yield on run number is compared in Fig. 5.45. This comparison reveals no online or offline problems. In the cases where the total yield is shown, bins are normalized to events per pb^{-1}, since otherwise bin content would be expected to be proportional to the integrated luminosity of each run. Consistency is observed across all the runs, though some of the runs had low integrated luminosity and contain zero events passing the selection criteria. In these figures, all runs up

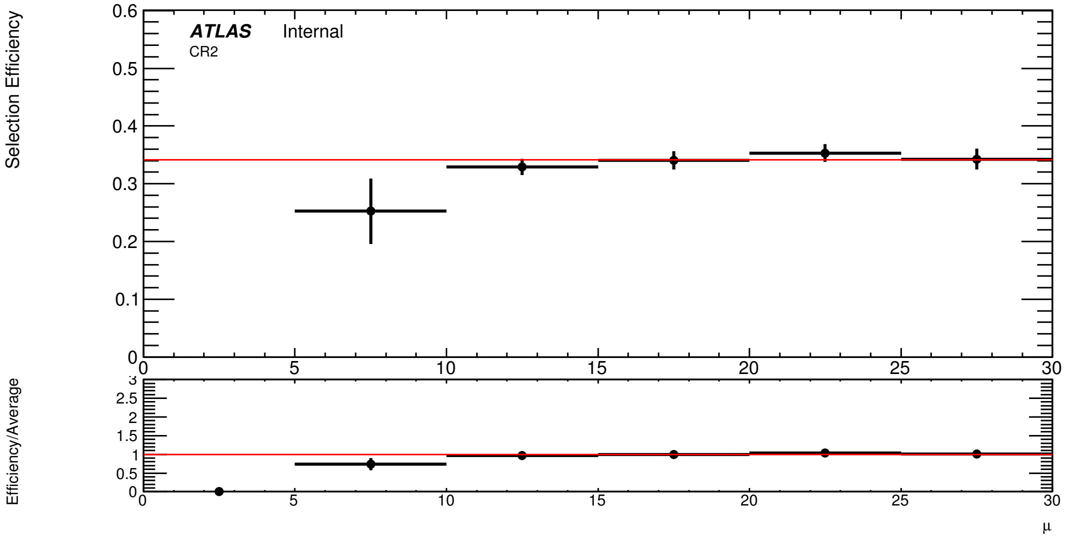

(a) 2L2l

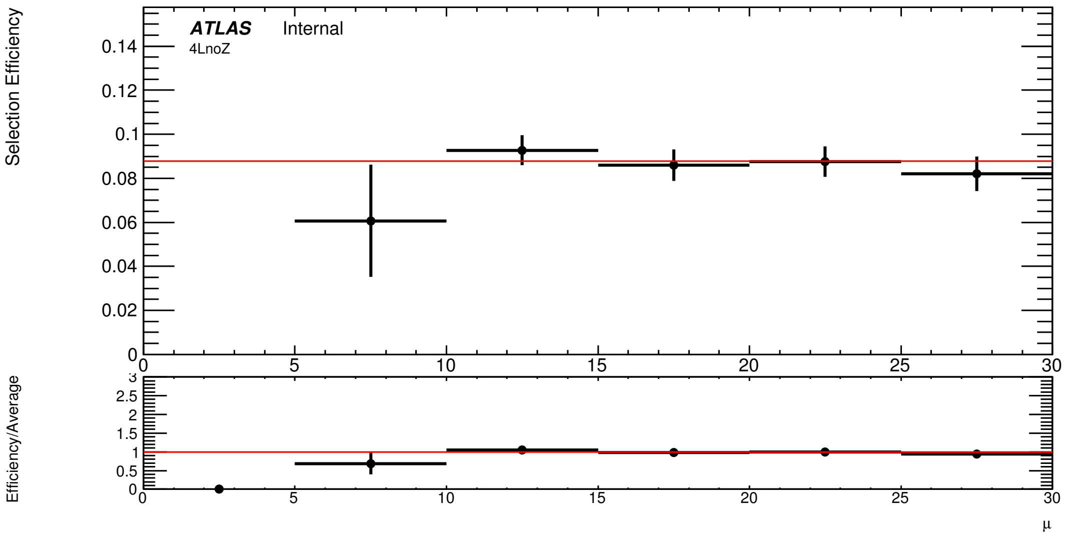

(b) 4L

Figure 5.44: Analysis selection efficiency for 2L2l and 4L as a function of μ.

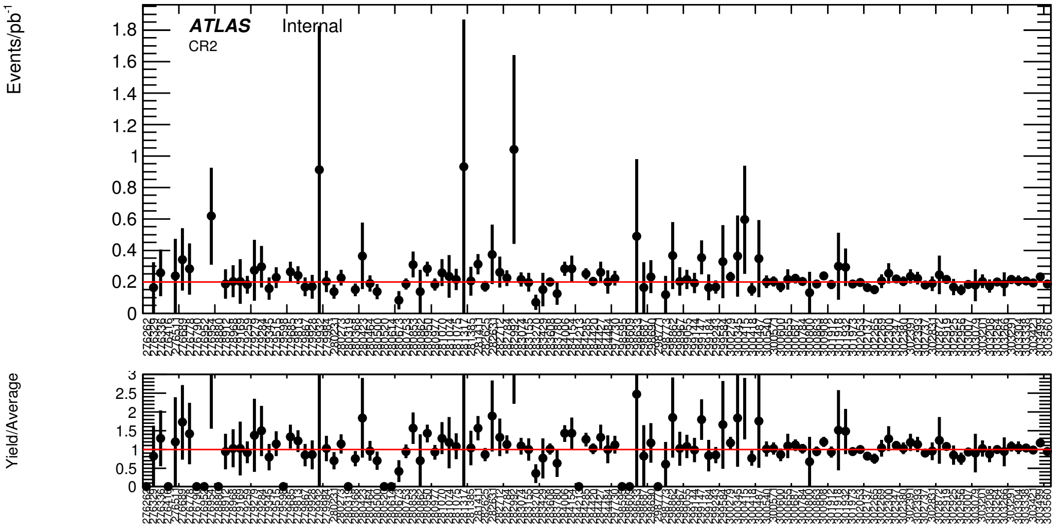

(a) 2L2l

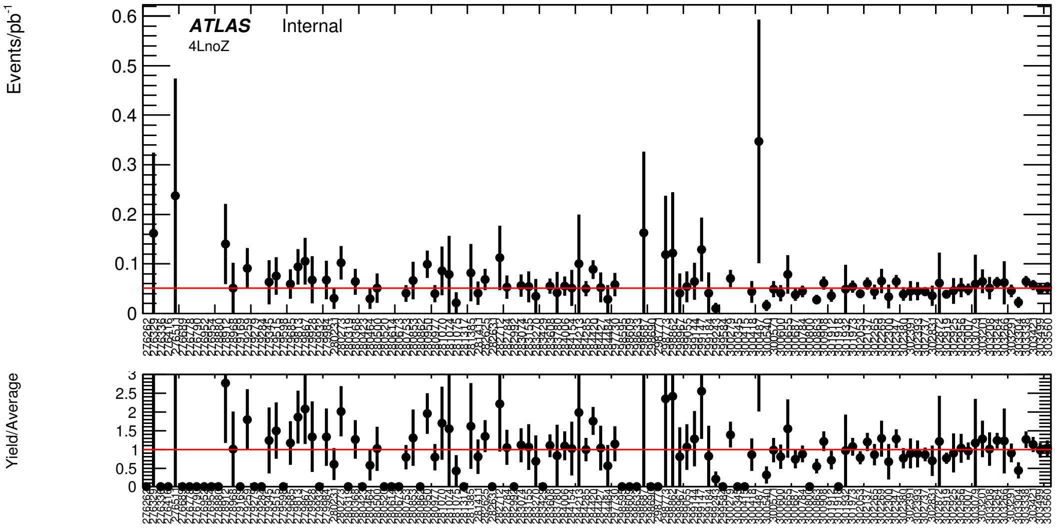

(b) 4L

Figure 5.45: Lumi-normalized yield for 2L2l and 4L as a function of the run number in data.

to and including 284484 corresponding to a total integrated luminosity of 3.2fb^{-1}, collected in 2015, and all runs after correspond to the 10.1fb^{-1} collected in the first half of 2016.

Chapter 6

Results

This section documents the results of the search. The first section (6.1) covers the final yield in the loose (SRA) and tight (SRB) signal regions 5.1, as well as a detailed look at all the signal region events. The second section (6.2) covers the SUSY limits set by the search.

6.1 Final Yields

Two events are observed in SRA, and zero events are observed in SRB. These results are consistent with the SM background and are not consistent with the SUSY models considered in this search. Fig. 6.1 includes a final comparison of the m_{eff} and $E_{\text{T}}^{\text{miss}}$ distributions in the signal regions and control region. The data distributions are found to be consistent with the SM MC distributions, when including the statistical and systematic uncertainties. A sample SUSY signal is shown for reference, which is not consistent with observed distribution.

A summary of the two signal region events is given in Table 6.2. In terms of leptons, the first event includes only muons, and the second event includes only electrons. Also included in the table are the different lepton and jet invariant mass combinations, to see if any combinations of objects are consistent with a mass resonance. Multiple either low mass lepton pairs or pairs of leptons or jets near the Z mass are observed, but it is difficult to draw strong conclusions about the nature of individual events. In the muonic event in particular, all four muons are spatially close

Sample	VR	SRA	SRB
Irreducible			
ZZ	29 ± 5	0.6 ± 0.4	0.20 ± 0.19
$t\bar{t}Z$	2.04 ± 0.23	1.42 ± 0.23	0.47 ± 0.09
Higgs	1.6 ± 1.4	0.4 ± 0.4	0.11 ± 0.11
VVZ	0.72 ± 0.14	0.31 ± 0.07	0.122 ± 0.027
Others	0.27 ± 0.07	0.32 ± 0.04	0.181 ± 0.022
1-fake ℓ reducible	1.14 ± 0.08	0.166 ± 0.018	0.068 ± 0.013
2-fake ℓ reducible	16 ± 6	0.48 ± 0.24	$0.00^{+0.05}_{-0.00}$
Σ SM	50 ± 6	3.6 ± 0.7	1.15 ± 0.26
Data	53	2	0
p_0	—	0.65	0.78
S^{95}_{obs}	—	4.3	3.0
S^{95}_{exp}	—	$5.4^{+1.8}_{-1.3}$	$3.7^{+1.4}_{-0.7}$
$\langle\epsilon\sigma\rangle^{95}_{obs}$ [fb]	—	0.32	0.23
CL$_b$	—	0.20	0.17

Table 6.1: Expected and observed yields for 13.3 fb^{-1} in the 4L validation region (VR) and signal regions (SRA and SRB). "Others" is the sum of the tWZ, $t\bar{t}WW$, $t\bar{t}t\bar{t}$ and $tt\bar{t}$ backgrounds. The final section of the table lists the results of the statistical analysis of the signal region yields, discussed in Section 6.2.

together. Somewhat coincidentally, both events have similar m_{eff} values, differing by 0.3 GeV.

A more detailed conceptual picture of the muonic event can be seen in Fig. 6.2 and Fig. 6.3. Diagrams of the electronic event can be seen in Fig. 6.4 and Fig. 6.5. Fig. 6.2 and Fig. 6.4 show event views in the x-y plane and the r-z plane. A schematic drawing of the inner detector is shown in gray. The EM (hadronic) calorimeter is shown in green (red), and the muon spectrometer is represented with blue. The colors of the tracks shown in each panel correspond to the origin vertex, with primary vertex tracks in red. Electrons are shown in orange, and muons are shown in yellow. Jets are pink, and the $E_{\mathrm{T}}^{\mathrm{miss}}$ direction is displayed as a dotted orange line. Lastly, the yellow dots in the calorimeter represent energy deposits in individual cells.

Fig. 6.3 and Fig. 6.5 show event views in 3D. Cells are shown in green, and electrons and muons are yellow. A cutout of the tile calorimeter is shown in order to give the orientation of the detector. In these figures, the proximity of the different objects can be directly observed.

Run 300863	Event	3089915083	$m_{\mathrm{eff}} = 649.5$	$E_{\mathrm{T}}^{\mathrm{miss}} = 22.5$	
Lepton	flavour	p_{T}	η	ϕ	
1	μ^{+}	77.1	-0.84	-2.9	
2	μ^{-}	56.0	-1.03	-2.5	
3	μ^{+}	41.1	-1.12	-2.4	
4	μ^{-}	15.1	-0.52	-2.3	
$m_{12} = 22.9$	$m_{34} = 5.6$	$m_{14} = 33.2$	$m_{23} = 15.1$	$m_{1234} = 57.3$	
Jet	p_{T}	η	ϕ	JVT	
1	220.4	2.42	0.2	1	
2	128.3	0.73	2.9	0.99	
3	88.9	-0.55	-0.4	0.99	
4	24.6	1.80	1.3	0.95	
$m_{12} = 456.6$	$m_{13} = 594.0$	$m_{14} = 89.4$	$m_{23} = 258.7$	$m_{24} = 100.9$	$m_{34} = 153.8$
Run 302872	Event	3255878142	$m_{\mathrm{eff}} = 649.2$	$E_{\mathrm{T}}^{\mathrm{miss}} = 66.2$	
Lepton	flavour	p_{T}	η	ϕ	
1	e^{+}	179.6	0.09	2.57	
2	e^{-}	115.8	0.38	2.51	
3	e^{-}	88.0	0.78	-0.98	
4	e^{+}	22.2	1.34	-1.23	
$m_{12} = 146.1$	$m_{34} = 202.9$	$m_{13} = 261.7$	$m_{24} = 10.9$	$m_{1234} = 381.4$	
Jet	p_{T}	η	ϕ	JVT	
1	122.6	-0.06	-1.50	1	
2	54.9	-0.54	-0.56	1	
$m_{12} = 84.5$					

Table 6.2: Details of the two events observed in SRA. Energies, momenta and masses are given in GeV. Within each section, the m_{ij} and m_{ijkl} values refer to the invariant mass of the combinations of objects with indices i, j, k, or l.

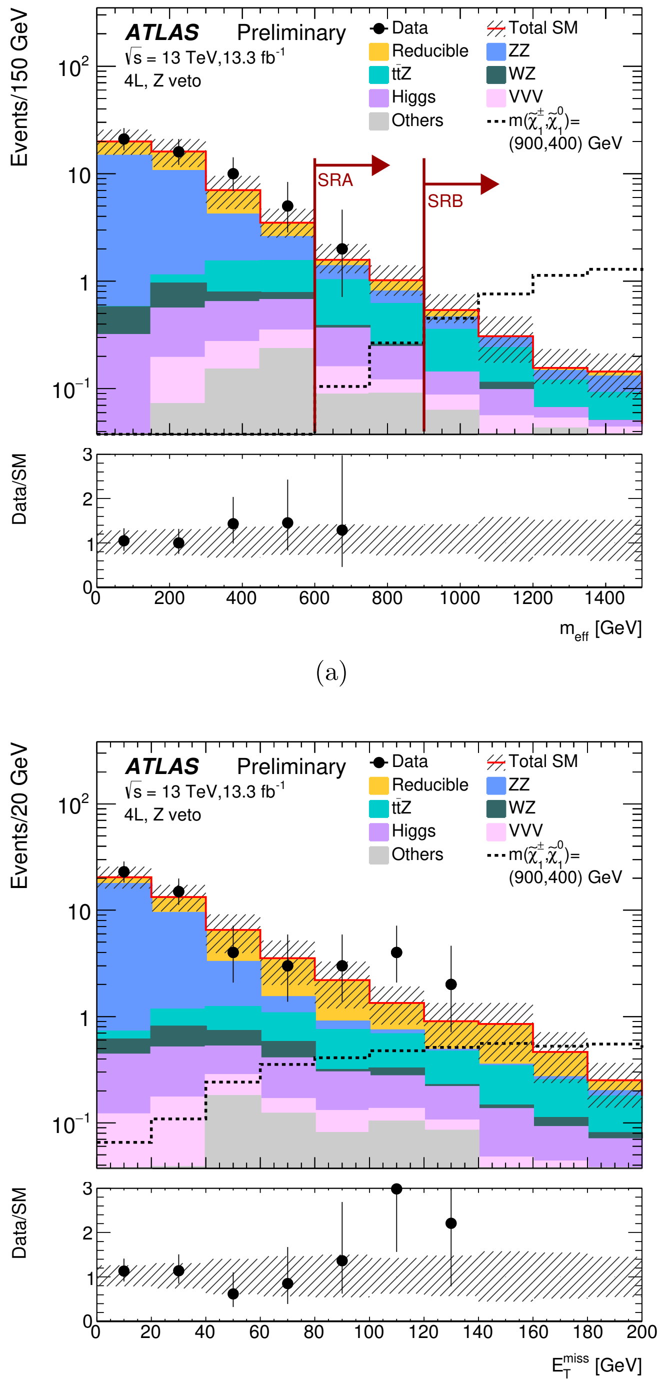

(a)

(b)

Figure 6.1: For four-lepton events with a Z veto requirement, (a) the m_{eff} and (b) the $E_{\text{T}}^{\text{miss}}$ distributions for data, the estimated SM backgrounds, and an example SUSY scenario. “Others” is the sum of the tWZ, $t\bar{t}WW$, $t\bar{t}t\bar{t}$, $tt\bar{t}$, $t\bar{t}W$, and WWW backgrounds. The red arrows indicate the m_{eff} selections in the signal regions.

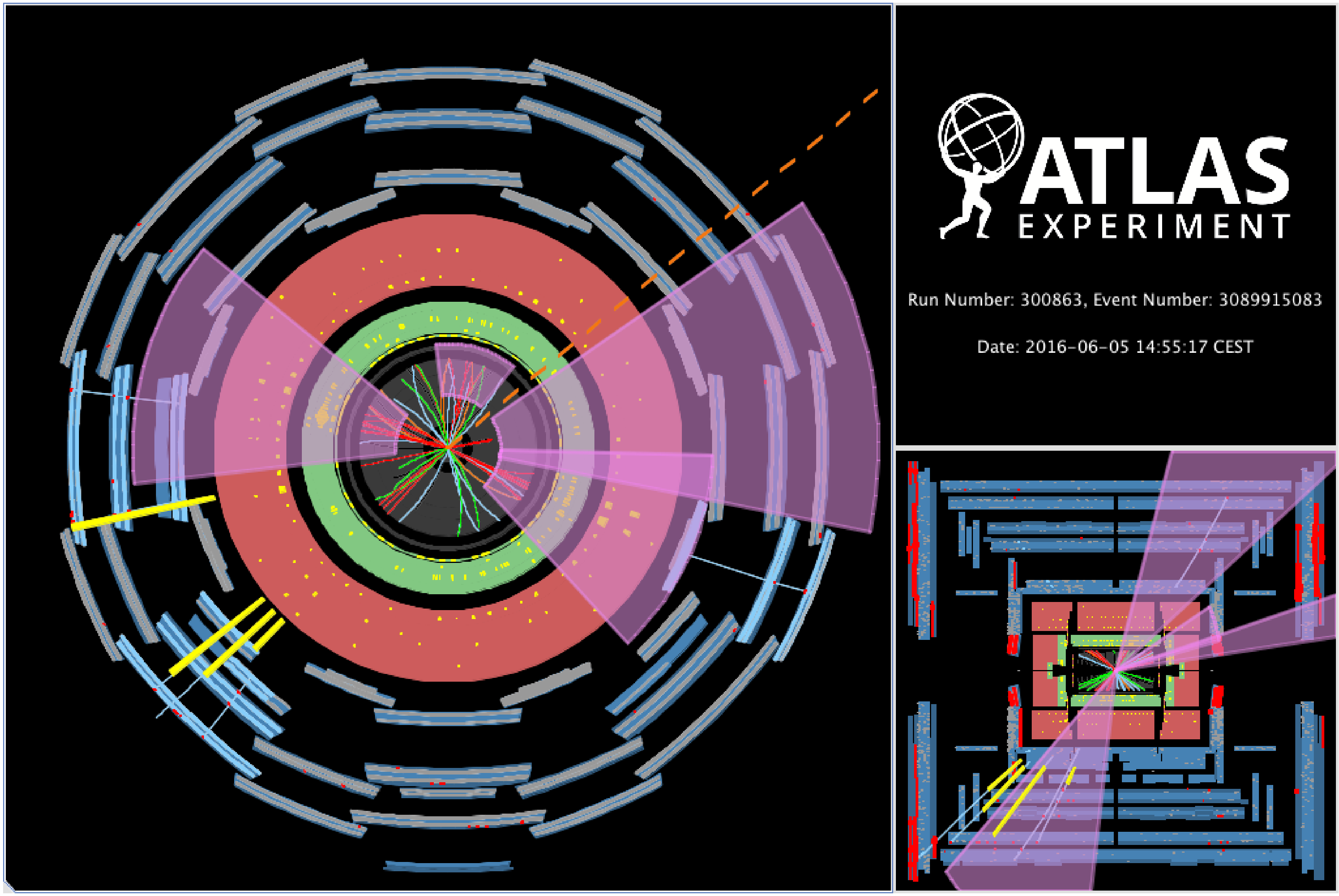

Figure 6.2: ATLANTIS display of Run 300863, Event 3089915083.

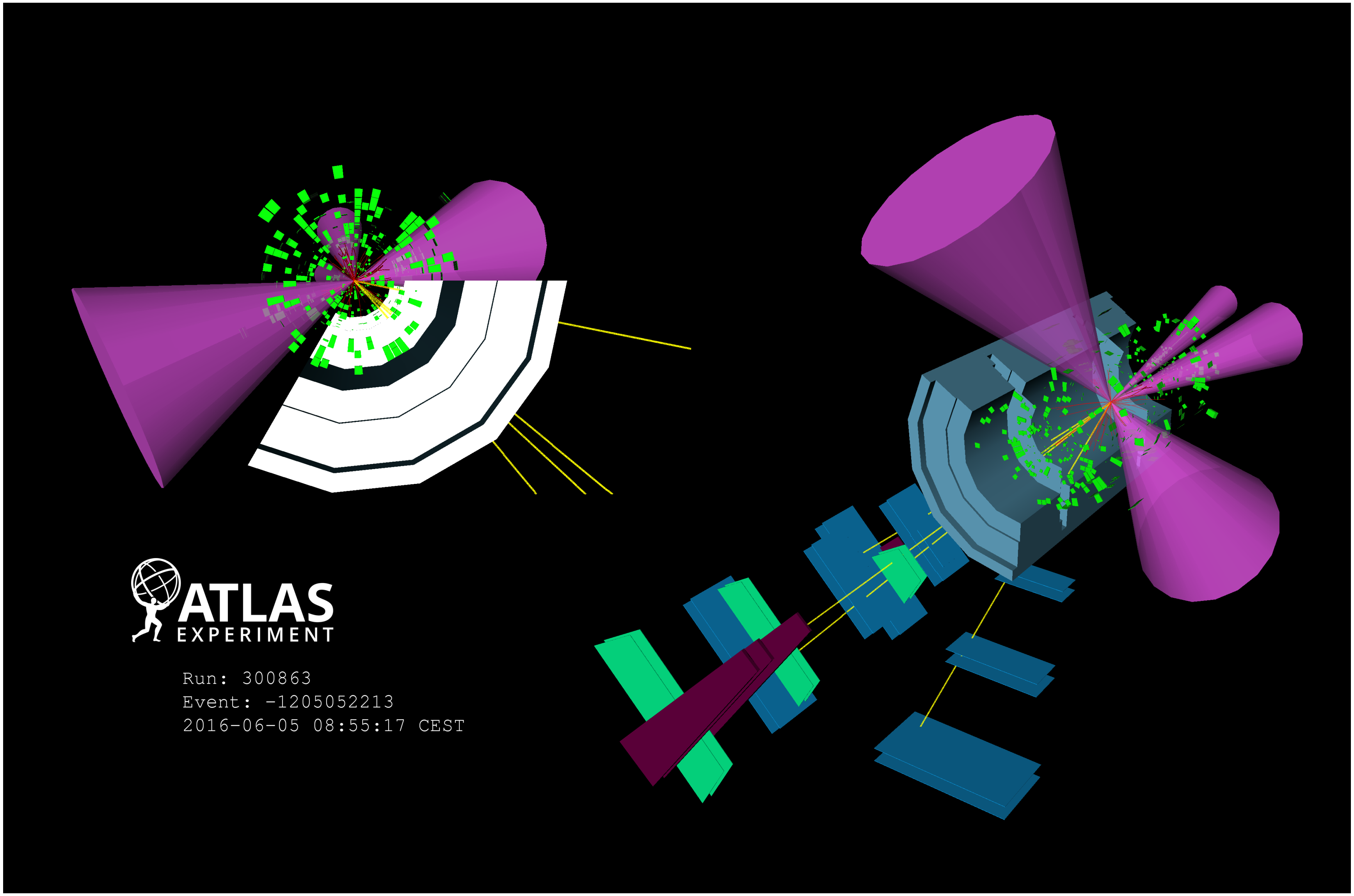

Figure 6.3: VP1 display of Run 300863, Event 3089915083.

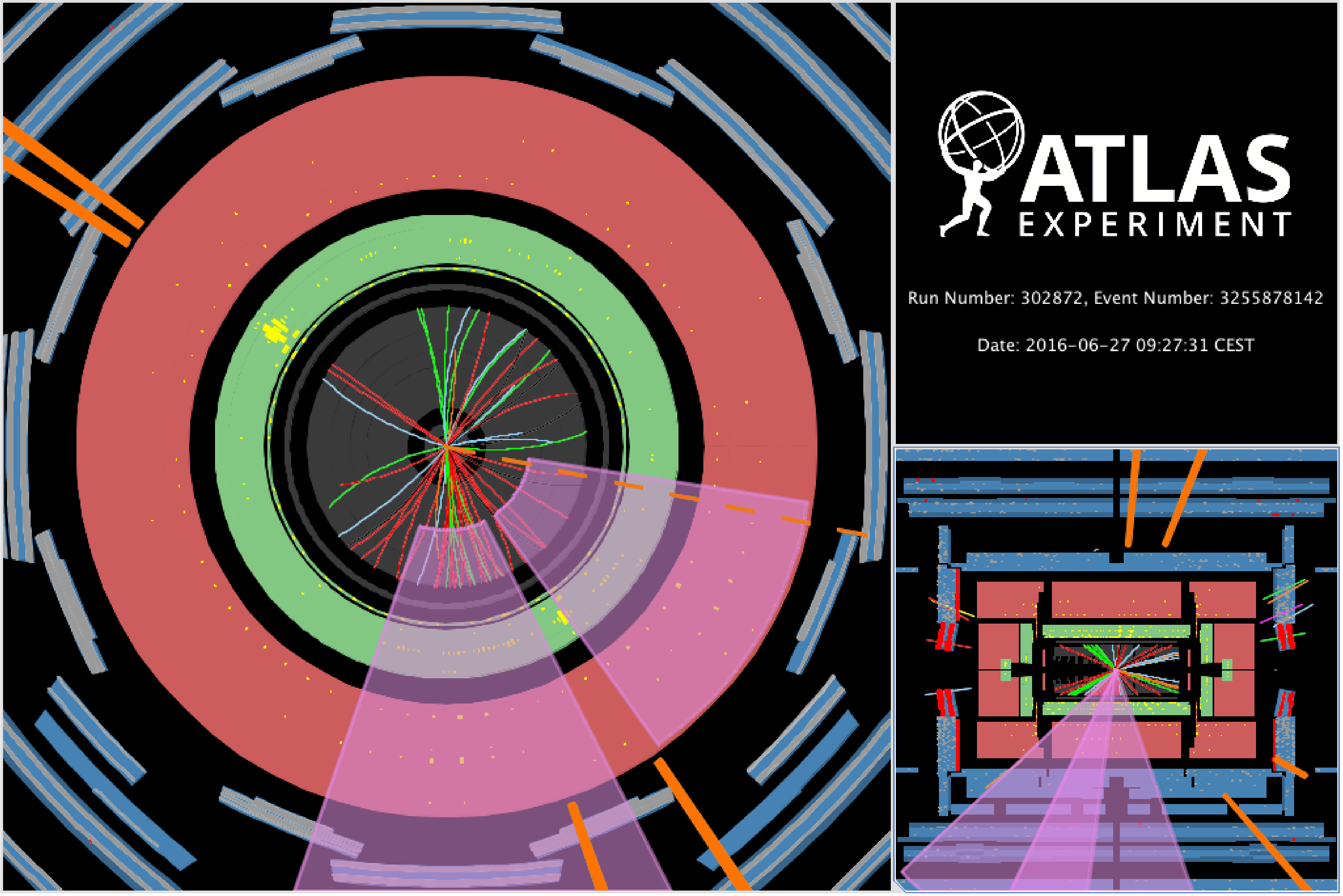

Figure 6.4: ATLANTIS display of Run 302872, Event 3255878142.

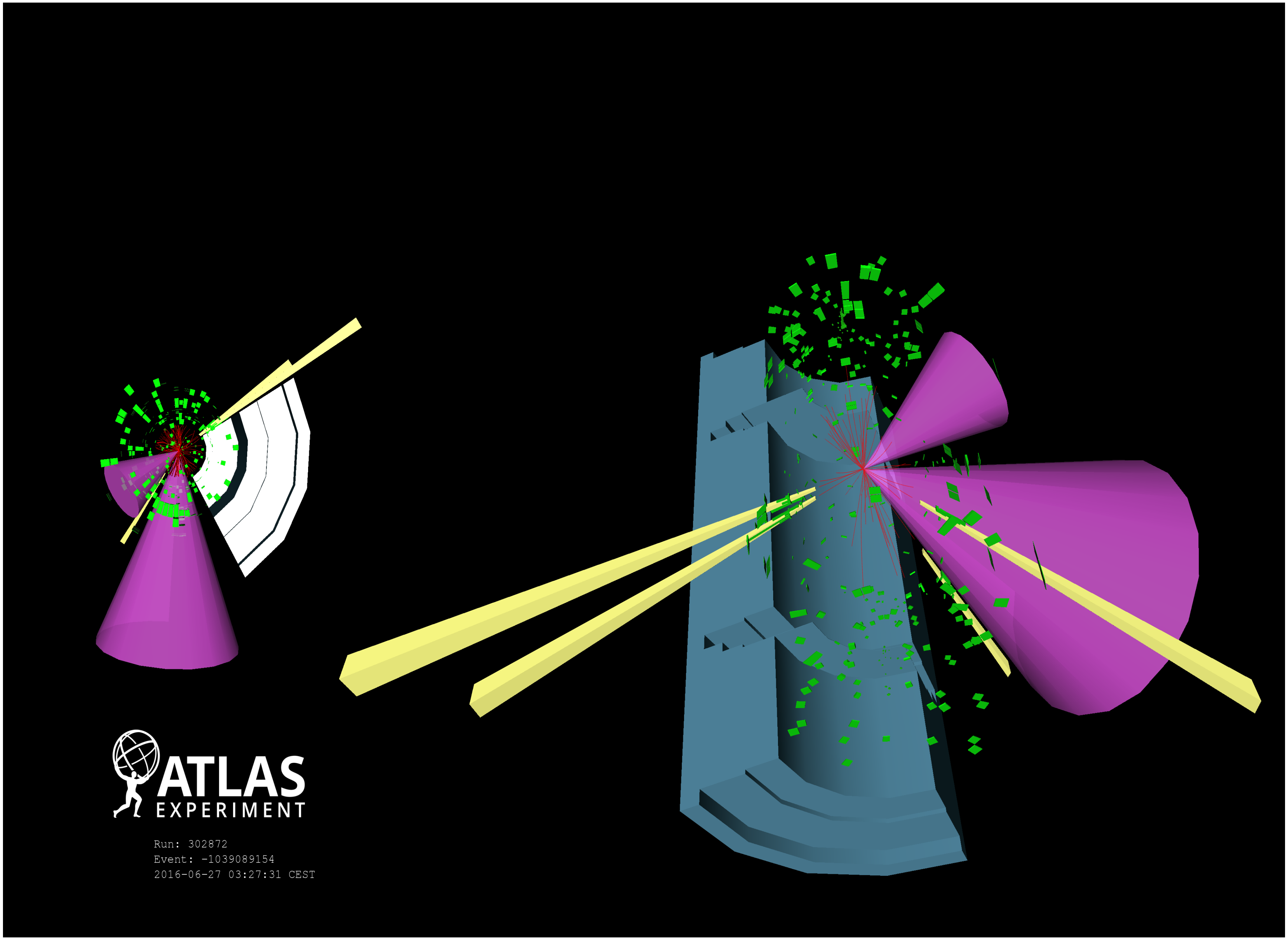

Figure 6.5: VP1 display of Run 302872, Event 3255878142.

6.2 New SUSY Limits

The `HistFitter` [86] software framework is used for the statistical interpretation of the results. The results of the statistical analysis are given in Table 6.1. In order to quantify the probability for the background-only hypothesis to fluctuate to the observed number of events or higher, a one-sided p_0-value is calculated using pseudoexperiments, where the profile likelihood ratio is used as a test statistic [87] to exclude the signal-plus-background hypothesis. For each region, p_0 gives the probability that the predicted SM background alone would result in a signal region yield greater than or equal to the observed yield. The p_0 values can be converted into discovery significance values (Z). Since the observed yields are smaller than the expected yields, the significance values are negative, with $Z_{SRA} = -0.38$ and $Z_{SRA} = -0.76$. S^{95}_{exp} and S^{95}_{obs} are the expected and observed upper limit at 95% CL on the number of beyond-the-SM. $\langle\epsilon\sigma\rangle^{95}_{obs}$ is the observed 95% CL upper limit on the signal cross-section times efficiency, and CL_b is the confidence level for the background-only hypothesis [82].

To set exclusion limits in the $LL\bar{E}12k$ models 2.3.2, the signal region with the best expected exclusion is used. For the exclusion limits, the observed and expected 95% CL limits are calculated using the Asimov dataset for each SUSY model point, taking into account the theoretical and experimental uncertainties on the SM background and the experimental uncertainties on the signal. The impact of the theoretical uncertainties on the signal cross-section is shown for the observed mass limit. Where quoted in the text, the mass limits refer to the observed limit without considering signal cross-section uncertainties.

Figure 6.6 shows the exclusion contour of the $LL\bar{E}12k$ model, which defines the region in $m_{\tilde{\chi}^{\pm}_1}$ versus $m_{\tilde{\chi}^0_1}$ space that is excluded by this study and previous studies. The gray region corresponds to the area excluded during Run 1, and the solid red line defines the region excluded in this study. The dotted red lines define the uncertainty on the limit. The dotted black line and orange band give the expected location of the limit in the absence of a signal. This extends the limits set in Ref. [88] by around 400 GeV. $\tilde{\chi}_1^\pm$ with masses up to 1.14 TeV are excluded for $m_{\tilde{\chi}_1^0} > 500$ GeV. The sensitivity is reduced where the decay products are boosted for large mass splittings between the $\tilde{\chi}_1^\pm$ and the $\tilde{\chi}_1^0$, and $\tilde{\chi}_1^\pm$ masses up to 1.07 TeV are excluded. Figure 6.7 gives the signal region that gives the best exclusion for each signal point. SRB is used for every grid point with $m_{\tilde{\chi}_1^\pm} > 500$ GeV [82]. This behavior is expected, as SRB was designed around the optimization of this particular signal grid [82].

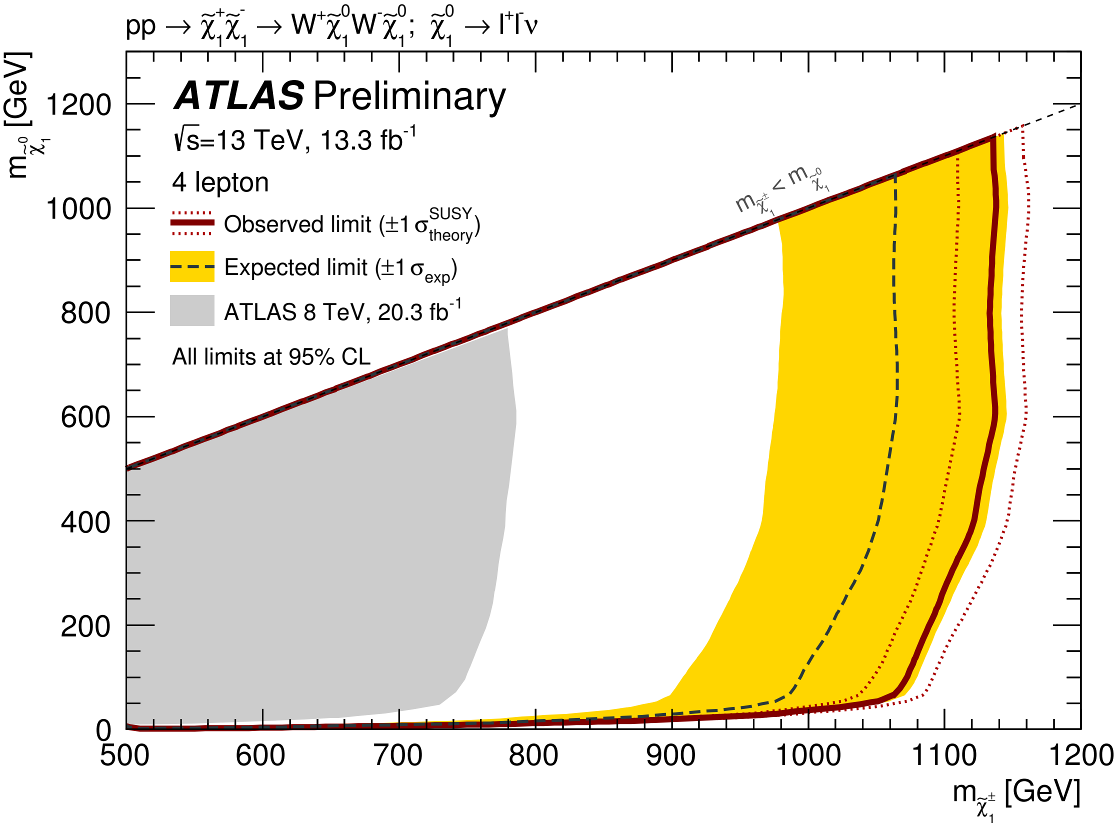

Figure 6.6: The 95% CL exclusion limits on chargino production with indirect RPV decays via λ_{12k}, where $k \in 1, 2$. The limits are set using the SR with the best expected exclusion. The 8 TeV limit from from Ref. [88] is also shown.

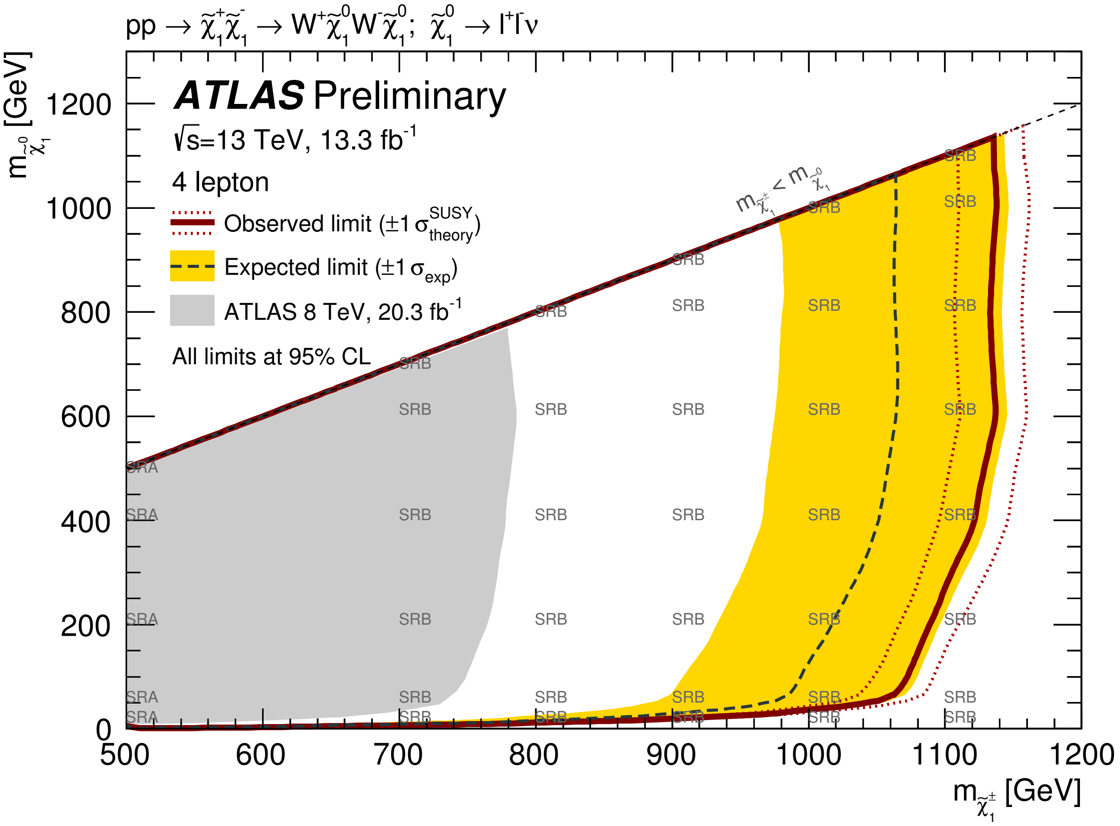

Figure 6.7: The signal region with the best expected exclusion power at each point in the signal grid.

Chapter 7

Conclusion

As of August 2016, a SUSY signal has not been observed by the ATLAS experiment. However, ATLAS searches in 2015 and 2016 have improved SUSY limits and eliminated large regions of the available SUSY phase space. A summary of the limits placed on different SUSY models before Run 2 is shown in Fig. 7.1. An updated set of limits is shown in Fig. 7.2, highlighting the searches that have produced new results in Run 2.

While a SUSY signal has not been discovered, large regions of phase space are still available, and the search for SUSY will continue through Run 2 and beyond. For the four lepton SUSY search, an increased integrated luminosity will allow for the consideration of a broader set of possible SUSY models that result in high lepton multiplicity final states.

Beyond the current Run 2 and the planned Run 3, the LHC will be upgraded to the HL-LHC (High Luminosity LHC), with a projected 10× higher instantaneous luminosity than Run 2. The low SM background and general pile-up independence of the four lepton search will allow for the ability to probe models with much lower cross-sections, and it is still possible that a SUSY signal will be discovered in the future. Nevertheless, as of August 2016, SUSY has not been discovered in any ATLAS search.

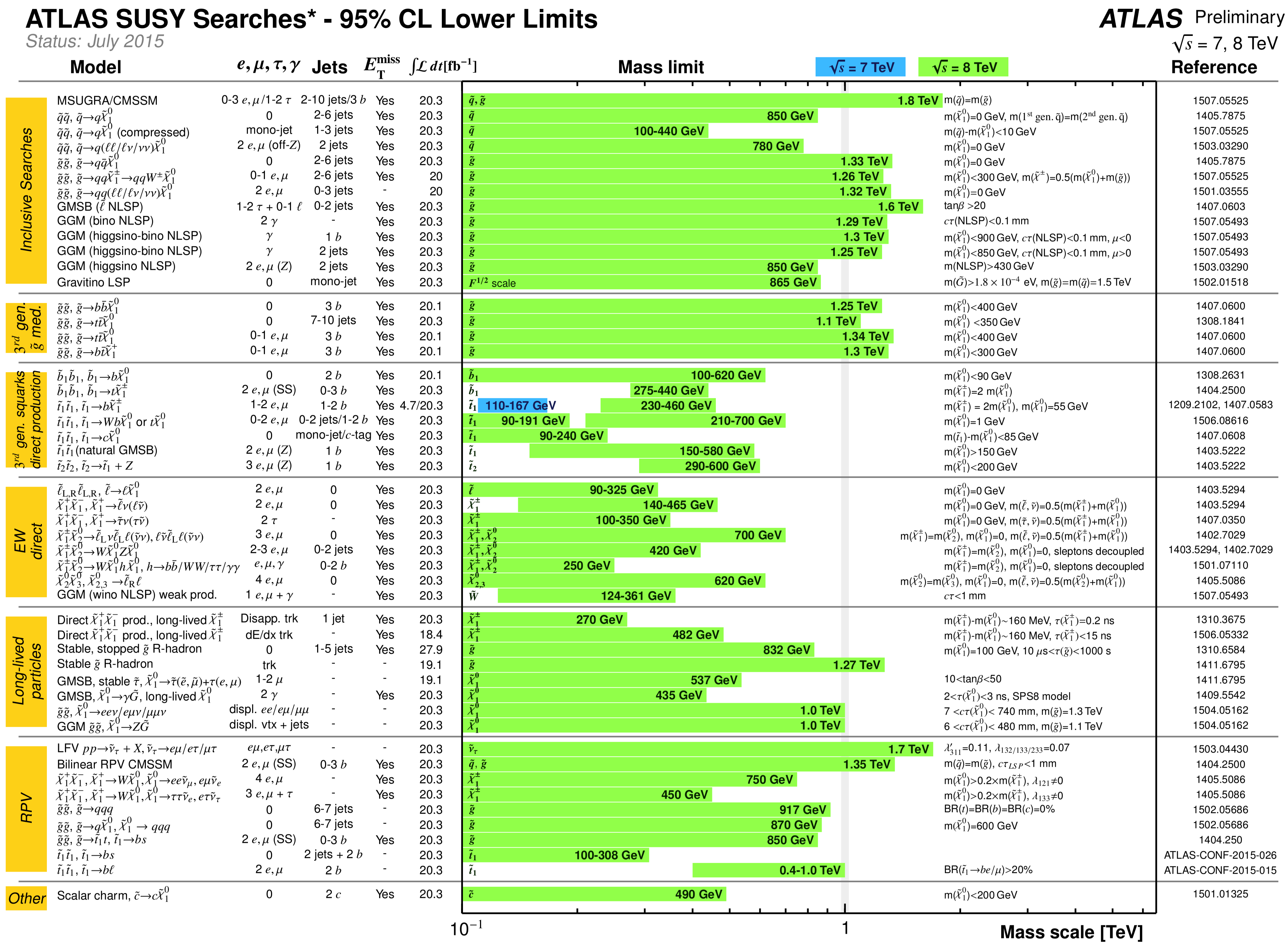

*Only a selection of the available mass limits on new states or phenomena is shown. All limits quoted are observed minus 1σ theoretical signal cross section uncertainty.

Figure 7.1: Overview of the limits set by ATLAS SUSY searches as of July 2015.

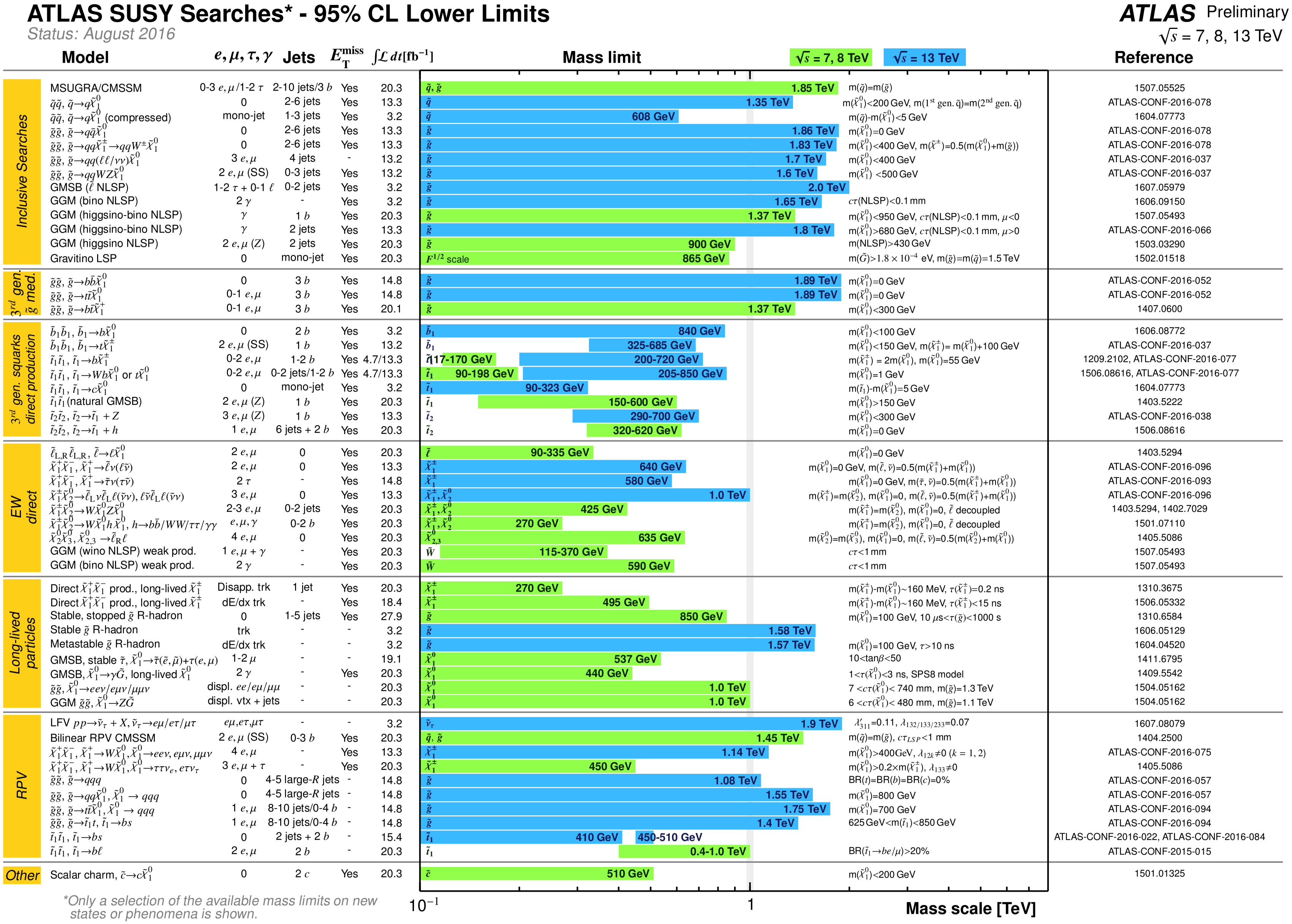

Figure 7.2: Overview of the limits set by ATLAS SUSY searches as of August 2016. The limits set by this search correspond to the third row of the RPV section.

Bibliography

[1] L. Evans and P. Bryant, *LHC Machine,* JINST **3** (2008) S08001, ed. by L. Evans.

[2] A. Collaboration et al., *A particle consistent with the Higgs boson observed with the ATLAS detector at the Large Hadron Collider*, Science **338**.6114 (2012) pp. 1576–1582.

[3] L. G. Ē. SHELDON, *Partial-symmetries of weak interactions*, Selected Papers on Gauge Theory of Weak and Electromagnetic Interactions (1981) p. 171.

[4] M.-Y. Han and Y. Nambu, *Three-triplet model with double SU (3) symmetry*, Physical Review **139**.4B (1965) B1006.

[5] D. D. B. Deschizeaux et al., *Determination of the Number of Light Neutrino Species* (1989).

[6] D. Griffiths, *Introduction to Elementary Particles*, 2004.

[7] H. Baer and X. Tata, *Weak scale supersymmetry: From superfields to scattering events*, Cambridge University Press, 2006.

[8] R. Aaij et al., *Observation of J/ψ p Resonances Consistent with Pentaquark States in Λ b 0$\rightarrow$ J/ψ K- p Decays*, Physical review letters **115**.7 (2015) p. 072001.

[9] M. Srednicki, *Quantum field theory*, Cambridge University Press, 2007.

[10] D. J. Gross and F. Wilczek, *Ultraviolet behavior of non-abelian gauge theories*, Physical Review Letters **30**.26 (1973) p. 1343.

[11] H. D. Politzer, *Reliable perturbative results for strong interactions?* Physical Review Letters **30**.26 (1973) p. 1346.

[12] P. D. Group et al., *REVIEW OF PARTICLE PHYSICS Particle Data Group*, Chinese physics. C, High energy physics and nuclear physics **38**.9 (2014) p. 090001.

[13] P. W. Higgs, *Broken symmetries and the masses of gauge bosons*, Physical Review Letters **13**.16 (1964) p. 508.

[14] S. Weinberg, *Mixing angle in renormalizable theories of weak and electromagnetic interactions*, Physical Review D **5**.8 (1972) p. 1962.

[15] N. Cabibbo, *Unitary symmetry and leptonic decays*, Physical Review Letters **10**.12 (1963) p. 531.

[16] M. Kobayashi and T. Maskawa, *CP-violation in the renormalizable theory of weak interaction*, Progress of Theoretical Physics **49**.2 (1973) pp. 652–657.

[17] B. Abbott et al., *GW151226: Observation of gravitational waves from a 22-solar-mass binary black hole coalescence*, Physical Review Letters **116**.24 (2016) p. 241103.

[18] R. Davis Jr, D. S. Harmer, and K. C. Hoffman, *Search for neutrinos from the sun*, Physical Review Letters **20**.21 (1968) p. 1205.

[19] J Schechter and J. W. Valle, *Neutrino masses in SU (2)xU (1) theories*, Physical Review D **22**.9 (1980) p. 2227.

[20] G. Bertone, D. Hooper, and J. Silk, *Particle dark matter: Evidence, candidates and constraints*, Physics Reports **405**.5 (2005) pp. 279–390.

[21] T. Mannel, *Theory and Phenomenology of CP Violation*, Nuclear Physics B-Proceedings Supplements **167** (2007) pp. 170–174.

[22] M. P. Hobson, G. P. Efstathiou, and A. N. Lasenby, *General relativity: an introduction for physicists*, Cambridge University Press, 2006.

[23] M. Gell-Mann and F. E. Low, *Quantum electrodynamics at small distances*, Physical Review **95**.5 (1954) p. 1300.

[24] H. Georgi and S. L. Glashow, *Unity of all elementary-particle forces*, Physical Review Letters **32**.8 (1974) p. 438.

[25] J. M. LoSecco, F. Reines, and D. Sinclair, *The search for proton decay*, Scientific American **252** (1985) pp. 54–62.

[26] S. Dimopoulos and H. Georgi, *Softly broken supersymmetry and SU (5)*, Nuclear Physics B **193**.1 (1981) pp. 150–162.

[27] R. Barbieri and G. F. Giudice, *Upper bounds on supersymmetric particle masses*, Nuclear Physics B **306**.1 (1988) pp. 63–76.

[28] P. Nath and R Arnowitt, *Generalized super-gauge symmetry as a new framework for unified gauge theories*, Physics Letters B **56**.2 (1975) pp. 177–180.

[29] S. P. Martin, *Some simple criteria for gauged R parity*, Physical Review D **46**.7 (1992) R2769.

[30] A. H. Chamseddine, R. Arnowitt, and P. Nath, *Locally supersymmetric grand unification*, Physical Review Letters **49**.14 (1982) p. 970.

[31] R. Barbier et al., *R-Parity-violating supersymmetry*, Physics reports **420**.1 (2005) pp. 1–195.

[32] A. Y. Smirnov and F. Vissani, *Upper bound on all products of R-parity violating couplings* λ*' and* λ *"from proton decay*, Physics Letters B **380**.3 (1996) pp. 317–323.

[33] ATLAS Collaboration, *Constraints on promptly decaying supersymmetric particles with lepton-number- and R-parity-violating interactions using Run-1 ATLAS data*, ATLAS-CONF-2015-018, 2015, URL: http://cdsweb.cern.ch/record/2017303.

[34] R. D. Ball et al., *Parton distributions with LHC data*, Nuclear Physics B **867**.2 (2013) pp. 244–289.

[35] J. Pumplin et al., *New generation of parton distributions with uncertainties from global QCD analysis*, Journal of High Energy Physics **2002**.07 (2002) p. 012.

[36] H.-L. Lai et al., *New parton distributions for collider physics*, Physical Review D **82**.7 (2010) p. 074024.

[37] S. Myers, *The LEP Collider, from design to approval and commissioning*, John Adams' Lecture, Delivered at CERN, 26 Nov 1990, Geneva: CERN, 1991, URL: https://cds.cern.ch/record/226776.

[38] ATLAS Collaboration, *The ATLAS Experiment at the CERN Large Hadron Collider*, JINST **3** (2008) S08003.

[39] C. Collaboration, R Adolphi, et al., *The CMS experiment at the CERN LHC*, JInst **3**.08 (2008) S08004.

[40] E Vercellin, A. Collaboration, et al., *The ALICE experiment at the LHC*, Nuclear Physics A **805**.1 (2008) pp. 511c–518c.

[41] L. Collaboration et al., *The LHCb experiment at the CERN LHC*, JINST **3** (2008) S08005.

[42] V. Avati, *The TOTEM Experiment at the LHC*, Progress of Theoretical Physics Supplement **187** (2011) pp. 281–288.

[43] O. Adriani et al., *The LHCf detector at the CERN large hadron collider*, Journal of Instrumentation **3**.08 (2008) S08006.

[44] J. L. Pinfold, "The MoEDAL experiment at the LHC," *EPJ Web of Conferences*, vol. 71, EDP Sciences, 2014 p. 00111.

[45] A. Team, "The four main LHC experiments," 1999, URL: https://cds.cern.ch/record/40525.

[46] P. Lebrun, *Interim Summary Report on the Analysis of the 19 September 2008 Incident at the LHC*, CERN EDMS document 973073 (2008).

[47] ATLAS Collaboration, *Improved luminosity determination in pp collisions at* $\sqrt{s} = 7$ *TeV using the ATLAS detector at the LHC*, Eur. Phys. J. C **73** (2013) p. 2518, arXiv: 1302.4393 [hep-ex].

[48] ATLAS Collaboration, *Luminosity determination in pp collisions at* $\sqrt{s} = 8$ *TeV using the ATLAS detector at the LHC* (2016), arXiv: 1608.03953 [hep-ex].

[49] *Total Integrated Luminosity and Data Quality in 2011 and 2012*, https://twiki.cern.ch/twiki/bin/view/AtlasPublic/LuminosityPublicResults.

[50] *Total Integrated Luminosity and Data Quality in 2015*, https://twiki.cern.ch/twiki/bin/view/AtlasPublic/LuminosityPublicResultsRun2.

[51] *Total Integrated Luminosity in 2016*, https://twiki.cern.ch/twiki/bin/view/AtlasPublic/LuminosityPublicResultsRun2.

[52] M Capeans et al., "ATLAS Insertable B-Layer Technical Design Report," tech. rep. CERN-LHCC-2010-013. ATLAS-TDR-19, 2010, URL: https://cds.cern.ch/record/1291633.

[53] ATLAS Collaboration, *A neural network clustering algorithm for the ATLAS silicon pixel detector*, JINST **9** (2014) P09009, arXiv: 1406.7690 [hep-ex].

[54] ATLAS Collaboration, *Performance of the ATLAS Inner Detector Track and Vertex Reconstruction in the High Pile-Up LHC Environment*, ATLAS-CONF-2012-042, 2012, URL: https://cdsweb.cern.ch/record/1435196.

[55] "Early Inner Detector Tracking Performance in the 2015 data at $\sqrt{s} = 13$ TeV," tech. rep. ATL-PHYS-PUB-2015-051, CERN, 2015, URL: https://cds.cern.ch/record/2110140.

[56] ATLAS Collaboration, *Electron efficiency measurements with the ATLAS detector using the 2012 LHC proton–proton collision data*, ATLAS-CONF-2014-032, 2014, URL: http://cdsweb.cern.ch/record/1706245.

[57] W Lampl et al., *Calorimeter Clustering Algorithms: Description and Performance*, ATL-LARG-PUB-2008-002, 2008, URL: https://cds.cern.ch/record/1099735.

[58] ATLAS Collaboration, *Muon reconstruction performance of the ATLAS detector in proton–proton collision data at* $\sqrt{s} = 13$ *TeV*, Eur. Phys. J. C **76** (2016) p. 292, arXiv: 1603.05598 [hep-ex].

[59] M Červ, *The ATLAS Diamond Beam Monitor*, Journal of Instrumentation **9**.02 (2014) p. C02026.

[60] "2015 start-up trigger menu and initial performance assessment of the ATLAS trigger using Run-2 data," tech. rep. ATL-DAQ-PUB-2016-001, CERN, 2016, URL: https://cds.cern.ch/record/2136007.

[61] G. Aad et al., *The ATLAS simulation infrastructure*, The European Physical Journal C **70**.3 (2010) pp. 823–874.

[62] ATLAS Collaboration, *Improved electron reconstruction in ATLAS using the Gaussian Sum Filter-based model for bremsstrahlung*, ATLAS-CONF-2012-047, 2012, URL: http://cdsweb.cern.ch/record/1449796.

[63] "Electron efficiency measurements with the ATLAS detector using the 2015 LHC proton-proton collision data," tech. rep. ATLAS-CONF-2016-024, CERN, 2016, URL: http://cds.cern.ch/record/2157687.

[64] M. Cacciari, G. P. Salam, and G. Soyez, *The anti-k_t jet clustering algorithm*, JHEP **0804** (2008) p. 063, arXiv: 0802.1189 [hep-ph].

[65] M. Cacciari, G. P. Salam, and G. Soyez, *The Catchment Area of Jets*, JHEP **0804** (2008) p. 005, arXiv: 0802.1188 [hep-ph].

[66] ATLAS Collaboration, *Pile-up subtraction and suppression for jets in ATLAS*, ATLAS-CONF-2013-083, 2013, URL: https://cds.cern.ch/record/1570994.

[67] ATLAS Collaboration, *Jet energy measurement with the ATLAS detector in proton-proton collisions at $\sqrt{s} = 7$ TeV*, Eur. Phys. J. **C73** (2013) p. 2304, arXiv: 1112.6426 [hep-ex].

[68] ATLAS Collaboration, *Tagging and suppression of pileup jets with the ATLAS detector*, ATLAS-CONF-2014-018, 2014, URL: https://cds.cern.ch/record/1700870.

[69] A. Hoecker et al., *TMVA: Toolkit for Multivariate Data Analysis*, PoS **ACAT** (2007) p. 040, arXiv: physics/0703039.

[70] B. Brunt et al., "Performance of missing transverse momentum reconstruction with the ATLAS detector using proton-proton collisions at $\sqrt{s} = 13$ TeV," tech. rep. ATL-COM-PHYS-2016-407, CERN, 2016, URL: https://cds.cern.ch/record/2149445.

[71] ATLAS Collaboration, *Data-Quality Requirements and Event Cleaning for Jets and Missing Transverse Energy Reconstruction with the ATLAS Detector in Proton–Proton Collisions at a Center-of-Mass Energy of $\sqrt{s} = 7$ TeV*, ATLAS-CONF-2010-038, 2010, URL: http://cdsweb.cern.ch/record/1277678.

[72] J. T. Linnemann, *Measures of Significance in HEP and Astrophysics*, ECONF C030908 **MOBT001** (2003), arXiv: physics.data-an/0312059.

[73] K. Cranmer, *Statistical Challenges for Searches for New Physics at the LHC*, 2006, arXiv: physics.data-an/0511028.

[74] J. T. Robert D. Cousins James T. Linnemann, *Evaluation of three methods for calculating statistical significance when incorporating a systematic uncertainty into a test of the background-only hypothesis for a Poisson process*, Nuclear Instruments and Methods in Physics Research A **595** (2008) pp. 480–501, arXiv: physics.data-an/0702156.

[75] A. Collaboration et al., *Measurement of the 4l Cross Section at the Z Resonance and Determination of the Branching Fraction of Z-¿ 4l in pp Collisions at sqrt (s)= 7 and 8 TeV with ATLAS*, arXiv preprint arXiv:1403.5657 (2014).

[76] K. Grevtsov et al., "Photon reconstruction using 18.6 pb^{-1} of pp collisions collected by ATLAS at $\sqrt{s} = 13$ TeV in 2015," tech. rep. ATL-COM-PHYS-2015-725, CERN, 2015, URL: https://cds.cern.ch/record/2034889.

[77] S. Alioli et al., *A general framework for implementing NLO calculations in shower Monte Carlo programs: the POWHEG BOX*, JHEP **06** (2010) p. 043, arXiv: 1002.2581 [hep-ph].

[78] G. Aad et al., *Measurement of the ZZ Production Cross Section in pp Collisions at $\sqrt{s} = 13$ TeV with the ATLAS Detector*, Phys. Rev. Lett. **116**.10 (2016) p. 101801, arXiv: 1512.05314 [hep-ex].

[79] J. Alwall et al., *The automated computation of tree-level and next-to-leading order differential cross sections, and their matching to parton shower simulations*, JHEP **07** (2014) p. 079, arXiv: 1405.0301 [hep-ph].

[80] *Recommendations for systematic uncertainties on modelling of MC processes from the Physics Modelling Group*, https://twiki.cern.ch/twiki/bin/view/AtlasProtected/MC15SystematicUncertainties.

[81] J Butterworth et al., "Single Boson and Diboson Production Cross Sections in pp Collisions at sqrts=7 TeV," tech. rep. ATL-COM-PHYS-2010-695, CERN, 2010, URL: https://cds.cern.ch/record/1287902.

[82] "Search for supersymmetry in events with four or more leptons in $\sqrt{s} = 13\,\mathrm{TeV}$ pp collisions using $13.3\,\mathrm{fb}^{-1}$ of ATLAS data.," tech. rep. ATLAS-CONF-2016-075, CERN, 2016, URL: https://cds.cern.ch/record/2206245.

[83] ATLAS Collaboration, *Measurements of four-lepton production in pp collisions at $\sqrt{s} = 8$ TeV with the ATLAS detector*, Phys. Lett. B **753** (2016) p. 552, arXiv: `1509.07844 [hep-ex]`.

[84] G. Aad et al., *Search for supersymmetry in events with four or more leptons in s= 8 TeV p p collisions with the ATLAS detector*, Physical Review D **90**.5 (2014) p. 052001.

[85] M. Flowerdew et al., "Search for supersymmetry in events with four or more leptons in $\sqrt{s} = 13$TeV pp collisions with the ATLAS detector," tech. rep. ATL-COM-PHYS-2016-465, CERN, 2016, URL: `https://cds.cern.ch/record/2151805`.

[86] M. Baak et al., *HistFitter software framework for statistical data analysis*, Eur. Phys. J. C **75** (2015) p. 153, arXiv: `1410.1280 [hep-ex]`.

[87] G. Cowan et al., *Asymptotic formulae for likelihood-based tests of new physics*, Eur. Phys. J. C **71** (2011) p. 1554, [Erratum: Eur. Phys. J.C73,2501(2013)], arXiv: `1007.1727 [physics.data-an]`.

[88] ATLAS Collaboration, *Search for supersymmetry in events with four or more leptons in $\sqrt{s} = 8$ TeV pp collisions with the ATLAS detector*, Phys. Rev. D **90** (2014) p. 052001, arXiv: `1405.5086 [hep-ex]`.

[89] "Expected performance of the ATLAS b-tagging algorithms in Run-2," tech. rep. ATL-PHYS-PUB-2015-022, CERN, 2015, URL: `https://cds.cern.ch/record/2037697`.

[90] ATLAS Collaboration, *Performance of b-Jet Identification in the ATLAS Experiment*, JINST **11** (2016) P04008, arXiv: `1512.01094 [hep-ex]`.

Appendix A

Further Optimization

At present, a simple m_{eff} threshold is sufficient for a discovery of the benchmark signal model described in Section 2.3.2. Further optimization is unnecessary, as any theory that predicts enough high m_{eff} events to allow for a discovery (i.e. any theory with a high enough cross-section in the relevant phase space) could easily be distinguished from the background at present. In effect, the background reduction is effective enough that the limiting factor of the search is the cross-section of the relevant signal models.

In the future, after enough data has been collected, it will be possible to probe models with lower cross-sections. In this case, further optimization may be required to separate signals from the Standard Model background. This section outlines optimization techniques that were studied in the process of optimizing the signal regions for this search.

Further optimization takes advantage of specific properties of the SM backgrounds. The reducible backgrounds Z+jets and $t\bar{t}$ can be controlled by tightening the lepton selection critera, discussed in Appendix B. The contribution of each of the two primary irreducible SM backgrounds, ZZ and $t\bar{t}Z$, can be dramatically reduced by adding two further signal regions requirements.

$t\bar{t}Z$ events contain b-jets (generally one from each t decay), and rejecting events that contain a b-tagged jet reduces the $t\bar{t}Z$ background. Flavor tagging [89, 90] has multiple defined working points, where the name of each point refers to the b-tag efficiency for true b-jets. Since b-tagging is not perfect and can potentially result in a significant number of incorrectly tagged jets, this section looks at each of these working points to find an optimal one. ZZ events generally do not contain $E_{\mathrm{T}}^{\mathrm{miss}}$, defined in Section 4.3, and rejecting events that have $E_{\mathrm{T}}^{\mathrm{miss}}$ greater than some threshold reduces the ZZ background.

Fig. A.1 shows the cumulative distributions of ZZ (A.1a) and $t\bar{t}Z$ (A.1b), varying the $E_{\mathrm{T}}^{\mathrm{miss}}$ cut and b-tagging tightness. In practice, a loose $E_{\mathrm{T}}^{\mathrm{miss}}$ cut and b-jet veto (b-veto) reduces most of each background. The benchmark grid does not contain many b-jets, so a b-veto does not significantly decrease the signal efficiency. Since the $\tilde{\chi}_1^0$ decays produce neutrinos, signal events also contain $E_{\mathrm{T}}^{\mathrm{miss}}$, and a $E_{\mathrm{T}}^{\mathrm{miss}}$ cut does not significantly reduce signal efficiency. Applying a loose $E_{\mathrm{T}}^{\mathrm{miss}}$ cut or b-veto may produce a large increase in projected significance across the signal grid, as shown in Fig. A.2. Generally, the looser cuts tend to perform best, as the loose cuts remove most of the SM background without significantly reducing the signal acceptance. Tighter cuts tend to produce a comparatively small improvement in background rejection, while rejecting a larger fraction of signal events.

Applying a $E_{\mathrm{T}}^{\mathrm{miss}}$ cut and b-veto simultaneously improves the significance more than each cut individually, as shown in Fig. A.3. Thus, for future studies, it may be advantageous to apply a direct $E_{\mathrm{T}}^{\mathrm{miss}}$ cut in the signal regions and to potentially have separate signal regions with and without b-tagged jets (in order to also accommodate signal models with b-jets).

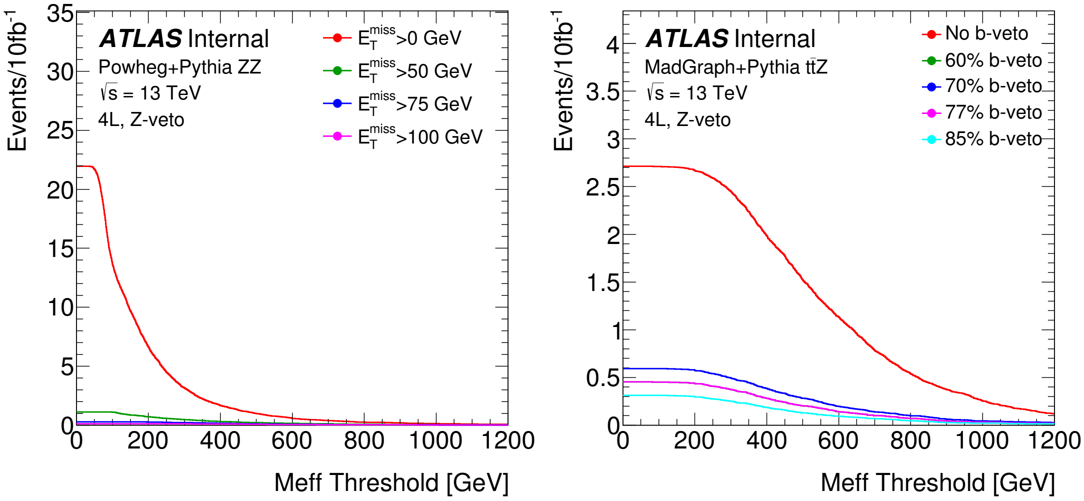

(a) (b)

Figure A.1: The reduction in the primary backgrounds from applying a $E_{\mathrm{T}}^{\mathrm{miss}}$ cut and a b-veto.

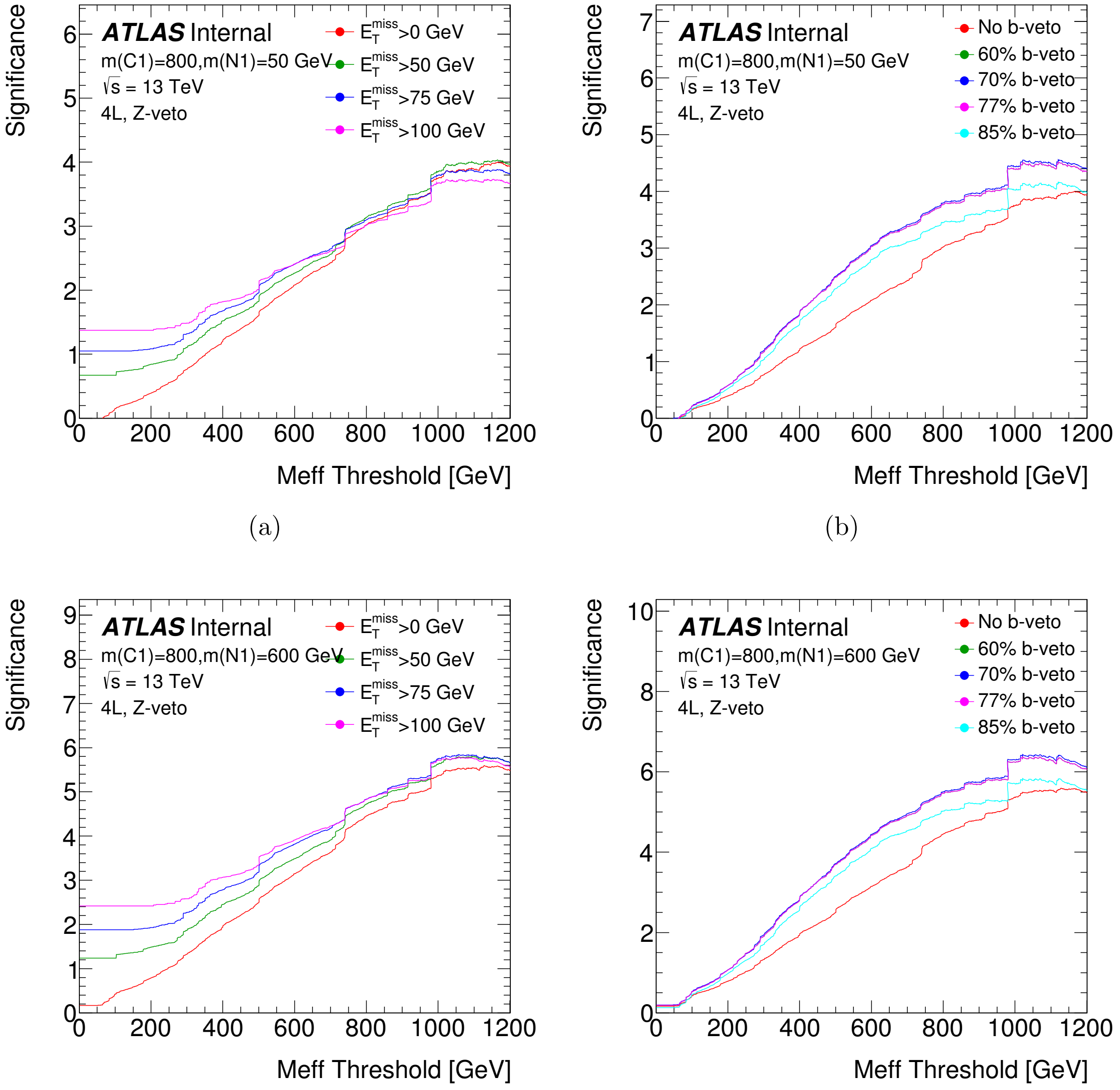

(a)

(b)

(c)

(d)

Figure A.2: Projected significance with different levels of $E_{\mathrm{T}}^{\mathrm{miss}}$ cuts and b-veto levels in two example signal grid points.

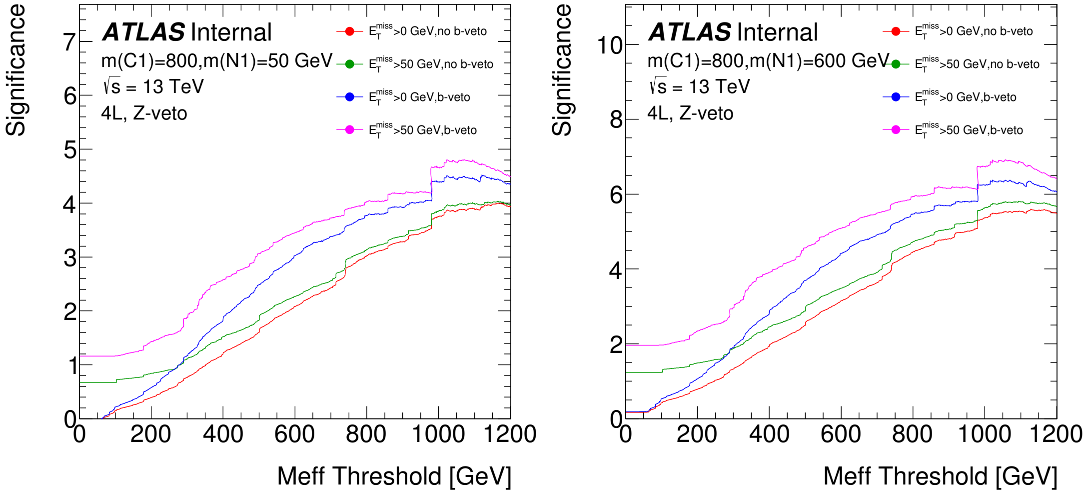

(a)

(b)

Figure A.3: Projected significance in two example grid points with different combinations of a $E_{\mathrm{T}}^{\mathrm{miss}}$ cut and b-veto.

Appendix B

Lepton Selection

As discussed in Section 5.4.2, the lepton selection criteria can have dramatic effects on the event yields in different signal, control, and validation regions. This section covers the optimization of the lepton selection criteria.

In all plots in this section, the red distribution (`Default selection`) corresponds to the lepton selection criteria used in this search, and the other curves correspond to the tightening of at least one of the following criteria:

- `no NearLepCorr.`: Lepton isolation is not corrected for nearby leptons
- p_{T}^{lep}: Muons and electrons are required to have $p_{\mathrm{T}} > 10\,\mathrm{GeV}$
- `LooseEl`: Baseline electrons are required to pass the LooseLH identification (this search uses VeryLooseLH)
- `bjet OR`: In the overlap removal, b-tagged jets are given priority over leptons

The orange curve ($p_{\mathrm{T}}^{lep} > 10\,\mathrm{GeV}$,`b-jet OR`, `LooseEl`) corresponds to the standard lepton selection used in SUSY searches.

To start with, Fig. B.1 shows the Standard Model background event yield, as a function of the m_{eff} threshold. Events are required to have at least four signal leptons and to pass the Z-veto, described in Section 5.4.1. Generally, tightening the lepton selection (i.e. going from the Default selection to any other line) results in a smaller background. Increasing the lepton p_{T} thresholds in particular decreases the background considerably. The lines labeled `LooseEl` only involve tightening the baseline lepton selection, not the signal lepton selection, so tightening that particular criterion has a minimal effect on event yields.

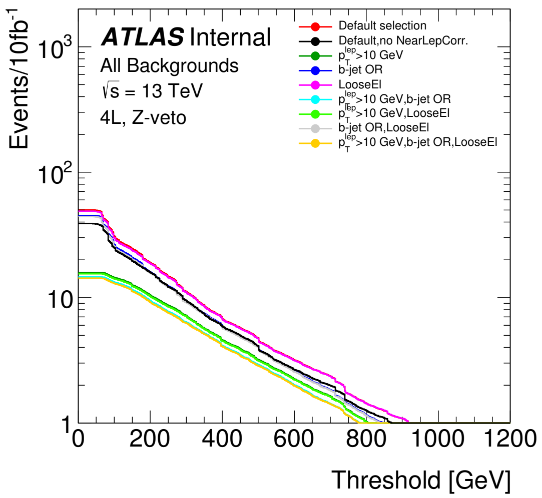

Figure B.1: Number of events in CR2 and SR from $t\bar{t}$ and inclusive backgrounds using more conventional overlap removal and lepton selection criteria.

The distributions for a sample of signal grid points are included in Fig. B.2. The signal acceptance is found to vary almost insignificantly when the lepton selection is tightened. The exception is the nearby lepton isolation correction (black) in cases where the $\tilde{\chi}_1^0$ has low mass 4.2.2. Based on this information alone, tightening the lepton selection increases the projected significance, as shown in Fig. B.3. In all four example grid points, the tightest selection, $p_{\mathrm{T}}^{lep} > 10\,\mathrm{GeV}$,`b-jet OR`,`LooseEl`, has the highest projected significance. This simplified picture ignores the issue of low event yields, however.

Fig. B.4 shows the control region yields, for both data and MC. There is no guarantee or requirement that data and MC agree in the control regions, but it is useful to see that the same general trends are observed. Tightening the lepton selection is observed to dramatically decrease the control region event yield. This behavior results in a large statistical uncertainty on the signal region reducible background measurement, where the reducible background measurement is described

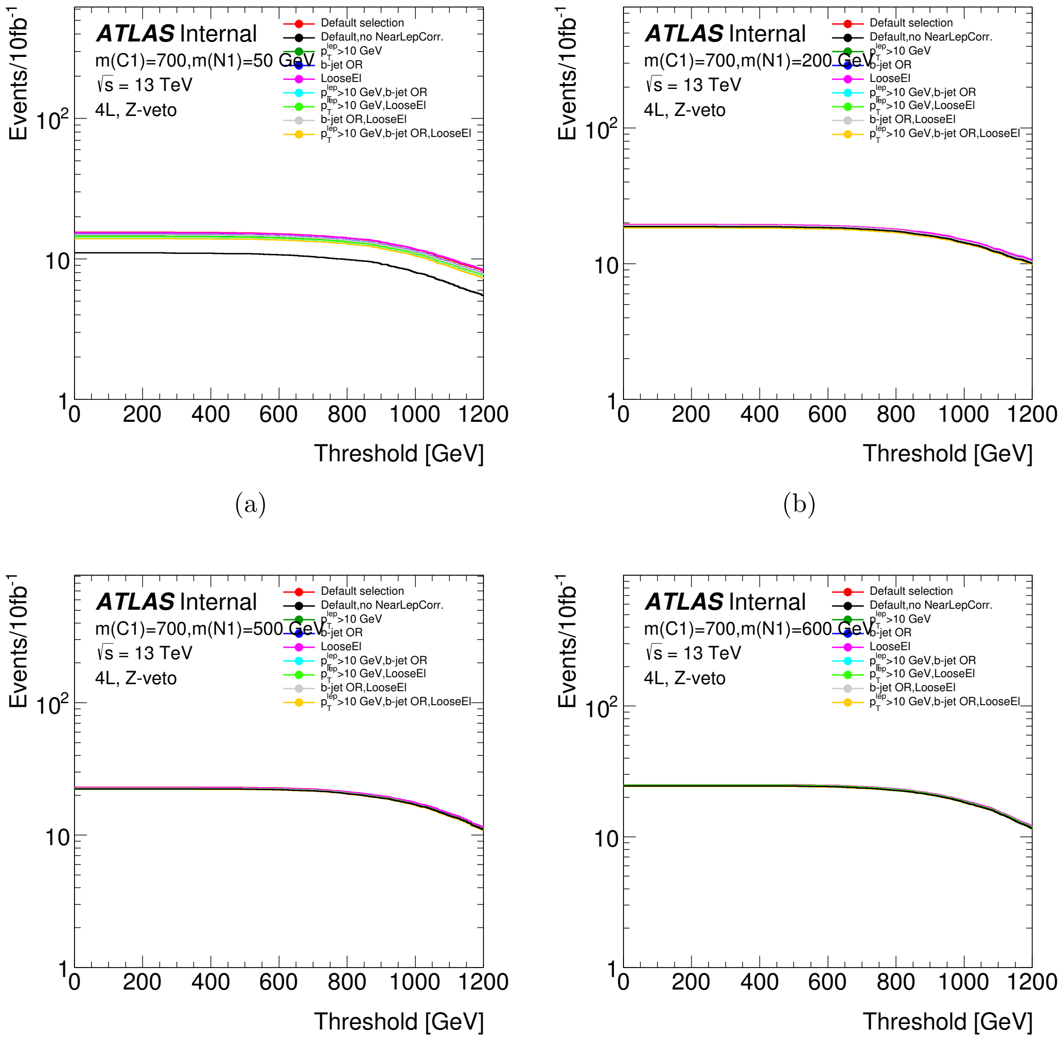

(a)

(b)

(c)

(d)

Figure B.2: Signal grid distributions of the invariant mass for four signal grid points. All distributions show the same $\tilde{\chi}_1^{\pm}$ mass but different $\tilde{\chi}_1^0$ mass.

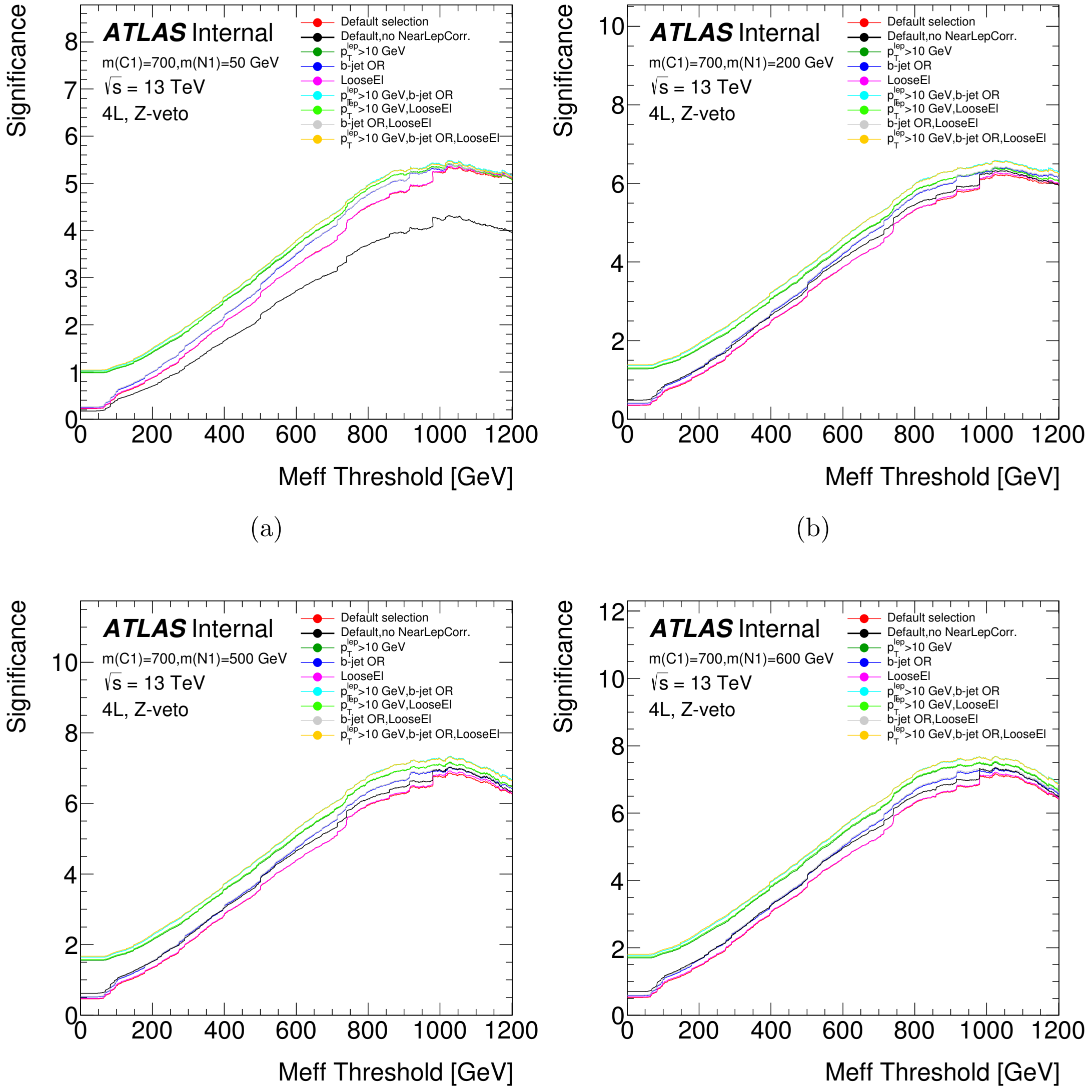

(a)

(b)

(c)

(d)

Figure B.3: Projected significance in two example grid points with different combinations of overlap removal and lepton identification criteria.

in Section 5.6. It is therefore necessary to require a minimum number of events in the control region and to treat this constraint as an extra requirement when defining the signal regions. Fig. B.5 shows the projected significance of four example grid points. In this case, the x-axis is a number of expected control region events, and the plotted value on the y-axis is the projected significance, using the m_{eff} threshold that gives that number of control region events. This figure is redundant with respect to previous figures, in that it can be reproduced directly from Fig. B.4 and Fig. B.3. In all example grid points, if a minimum number of control region events are required, tightening the lepton selection degrades the projected significance. If lepton selection is tightened, then the m_{eff} threshold defining the signal region must be decreased so as not to be dominated by statistical uncertainty, so that the best behavior is observed by using the loosest lepton selection.

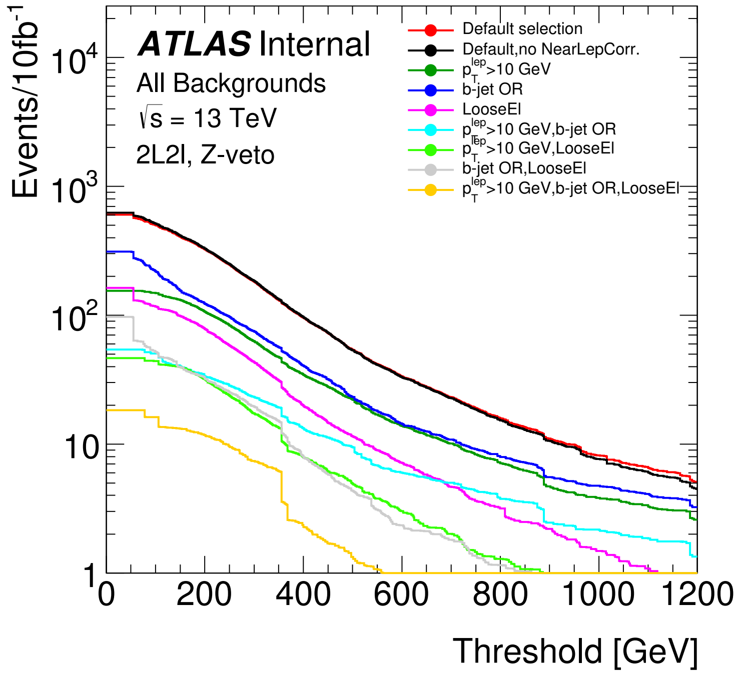

(a) MC

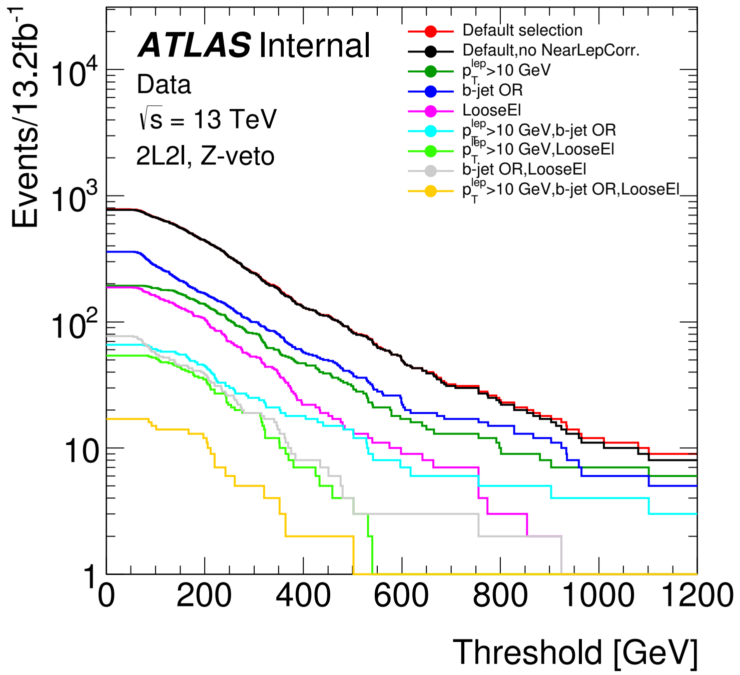

(b) Data

Figure B.4: Number of events in CR2 in MC and data, using different lepton selection criteria.

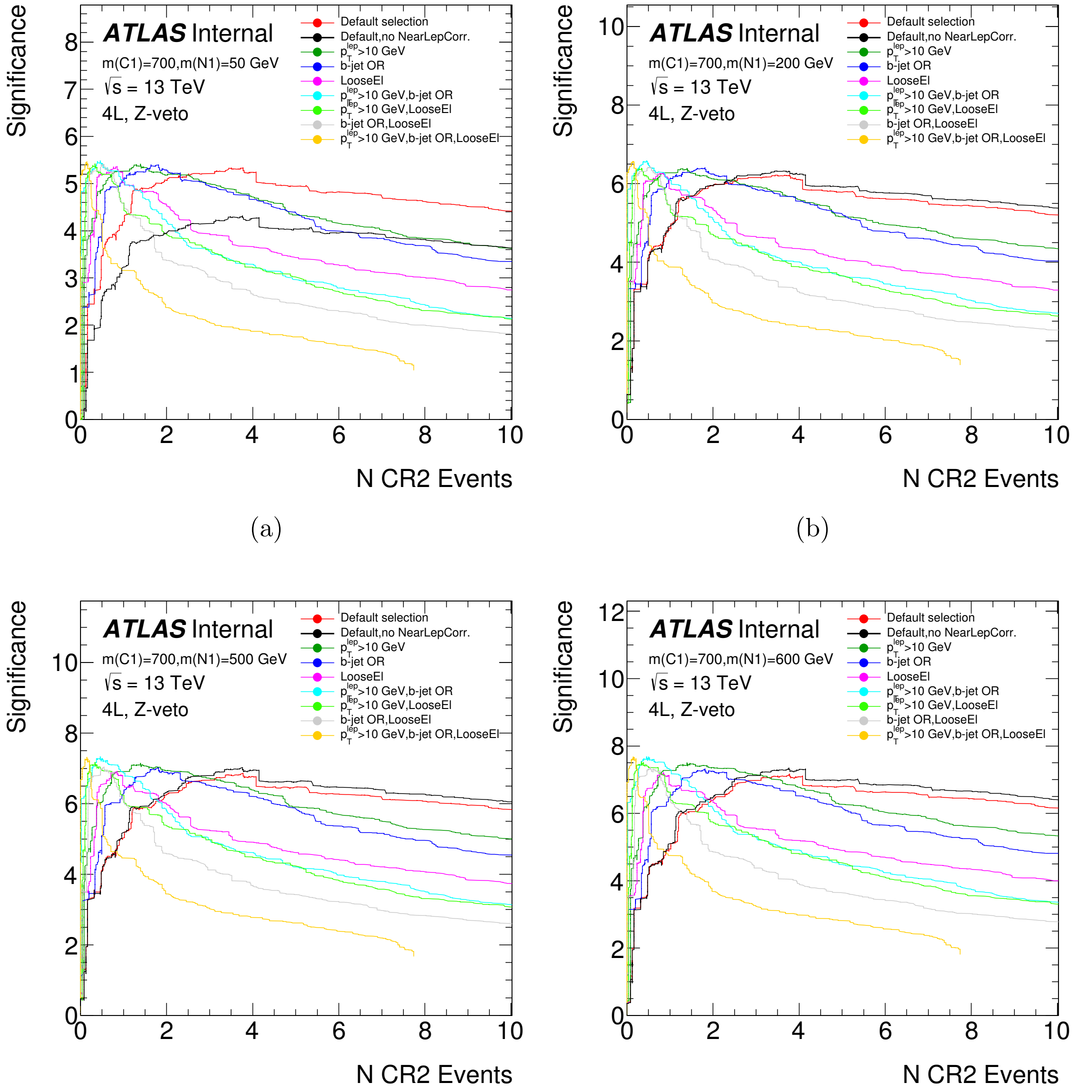

(a) (b)

(c) (d)

Figure B.5: Projected significance in two example grid points with different combinations of a overlap removal and lepton identification criteria, as a function of the number of events in CR2.

Appendix C

Monte Carlo Samples

The Standard Model background and SUSY samples are listed in this section. The SM cross-sections, k-factors (higher order corrections to the cross-section calculation) and generator efficiencies are shown in Table C.1 and Table C.2 for the irreducible backgrounds, Table C.3 for the reducible backgrounds, and Table C.4 for the signal samples. For this search, filter efficiencies are only relevant for $t\bar{t}$ samples, where they correspond to the fraction of $t\bar{t}$ events decaying to each lepton multiplicity final state.

Sample	σ [pb]	k	ϵ
ZZ			
mc15_13TeV.361603.PowhegPy8EG_CT10nloME_AZNLOCTEQ6L1_ZZllll_mll4	1.2568	1.	1.
mc15_13TeV.361073.Sherpa_CT10_ggllll	0.02095	0.91	1.
For a cross-check of systematics			
mc15_13TeV.361063.Sherpa_CT10_llll	12.849	0.91	1.
mc15_13TeV.361073.Sherpa_CT10_ggllll	as above		
mc15_13TeV.363042.Sherpa_CT10_llll_fac4	as 361063		
mc15_13TeV.363043.Sherpa_CT10_llll_fac025	as 361063		
mc15_13TeV.363044.Sherpa_CT10_llll_renorm4	as 361063		
mc15_13TeV.363045.Sherpa_CT10_llll_renorm025	as 361063		
mc15_13TeV.363046.Sherpa_CT10_llll_qsf4	as 361063		
mc15_13TeV.363047.Sherpa_CT10_llll_qsf025	as 361063		
mc15_13TeV.363078.Sherpa_CT10_ggllll_fac4	as 361073		
mc15_13TeV.363079.Sherpa_CT10_ggllll_fac025	as 361073		
mc15_13TeV.363080.Sherpa_CT10_ggllll_renorm4	as 361073		
mc15_13TeV.363081.Sherpa_CT10_ggllll_renorm025	as 361073		
mc15_13TeV.363082.Sherpa_CT10_ggllll_qsf4	as 361073		
mc15_13TeV.363083.Sherpa_CT10_ggllll_qsf025	as 361073		
mc15_13TeV.363484.Sherpa_CT10_llll_ckkw15	as 361063		
mc15_13TeV.363485.Sherpa_CT10_llll_ckkw30	as 361063		
$t\bar{t}Z$			
mc15_13TeV.410111.MadGraphPythia8EvtGen_A14NNPDF23LO_ttee_Np0	0.0096235	1.51	1.
mc15_13TeV.410112.MadGraphPythia8EvtGen_A14NNPDF23LO_ttee_Np1	0.017344	1.51	1.
mc15_13TeV.410113.MadGraphPythia8EvtGen_A14NNPDF23LO_ttmumu_Np0	0.0096462	1.51	1.
mc15_13TeV.410114.MadGraphPythia8EvtGen_A14NNPDF23LO_ttmumu_Np1	0.017361	1.51	1.
mc15_13TeV.410115.MadGraphPythia8EvtGen_A14NNPDF23LO_tttautau_Np0	0.0098874	1.51	1.
mc15_13TeV.410116.MadGraphPythia8EvtGen_A14NNPDF23LO_tttautau_Np1	0.017790	1.51	1.
For the evaluation of systematics			
mc15_13TeV.410202.MadGraphPythia8EvtGen_A14NNPDF23LO_ttee_Np0_scaleUp	as 410111		
mc15_13TeV.410203.MadGraphPythia8EvtGen_A14NNPDF23LO_ttee_Np0_scaleDn	as 410111		
mc15_13TeV.410204.MadGraphPythia8EvtGen_A14NNPDF23LO_ttee_Np1_scaleUp	as 410112		
mc15_13TeV.410205.MadGraphPythia8EvtGen_A14NNPDF23LO_ttee_Np1_scaleDn	as 410112		
mc15_13TeV.410206.MadGraphPythia8EvtGen_A14NNPDF23LO_ttmumu_Np0_scaleUp	as 410113		
mc15_13TeV.410207.MadGraphPythia8EvtGen_A14NNPDF23LO_ttmumu_Np0_scaleDn	as 410113		
mc15_13TeV.410208.MadGraphPythia8EvtGen_A14NNPDF23LO_ttmumu_Np1_scaleUp	as 410114		
mc15_13TeV.410209.MadGraphPythia8EvtGen_A14NNPDF23LO_ttmumu_Np1_scaleDn	as 410114		
mc15_13TeV.410210.MadGraphPythia8EvtGen_A14NNPDF23LO_tttautau_Np0_scaleUp	as 410115		
mc15_13TeV.410211.MadGraphPythia8EvtGen_A14NNPDF23LO_tttautau_Np0_scaleDn	as 410115		
mc15_13TeV.410212.MadGraphPythia8EvtGen_A14NNPDF23LO_tttautau_Np1_scaleUp	as 410116		
mc15_13TeV.410213.MadGraphPythia8EvtGen_A14NNPDF23LO_tttautau_Np1_scaleDn	as 410116		

Table C.1: Primary irreducible background samples

Sample	σ [pb]	k	ϵ
$\boldsymbol{t\bar{t}WW}$			
mc15_13TeV.410081.MadGraphPythia8EvtGen_A14NNPDF23_ttbarWW	0.0080975	1.2231	1.
$\boldsymbol{VVV}$			
mc15_13TeV.361620.Sherpa_CT10_WWW_3l3v	0.008343	1.	1.
mc15_13TeV.361621.Sherpa_CT10_WWZ_4l2v	0.001734	1.	1.
mc15_13TeV.361623.Sherpa_CT10_WZZ_5l1v	0.00021783	1.	1.
mc15_13TeV.361626.Sherpa_CT10_ZZZ_4l2v	0.00044125	1.	0.22542
mc15_13TeV.361625.Sherpa_CT10_ZZZ_6l0v	1.7059e-05	1.	1.
mc15_13TeV.361072.Sherpa_CT10_lllljj_EW6	0.031496	0.91	1.
$\boldsymbol{t\bar{t}t\bar{t}}$/ $\boldsymbol{tt\bar{t}}$ (includes ttW)			
mc15_13TeV.410080.MadGraphPythia8EvtGen_A14NNPDF23_4topSM	0.0091622	1.0042	1.
mc15_13TeV.304014.MadGraphPythia8EvtGen_A14NNPDF23_3top_SM	0.00164	1.	1.
$\boldsymbol{tWZ}$			
mc15_13TeV.410215.aMcAtNloPythia8EvtGen_A14_NNPDF23LO_260000_tWZDR	0.015558	1.	1.
Higgs			
mc15_13TeV.341421.PowhegPythia8EvtGen_CT10_AZNLO_WmH125J_MINLO_eveWWlvlv	0.00133518	0.987551064706	1.0
mc15_13TeV.341423.PowhegPythia8EvtGen_CT10_AZNLO_WmH125J_MINLO_muvmuWWlvlv	0.00133477	0.987852755431	1.0
mc15_13TeV.341427.PowhegPythia8EvtGen_CT10_AZNLO_WmH125J_MINLO_tauvtauWWlvlv	0.00119259	1.1056182392	1.0
mc15_13TeV.341429.PowhegPythia8EvtGen_CT10_AZNLO_WpH125J_MINLO_eveWWlvlv	0.00192652	1.07134893874	1.0
mc15_13TeV.341431.PowhegPythia8EvtGen_CT10_AZNLO_WpH125J_MINLO_muvmuWWlvlv	0.00192652	1.07134893874	1.0
mc15_13TeV.341435.PowhegPythia8EvtGen_CT10_AZNLO_WpH125J_MINLO_tauvtauWWlvlv	0.00192666	1.07127335768	1.0
mc15_13TeV.341447.Pythia8EvtGen_A14NNPDF23LO_WH125_Zllgam	0.00017831	1.20353707588	1.0
mc15_13TeV.341448.Pythia8EvtGen_A14NNPDF23LO_ttH125_Zllgam	4.6193e-05	1.7118703743	1.0
mc15_13TeV.341449.PowhegPythia8EvtGen_CT10_AZNLO_ZH125J_MINLO_eeWWlvlv_VpT	0.024531	1.	1.
mc15_13TeV.341451.PowhegPythia8EvtGen_CT10_AZNLO_ZH125J_MINLO_mumuWWlvlv_VpT	0.024536	1.	1.
mc15_13TeV.341453.PowhegPythia8EvtGen_CT10_AZNLO_ZH125J_MINLO_tautauWWlvlv_VpT	0.0249	1.	1.
mc15_13TeV.344376.PowhegPythia8EvtGen_CT10_AZNLO_ggZH125_eeWWlvlv	0.00183	1.	1.
mc15_13TeV.344378.PowhegPythia8EvtGen_CT10_AZNLO_ggZH125_mumuWWlvlv	0.00183	1.	1.
mc15_13TeV.344380.PowhegPythia8EvtGen_CT10_AZNLO_ggZH125_tautauWWlvlv	0.00183	1.	1.
mc15_13TeV.341471.PowhegPythia8EvtGen_CT10_AZNLOCTEQ6L1_ggH125_ZZ4lep	0.0081266	1.45488273486	1.0
mc15_13TeV.341488.PowhegPythia8EvtGen_CT10_AZNLOCTEQ6L1_VBFH125_ZZ4lep	0.00103101	0.978615629651	1.0
mc15_13TeV.341947.Pythia8EvtGen_A14NNPDF23LO_ZH125_ZZ4l	0.015767	1.45604363544	0.010256
mc15_13TeV.341964.Pythia8EvtGen_A14NNPDF23LO_WH125_ZZ4l	0.00029076	1.27767114215	1.0
mc15_13TeV.343365.aMcAtNloPythia8EvtGen_A14_NNPDF23_NNPDF30ME_ttH125_dilep	0.048237	1.	1.
mc15_13TeV.343366.aMcAtNloPythia8EvtGen_A14_NNPDF23_NNPDF30ME_ttH125_semilep	0.200556788	1.	1.
mc15_13TeV.343367.aMcAtNloPythia8EvtGen_A14_NNPDF23_NNPDF30ME_ttH125_allhad	0.20890322	1.	1.

Table C.2: Secondary irreducible background samples

Sample	σ [pb]	k	ϵ
$t\bar{t}$			
mc15_13TeV.410009.PowhegPythiaEvtGen_P2012_ttbar_hdamp172p5_dil	696.12	1.1949	0.1053
For a cross-check			
mc15_13TeV.410000.PowhegPythiaEvtGen_P2012_ttbar_hdamp172p5_nonallhad	696.11	1.1949	0.543
mc15_13TeV.410500.PowhegPythia8EvtGen_A14_ttbar_hdamp172p5_nonallhad	730.28	1.139	0.543
Z+jets			
mc15_13TeV.361500.MadGraphPythia8EvtGen_A14NNPDF23LO_Zee_Np0	1401.6	1.232	1.
mc15_13TeV.361501.MadGraphPythia8EvtGen_A14NNPDF23LO_Zee_Np1	211.99	1.232	1.
mc15_13TeV.361502.MadGraphPythia8EvtGen_A14NNPDF23LO_Zee_Np2	67.305	1.232	1.
mc15_13TeV.361503.MadGraphPythia8EvtGen_A14NNPDF23LO_Zee_Np3	18.679	1.232	1.
mc15_13TeV.361504.MadGraphPythia8EvtGen_A14NNPDF23LO_Zee_Np4	7.2910	1.232	1.
mc15_13TeV.361505.MadGraphPythia8EvtGen_A14NNPDF23LO_Zmumu_Np0	1402.0	1.232	1.
mc15_13TeV.361506.MadGraphPythia8EvtGen_A14NNPDF23LO_Zmumu_Np1	211.95	1.232	1.
mc15_13TeV.361507.MadGraphPythia8EvtGen_A14NNPDF23LO_Zmumu_Np2	67.353	1.232	1.
mc15_13TeV.361508.MadGraphPythia8EvtGen_A14NNPDF23LO_Zmumu_Np3	18.633	1.232	1.
mc15_13TeV.361509.MadGraphPythia8EvtGen_A14NNPDF23LO_Zmumu_Np4	7.3013	1.232	1.
mc15_13TeV.361510.MadGraphPythia8EvtGen_A14NNPDF23LO_Ztautau_Np0	1397.8	1.232	1.
mc15_13TeV.361511.MadGraphPythia8EvtGen_A14NNPDF23LO_Ztautau_Np1	211.40	1.232	1.
mc15_13TeV.361512.MadGraphPythia8EvtGen_A14NNPDF23LO_Ztautau_Np2	67.176	1.232	1.
mc15_13TeV.361513.MadGraphPythia8EvtGen_A14NNPDF23LO_Ztautau_Np3	18.609	1.232	1.
mc15_13TeV.361514.MadGraphPythia8EvtGen_A14NNPDF23LO_Ztautau_Np4	7.2749	1.232	1.
mc15_13TeV.361628.MadGraphPythia8EvtGen_A14NNPDF23LO_Zee_lowMll_Np0	2677.1	1.232	1.
mc15_13TeV.361629.MadGraphPythia8EvtGen_A14NNPDF23LO_Zee_lowMll_Np1	44.988	1.232	1.
mc15_13TeV.361630.MadGraphPythia8EvtGen_A14NNPDF23LO_Zee_lowMll_Np2	29.292	1.232	1.
mc15_13TeV.361631.MadGraphPythia8EvtGen_A14NNPDF23LO_Zee_lowMll_Np3	6.117	1.232	1.
mc15_13TeV.361632.MadGraphPythia8EvtGen_A14NNPDF23LO_Zee_lowMll_Np4	2.2091	1.232	1.
mc15_13TeV.361633.MadGraphPythia8EvtGen_A14NNPDF23LO_Zmumu_lowMll_Np0	2677.1	1.232	1.
mc15_13TeV.361634.MadGraphPythia8EvtGen_A14NNPDF23LO_Zmumu_lowMll_Np1	44.98	1.232	1.
mc15_13TeV.361635.MadGraphPythia8EvtGen_A14NNPDF23LO_Zmumu_lowMll_Np2	29.302	1.232	1.
mc15_13TeV.361636.MadGraphPythia8EvtGen_A14NNPDF23LO_Zmumu_lowMll_Np3	6.1088	1.232	1.
mc15_13TeV.361637.MadGraphPythia8EvtGen_A14NNPDF23LO_Zmumu_lowMll_Np4	2.2231	1.232	1.
mc15_13TeV.361638.MadGraphPythia8EvtGen_A14NNPDF23LO_Ztautau_lowMll_Np0	2412.4	1.232	1.
mc15_13TeV.361639.MadGraphPythia8EvtGen_A14NNPDF23LO_Ztautau_lowMll_Np1	46.019	1.232	1.
mc15_13TeV.361640.MadGraphPythia8EvtGen_A14NNPDF23LO_Ztautau_lowMll_Np2	28.852	1.232	1.
mc15_13TeV.361641.MadGraphPythia8EvtGen_A14NNPDF23LO_Ztautau_lowMll_Np3	6.0513	1.232	1.
W+jets			
mc15_13TeV.361520.MadGraphPythia8EvtGen_A14NNPDF23LO_Wenu_Np0	13939.	1.20185	1.
mc15_13TeV.361521.MadGraphPythia8EvtGen_A14NNPDF23LO_Wenu_Np1	1894.0	1.20185	1.
mc15_13TeV.361522.MadGraphPythia8EvtGen_A14NNPDF23LO_Wenu_Np2	642.66	1.20185	1.
mc15_13TeV.361523.MadGraphPythia8EvtGen_A14NNPDF23LO_Wenu_Np3	179.18	1.20185	1.
mc15_13TeV.361524.MadGraphPythia8EvtGen_A14NNPDF23LO_Wenu_Np4	70.785	1.20185	1.
mc15_13TeV.361525.MadGraphPythia8EvtGen_A14NNPDF23LO_Wmunu_Np0	13935.	1.20185	1.
mc15_13TeV.361526.MadGraphPythia8EvtGen_A14NNPDF23LO_Wmunu_Np1	1893.3	1.20185	1.
mc15_13TeV.361527.MadGraphPythia8EvtGen_A14NNPDF23LO_Wmunu_Np2	642.70	1.20185	1.
mc15_13TeV.361528.MadGraphPythia8EvtGen_A14NNPDF23LO_Wmunu_Np3	179.19	1.20185	1.
mc15_13TeV.361529.MadGraphPythia8EvtGen_A14NNPDF23LO_Wmunu_Np4	70.761	1.20185	1.
mc15_13TeV.361530.MadGraphPythia8EvtGen_A14NNPDF23LO_Wtaunu_Np0	13920.	1.20185	1.
mc15_13TeV.361531.MadGraphPythia8EvtGen_A14NNPDF23LO_Wtaunu_Np1	1891.9	1.20185	1.
mc15_13TeV.361532.MadGraphPythia8EvtGen_A14NNPDF23LO_Wtaunu_Np2	641.87	1.20185	1.
mc15_13TeV.361533.MadGraphPythia8EvtGen_A14NNPDF23LO_Wtaunu_Np3	179.21	1.20185	1.
mc15_13TeV.361534.MadGraphPythia8EvtGen_A14NNPDF23LO_Wtaunu_Np4	71.012	1.20185	1.
WZ			
mc15_13TeV.361601.PowhegPy8EG_CT10nloME_AZNLOCTEQ6L1_WZlvll_mll4	4.4625	1.	1.
$t\bar{t}W$			
mc15_13TeV.410066.MadGraphPythia8EvtGen_A14NNPDF23LO_ttW_Np0	0.17656	1.32	1.
mc15_13TeV.410067.MadGraphPythia8EvtGen_A14NNPDF23LO_ttW_Np1	0.14062	1.32	1.
mc15_13TeV.410068.MadGraphPythia8EvtGen_A14NNPDF23LO_ttW_Np2	0.13680	1.32	1.
$b\bar{b}$/ $c\bar{c}$ for HF sf			
mc15_13TeV.361250.Pythia8B_A14_NNPDF23LO_bbTomu15	187710.0	1.	1.
mc15_13TeV.361251.Pythia8B_A14_NNPDF23LO_ccTomu15	58528.0	1.	1.

Table C.3: Reducible background samples

Sample	σ [pb]	k	ϵ
Signal			
mc15_13TeV.402200.MGPy8EG_A14N_C1C1_500_10_LLE12k	0.017055	1.	1.
mc15_13TeV.402201.MGPy8EG_A14N_C1C1_500_50_LLE12k	0.01705	1.	1.
mc15_13TeV.402202.MGPy8EG_A14N_C1C1_500_200_LLE12k	0.01699	1.	1.
mc15_13TeV.402203.MGPy8EG_A14N_C1C1_500_400_LLE12k	0.01705	1.	1.
mc15_13TeV.402204.MGPy8EG_A14N_C1C1_500_490_LLE12k	0.017	1.	1.
mc15_13TeV.402205.MGPy8EG_A14N_C1C1_700_10_LLE12k	0.0032396	1.	1.
mc15_13TeV.402206.MGPy8EG_A14N_C1C1_700_50_LLE12k	0.003239	1.	1.
mc15_13TeV.402207.MGPy8EG_A14N_C1C1_700_200_LLE12k	0.00324	1.	1.
mc15_13TeV.402208.MGPy8EG_A14N_C1C1_700_400_LLE12k	0.003239	1.	1.
mc15_13TeV.402209.MGPy8EG_A14N_C1C1_700_600_LLE12k	0.003236	1.	1.
mc15_13TeV.402210.MGPy8EG_A14N_C1C1_700_690_LLE12k	0.003239	1.	1.
mc15_13TeV.402211.MGPy8EG_A14N_C1C1_800_10_LLE12k	0.001586	1.	1.
mc15_13TeV.402212.MGPy8EG_A14N_C1C1_800_50_LLE12k	0.001588	1.	1.
mc15_13TeV.402213.MGPy8EG_A14N_C1C1_800_200_LLE12k	0.001586	1.	1.
mc15_13TeV.402214.MGPy8EG_A14N_C1C1_800_400_LLE12k	0.001587	1.	1.
mc15_13TeV.402215.MGPy8EG_A14N_C1C1_800_600_LLE12k	0.001587	1.	1.
mc15_13TeV.402216.MGPy8EG_A14N_C1C1_800_790_LLE12k	0.001586	1.	1.
mc15_13TeV.402217.MGPy8EG_A14N_C1C1_900_10_LLE12k	0.00081708	1.	1.
mc15_13TeV.402218.MGPy8EG_A14N_C1C1_900_50_LLE12k	0.0008185	1.	1.
mc15_13TeV.402219.MGPy8EG_A14N_C1C1_900_200_LLE12k	0.0008179	1.	1.
mc15_13TeV.402220.MGPy8EG_A14N_C1C1_900_400_LLE12k	0.0008182	1.	1.
mc15_13TeV.402221.MGPy8EG_A14N_C1C1_900_600_LLE12k	0.0008195	1.	1.
mc15_13TeV.402222.MGPy8EG_A14N_C1C1_900_800_LLE12k	0.0008173	1.	1.
mc15_13TeV.402223.MGPy8EG_A14N_C1C1_900_890_LLE12k	0.0008176	1.	1.
mc15_13TeV.402224.MGPy8EG_A14N_C1C1_1000_10_LLE12k	0.00043773	1.	1.
mc15_13TeV.402225.MGPy8EG_A14N_C1C1_1000_50_LLE12k	0.0004379	1.	1.
mc15_13TeV.402226.MGPy8EG_A14N_C1C1_1000_200_LLE12k	0.0004372	1.	1.
mc15_13TeV.402227.MGPy8EG_A14N_C1C1_1000_400_LLE12k	0.0004382	1.	1.
mc15_13TeV.402228.MGPy8EG_A14N_C1C1_1000_600_LLE12k	0.0004372	1.	1.
mc15_13TeV.402229.MGPy8EG_A14N_C1C1_1000_800_LLE12k	0.000438	1.	1.
mc15_13TeV.402230.MGPy8EG_A14N_C1C1_1000_990_LLE12k	0.0004373	1.	1.
mc15_13TeV.402231.MGPy8EG_A14N_C1C1_1100_10_LLE12k	0.00024225	1.	1.
mc15_13TeV.402232.MGPy8EG_A14N_C1C1_1100_50_LLE12k	0.0002423	1.	1.
mc15_13TeV.402233.MGPy8EG_A14N_C1C1_1100_200_LLE12k	0.0002426	1.	1.
mc15_13TeV.402234.MGPy8EG_A14N_C1C1_1100_400_LLE12k	0.0002425	1.	1.
mc15_13TeV.402235.MGPy8EG_A14N_C1C1_1100_600_LLE12k	0.0002425	1.	1.
mc15_13TeV.402236.MGPy8EG_A14N_C1C1_1100_800_LLE12k	0.0002426	1.	1.
mc15_13TeV.402237.MGPy8EG_A14N_C1C1_1100_1000_LLE12k	0.0002426	1.	1.
mc15_13TeV.402238.MGPy8EG_A14N_C1C1_1100_1090_LLE12k	0.0002426	1.	1.
mc15_13TeV.402239.MGPy8EG_A14N_C1C1_1200_10_LLE12k	0.00013743	1.	1.
mc15_13TeV.402240.MGPy8EG_A14N_C1C1_1200_50_LLE12k	0.0001376	1.	1.
mc15_13TeV.402241.MGPy8EG_A14N_C1C1_1200_200_LLE12k	0.0001377	1.	1.
mc15_13TeV.402242.MGPy8EG_A14N_C1C1_1200_400_LLE12k	0.0001377	1.	1.
mc15_13TeV.402243.MGPy8EG_A14N_C1C1_1200_600_LLE12k	0.0001375	1.	1.
mc15_13TeV.402244.MGPy8EG_A14N_C1C1_1200_800_LLE12k	0.0001376	1.	1.
mc15_13TeV.402245.MGPy8EG_A14N_C1C1_1200_1000_LLE12k	0.0001374	1.	1.
mc15_13TeV.402246.MGPy8EG_A14N_C1C1_1200_1190_LLE12k	0.0001376	1.	1.

Table C.4: Signal samples